



University
of Basel

Swiss Nanoscience Institute



EINE INITIATIVE DER UNIVERSITÄT BASEL
UND DES KANTONS AARGAU

Annual Report 2019 Supplement Swiss Nanoscience Institute University of Basel

The Swiss Nanoscience Institute (SNI) is a research initiative of the Canton of Aargau and the University of Basel.

This report summarizes work conducted at the Swiss Nanoscience Institute (SNI) in 2019.

Swiss Nanoscience Institute
Klingelbergstrasse 82
4056 Basel
Switzerland
www.nanoscience.ch

Cover image: Drug-loaded microparticles from polycaprolactone produced by electrospraying in the Nano Argovia project PERIONANO
F. Costanzo (University of Basel), J. Föhr, O. Germershaus, (School of Life Sciences, FHNW)

© Swiss Nanoscience Institute, March 2020

Contents

	SNI PhD School reports	
P1304	Monitoring beta-barrel membrane protein folding	2
P1307	Graphene nanoribbon characterization by Raman spectroscopy and electrical transport	4
P1309	Strong coupling of a nanomechanical membrane to an atomic spin ensemble	6
P1401	Visual proteomics to study Parkinson's disease	8
P1402	Pushing the limits of lightweight materials	10
P1403	Efficient charge manipulation of insulin in high vacuum	12
P1405	Optimization of single crystalline all diamond scanning probes for quantum sensing applications	14
P1406	Investigations of processes relevant for artificial photosynthesis	16
P1501	Nanomechanical microviscometer used to measure protein assembly in real-time	18
P1502	Direct observation of spin fluctuations in antiferromagnetic CoO nanoparticles	20
P1503	Filming biological factories	22
P1504	In situ strain tuning in graphene and study of random strain fluctuations	24
P1505	Programmable electrostatic phased apertures	26
P1601	High aspect ratio gold nanoparticles for enhanced water splitting	28
P1602	Magnetic interactions in adsorbed supra molecular architectures containing trigonal prismatic units	30
P1603	Watching molecular transport in a biological nanopore	32
P1604	Polymer-lipid hybrid membrane: a platform to enhance the activity of Cytochrome c	34
P1606	Smart peptide nanoparticles for efficient and safe gene therapy	36
P1607	Understanding phonon propagation in nanodevices	38
P1701	Towards few layer semiconducting MoS ₂ with superconducting contacts	40
P1702	Grayscale lithography for 3D microfluidics towards the diagnosis of Parkinson's disease	42
P1704	Directed evolution of affinity proteins for biomedical applications	44
P1705	Towards label-free HTS in enzyme engineering	46
P1706	Fiber-based cavity optomechanics	48
P1707	First-order magnetic phase-transition of mobile electrons in monolayer MoS ₂	50
P1708	Freeform optical structure	52
P1801	Bioinspired nanoscale drug delivery systems for efficient targeting and safe in vivo application	54
P1803	Energy dissipation on suspended graphene	56
P1807	Circuit quantum electrodynamics with semi-conducting nanowires	58
P1808	Coupling an ultracold ion to a metallic nanowire	60
	Argovia project reports	
A12.10	Microfluidics to determine the atomic structure of proteins	62
A12.17	3D printable nanoporous Cellophil® membranes for tissue regeneration applications	64
A13.04	Efficient capturing of mRNA for single-cell-transcriptomics	66
A13.08	Disruptive power storage technology applying electrolyte nano dispersions	68
A13.09	Biomimetic growth of calcium phosphate ceramics on Ti implants	70
A13.12	Nano-switchable GPCR-arrestin biochip for drug discovery	72
A13.15	Nanophotonics for quantum sensing technology	74
A14.04	A detector for pesticides in drinking water	76
A14.07	Origami heart model based on nano-patterned paper scaffold for tissue engineering	78
A14.08	Laser ablation of polymers for advanced origination of micro-optical elements	80
A14.13	Novel cancer-targeted nanoparticles	82
A14.15	Nano-in-nano composites for bioresponsive drug delivery	84
A14.19	Customized, nanostructured grating compressors for high repetition rate ultrafast laser	86
	Publication list	88

Monitoring β -barrel membrane protein folding

Project P1304: Folding mechanisms of β -barrel outer membrane proteins and their catalysis by natural holoenzymes and foldases

Project Leader: S. Hiller and D. J. Müller

Collaborators: N. Ritzmann (SNI PhD Student), P. Rios Flores, T. Raschle, and J. Thoma

β -barrel membrane proteins are essential functional components of the outer membrane of Gram-negative bacteria, mitochondria and chloroplasts. Membrane proteins have highly interesting folding properties, since they fold in an external environment that comprises hydrophobic and hydrophilic phases. The biogenesis of these outer membrane proteins (Omps) poses a complex biophysical challenge to the pro- and eukaryotic cell, because the Omps are synthesized at locations distant from their target membrane. The overall essential biological function of Omp biogenesis is accomplished by molecular chaperones that pass the unfolded substrates from the ribosome to the destination membrane [1]. In the Gram-negative bacterium *E. coli*, the periplasmic chaperones SurA and Skp transport the substrate to the Bam complex, which folds and inserts them into the outer membrane [2]. The *in vitro* and the *in vivo* folding mechanisms of β -barrel Omps from mitochondria or Gram-negative bacteria are so far not understood at atomic resolution. The same polypeptide chains can refold *in vitro* in the absence of chaperones and other proteins, resulting in the same three-dimensional β -barrel structures. In this project, we employ structural biological and nanotechnological approaches to characterize the folding process of complex Omps at atomic resolution. In the following, we report on recent papers, which we published since starting our project and thereafter provide an overview of the following challenges in this project.

Monitoring Backbone Hydrogen Bond Formation

The three-dimensional structure of a β -barrel membrane protein is defined by backbone hydrogen bonds between adjacent strands. The biogenesis pathways of β -barrel membrane proteins are essential, but the underlying mechanism is still unclear. To obtain insight into this process, we characterized folding of the 8-stranded OmpX from *E. coli* as a model system and found that the residue-specific kinetics of interstrand hydrogen-bond formation are uniform in the entire β -barrel and synchronized to formation of the tertiary structure [3]. OmpX folding thus propagates via a long-lived conformational ensemble state in which all backbone amide protons engage in hydrogen bonds only transiently. Stable formation of the

entire OmpX hydrogen bond network occurs downhill of the rate-limiting transition state and thus appears cooperative on the overall folding time scale.

Chaperone Assisted Insertion and Folding

The correct insertion and folding of membrane proteins is essential to function in living cells. Whereas in living cells molecular chaperones increase the folding yields of soluble proteins by suppressing misfolding and aggregation, it is not understood how they modulate the insertion and folding of integral membrane proteins into membranes. To study this process, we used single-molecule force spectroscopy (SMFS) and NMR spectroscopy to characterize how periplasmic holoenzyme chaperones SurA and Skp shape the folding trajectory of the large β -barrel Omp FhuA from *E. coli* [4]. After having unfolded and extracted a single FhuA from the lipid membrane by SMFS, we thus monitored how the unfolded polypeptide inserts and folds back into the membrane. The presence of either of the two periplasmic chaperones SurA or Skp prevented misfolding of FhuA by stabilizing a dynamic, unfolded state. Thereby SurA allowed the unfolded substrate to stepwise insert and fold the unfolded FhuA polypeptide towards its native structure.

Directed Insertion of Membrane Proteins

To study whether we could apply the knowledge gained in this proposal and guide the insertion of membrane proteins, we engineered light-driven proton pumps having either a red (RFP) or green (GFP) fluorescent protein fused to its N- or C-terminus [5]. The hydrophilic fluorescent proteins allowed the directed insertion of proton pumps into liposomes and to select the liposomes depending on fluorescence. The manufactured nanoreactors were used to generate proton gradients by light, which is a prerequisite to power a broad variety of biomolecular processes. In the future, this side project will enable to supply nanoscopic factories with energy and to translocate polypeptides or other molecules across membranes.

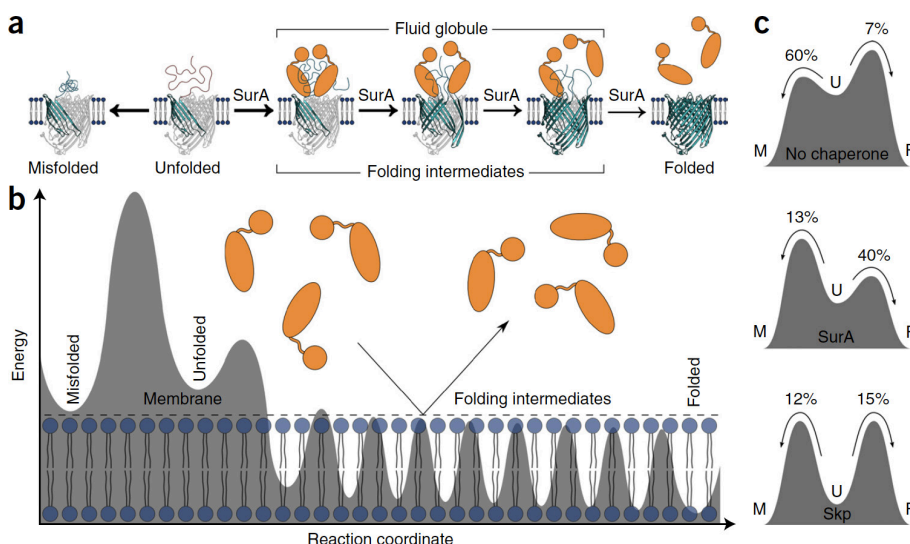


Fig. 1 Folding pathways and free-energy landscape of FhuA receptors. a) Insertion and folding pathways of FhuA in the absence of chaperones and in the presence of SurA (orange). Without chaperones, the majority of unfolded FhuA receptors misfold. SurA stabilizes the unfolded state of FhuA and promotes stepwise insertion and folding of β -hairpins in the lipid membrane. This stepwise insertion of secondary structures proceeds until the receptor completed folding. b) Hypothetical folding free-energy landscape of FhuA in the presence of SurA. SurA (orange) is spatially excluded from the lipid membrane (blue). Each β -hairpin inserted into the lipid membrane is stabilized by a free-energy well. c) Modulation of the folding free-energy landscape by chaperones. The free-energy barriers separating the unfolded (U) from the misfolded (M) and folded (F) states, are determined from the observed folding probabilities. Image taken from ref [4].

Maltoporin Unfolding Pathways

The next challenge in this project was to study whether Omps generally unfold and fold similarly to FhuA. We hence first unfolded maltoporin LamB from *E. coli* by SMFS [6]. It was observed that also maltoporin stepwise unfolds β -hairpins until the β -barrel has been completely unfolded and extracted from the membrane. Thereby, the folding probability of a β -hairpin was found to be correlated to its mechanical stability. The study was fundamental to characterize at later stage the insertion and folding of other Omps by BAM.

BamA Unfolding Pathways

The next challenge in this project was to characterize the unfolding pathways of BamA. These unfolding pathways can then later be used as fingerprint to study the folding of BamA. To approach as native as possible conditions for the unfolding and later for the unfolding process, we developed the utilization of outer membrane vesicles (OMVs) released from *E. coli* to study Omps in the native membrane environment. Enriched in the native membrane of the OMV, we characterize the assembly, folding, and structure of OmpG, FhuA, Tsx, and BamA. Comparing Omps in OMVs to those reconstituted into artificial lipid membranes, we observe different unfolding pathways for some Omps. The observation highlights the importance of the native membrane environment to maintain the native structure and function relationship of Omps.

Next, we studied the unfolding pathways of BamA in OMV in detail [8]. It was observed that the core component of BamA adopts several conformations, which are thought to facilitate the insertion and folding of β -barrel proteins into the bacterial outer membrane. Which factors alter the stability of these conformations remains to be quantified. We thus applied SMFS to characterize the mechanical properties of BamA from *E. coli*. In contrast to the N-terminal periplasmic polypeptide-transport-associated (POTRA) domains, it was found that the C-terminal transmembrane β -barrel domain of BamA is mechanically much more stable. Exposed to mechanical stress, this β -barrel stepwise unfolds β -hairpins until unfolding has been completed. Thereby, the mechanical stabilities of β -barrel and β -hairpins are modulated by the POTRA domains, the membrane composition and the extracellular lid closing the β -barrel. We anticipate that these differences in stability, which are caused by factors contributing to BAM function, promote conformations of the BamA β -barrel required to insert and fold outer membrane proteins.

Latest progress and Challenges Ahead

Currently we are in the process of gathering enough SMFS and NMR data to understand how the Bam complex facilitates the insertion and folding of complex Omps. However, given the complexity of the insertion and folding process and the multiple molecular machines involved in this process (BamA, -B, -C, -D and SurA, Skp, etc), the systematic study of this process requires much more efforts than anticipated. Encouraged by the preliminary results, we are confident that now after all these years of hard work we made a big step towards understanding how the periplasmic chaperones SurA and Skp transport the Omp substrate to the Bam complex, and how they together fold and insert the substrates into functional Omp structure. It may be only a matter of time until we can then use these insights to assemble nanomachines in membranes.

References

- [1] T. J. Knowles, A. Scott-Tucker, M. Overduin, I. R. Henderson, *Membrane protein architects: the role of the BAM complex in outer membrane protein assembly*, *Nat Rev Microbiol* **7**, 206 (2009)
- [2] J. G. Sklar, T. Wu, D. Kahne, T. J. Silhavy, *Defining the roles of the periplasmic chaperones SurA, Skp, and DegP in Escherichia coli*, *Genes Dev* **21**, 2473 (2007)
- [3] T. Raschle, P. Rios Flores, C. Opitz, D. J. Müller, S. Hiller, *Monitoring backbone hydrogen bond formation in β -barrel membrane protein folding*, *Angew Chem Int Ed* **55**, 5952 (2016)
- [4] J. Thoma, B. M. Burmann, S. Hiller, D. J. Müller, *Impact of holdase chaperones Skp and SurA on the folding of β -barrel outer membrane proteins*, *Nat Struct Mol Biol* **22**, 795 (2015)
- [5] N. Ritzmann, J. Thoma, S. Hirschi, D. Kalbermatter, D. Fotiadis, D. J. Müller, *Fusion domains guide the oriented insertion of light-driven proton pumps into liposomes*, *Biophys J* **113**, 1181 (2017)
- [6] J. Thoma, N. Ritzmann, D. Wolf, E. Mulvihill, S. Hiller, D. J. Müller, *Maltoporin LamB unfolds beta-hairpins along mechanical stress-dependent unfolding pathways*, *Structure* **25**, 1139 (2017)
- [7] J. Thoma, S. Manioglou, D. Kalbermatter, P. D. Bosshart, D. Fotiadis, D. J. Müller, *Protein-enriched outer membrane vesicles as a native platform for outer membrane protein studies*, *Communications Biology* **1**, 23 (2018)
- [8] J. Thoma, Y. Sun, N. Ritzmann, D. J. Müller, *POTRA-domains, extracellular lid and membrane composition modulate the conformational stability of the beta-barrel assembly factor BamA*, *Structure* **26**, 987 (2018)

Graphene nanoribbon characterization by Raman spectroscopy and electrical transport

Project P1307: Optoelectronic nanojunctions

Project Leader: M. Calame and M. Mayor

Collaborators: J. Overbeck (SNI PhD Student), O. Braun, M. Perrin, G. Borin Barin, Q. Sun, R. Darawish, Marta De Luca, P. Ruffieux, R. Fasel, C. Daniels, and V. Meunier

Introduction

In this project, we investigate the properties of nanojunctions and their constituents with optical and electronic techniques. Building on the experience from previous years' studies on small molecules [1] and graphene [2], we more recently focussed on bottom-up synthesized graphene nanoribbons (GNRs). These thin strips of graphene promise a variety of properties relevant for future electronic applications.

Optimized Measurement Approaches for Raman Spectroscopy of Graphene Nanoribbons

We use Raman spectroscopy to characterize the GNRs synthesized under UHV conditions by our collaborators at Empa, as this is the only method that currently can provide information about their atomically well-defined structure after transferring from their gold growth-substrates to technologically relevant silicon-based devices.

To attain the most representative and highest signal-to-noise spectra we have optimized the measurement approach used for GNR characterization [3]. Figure 1 shows a sketch of a Si-based device substrate with an optimized layer structure for Raman spectroscopy on a monolayer of GNRs. It further shows spectra extracted from a large area Raman map, highlighting the intensity enhancement and background suppression that is achieved in this way.

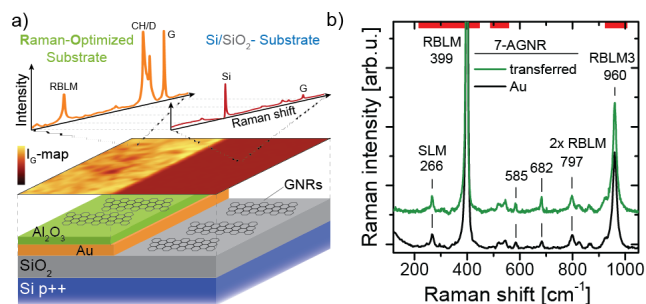


Fig. 1 a) Sketch of the layer structure for a Raman-optimized (RO) device vs. a conventional Si-based substrate. The intensity of the Raman map and the extracted spectra show the advantage of this measurement approach. b) High signal-to-noise spectra obtained by Raman mapping on gold and after transfer to an RO-substrate, revealing low intensity Raman modes of GNRs. The wavenumber ranges indicated by red bars are usually masked by background from the silicon substrate.

Finite element simulations show that the intensity enhancement can be explained by constructive interference when the correct layer thicknesses are chosen for the employed wavelength. Consequently, we can detect low intensity Raman modes and monitor the influence of the transfer process on low frequency ribbons-size-dependent vibrational modes.

Length-Dependent Modes

The above technique has allowed us to identify a longitudinal compressive mode (LCM) that strongly depends on the overall length of the GNRs [4]. In addition to a unique sensitivity to the underlying substrate, which is the focus of an ongoing

investigation, this low energy mode is particularly sensitive to GNR-damage. Figure 2a depicts Raman spectra before and after laser-induced damage to the GNRs, as indicated by the progressive decay in mode intensity shown in the inset. The intensity decay is most prominent for the LCM. Similarly, Figure 2b shows that the LCM can be used to assess damage to the GNR introduced during the transfer process.

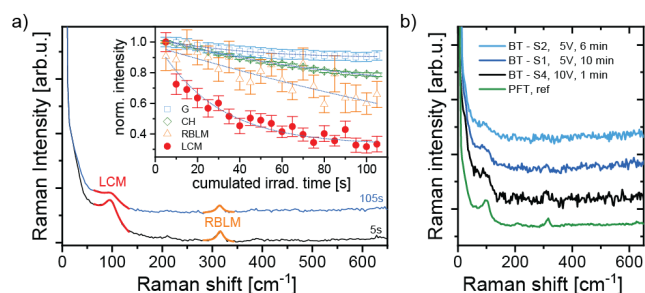


Fig. 2 Damage monitoring via the LCM. a) Low-energy spectra of 9-AGNR as a function of cumulated irradiation time. Inset: Laser-induced decay of mode intensity is most prominent for the LCM. b) Low-energy spectra for different transfer process parameters of bubbling transfer (BT) and a polymer free transfer (PFT) for reference.

Determining GNR-alignment for Optical and Transport Measurements

We have additionally used polarization dependent measurements to verify the alignment preserving transfer of armchair-edge GNRs, enabling the optical characterization of their band structure through a polarization spectroscopy scheme [5]. Such measurements as a function of polarization angle can further be used to determine the relative alignment of GNRs with the source drain axis of samples studied in transport measurements [6].

Pyrene-Based GNRs

In order to unlock the full potential of this material system, GNRs with zigzag or nontrivial edge structure need to be available for device integration.

We have thus investigated a new ribbon designated pGNR with a mixed armchair and zigzag edge structure using both Raman spectroscopy and transport experiments. Figure 3 shows Raman spectra acquired with multiple wavelengths, showing a strong dependence of the Raman cross-section of photon energy [7]. Furthermore, DFT-calculations performed by our collaborators at Rensselaer Polytechnic Institute allow us to assign specific normal mode displacements to each many of the observed peaks.

As a first step, the preservation of the Raman signatures upon transfer to devices leads us to conclude, that the coulomb blockade observed in electrical transport can be attributed to the properties of mostly intact pGNRs. Next, we will investigate in detail the changes in relative intensity between the different GNR modes as a function excitation wavelength, for these and other types of GNRs.

Summary and Outlook

We have developed measurement approaches for Raman spectroscopy tailored to the investigation of GNRs, which has allowed us to characterize them with unprecedented detail. We have identified a longitudinal vibrational mode with a universal length-dependence over all families of armchair GNRs. These findings are now routinely used to provide feedback for GNR growth to improve the material and its processing, with the overall aim of realizing the full potential of GNRs as a nanoelectronic material platform with properties tailored by bottom-up design.

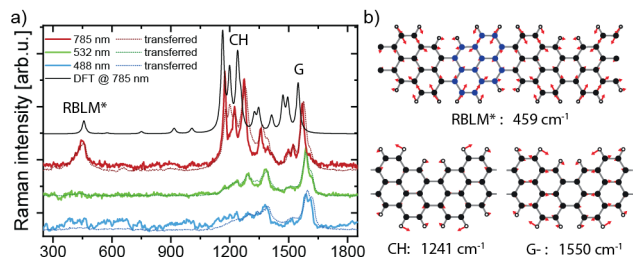


Fig.3 a) Raman spectra of pyrene-based GNR acquired before and after transfer for three different excitation wavelengths, and calculated spectrum for reference. b) DFT-calculated normal mode displacements and Raman shifts for the three modes labelled in a).

Acknowledgements

We thank Roman Furrer for help with CVD-Graphene growth, and Erwin Hack and Ilaria Zardo for fruitful discussions.

References

- [1] A. Vladyka, M. L. Perrin, J. Overbeck, R. R. Ferradás, R. V. García-Suárez, M. Gantenbein, J. Brunner, M. Mayor, J. Ferrer, M. Calame, *In-situ formation of one-dimensional coordination polymers in molecular junctions*, *Nat commun* **10**, 262 (2019)
- [2] L. Wang, S. Zihlmann, A. Baumgartner, J. Overbeck, K. Watanabe, T. Taniguchi, P. Makk, C. Schönenberger, *In Situ Strain Tuning in hBN-Encapsulated Graphene Electronic Devices*, *Nano letters* **19**, 4097–4102 (2019)
- [3] J. Overbeck, G. B. Barin, C. Daniels, M. Perrin, L. Liang, O. Braun, R. Darawish, B. Burkhardt, T. Dumsloff, X.-Y. Wang, et al. *Optimized Substrates and Measurement Approaches for Raman Spectroscopy of Graphene Nanoribbons*. *Phys. Stat. Sol. (b)*(2019)
- [4] J. Overbeck, G. B. Barin, C. Daniels, M. L. Perrin, O. Braun, Q. Sun, R. Darawish, M. de Luca, X.-Y. Wang, T. Dumsloff et al. *A Universal Length-Dependent Vibrational Mode in Graphene Nanoribbons*, *ACS nano* **13**, 13083–13091 (2019)
- [5] S. Zhao, G. B. Barin, T. Cao, J. Overbeck, R. Darawish, T. Lyu, S. Drapcho, S. Wang, S. G. Louie, P. Ruffieux et al. *Optical imaging and spectroscopy of atomic-precise armchair graphene nanoribbons*, *Nano letters*; 10.1021/acs.nanolett.9b04497 (2020)

- [6] M. El Abbassi, M. L. Perrin, G. B. Barin, S. Sangtarash, J. Overbeck, O. Braun, C. Lambert, Q. Sun, T. Prechtl, A. Narita, et al. *Controlled quantum dot formation in atomically engineered graphene nanoribbons field-effect transistors* (2019) arXiv:1912.10712
- [7] Q. Sun, K. Eimre, J. Overbeck, O. Braun, M. L. Perrin, E. Dittler, G. Borin Barin, C. Daniels, V. Meunier, O. Gröning et al. *Massive Dirac fermion behavior in a low band gap graphene nanoribbon near a topological phase boundary*. To appear in *Adv. Mat.* (2020).

Strong coupling of a nanomechanical membrane to an atomic spin ensemble

Project P1309: Cooling and control of a nanomechanical membrane with cold atoms

Project Leader: P. Treutlein and P. Maletinsky

Collaborators: T. Karg (SNI PhD Student), B. Gouraud, C. T. Ngai, G.-L. Schmid, and K. Hammerer

Engineering tailored interactions between quantum systems lies at the heart of many of the recent breakthroughs in quantum science and technology. In this project, we engineer Hamiltonian interactions between the vibrations of a nanomechanical membrane oscillator and the spin precession of an ultracold atomic ensemble [1, 2, 3]. During the past year we reached a major goal of the project by demonstrating strong coupling between the membrane and the spin. Remarkably, the coupling is established over a macroscopic distance of one meter by connecting the atoms and the membrane with laser light [4]. The coupling is highly tunable and allows us to observe normal mode splitting, coherent energy exchange oscillations, two-mode thermal noise squeezing and dissipative coupling of the two systems [4]. Strong coupling between quantum systems typically relies on short-range forces or on high-quality electromagnetic resonator structures in which the systems are placed, restricting the range of the coupling to small distances. Our approach to engineer coherent long-distance interactions with free-space laser beams makes it possible to couple physically very different systems in a modular way, opening up a range of new opportunities for quantum control and sensing in hybrid quantum networks.

Strong light-mediated coupling over a distance

Light is a powerful carrier of quantum information and a versatile tool that allows to remotely couple different quantum systems. In the past year, we published a detailed recipe for generating light-mediated Hamiltonian interactions [4]. Our method relies on connecting the systems in a loop geometry where they couple to the optical field twice. In this way, one can achieve destructive interference of the light-induced quantum noise while at the same time realizing strong bidirectional Hamiltonian coupling.

Our experimental setup allows us to realize such a coherent Hamiltonian coupling between the collective spin of an ensemble of ultracold atoms in an optical dipole trap and a nanomechanical membrane oscillator in an optical cavity, see figure 1. A linearly polarized laser beam first probes the atomic spin precession about a transverse magnetic field via Faraday rotation such that the spin component X_s parallel to the laser axis modulates the light polarization. Using suitable polarization optics we convert this into an optical amplitude modulation between the two arms of a Mach-Zehnder interferometer. By coupling one interferometer arm to the optomechanical cavity the membrane oscillator experiences a radiation pressure force proportional to X_s , resulting in atom-membrane coupling. Oscillations of the membrane position X_m generate a phase modulation of the cavity output field. Recombination of the interferometer arms translates this into a modulation of the laser's circular polarization. The laser beam is directed back at the atomic ensemble with a small angle to spatially separate it from the input beam. The circular polarization modulation proportional to X_m now produces an effective magnetic field that drives Rabi oscillations of the spins, thus generating membrane-atom coupling. As both directions of the light-mediated interaction act simultaneously, mechanical and spin excitations are exchanged in a coherent fashion if the Larmor frequency of the spin is tuned into resonance with the vibration frequency of the membrane.

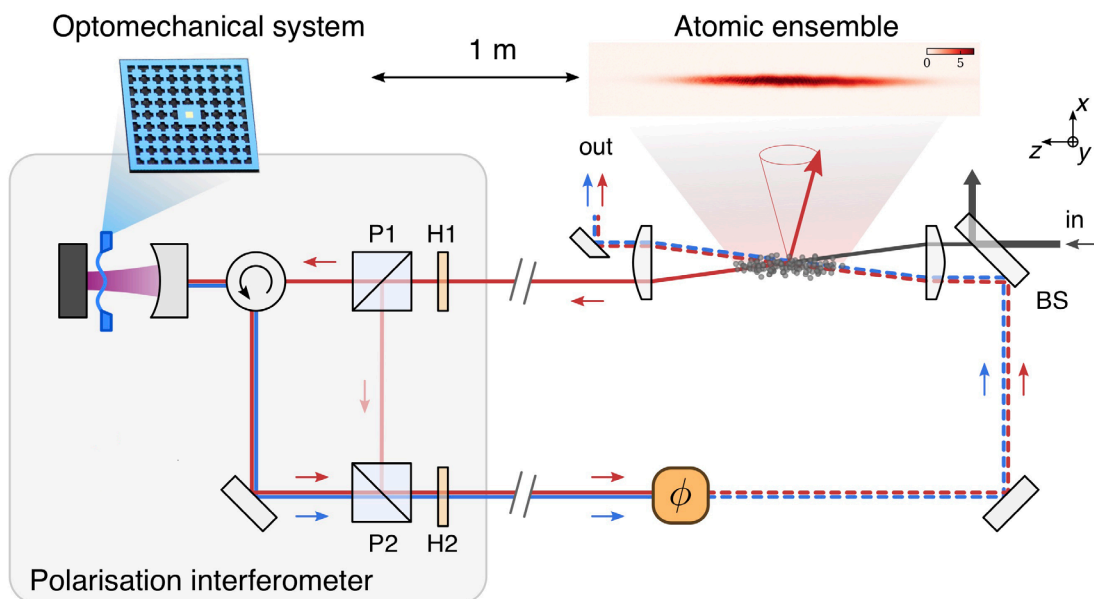


Fig. 1 Sketch of the experimental setup. A laser beam mediates strong Hamiltonian coupling between a collective atomic spin and a nanomechanical membrane oscillator inside an optical cavity.

Spin-membrane normal mode splitting

Using this scheme we were able to experimentally demonstrate strong spin-membrane coupling, mediated by light over a distance of one meter. The coupling leads to a normal-mode splitting if the two systems are tuned into resonance, which we observe by performing spectroscopy of the membrane with an independent drive and detection beam coupled to the optomechanical cavity. Figure 2 shows spectra of the membrane amplitude and phase response with spin-membrane coupling turned off (uncoupled) and with coupling beam turned on (coupled). The uncoupled membrane exhibits a Lorentzian resonance of linewidth $2\pi \times 0.3$ kHz, broader than the intrinsic linewidth due to optomechanical damping by the red-detuned cavity field. When we turn on the coupling to the spin, the resonance splits into two hybrid spin-mechanical normal modes. This signals strong coupling, where the spin-membrane coupling g dominates over local damping. Fitting the well-resolved splitting yields $2g = 2\pi \times 6.1$ kHz, which exceeds the average linewidth of $2\pi \times 2$ kHz and agrees with the expectation based on an independent calibration of the systems.

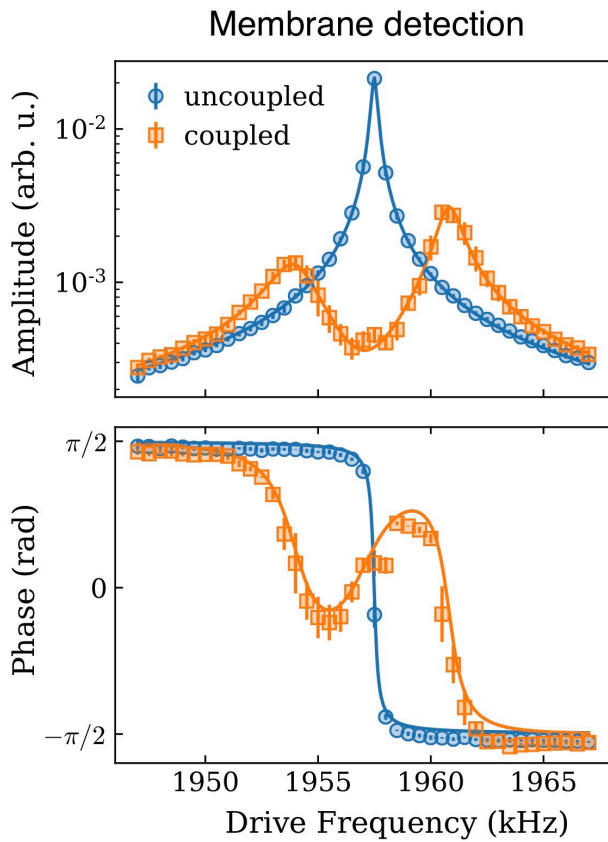


Fig. 2 Spin-membrane normal mode splitting. Spectra of the membrane amplitude and phase response as a function of drive frequency. The uncoupled membrane shows a single Lorentzian line at the mechanical vibration frequency. When resonantly coupled to the atomic spin, the line splits into two well-resolved spin-membrane normal modes, a signature of strong coupling.

Coherent energy exchange oscillations

Having observed the spectroscopic signature of strong coupling, we explore the time domain dynamics in a pulsed experiment. We start by coherently exciting the membrane to $\approx 2 \times 10^6$ phonons, a factor of 100 above its mean equilibrium energy, by applying an amplitude modulation pulse to the drive and detection beam (Fig. 3, top). At the same time, the spin is prepared in its ground state and tuned into resonance with the membrane. The spin-membrane coupling beam is switched on at time $t = 0$ and the displacements $X_s(t)$ and $X_m(t)$ of spin and membrane are continuously monitored via independent detection. From the measured mean square displacements we determine the excitation number of each system, which is shown in figure 3, bottom as a function of the interaction time. The data show coherent and reversible energy ex-

change oscillations from the membrane to the spin and back with an oscillation period of $T \approx 150 \mu\text{s}$, in accordance with the value π/g extracted from the observed normal-mode splitting.

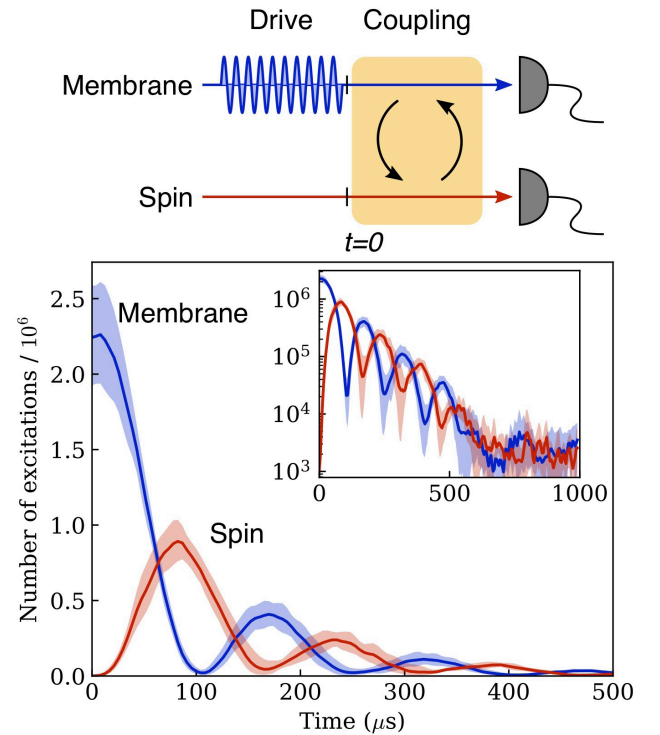


Fig. 3 Coherent energy exchange oscillations between spin and membrane demonstrate strong coupling in the time domain.

We also studied several other dynamical regimes of the coupled spin-membrane system, demonstrating among others two-mode thermal noise squeezing and switching from Hamiltonian to dissipative dynamics. These results will be published in the near future. Our experiments demonstrate a rather general method to create coherent Hamiltonian links between separate and physically distinct systems in a reconfigurable way. This extends the toolbox for quantum networks and opens up a range of exciting opportunities for quantum information processing, simulation and metrology.

References

- [1] M. Aspelmeyer, P. Meystre, K. Schwab, *Quantum optomechanics*, Phys. Today **65**, 7, 29 (2012)
- [2] P. Treutlein, C. Genes, K. Hammerer, M. Poggio, P. Rabl, *Hybrid Mechanical Systems*, in “Cavity Optomechanics” (eds M. Aspelmeyer, T. Kippenberg, and F. Marquardt) 327–351 (Springer, 2014)
- [3] A. Jöckel, A. Faber, T. Kampschulte, M. Korppi, M. T. Rakher, P. Treutlein, *Sympathetic cooling of a membrane oscillator in a hybrid mechanical-atomic system*, Nat. Nanotechnol., **10**, 55–59 (2015)
- [4] T. M. Karg, B. Gouraud, P. Treutlein, and K. Hammerer, *Remote Hamiltonian interactions mediated by light*, Phys. Rev. A **99**, 063829 (2019)

Visual proteomics to study Parkinson's disease

Project P1401: Targeted single cell proteomics using magnetic nanoparticles to study prion-like spreading of amyloid nanoparticles

Project Leader: T. Braun and H. Stahlberg

Collaborators: C. Schmidli (SNI PhD Student), A. Bieri, A. Syntychaki, R. Sütterlin, A. Hierlemann, M. Leist, and S. Gutbier

Introduction

Stereotypic spreading of protein aggregation through the nervous system is a hallmark of many neurodegenerative diseases. For Parkinson's disease (PD), evidence accumulates that 'structural information' for α -synuclein (α -syn) is transmitted between cells, leading to the typical protein aggregation in the target cell. Prion-like proliferation is a potential mechanism for disease progression.

This project aims to study this proliferation of protein aggregates by combining two technologies: (i) Minimalistic tissues: Dopaminergic, neuron-like cells are cultivated in microfluidic chips, enforcing a defined geometrical arrangement of the cell to cell contacts. Two chambers hosting the cell bodies are connected via narrow channels, only allowing the growth of neurites between the chambers (Fig. 1). (ii) Microfluidic sample preparation for electron microscopy (EM): This new technology allows the lossless preparation of whole cell lysate for electron microscopy. The analysis is performed at the nL scale using the cryoWriter set-up developed at the C-CINA. The cell lysate can be analyzed in two ways: Firstly, by a novel untargeted approach called "differential visual proteomics," which allows the proteome-wide detection of structural rearrangements. Secondly, by a targeted approach: proteins are specifically extracted from the cell lysate, which subsequently also allows interaction labeling.

Minimalistic tissue model system for PD

To study the prion-like cell-intrusion and spreading of protein aggregation of α -syn, we use the Lund human mesencephalic (LUHMES) cell line, which can be differentiated to dopaminergic neurons. To enforce two spatially separated cell populations, such as diseased and healthy cells, we use microfluidic chips, as shown in figure 1. These chips now allow to "infect" cells in one compartment and with α -syn filament fragments and to observe the spreading of the α -syn aggregation via the neuritis to cells at the other side of the chip by "seeding and transmission" experiments.

These experiments are now analyzed by classical methods, e.g., fluorescence light microscopy. However, today's biophysical and biochemical methods can trace the presence of proteins, but do not allow detecting and monitoring the structural arrangement of the involved proteins or structural strains. Visual proteomics [1, 2] promises to overcome these limitations and complements classical analysis methods.

Differential visual proteomics

We present a method called "differential visual proteomics" geared to study proteome-wide structural changes of proteins and protein-complexes between a disturbed and an undisturbed cell or between two cell populations. To implement this method, the cells are lysed, and the lysate is prepared in a lossless manner for single-particle electron microscopy (EM). The samples are subsequently imaged in the EM. Individual particles are computationally extracted from the images and pooled together while keeping track of which particle originated from which specimen. The obtained particles are then aligned and classified.

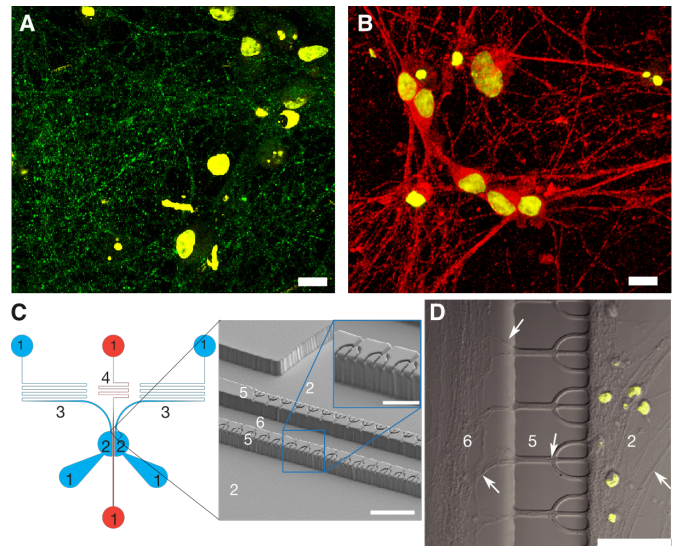


Fig. 1 Cellular model system and minimalistic tissue chip to study the prion-like spreading of amyloid particles. A&B) Differentiation LUHMES cells (day 14). DAPI staining in yellow labeled the cell nuclei. Synaptophysin is a typical marker for the late differentiation stages (A). Tyrosine hydroxylase is a marker for dopaminergic cells, and LUHMES-cells are almost 100 % dopaminergic (B). The synaptophysin labeling shows that the LUHMES cell line can be differentiated to a major neuronal state. Scale bars: 10 μ m. C) Design of the microfluidics for the minimalistic tissue (Bieri et al., to be submitted). Left: Three independent channels exhibit each an inlet and outlet port (1). Two cell culturing chambers (2, blue) are symmetrically arranged towards a central channel (red). The cell culturing channels and central channel are separated by micro-channels (not visible). All three main channels exhibit a flow, which is controlled by resistive channels (3, 4). The flow in the central channel is higher since the restriction (4) is shorter. At the right, an SEM image of the micro-channel region is shown. Note the cell growth chamber (2), and the central channel has a height of approximately 30 μ m, but the micro-channels exhibit only a height of 4 μ m, preventing the passage of the cell somas and only permitting the outgrowth of neurites. The inset shows the indicated region at higher magnification. D) DIC image of LUHMES cells differentiated for 10 d. Nuclei DNA is stained by the DAPI fluorescence dye (yellow) in the cell growth chamber (2). White arrows indicate some neurites. Note the absence of nuclei in the central channel (6), demonstrating the specific permissibility of neurite outgrowth through the microchannel region (5). Scale bars: 50 μ m.

A final quantitative analysis of the particle classes found identifies the particle structures that differ between positive and negative control samples. The algorithm and a graphical user interface developed to perform the analysis and to visualize the results were tested with simulated and experimental data.

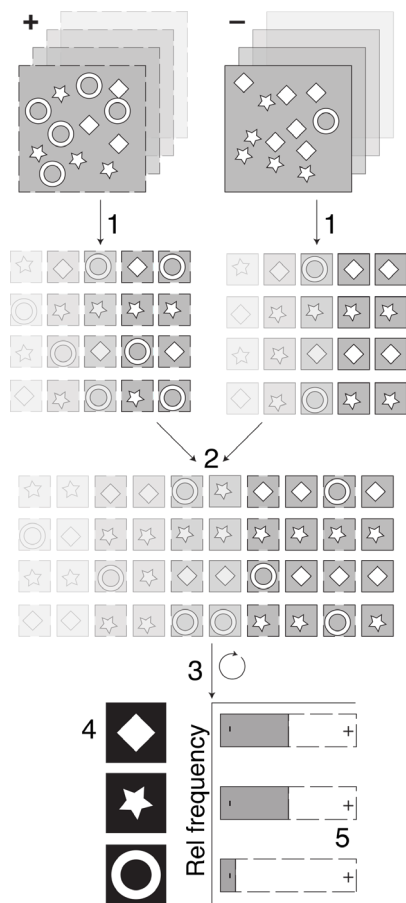


Fig. 2 Principles of “differential visual proteomics” algorithm. Pulse-chase like experiments are performed as positive (+) and negative control (-). Single-cell lysates are prepared for imaging in the EM from both experiments resulting in two stacks of projections of cell lysate constituents (dotted frame for positive control). Three different proteins are shown in white. For analysis, all particles are picked (1) resulting in two galleries of protein projections. Subsequently, the particle galleries are pooled (2). For every particle, the origin (positive or negative control) is known. The combined particle gallery is now subjected to a maximum-likelihood based alignment and classification algorithm (3). The classification and averaging results in class-averages of higher signal to noise ratio compared to the original projections of single molecules (4). Since we know the origin of every particle contributing to a given class, we can screen for classes with significant differences between the positive and negative control (5). These classes are likely responsible for the biological reaction upon the pulse-chase disturbance.

Interaction labeling

This method is using antibodies for target protein recognition and binding. These antibodies are coupled to superparamagnetic particles. An electro-magnetic trap [3] can immobilize both particle types in our microfluidic systems (Fig. 3).

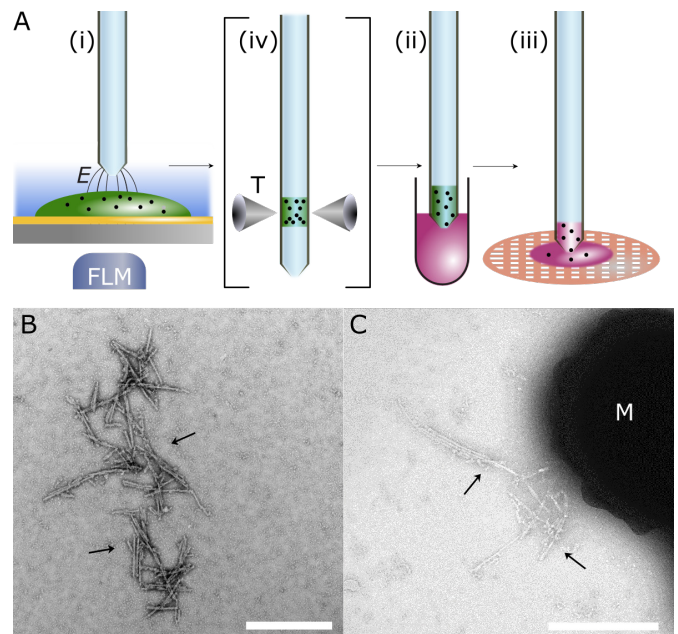


Fig. 3 Single-cell preparation for visual proteomics to analyze incorporated seeds of neuronal cells. A) Single cell lysis of a selected adherent eukaryotic cell by electroporation and simultaneous aspiration of the cell-content (i) in a volume of ≈ 3 nL, conditioning to remove endogenous salts and introduce heavy metal salts for staining (ii), and dispensing of stained single-cell lysate onto an EM-grid (iii). Note that the selection of the cell and the lysis process is monitored by fluorescence light microscopy (FLM). Optionally, the electromagnetic trap (T, see Fig. 2) can be used to immobilize and extract target proteins from the single-cell lysate (iv). B) Typical preparation of a LUHMES cell after seeding with α -syn-fibril fragments. LUHMES cells were grown on a poly-lysine functionalized indium thin oxide (ITO) coated glass-slide and differentiated to dopaminergic neurons. Fluorescently labeled α -syn-seeds were added for several hours and extensively washed away afterward. The uptake of the seeds was confirmed by confocal light microscopy. In the cryoWriter system, an individual cell containing visible seeds in the integrated fluorescence microscope was selected, lysed, and prepared, as shown in panel A (i)-(iii). The seeds can be found again, with the same dimensions as the in vitro generated seeds; however, they seem to be processed by the cell, as it is visible by the attached proteins. The arrows indicate the seeds. C) Similar experiment, but the synthetic seeds were biotinylated before the experiment. Streptavidin-coated superparamagnetic beads (M) were used in a preliminary test to extract the seeds from the single-cell lysate. Scale bars: 500 nm.

References

- [1] A. Syntychaki, L. Rima, C. Schmidli, T. Stohler, A. Bieri, R. Sütterlin, H. Stahlberg, T. Braun, *Differential visual proteomics’: Enabling the proteome-wide comparison of protein structures of single-cells*, *J. Proteome Res.*, **18**(9), 3521–3531 (2019)
- [2] D. Giss, S. Kemmerling, V. Dandey, S. Stahlberg, T. Braun, *Exploring the inter-actome: microfluidic isolation of proteins and interacting partners for quantitative analysis by electron microscopy*, *Anal. Chem.* **86**, 4680–4687 (2014)
- [3] C. Schmidli, S. Albiez, L. Rima, R. Righetto, I. Mohammed, P. Oliva, L. Kovacic, H. Stahlberg, T. Braun, *Microfluidic protein isolation and sample preparation for high-resolution cryo-EM*, *Proc. Natl. Acad. Sci. U.S.A.*, **116**(30), 15007 (2019)

Pushing the limits of lightweight materials

Project P1402: Lightweight structures based on hierarchical composites

Project Leader: C. Dransfeld and C. Schönerberger

Collaborators: W. Szmyt (SNI PhD Student) and C. Padeste

Context

Modern high-performance structural parts are often made of carbon fibre (CF)-reinforced plastics because of their excellent mechanical properties and low weight. Their mechanical advantages are well-pronounced mainly in the fibre direction, dominated by the CF properties. However, in the direction perpendicular to the fibre or upon shear loading, the mechanical performance is significantly weaker, governed by the properties of the polymer matrix and fibre-matrix interface in particular.

We aim to significantly enhance the fibre-matrix interface by synthesizing carbon nanotubes (CNTs) directly on the surface of the CF, thus creating a hierarchical composite (see Fig. 1). The CNTs exhibit outstanding mechanical properties, which makes them a great choice for the nanoscale reinforcement. We are synthesizing CNTs directly on the CF in an aligned and dense manner. This approach results in the higher load and alignment of CNTs in the matrix between the fibres as compared to other approaches, e.g. CNT dispersion in the matrix or grafting of CNTs onto CF using electrophoresis [1].

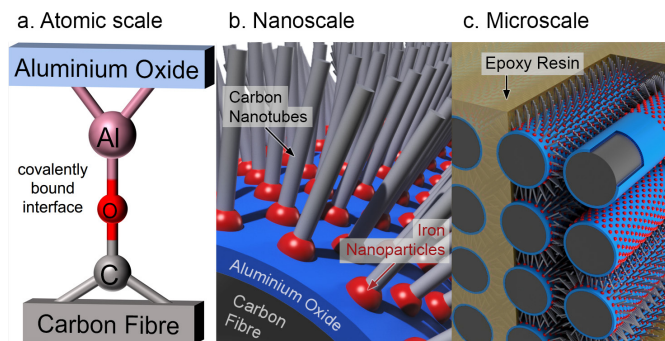


Fig. 1 Schematic illustration of the considered scales of the hierarchical composite; a. atomic scale - covalent bonds need to be ensured; b. nanoscale - the CNT synthesis and nano-reinforcement takes place, c. microscale - multiple fibres pack together in a bulk composite.

It has been shown, that in the chemical vapour deposition (CVD) process of CNT synthesis, the CF mechanical properties are severely deteriorated [2], which poses a challenge. We have identified that the migration of the iron catalyst nanoparticles into CF is contributing to this process and that a 12 nm thick aluminium oxide film provides a sufficient diffusion barrier, ensuring the protection of the CF in the harsh CVD conditions [3]. However, the adhesion of the alumina to the CF, measured as interfacial shear strength (IFSS), diminishes substantially at the high temperature conditions of the CNT synthesis. This issue is addressed in this study. We have developed a process that relies on an increase of the number of covalent bonds between the film and the fibre. For this purpose, we have modified the atomic layer deposition (ALD) process used to coat the CF with alumina. In the classical ALD process, one alternately exposes the substrates to vapours of water and trimethylaluminium (TMA), forming an extremely uniform layer of aluminium oxide with atomic-precision control of thickness. In

the new approach, we are employing a pre-treatment of CF with ozone and we entirely replace water with ozone in order to promote the covalent bonding.

We have been testing the IFSS between alumina and CFs by means of single fibre pull-out test using the FIMATEST setup by Textechno Herbert Stein GmbH & Co. KG, Germany [4]. In order to elucidate the particular mechanisms of failure, the pulled-out fibre tips were analysed by scanning electron microscopy (SEM).

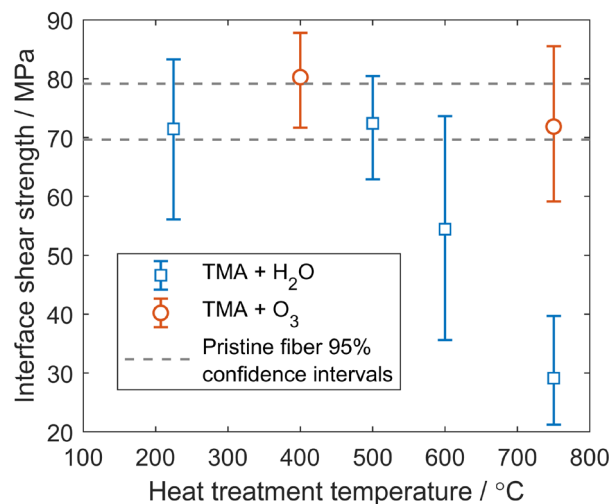


Fig. 2 IFSS of the CF-alumina interface with as a function of the heat treatment temperature. The original IFSS is retained with for fibres coated using the TMA+O₃ process.

Experiments and results

The results of the mechanical testing of the fibre-matrix interface are summarised in figure 2. The declining trend of the IFSS at increasing heat treatment temperatures for the CFs coated with aluminium oxide with the classical TMA+H₂O ALD is in agreement with our previous findings from single fibre fragmentation testing. Our new approach of pretreatment of the CF with ozone and replacing water with ozone entirely in the ALD process (TMA+O₃) is found to improve on the thermo-mechanical stability of the interface as compared to TMA+H₂O and to retain the IFSS at the level of the interface between the matrix and pristine fibres.

SEM examination of the CF tips after the pull-out test (Fig. 3) showed that the alumina film has been partially peeled off from the TMA+H₂O sample heat-treated at 600°C. This means, that the alumina-CF interface failed on a large fraction of the embedded surface. In contrast, the TMA+O₃ sample heat-treated at 750°C does not exhibit this kind of feature, i.e. the alumina film remained on the CF surface and the failure occurred at the alumina-resin interface. This leads to the conclusion, that we have established a CF-alumina interface, which is able to withstand the harsh CVD conditions of CNT growth.

The other goal of this study has been to achieve a controlled, dense and aligned growth of CNTs on complex surfaces such as CF fabrics or tows. Here, we are showing the results of CNT syntheses that we found applicable to alumina-coated surfaces. For a homogeneous CNT growth, it is critical to coat the surface uniformly with a thin film of catalyst. We developed a method of catalyst coating that relies on amine surface functionalization, which subsequently facilitates the uniform precipitation of catalyst precursor from an iron salt solution. The CVD of CNTs was performed at 725°C in a similar way as described in our previous work [3]. The SEM images of growth results are given in figure 4. The growth is remarkably homogeneous. The higher magnification images (Fig. 6b,c) qualitatively indicate a high apparent degree of CNT alignment and high areal density of the CNT forests on the Si substrate. The images in figure 6 d-f demonstrate the homogeneous, dense and aligned CNT growth obtained on the CF woven.

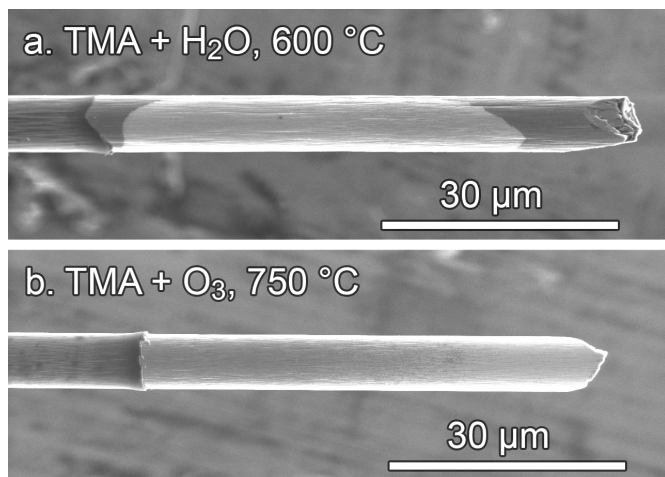


Fig. 3. Interface failure analysis by SEM imaging of the typical fibre tips after pull-out test. The ALD configuration and heat treatment temperatures are noted in the figure.

Summary and conclusion

The current results show a new perspective on achieving the CNT synthesis on CFs while successfully mitigating the detrimental effects on the mechanical properties of the fibres in the process. The 12 nm thick alumina film protects the fibre under the CVD conditions and we have developed a method that allows to preserve the CF-alumina IFSS. As a consequence, the CF-alumina interface shear strength will not constitute a weak spot of the composite after the CNT growth is performed. Moreover, we have presented the CNT growth of high degree of apparent alignment and density. The CVD parameters still need to be optimized for the desired length of the CNTs and the influence of CNTs on the fibre-matrix IFSS remains yet to be tested. The findings of this study constitute a significant step in the close investigation and development of hierarchical fibre architectures in polymer matrices.

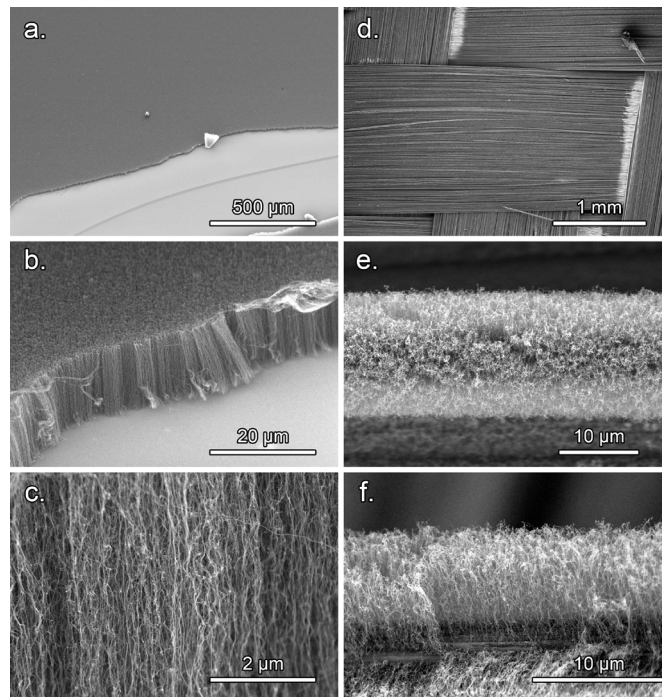


Fig. 4. SEM imaging of CNT growth on a flat surface of a Si wafer (images a-c) and on complex surface of CF (images d-f) at increasing levels of magnification.

References

- [1] H. Qian, E. S. Greenhalgh, M. S. P. Shaffer, A. Bismarck, *Carbon nanotube-based hierarchical composites: a review*, *J. Mater. Chem.* **20**, 4751 (2010)
- [2] Q. Zhang, J. Liu, R. Sager, L. Dai, J. Baur, *Hierarchical composites of carbon nanotubes on carbon fiber: Influence of growth condition on fiber tensile properties*, *Compos. Sci. Technol.* **69**, 594–601 (2009)
- [3] W. Szmyt, S. Vogel, A. Diaz, M. Holler, J. Gobrecht, M. Calame, C. Dransfeld, *Protective effect of ultrathin alumina film against diffusion of iron into carbon fiber during growth of carbon nanotubes for hierarchical composites investigated by ptychographic X-ray computed tomography*, *Carbon* **115**, 347–362 (2017)
- [4] S. Zhandarov et al. *Investigation of interfacial strength parameters in polymer matrix composites: Compatibility and reproducibility*, *Adv. Ind. Eng. Polym. Res.* **1**, 82–92 (2018)

Efficient charge manipulation of insulin in high vacuum

Project P1403: Tailor-made proteins and peptides for quantum interference experiments

Project Leader: V. Köhler and M. Mayor

Collaborators: J. Schätti (SNI PhD Student), U. Sezer, S. Pedalino, J. P. Cotter, M. Debiossac, M. Kriegleder, P. Geyer, A. Shayegi, P. Rieser, G. Richter, G. G. Rondina, D. Häussinger, M. Kerschbaum, L. Mairhofer, Y. Fein, S. Gehrlich, and M. Arndt

Molecular beams for metrology

While analytical chemistry is both a mature and progressing field, experiments on charge-neutral molecules in the gas-phase under high vacuum are scarce and constitute a blind spot. Such experiments hold the potential for highly sensitive measurements of molecular properties in the absence of matrix effects such as magnetic and electric susceptibilities, dipole moments and destruction free UV-VIS and IR spectroscopy [1]. Together with other methods, (i.e. mass spectrometry based tools) they would help to elucidate further the underlying principles of e.g. protein folding and specific intermolecular interactions. While matrix-assisted-laser-desorption-ionization (MALDI) and electro-spray-ionization (ESI) are firmly established methods to launch biomolecules as charged species into the gas phase, such broadly applicable methods are missing for the launch of neutral biomolecules. During the course of this SNI-PhD School project, we have investigated different approaches to enable the destruction free launch of peptides and small proteins: i) thermal evaporation of fluoroalkyl-modified tripeptides [2], ii) femtosecond laser desorption of large fluoroalkyl-decorated peptide constructs with a molecular weight of up to 20 kDa [3], and finally, iii) the controlled charge reduction by photo-cleavage of electro-sprayed ion beams where the analyte carries tailored photoactive tags [4]. While this last method required only a moderate modification of the peptide of interest, the efficiency of the charge reduction process strongly depended on the peptide length, and thus turned out to be not applicable for peptides with more than 6 amino acids.

Tag-design for charge control of large peptides

Our initial design of the photo-cleavable tags, which are based on benzylic ortho-nitroarylethers [5], relied on heterolytic cleavage for charge reduction of electro-sprayed peptide ions in negative ion mode [4]. The heterolytic cleavage pathway, which results in the transfer of a negative charge to the leaving group, dominates for short peptides, but is rapidly outcompeted by a pathway under concomitant H-transfer at increased peptide length. Consequently, a permanent charge ($-SO_3^-$ or $-NMe_3^+$) was installed on the leaving group. As anticipated, this new design permitted efficient neutralization of nonapeptides in positive or negative ion mode, respectively [6]. Surprisingly, also homolytic cleavage was observed as a competing charge depleting cleavage pathway (Fig. 1).

Charge-depletion of insulin

In order to probe the applicability of the method for considerably larger peptides, insulin was modified with three photo-cleavable tags carrying either negatively (negLG $^-$) or positively (posLG $^+$) charged leaving groups. The human insulin employed for modification contains 2 peptide chains, has 51 amino acids and 3 disulfide bonds, which are potentially prone to photo-cleavage [7]. It contains 7 aromatic amino acids, which have a combined extinction coefficient of roughly 1/5 of the photo-cleavable tags at the wavelength of 266 nm employed for photo-cleavage.

Electrosprayed peptide ions of increasing size populate multiple charge states in the gas phase due to an increasing number of ionizable groups and reduced Coulomb repulsion.

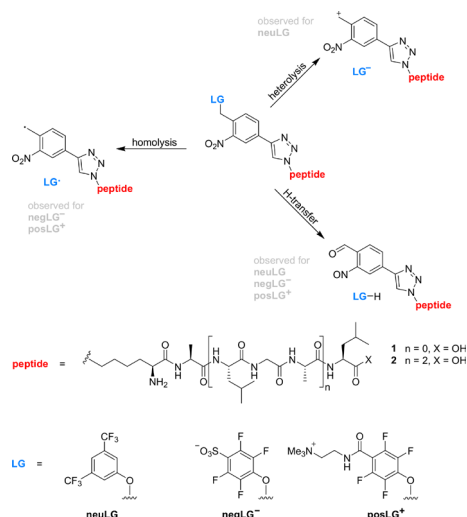


Fig. 1 Cleavage pathways for electro-sprayed model peptides upon laser irradiation under high vacuum. The prevalent cleavage mechanism depends on the nature of the leaving group (LG) and peptide length. While charge reduction was limited to small peptides with neutral leaving groups (neuLG), charged leaving groups (negLG $^-$, posLG $^+$) enable charge depletion for molecules as big as insulin [6].

For charge-reduction-experiments, a single charge state was mass-selected by means of a quadrupole mass filter and formation of the charge reduced species and the leaving group fragment was observed upon laser irradiation. The distribution of charge states was optimized before mass selection by collision with bipolar air formed upon a high voltage discharge (Fig. 2).

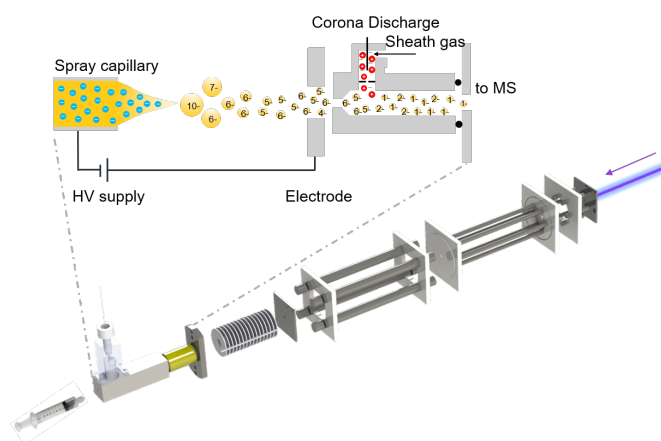


Fig. 2 Experimental set-up for charge-reduction- and neutralization experiments. The charge state distribution of large peptides is first optimized by collision with bipolar air generated by a high-voltage corona discharge. A single charge state is then selected by a quadrupole mass filter and photo-cleavage is realized by a colinear laser beam (266 nm) in a hexapole ion-guide [6].

Cleavage of a single tag is the major process observed upon laser irradiation for all investigated charge states of the tagged insulin (*negIns*). While cleavage efficiency decreases to a certain extent for lower charge states, the process also becomes cleaner and competing electron-detachment or cleavage of a second photo-cleavable tag is not observed anymore. Based on the depletion of the parent peak and concurrent appearance of the leaving group signal, the gas phase neutralization of insulin in high vacuum was demonstrated (Fig. 3).

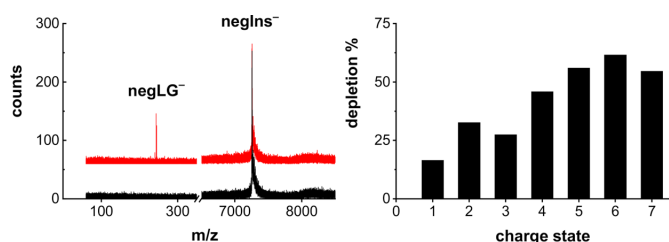


Fig. 3 Neutralization of an insulin construct (*negIns*) carrying three photo-cleavable tags with negatively charged leaving groups (*negLG*⁻). Left: The mass spectrum of *negIns*⁻ with (red) and without (black) laser irradiation is shown. Right: The depletion efficiency decreases as a function of the charge state [6].

References

- [1] P. Geyer, U. Sezer, J. Rodewald, L. Mairhofer, N. Dörre, P. Haslinger, S. Eibenberger, C. Brand, M. Arndt, *Perspectives for quantum interference with biomolecules and biomolecular clusters*, *Phys. Scr.* **91**, 063007 (2016)
- [2] J. Schätti, U. Sezer, S. Pedalino, J. P. Cotter, M. Arndt, M. Mayor, V. Köhler, *Tailoring the volatility and stability of oligopeptides*, *J. Mass. Spectrom.* **52**, 550 (2017)
- [3] J. Schätti, P. Rieser, U. Sezer, G. Richter, P. Geyer, G. Rondina, D. Häussinger, M. Mayor, A. Shayeghi, V. Köhler, M. Arndt, *Pushing the mass limit for intact launch and photoionization of large neutral biopolymers*, *Commun. Chem.* **1**, 93 (2018)
- [4] M. Debiossac, J. Schätti, M. Kriegleder, P. Geyer, A. Shayeghi, M. Mayor, M. Arndt, V. Köhler, *Tailored photocleavable peptides: fragmentation and neutralization pathways in high vacuum*, *Phys. Chem. Chem. Phys.* **20**, 11412 (2018)
- [5] U. Sezer, P. Geyer, M. Kriegleder, M. Debiossac, A. Shayeghi, M. Arndt, L. Felix, M. Mayor, *Selective photodissociation of tailored molecular tags as a tool for quantum optics*, *Beilstein J. Nanotechnol.* **8**, 325 (2017)
- [6] J. Schätti, M. Kriegleder, M. Debiossac, M. Kerschbaum, P. Geyer, M. Mayor, M. Arndt, V. Köhler, *Neutralization of insulin by photocleavage under high vacuum*, *Chem. Commun.* **55**, 12507 (2019)
- [7] A. Agarwal, J. K. Diedrich, R. R. Julian, *Direct elucidation of disulfide bond partners using ultraviolet photodissociation mass spectrometry*, *Anal. Chem.* **83**, 6455 (2011)

Optimization of single crystalline all diamond scanning probes for quantum sensing applications

Project P1405: Surface-functionalization of diamond nano-magnetometers for applications in nano- and life-sciences

Project Leader: U. Pieleles and P. Maletinsky

Collaborators: M. Batzer (SNI PhD Student), P. Appel, A. Barfuss, L. Thiel, and S. Saxer

Introduction

This project aimed to explore different avenues to optimize the performance of single spins in diamond as quantum sensors for applications in material- and life-sciences. Over the last years, such spins in diamond have been established as highly attractive platforms to perform nanoscale quantum sensing with highest spatial resolution and sensitivity [1]. Various architectures are being pursued [2], from scanning probe tips [3], over diamond mechanical oscillators to “wide-field imaging” geometries [4] containing spin ensembles for magnetometry. Common to all these approaches is the fact that the spins in question need to be placed to within few nanometers of the diamond surface to maximize sensing performance. Such proximity, however, is also known to negatively affect the spin’s quantum coherence properties through ubiquitous, but poorly understood noise sources (creating fluctuating electric-, magnetic- or strain-fields). The goal of this project was to overcome these key limitations for diamond-based sensing technologies by understanding and reducing these noise sources and optimizing the sensor performance itself.

Key experimental results

1. All diamond pyramids

Last year we have successfully implemented and published a novel fabrication technique combining top-down fabrication with bottom over growth to fabricate all diamond nano-pyramids with a sharp tip and native diamond surfaces [5].

Our conventional and established approach consists in placing such emitters into diamond nanopillars, which we fabricate in-house, using advanced nanofabrication tools, including plasma etching of diamond. Such nanopillars enhance light-extraction efficiencies from spins in diamond by at least one order of magnitude and we employ the resulting cylinders as scanning probes for nanoscale magnetometry. One downside of such cylindrical nanopillars (with typical diameters ~200 nm) is that the proximity of the spins to the scanned surface is only poorly controlled – small misalignments in the angle of the pillar with respect to a scanned surface can lead to a significant increase of this distance.

We have developed a new approach which may overcome this issue by a radical change of the geometry of the diamond nanostructure from cylindrical to pyramidal. The diamond nano pyramids are formed by overgrowth of our diamond nanopillars using chemical vapor deposition (CVD) of ultrapure diamond, which is performed at a partner lab at the Fraunhofer Institute in Freiburg. Such CVD growth is highly anisotropic with respect to diamond’s crystalline axes, in that growth along the [111] axes is much faster than growth along [001]. Such overgrowth therefore continuously converts a [001]-oriented diamond nanopillar into a pyramid with [111]-facets. Overgrowth of just few microns of diamond material then yields the near-perfect pyramids shown in figure 1a, with tip-apex radii on the order of 10 nm and a surface roughness of the top facets of below one nanometer.

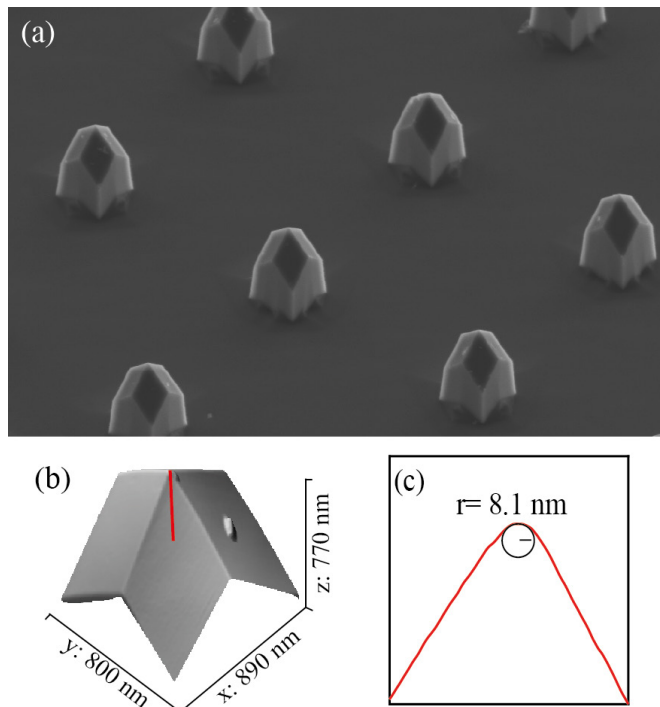


Fig. 1 (a) Single-crystalline diamond nanostructures in form of nanoscale pyramids. The pyramids were created by overgrowth of diamond nanopillars with high-purity diamond material. (b) AFM topography of the top facets of the pyramid structures. (c) shows the in (b) with a red line indicated line cut and the fitted tip radius.

After fabrication of these structures, we have successfully incorporated color center spins into the pyramids by ion implantation. We subsequently conducted systematic studies of the fluorescence properties of these centers, experimentally and by means of simulations. We have observed optically detected electron spin resonance (not shown) and, more importantly, a highly directed fluorescence emission from the pyramids. In particular, we have demonstrated directional emission towards the pyramid base by back-focal plane imaging, which represents a measurement of the angular emission characteristics of the device. We further found a position dependence of the emission resulting in a stronger wave guiding effect for centers placed close to the pyramid apex.

2. Color centers under hydrogen termination at cold temperatures

Hydrogen-terminated surfaces result in a band-bending within the diamond, which typically leads to de-ionization (from negative to neutral or positive) of color centers [6]. While this charge conversion is undesired in the case of NV centers, recent results [6] showed the contrary for SiV centers. Remarkably, such neutral Silicon-Vacancy centers (SiV⁰) have recently been shown to exhibit excellent coherence properties and could therefore be very well suited for quantum sensing [6]. A key difficulty there, however, is the required charge state control to favor SiV⁰ over the normally prevalent SiV⁻ state.

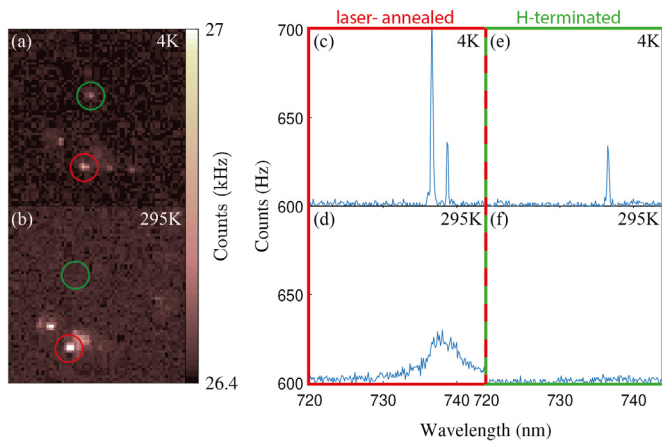


Fig. 2 Hyperspectral mapping of SiV fluorescence from H-terminated diamond: on each point of the map, a full optical emission spectrum was recorded, under 532 nm excitation. (a) and (b) show the integrated counts in the spectral range from 735 nm to 740 nm as a function of position. The spectra were recorded at 4 K (a), (c) and (e) with an excitation power of 100 μ W or at room temperature (b), (d) and (f) with an excitation of 2 mW. In (c) and (d) the spectrum of the laser annealed pillar (see red circle Fig. 2a) is shown at 4 K (c) and 295 K (d). In (e) and (f) the spectrum of an untreated, hydrogen terminated pillar is shown at 4 K (e) and 295 K (f).

During our studies of color centers under hydrogen termination we discovered two interesting phenomena. One is the selective removal of the termination by laser illumination of diamond nano-pillars and the other is a reduction of the band bending effect of hydrogen termination. The former could enable us to develop novel techniques to terminate the diamond surface in situ.

Summary

Project P1405 ended in winter of 2019 with the successful defence of Marietta Batzer's thesis. This project yielded one publication and provided the basic understanding needed of the surface termination and charge state stability needed for the development of a new sensor generation.

References

- [1] J. M. Taylor, P. Cappellaro, L. Childress, L. Jiang, D. Budker, P. R. Hemmer, A. Yacoby, R. Walsworth, M.D. Lukin, *High-sensitivity diamond magnetometer with nanoscale resolution*, Nature Physics **4**, 482 (2008)
- [2] L. Rondin, J.-P. Tetienne, T. Hingant, J.-F. Roch, P. Maletinsky, V. Jacques, *Magneto-metry with nitrogen-vacancy defects in diamond*, Rep. Prog. Phys. **77**, 056503 (2014)
- [3] P. Appel, E. Neu, M. Ganzhorn, A. Barfuss, M. Batzer, M. Gratz, A. Tschoepe, P. Maletinsky, *Fabrication of all diamond scanning probes for nanoscale magnetometry*, Rev. Sci. Instrum. **87**, 063703 (2016)
- [4] M. V. Hauf et al., *Chemical control of the charge state of nitrogen-vacancy centers in diamond*, PRB **83**, 081304 (2011)
- [5] M. Batzer, B. Shields, E. Neu, C. Widmann, C. Giese, C. Nebel, P. Maletinsky, *Single crystal diamond pyramids for applications in nanoscale quantum sensing*, Optical Materials Express **10**, 492 (2020)

- [6] M. V. Hauf, B. Grotz, B. Naydenov, S. Pezzagna, J. Meijer, F. Jelezko, J. Wrachtrup, M. Stutzmann, F. Reinhard, J.A. Garrido, *Chemical control of the charge state of nitrogen-vacancy centers in diamond*, PRB **83**, 081304 (2011)
- [7] B. C. Rose et al., *Observation of an environmentally insensitive solid-state spin defect in diamond*, Science **361**(6397), 60-63 (2018)

Investigations of processes relevant for artificial photosynthesis

Project P1406: Charge transfer versus charge transport in molecular systems

Project Leader: O. S. Wenger and M. Calame

Collaborators: S. Neumann (SNI PhD Student) and J. Overbeck

Introduction

One of the challenges humankind is facing today is the substitution of fossil fuels with more sustainable and less harmful energy sources like the sun. Natural photosynthesis can be seen as a blueprint for solar energy conversion and solar energy storage, which is why a deep understanding of relevant processes is highly desirable. In the course of this SNI-funded project, we aimed to shed more light on two of these processes. Over the past year of the funding period, we have made significant progress along this line of research and consequently there is less focus here on the charge transport studies emphasized in prior annual reports.

Distance dependence of electron-transfer rates

Electron transfer rates (k_{ET}) commonly decrease with increasing distance (r_{DA}) between a donor and an acceptor after photoexcitation [1, 2]. Recently, our group discovered that under some conditions, k_{ET} increases over a certain distance range before the usually observed trend of decreasing k_{ET} with increasing r_{DA} is detected [3, 4]. This counterintuitive phenomenon is relevant in the context of solar energy storage and was therefore investigated in more detail [5].

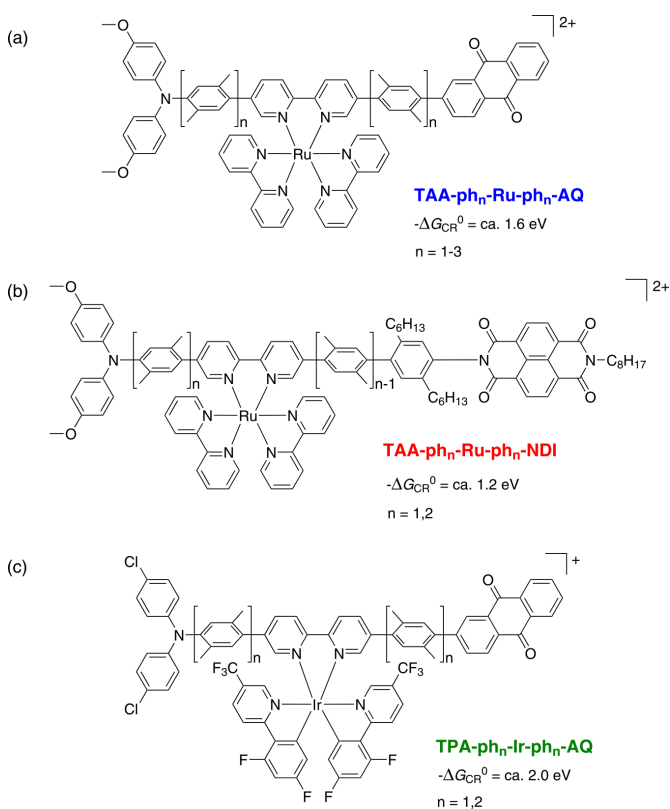


Fig. 1 Donor-sensitizer-acceptor (D-S-A) triads. Reaction free energies (ΔG_{CR}^0) for thermal charge recombination of D^+ / A^- pairs are as indicated.

Our studies concentrated on photoinduced electron transfer in donor-sensitizer-acceptor (D-S-A) compounds in fluid solution and on studying the rates for subsequent thermal elec-

tron-hole pair recombination (k_{CR}). We previously reported on a series of D-S-A systems comprised of a triarylamine (TAA) donor, a $[\text{Ru}(\text{bpy})_3]^{2+}$ (Ru) sensitizer, and an anthraquinone (AQ) acceptor (Fig. 1a)[3, 4]. The driving force for charge recombination in these systems is approximately 1.6 eV according to cyclic voltammetry. We found that the shortest member ($n=1$) of this D-S-A triad series exhibits k_{CR} of ca. 10^5 s^{-1} at r_{DA} of 22.0 Å. Elongating r_{DA} to 30.6 Å accelerated charge recombination and led to k_{CR} of ca. 10^6 s^{-1} [3, 4].

This unusual distance dependence was interpreted in the framework of Marcus theory. With a reaction free energy (ΔG_{CR}^0) of ca. -1.6 eV, charge recombination likely occurs in the so-called inverted regime for the shortest member of this D-S-A series (Fig. 2, purple square). Upon increasing r_{DA} , the reorganization energy (λ) associated with charge recombination increases, shifting the Marcus parabola to the right in figure 2 [3, 4]. In the inverted regime, this can then lead to an increase of k_{CR} upon increasing r_{DA} (right vertical dotted line in Fig. 2), and consequently charge recombination is faster for the compound with $n=2$ (brown square) than for $n=1$ (purple square). If this interpretation is correct, then one would expect this effect to disappear when going to lower driving forces (left vertical dotted line in Fig. 2). Conversely, the effect could become even more pronounced when the driving force is increased. In order to test these two hypotheses, we synthesized and explored two new series of D-S-A triads (Fig. 1b and 1c).

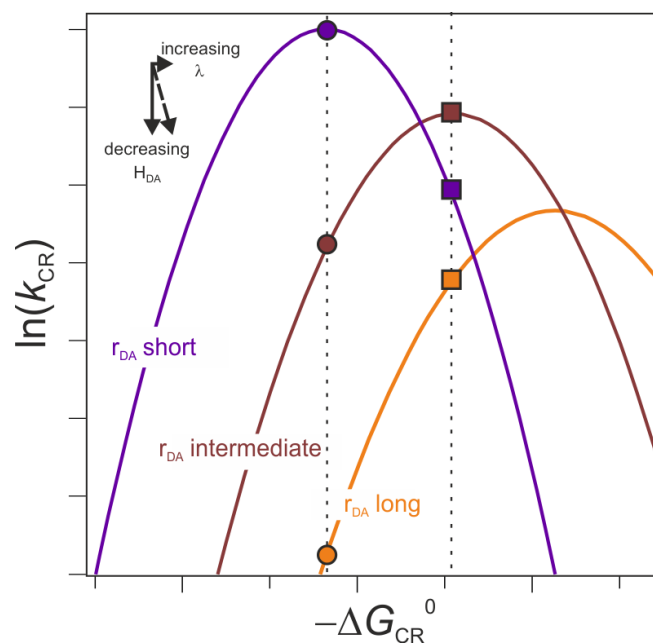


Fig. 2 Schematic driving force dependence of the electron transfer rate (k_{CR}) for different donor-acceptor distances. Squares: Representative for a reaction with a large driving-force; circles: Representative for the expected behavior for a reaction with a small driving-force.

The D-S-A triad series in figure 1b combines a TAA donor and a Ru sensitizer with a naphthalene diimide (NDI) acceptor. This new combination leads to a driving force for thermal charge

recombination of only ca. 1.2 eV. Conversely, in the D-S-A in figure 1c, an electron-deficient TPA donor is combined with an iridium photosensitizer and an anthraquinone acceptor, leading to a driving force of ca. 2.0 eV. Thus, we are now in a position to explore the distance dependence of k_{CR} as a function of driving force. ΔG_{CR}^0 is varied from -1.2 to -1.6 and -2.0 eV, while the distance is increased from 22.0 to 30.6 to 39.2 Å.

We found that in the D-S-A system with a comparatively low driving force of 1.2 eV, k_{CR} decreases with increasing r_{DA} , i. e., the distance dependence is as intuitively expected. This confirms our hypothesis that at lower driving force the distance dependence of k_{CR} is normal (left dotted vertical line in Fig. 2). In the D-S-A system with maximized driving force (2.0 eV), the distance dependence is similar to what we initially observed for the previously investigated system with $\Delta G_{CR}^0 = -1.6$ eV [5]. The unusual distance dependence with electron transfer rate maxima at large donor-acceptor distances is evidently a phenomenon that is encountered only at large driving forces.

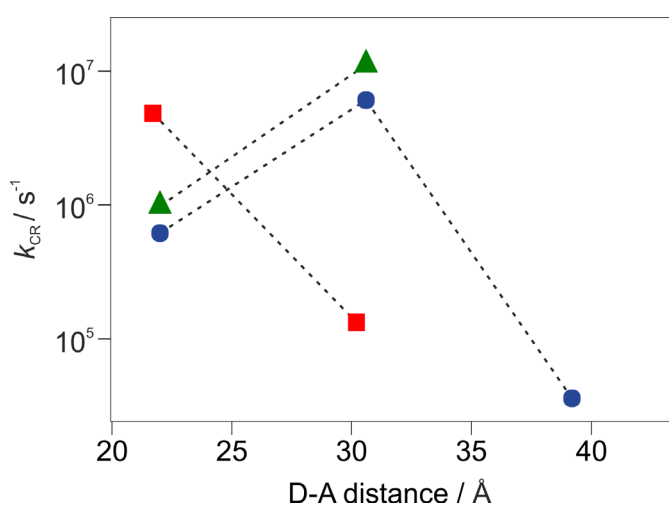


Fig. 3 Distance-dependence of the electron transfer rate for thermal charge recombination for TAA-phn-Ru-phn-NDI (red), TPA-phn-Ir-phn-AQ (green) and TAA-phn-Ru-phn-AQ (blue)[3, 5].

Formation and decay of charge-separated states

The investigation discussed above relies on the formation of charge-separated states (CSSs) in the given compounds. CSSs are also key intermediates in natural photosynthesis, e. g. in the context of charge accumulation[6], but the factors that govern their formation efficiencies are still poorly understood [7].

Our new study on CSSs provides the first complete investigation of all CSS properties and processes that are relevant for artificial photosynthesis, including unwanted reaction pathways that are counterproductive for solar energy conversion and solar energy storage (Fig. 4)[8].

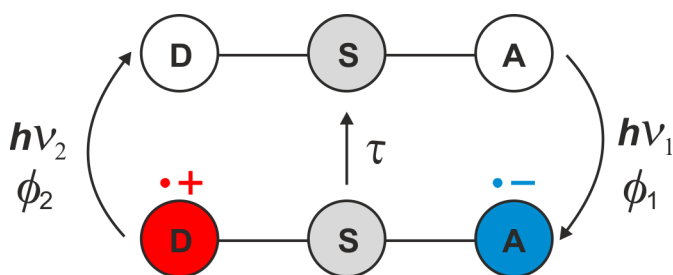


Fig. 4 Schematic representation of the mechanism for light-induced ($h\nu$) formation of a charge-separated state in a molecular donor-sensitizer-acceptor triad together with thermal (τ) and light-induced ($h\nu$) charge recombination [8].

The investigations were performed with the triads TPA-phn-Ir-phn-AQ (Fig. 1c), which can store the unusually large amount of ca. 2 eV of energy in their CSSs. The use of these triads furthermore allowed us to include distance dependence studies. One-pulse laser flash photolysis (LFP) provided deep insights into the CSS formation and we found formation quantum yields of up to 80% when metal-to-ligand charge transfer is the main CSS formation pathway. However, admixture of more unproductive intraligand charge transfer decreases the quantum yield significantly. Additionally, two-color two-pulse LFP revealed a distance dependence of light-induced charge recombination that was unknown so far. The unwanted process of light-induced charge recombination was only observed in the shorter system ($n=1$).

Conclusion

Our new work demonstrates that the distance dependences of electron transfer rates can be controlled by variation of the reaction free energy. Very high driving forces (1.6 or 2.0 eV) lead to qualitatively different distance dependences than lower driving forces (1.2 eV). Additionally, it was shown in the project that donor-acceptor distances also play a key role in light-induced charge recombination reactions. The unique insights we obtained with our studies are highly relevant in the context of artificial photosynthesis and can help to improve future systems.

References

- [1] P. P. Edwards, H. B. Gray, M. T. J. Lodge, R. J. P. Williams, *Electron transfer and electronic conduction through an intervening medium*, *Angew. Chem. Int. Ed.* **47**, 6758 (2008)
- [2] M. Cordes, B. Giese, *Electron transfer in peptides and proteins*, *Chem. Soc. Rev.* **38**, 892 (2009)
- [3] M. Kuss-Petermann, O. S. Wenger, *Increasing Electron-Transfer Rates with Increasing Donor-Acceptor Distance*, *Angew. Chem. Int. Ed.* **55**, 815 (2016)
- [4] M. Kuss-Petermann, O. S. Wenger, *Electron Transfer Rate Maxima at Large Donor-Acceptor Distances*, *J. Am. Chem. Soc.* **138**, 1349 (2016)
- [5] S. Neumann, O. S. Wenger, *Fundamentally Different Distance Dependences of Electron-Transfer Rates for Low and High Driving Forces*, *Inorg. Chem.* **58**, 855 (2019)
- [6] L. Hammarström, *Accumulative Charge Separation for Solar Fuels Production: Coupling Light-Induced Single Electron Transfer to Multielectron Catalysis*, *Acc. Chem. Rev.* **48**, 840 (2015)
- [7] T. Higashino et al., *Remarkable Dependence of the Final Charge Separation Efficiency on the Donor-Acceptor Interaction in Photoinduced Electron Transfer*, *Angew. Chem. Int. Ed.* **55**, 629 (2016)
- [8] S. Neumann, C. Kerzig, O. S. Wenger, *Quantitative Insights into Charge-Separated States from One- and Two-Pulse Laser Experiments Relevant for Artificial Photosynthesis*, *Chem. Sci.* **10**, 5624 (2019)

Nanomechanical microviscometer used to measure protein assembly in real-time

Project P1501: Nanomechanical mass and viscosity measurement-platform for cell imaging

Project Leader: T. Braun and E. Meyer

Collaborators: P. Oliva (SNI PhD Student), B. Bircher, C.-A. Schönenberger, F. Huber, and H. P. Lang

Introduction

To date, most methods used to determine the viscosity and mass density of liquids have several drawbacks: (i) long measurement time (in the range of minutes), (ii) high sample consumption (in the range of milliliters), (iii) the liquid-density and viscosity cannot be measured simultaneously, and, (iv) the measurements cannot be multiplexed. Nano-mechanical transducers promise to overcome these limitations [1, 2].

The viscosity of protein solutions depends on the form and aggregation state of the protein assemblies. Here we demonstrate that nanomechanical viscometers allow the label and functionalization free, time-resolved characterization of protein assembling processes.

Micro-viscometer using nanomechanical membranes

We modified a previously developed high-throughput micro-viscometer [1]. These components allow the liquid characterization using fully clamped, and gold coated silicon-nitride membranes with a thickness of 200 nm (Fig. 1). These Si_3N_4 membranes on a silica wafer form a well for sample deposition. The sample can be loaded from the top using a micro-capillary coupled to a high-precision pump. Typical sample volumes are below 1 μL . To avoid the evaporation of the sample, and to control the temperature, the membrane is placed in a climate chamber (Fig. 1b).

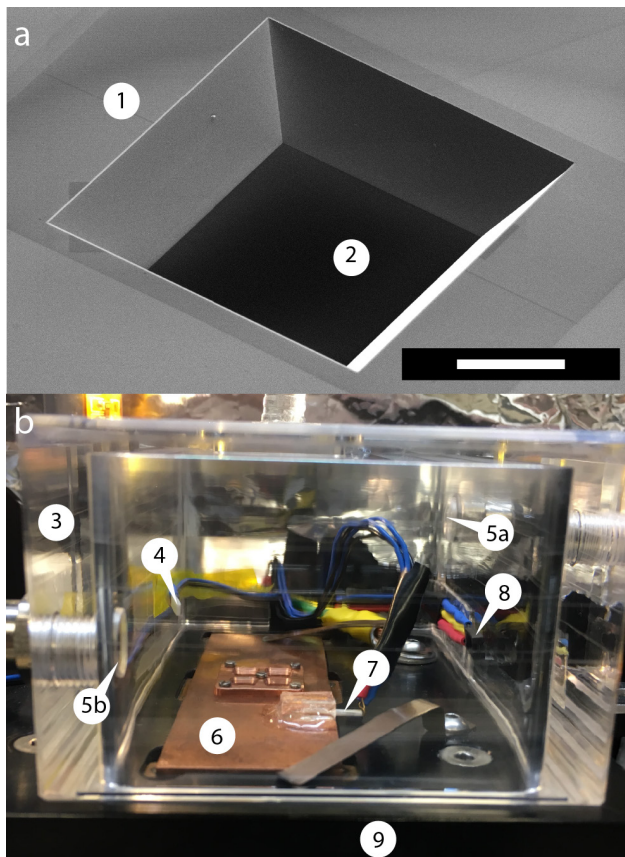


Fig. 1 Membrane transducer and environment control. (a) SEM-image of a single membrane transducer: silicon-frame (1) and the silicon-nitride membrane form a well that can be filled with the test

sample. Scale bar: 400 μm . (b) Temperature and humidity-controlled chamber: (3) Humidity chamber mounted on a movable XY-stage; (4) Temperature sensor monitoring the temperature of the humidity chamber; (5a) Inlet and (5b) outlet of the humid air; (6) Temperature-controlled copper plate; (7) Temperature sensor controlling the temperature of the plate; (8) Humidity sensor monitoring the humidity of the chamber; (9) Movable XY-stage.

The chamber is placed above an optical setup and photo-thermal actuation is used to drive the membrane. The response is measured using a classical beam deflection system. Schematics of the optical system and the electronics are shown in figure 2.

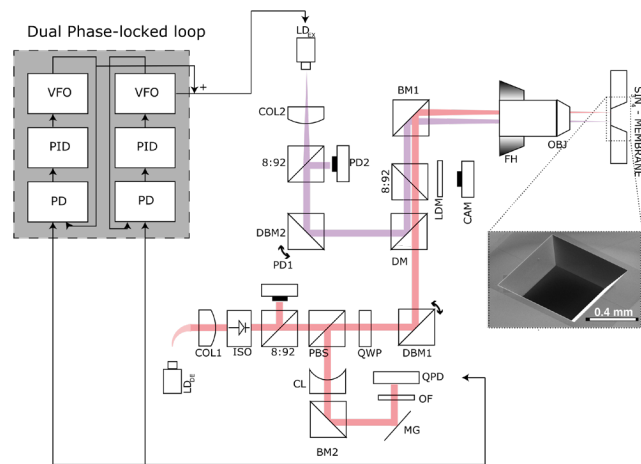


Fig. 2 Schematic view of the electronics and optical components. Optical beam deflection (red line) is used to detect the oscillations of the silicon-nitride membrane. A laser beam (LDDE) with a wavelength of 785.4 nm sequentially passes a collimator (COL1), a polarizing beam-splitter (PBS) and a quarter-wave plate (QWP). To align the detection-laser placement on the membrane, we inserted a dielectric broadband mirror (DBM1). The excitation part of the setup (violet line) consists of a laser beam (LDEX) with a wavelength of 405 nm passing through a collimator (COL2), a dielectric broadband mirror (DBM2) and a dichroic mirror (DM). Both laser beams are reflected by a broadband mirror (BM1) and focused onto the membrane by a microscope objective (OBJ, 4 \times). The excitation laser is driven by a variable frequency oscillator (VFO), and a lock-in amplifier (LIA) detects the response amplitude; both electronic components are integrated within the ZI-HF2LI (Zurich Instruments). The reflected beam passes through two broadband mirrors (BM) and is finally detected by a quadrant photo-diode (QPD). To optimize the detection of a specific wavelength an optical filter (OF) is mounted in front of the QPD.

Using the internal variable frequency oscillator integrated with Zurich Instruments HF2LI (ZI-HF2LI), amplitude and phase spectra of different modes were recorded. These were used to determine the eigenfrequency and the quality factor. A reduced order model (ROM) allows the calculation of the mass density and viscosity after a three-point calibration [3]. The measurement workflow is depicted in figure 3.

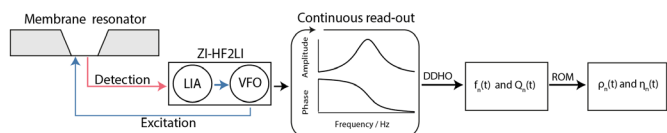


Fig. 3 Schematic overview of the measurement workflow: the membrane resonator is actuated by a modulated laser diode (blue) driven by the variable frequency oscillator (VFO). The membrane response is optically read out (red laser) and quantified by a digital lock-in amplifier (LIA). Note that the gold layer on the membrane absorbs 67% of the incoming blue light leading to a photo-thermal actuation of the membrane, and reflects 97% of the red light for the read-out of the membrane response. Spectra are recorded continuously by sweeping the frequency space, resulting in a time series of amplitude and phase spectra. From the series of amplitude and phase response spectra, the time-dependent eigenfrequency $f_n(t)$ and the time-dependent quality factors $Q_n(t)$ can be determined by fitting a driven damped harmonic oscillator model (DDHO) to each spectrum. After the determination of these parameters the liquid density $\rho_n(t)$ and the viscosity $\eta_n(t)$ can be calculated by applying the reduced order model (ROM).

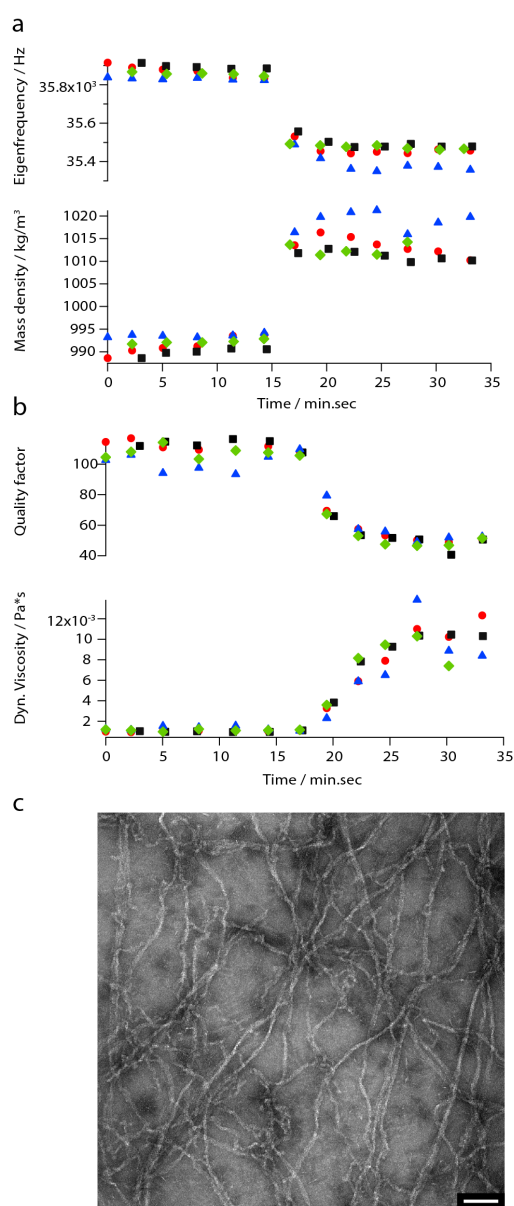


Fig. 4 Real-time characterization of F-actin formation: (a) & (b) Measured eigenfrequencies, quality factors and the corresponding mass densities and viscosities of polymerizing actin. The values were calculated by applying the reduced order model. Each color and each mark represents one measurement performed with the same silicon-nitride membrane. The red, black, blue and green marks represent the first, second, third, and fourth run respectively. (c) After

the real-time measurement of the viscosity the sample was removed from the membrane and negative stain electron microscopy was performed. The images confirmed the fibrillization of the G-actin to F-actin. Scale bar: 500nm.

Real-time measurements of protein fibrillization

By measuring mass density and viscosity, we were able to follow G-actin polymerization in real-time in a label-free manner. In previous studies, the filament formation and bundling were analyzed using microfluidic devices by observing the polymerization of fluorescently labeled actin monomers in KCl and $MgCl_2$ gradients.

During the data acquisition, a decreasing amplitude and a slight frequency shift were observed [2]. These two behaviors are related to the formation of actin filaments (F-actin) where the increasing viscosity leads to higher damping which implicate decreasing quality factors (Fig. 4). At the same time, filament growth results in a denser liquid. Corresponding to the three steps of actin polymerization, i.e., a nucleation, an elongation and a steady-state phase, three states are revealed by the curves presented in figure 4a and 4b.

The ability to follow filament formation in real-time was also confirmed by the negative control (Fig. 4c). In the absence of polymerization inducing buffer, fluctuating eigenfrequencies and quality factors were visible, but no significant decrease or increase of the quality factor and eigenfrequency were observed over time.

Summary and outlook

The instrument is now ready for the real-time characterization of biological samples in a label and functionalization free manner. Experiments with amyloid proteins are ongoing.

References

- [1] B.A. Bircher, R. Krenger T. Braun, *Automated high-throughput viscosity and density sensor using nanomechanical resonators*, Sens. Actuators, B, **223(C)**, 784–90 (2016)
- [2] P. Oliva, B. A. Bircher, C.-A. Schoenenberger, and T. Braun, *Array based real-time measurement of fluid viscosities and mass-densities to monitor biological filament formation*, Lab Chip, **19**, 1305–1313, (2019)
- [3] M. Heinisch, T. Voglhuber-Brunnmaier, E.K. Reichel, I. Dufour, B. Jakoby, *Reduced order models for resonant viscosity and mass density sensors*, Sens. Actuators, B, **220(C)**, 76–84 (2014)

Direct observation of spin fluctuations in antiferromagnetic CoO nanoparticles

Project P1502: Investigating individual multiferroic and oxidic nanoparticles

Project Leader: A. Kleibert and M. Poggio

Collaborators: D. Bracher (SNI PhD Student), M. Testa Anta, T. M. Savchenko, M. Wyss, F. Nolting, and V. Salgueiriño

Introduction

Antiferromagnetic materials become increasingly important for modern spintronics devices such as spin valves and magnetic random access memories and for the development of novel ultra-hard magnetic materials [1, 2]. While the properties of antiferromagnetic materials are intensively investigated in the bulk and thin films their nanoscale properties are still poorly understood. In particular, the spin structure and its stability with respect to thermal excitations are crucial for applications and can significantly deviate from the respective bulk in nanoscaled antiferromagnetic systems [3]. However, the weak net magnetic moment, which results mostly from uncompensated spins due to defects and surface facets, makes studying nanostructures with antiferromagnetic order very challenging. In this project, we address the spin structure, the orientation and the thermal stability of the antiferromagnetic spin axes of individual cobalt oxide nanoparticles. Additionally, uncompensated magnetic moments of the nanoparticles are probed. This is achieved by combining x-ray photoemission electron microscopy (XPEEM) with x-ray magnetic linear dichroism (XMLD) and x-ray magnetic circular dichroism (XMCD).

This experimental approach is used to investigate single crystalline cobalt oxide CoO/Co₃O₄ nanooctahedra [2]. Previously, we have reported (SNI reports P1502 2017 and 2018) the temperature and orientation dependence of XMLD spectra of individual CoO nanoparticles. Here, we present the results of XMLD and XMCD contrast imaging, which are used to study the orientation of the antiferromagnetic spin axis and the uncompensated magnetic moments of individual nanoparticles. This approach allows to study the azimuthal and orientation dependence of the XMLD and ultimately helps to identify the antiferromagnetic spin axis of individual CoO nanoparticles [4]. Further, the x-ray magnetic circular dichroism of the very same nanoparticles is investigated in order to probe uncompensated magnetic moments, which may arise from defects such as vacancies.

Experimental

The CoO/Co₃O₄ nanooctahedra are dispersed on silicon substrates with gold marker structures by drop casting. XPEEM experiments are performed at the Surface/Interface: Microscopy (SIM) beamline of the Swiss Light Source. XMLD contrast maps are obtained by recording XPEEM images at two photon energies (777.8 eV/778.4 eV) at the Co L₃ edge, where the XMLD effect exhibits opposite signs at a given linear polarization of the x-rays. The XMLD contrast is proportional to $\cos^2\alpha$, where α is the angle between the E vector of the x-rays and the spin axis S of an individual nanoparticle. The dependence of the XMLD effect on the azimuthal sample orientation and arbitrary polarization vector can be analytically expressed [4]. This description is used to determine the spin axis of antiferromagnetic materials from the azimuthal and polarization dependent XMLD contrast measurements. Here, the linear polarization vector is generally denoted as $E(\Theta_s, \Phi_s)$, with Θ_s the polarization angle relative to the scattering plane and Φ_s is the azimuthal sample orientation. In order to study uncompensated magnetic moments the XMCD contrast is obtained as the difference of two images recorded at one photon energy (777.8 eV) with C⁺ and C⁻ polarized x-rays. XMLD and XMCD contrast image were recorded at 100 K.

Results

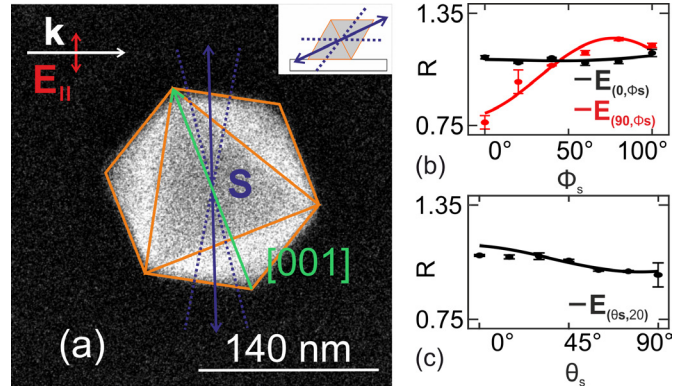


Fig. 1 (a) SEM image of a CoO nanoparticle together with the x-ray propagation direction k , the E-field vector of the linear polarization $E(90^\circ, 0^\circ)$, which is parallel to the substrate, the [001] (green) direction of the nanoparticle, and the obtained spin axis (purple arrow) and the fit error range (dashed purple lines) indicated. The inset displays the out-of-plane orientation of the spin axis together with a cross section of the nanoparticle perpendicular to the substrate and parallel to the [001] direction. (b) Azimuthal dependent XMLD contrast for $E(90^\circ, \Phi_s)$ (red) and $E(0^\circ, \Phi_s)$ (black) as well as (c) the polarization dependent XMLD contrast for $E(\Theta_s, 20^\circ)$.

Figure 1a shows an SEM image of a CoO nanoparticle together with a schematics of its shape (orange lines), the k vector (white arrow), and the E-field vector at $\Theta_s=90^\circ$ and $\Phi_s=0^\circ$ (red arrow). The orange lines highlight the edges of the nanoparticle according to its octahedral shape and orientation on the substrate. Figure 1b displays the azimuthal dependent XMLD contrast obtained with $E(90^\circ, \Phi_s)$ (red dots) and $E(0^\circ, \Phi_s)$ (black dots). The error bars correspond the statistical errors of the measurements. The solid curves are obtained by fitting the model described by Czekaj et al. [4] to the two data sets. Figure 1c displays the polarization dependence of the XMLD contrast (black dots) and the curve (solid black) derived from the global fit parameters obtained from the data in figure 1b. The agreement between the experimental data and the simulated curves confirms a single domain state in this nanoparticle. From the fit parameters, the orientation of the spin axis of the nanoparticle is extracted as depicted by the purple arrows in figure 1a and the inset, respectively. The spin axis can be compared to bulk CoO, which exhibits its spin axis tilted out the [001] direction by about 11° [5]. Within the error bars we find a similar orientation of S of the nanoparticle in figure 1a, which can be seen, when comparing S with the respective [001]-direction of the nanoparticle. The green arrow in figure 1a highlights the latter. Hence, the spin axis of this nanoparticle is consistent with the corresponding bulk behavior. However, we also find nanoparticles which display a significant deviation from the spin axis orientation of bulk CoO. This suggests that microstructural defects might have an effect on the spin axis orientation.

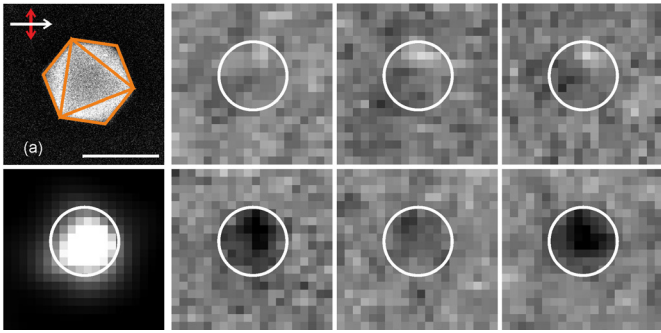


Fig. 2 a) SEM micrograph and (b) XPEEM elemental contrast map recorded at the Co L3 edge. c)-h) time dependent XMCD contrast of the nanoparticle as shown in panel a) and Fig. 1, respectively.

Uncompensated magnetic moments are probed by means of the XMCD effect. In figure 2a the SEM image and in figure 2b the elemental contrast XPEEM image of the same CoO nanoparticle as in figure 1 are shown. It is important to note that the XMCD effect is recorded at $\Phi_s=0^\circ$, where the antiferromagnetic spin axis is almost perpendicular to k . The XMCD effect displays a $\cos\alpha$ dependence, where α is the angle between the magnetic moment M and k . The result of the time dependent XMCD measurements are shown in figure 2 c-h. Surprisingly, fluctuating white and black XMCD contrast is found as a function of time indicating that the uncompensated magnetic moments behave superparamagnetic. Further, the appearance of black and white contrast suggest that the moments have a sizable component parallel or antiparallel to k . This behavior is unexpected since the antiferromagnetic spin axis of the nanoparticle is almost perpendicular to k . Hence, the uncompensated magnetic moments have a component perpendicular to the antiferromagnetic sublattices, which indicates a non-collinear or even a perpendicular orientation between M and S .

Indeed, recent theoretical investigations suggest that thermal excitations of antiferromagnetic nanoparticles can lead to a fluctuating net magnetic moment perpendicular to the antiferromagnetic spin axis due opposite excitation of the two spin lattices [3]. In systems with low damping, this mechanism leads to a reduction of thermal stability by a few orders of magnitude when compared to a ferromagnetically ordered nanoparticle with similar atomic magnetic moments and magnetic anisotropy. Such a reduction of thermal stability could explain the magnetic fluctuations observed in the present experiments. We may note that bulk CoO possesses a very high magnetic anisotropy, which would suggest magnetic stability of the present nanoparticles even far above room temperature. To further investigate the coupling of antiferromagnetic sublattices and uncompensated magnetic moments additional integral XMCD and XMLD measurements have been carried out. However, the data need to be to further evaluated before additional conclusions can be presented.

In summary, we have combined XPEEM with XMCD and XMLD to investigate the magnetic properties of individual, antiferromagnetic CoO nanoparticles. Some of the nanoparticles exhibit a single domain state with a spin axis close to the respective bulk material, while deviations from such a spin structure were observed in other nanoparticles. In addition, uncompensated and thermally fluctuating magnetic moments were directly addressed. These observations seem to confirm recent theoretical predictions about a significantly reduced magnetic stability in antiferromagnetically ordered nanostructures. If confirmed, these findings will have impact on the design of antiferromagnetic building blocks in future applications, where in addition to the thickness also the lateral dimensions will reach the nanometer size range.

References

- [1] S. Morup, D. E. Madsen, C. Frandsen, C. R. H. Bahl, M. F. Hansen, *Experimental and theoretical studies of antiferromagnetic materials*, J. Phys. Condens. Matter **19**, 213202 (2007)
- [2] N. Fontaíña-Troitiño, S. Liébana-Viñas, B. Rodríguez-Gonzalez, Z-A. Li, M. Spasova, M. Farle, V. Salgueiriño, *Room-temperature ferromagnetism in antiferromagnetic cobalt oxide nanooctahedra*, Nano Lett. **14**, 640 (2014)
- [3] L. Rózsa, S. Selzer, T. Birk, U. Atxitia, U. Nowak, *Reduced thermal stability of antiferromagnetic nanostructures*, Phys. Rev. B. **100**, 064422 (2019)
- [4] S. Czekaj, F. Nolting, L. J. Heydermann, P. R. Willmott, G. van der Laan, *Sign dependence of the x-ray magnetic linear dichroism on the antiferromagnetic spin axis in LaFeO₃ thin films*, Phys. Rev. B **73**, 020401 (2006)
- [5] W. L. Roth, *Magnetic structure of MnO, FeO, CoO, and NiO*, Phys. Rev. **110**, 1333 (1958)
- [6] J. Kanamori, *Theory of the magnetic properties of ferrous and cobaltous oxides I*, Prog. Theor. Phys. **17**, 177 (1957)

Filming biological factories

Project P1503: Watching giant multienzymes at work using high-speed AFM

Project Leader: T. Maier and R. H. Y. Lim

Collaborators: S. Singh (SNI PhD Student), Y. Sakiyama, and F. Benning

Multienzymes are biological assembly lines

Enzymes are biological catalysts that are responsible for the biosynthesis of almost all biomolecules, hence they are essential for any living system. One enzyme generally catalyses one type of chemical reaction. But even the biosynthesis of a simple biomolecule such as a sugar or fatty acid requires several biosynthetic reaction steps. This is achieved via a reaction pathway, where many different enzymes act sequentially on intermediates. To increase the efficiency of a biochemical pathway, the enzymes are often placed in close proximity inside the cell. One option to achieve this proximity is placement of multiple enzymatic sites on the same polypeptide chain. Such an enzymatic system is known as a multienzyme. Different enzymatic domains of multienzymes exhibit a very dynamic behavior [1] but the link between these large-scale domain movements and their overall catalytic function is poorly understood.

In order to elucidate this relationship, we are (i) developing methods to analyze large-scale motions of multienzyme domains and (ii) aiming to employ these methods to study catalysis by multienzymes of human metabolism and microbial secondary metabolite production. Our approach involves development of two complimentary methods for studying multienzyme dynamics. The first is High Speed Atomic Force Microscopy (HS-AFM), which allows direct albeit low spatio-temporal resolution visualization of protein dynamics. The second one builds on efficient multi-site fluorescence labelling for single molecule Förster resonance energy transfer (smFRET), which provides highest available spatiotemporal resolution for dynamic studies.

The model system we are studying is human fatty acid synthase (FAS), one of the most complex multienzymes [2]. FAS is responsible for all steps of the synthesis of palmitoyl-coenzyme A by iterative elongation of carbohydrate-derived precursors. It iteratively employs six types of enzymatic domains, which together catalyze over 40 biochemical reaction steps, and a flexibly-tethered integral acyl carrier protein (ACP) domain, which shuttles covalently-bound intermediates to the enzymatic sites. FAS upregulation is linked to cancer [3] and several metabolic disorders, making FAS an interesting target for therapeutic intervention. Polyketide synthases (PKS) are microbial enzymes that use the same basic synthetic logic FAS but produce considerable more complex natural products of outstanding therapeutic value, including antibiotics, immunosuppressants and statins. Instead of an iterative mode of precursor elongation as in FAS, PKS can form large assembly lines of multiple modules, each carrying out only one round of precursor elongation and modification. The intermediates are vectorially shuttled from module to module in these nanomachines. Variations in the domain composition of modules result in altered substrate selectivity and distinct extents of precursor modification by different PKS resulting in a huge diversity of polyketide products in nature. This property makes PKS one of the most relevant systems for customized synthesis of drug candidates using biocombinatorial approaches. Poor understanding of substrate transfer in PKS is a major hindrance of this potential. We are addressing this problem in our lab already by high-resolution analysis of transient trapped states of substrate transfer in PKS [4] (Fig. 1). Expansion of our

current work on combining smFRET and HS-AFM to PKS is a highly promising route towards further understanding the dynamics of substrate transfer.

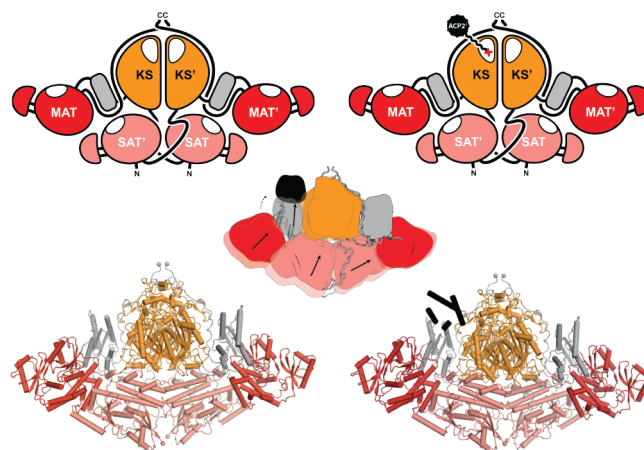


Fig. 1 Trapped state of substrate transfer in a PKS. Left column: ground-state of a six-domain PKS fragment, right column: covalently trapped transient state of initial substrate loading. Upper panel: Schematic representations, lower panel: models derived by experimental structure determination.

High-speed AFM analysis of multienzymes

Atomic Force Microscopy (AFM) is a non-invasive, sub-nanometer surface topography imaging technique. HS-AFM is a variant of conventional AFM and uses relatively low imaging force and higher imaging rates (usually 15-25 frames per second) to visualize the movements in biomolecular assemblies in native conditions. By using FAS as the model protein, we have already demonstrated the feasibility of filming multienzymes using HS-AFM to analyze their large-scale conformational dynamics [5]. We were able to collect HS-AFM movies of surface immobilized and lipid tethered FAS molecules with up to 10 frames per second, with 2-5 nm lateral and 1.5 nm vertical resolution, which allowed us to observe large scale domain motions in FAS. We are aiming to extend this work to PKS assembly lines.

A toolkit for multienzyme fluorescent labelling

The highest spatial ($\pm 3 \text{ \AA}$) and temporal resolutions ($\pm 1 \text{ ms}$) in analyzing the dynamics of large macromolecular assemblies are currently achieved via fluorescent labelling. Single molecule FRET (smFRET) offers a precise molecular ruler for measuring 2-8 nm distances between two labels, and Fluorescence Correlation Spectroscopy (FCS) reveals diffusional properties of a dilute sample (with fluorophores present in the order of nano-molar to pico-molar concentrations) in a diffraction-limited confocal volume (order of 1-10 femtolitres). Both methods are suitable for in vivo studies and permit measurements on the typical time- and length-scale of multienzyme dynamics.

The prerequisite of fluorophore-labelling is a major limiting factor for single molecule fluorescence studies of multienzymes. Chemical modification based on sulfhydryl or primary-amine-reactive dyes is the most efficient labelling tech-

nique for small proteins with a limited number of reactive sites without functional relevance. However, multienzymes are giant polypeptides with hundreds of functional groups and they critically require cysteine and lysine side chains for their enzymatic functions.

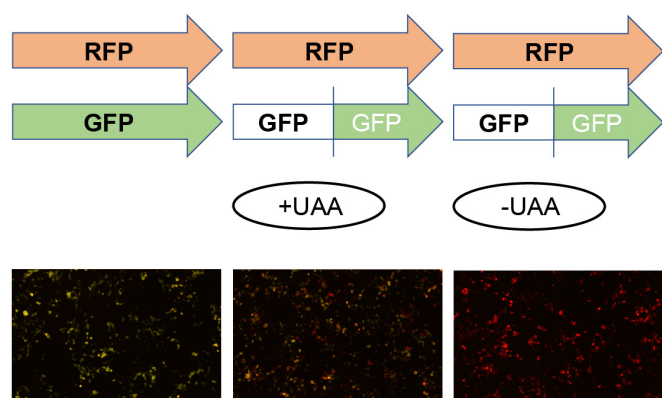


Fig. 2 Imaging analysis of GCE-based incorporation of unnatural amino acids. Right: Positive control: Production of RFP and GFP. Centre: Production of RFP and a GFP variant containing a UAA incorporation site in the presence of a full GCE system. Left: Negative control: As in center; but without addition of UAA. Images are merges of red and green fluorescence channels, yellow color indicates production of RFP and GFP.

Genetic code expansion (GCE) is a method to biosynthetically introduce either fluorescent amino acids or biorthogonal chemically-reactive groups, which can later be used as unique sites for specific labelling via biorthogonal reactions, at specific positions in proteins. GCE involves supplementing a protein expression host with a non-native protein-production machinery which introduces unnatural amino acids or UAA (i.e. amino acids with biorthogonal functional groups as side chains) in polypeptides in response to specific genetic codons. We focus on mammalian protein expression systems because those are the most suitable for (i) introducing the necessary post translational modifications of multienzymes and (ii) producing the very large polypeptides of multienzymes. For human protein expression systems, several GCE systems have already been developed [6], but they have been shown to work mostly for small and relatively simple proteins, while extensive screening is often required even for obtaining low yields in single-site labeling of more complex proteins using a single GCE system. Critical screening parameters include the choice of GCE systems as well as the targeted positions in the protein sequence.

We aim at developing an efficient toolkit for GCE-based labelling of complex proteins and multienzyme in particular. To this aim, we have developed a system of gene vectors for transiently transfecting different GCE systems and fluorescent reporters into HEK293 cells. A tandem RFP (Red Fluorescent Protein)-GFP (Green Fluorescent Protein)-based fluorescent reporter allows rapid quantitative comparison of the inherent yields of different GCE systems (Fig. 2).

We have established protocols for mammalian cell expression in adherent form for high-throughput imaging (for screening different conditions of UAA incorporation in multienzymes) and in suspension form (for large scale production of UAA labelled multienzymes). Preliminary results indicate that the reduction of yield of labelled vs. native protein due to the competition between the GCE and the cellular machinery is approximately 3-fold per labeling site under optimized conditions. Based on native yields exceeding 10 mg of protein per liter of cell culture, this yields fully sufficient for multienzyme labelling for fluorescent analysis.

Currently we set up an automated cell culture system combining liquid handling and imaging. On this platform, we will

screen all GCE systems available in our toolkit for mammalian expression to determine optimal combinations of GCE systems for FRET pair labelling and to demonstrate the feasibility of extensive positional screening of insertion sites in multienzymes. Final evaluation and fluorescent dynamics studies will be carried out on FAS and related multienzyme systems such as PKS.

References

- [1] A. Hagmann, M. Hunkeler, E. Stüttfeld, T. Maier, *Hybrid Structure of a Dynamic Single-Chain Carboxylase from Deinococcus radiodurans*, *Structure*, **24**(8), 1227-1236, (2016)
- [2] T. Maier, M. Leibundgut, N. Ban, *The crystal structure of a mammalian fatty acid synthase*, *Science*, **321**(5894), 1315-1322 (2008)
- [3] J. V. Swinnen, K. Brusselmans, G. Verhoeven, *Increased lipogenesis in cancer cells: new players, novel targets*, *Curr. Opin. Clin. Nutr. Metab. Care*, **9**(4), 358-365 (2006)
- [4] D. A. Herbst, C. R. Huitt-Roehl, R. P. Jakob, J. M. Kravetz, P. A. Storm, J. R. Alley, C. A. Twonsend, T. Maier, *The structural organization of substrate loading in iterative polyketide synthases*, *Nat. Chem. Biol.* **14**, 474-79 (2018)
- [5] F. M. C. Benning, Y. Sakiyama, A. Mazur, H. S. T. Bukhari, R. Y. H. Lim, T. Maier, *High-Speed Atomic Force Microscopy Visualization of the Dynamics of the Multienzyme Fatty Acid Synthase*, *ACS Nano*, **11**(11), 10852-10859 (2017)
- [6] A. R. Nodding, L. A. Spear, T. L. Williams, L. Y. P. Luk, Y. H. Tsai, *Using genetically incorporated unnatural amino acids to control protein functions in mammalian cells*, *Essays Biochem.* **63**(2), 237-266 (2019)

In situ strain tuning in graphene and study of random strain fluctuations

Project P1504: Valleytronics in strain-engineered graphene

Project Leader: C. Schönberger and M. Calame

Collaborators: L. Wang (SNI PhD Student), P. Makk, S. Zihlmann, A. Baumgartner, and D. Indolese

The large mechanical strength of graphene enables one to modify the electronic properties of graphene by strain engineering. A series of fascinating phenomena have been predicted for strained graphene, such as the appearance of strain-induced scalar potentials and pseudo-magnetic fields [1]. In order to study strain effects in transport experiments, several challenges need to be overcome simultaneously. First, the graphene quality must be preserved after complex fabrication processes, since the observation of strain effects might be hindered by disorder. Second, the strain generation must be compatible with transport measurements, namely the devices should be equipped with electrical contacts and gate structures. Furthermore, mechanical deformations should not degrade the sample quality or generate any artificial effects, such as changes in the gate capacitance, that complicates the analysis of actual strain effects. Most importantly, the strain should be in situ tunable so that strain effects can be disentangled from other effects.

We successfully developed a straining method that meets all the above requirements. Instead of suspending the graphene, we encapsulate the graphene with hexagonal boron-nitride (hBN) and directly strain the van der Waals (vdW) heterostructure on-substrate. This approach preserves the exceptional quality of pristine graphene, which is a significant advantage for transport experiments. We use Raman spectroscopy to demonstrate that our method is versatile and allows one to engineer various strain fields, such as strain gradients, which are important for the generation of pseudomagnetic fields. The edge contacts work reliably and can sustain strain up to $\sim 1\%$. Therefore, our approach of on-substrate encapsulated graphene offers an ideal platform for studying strain effects in transport experiments.

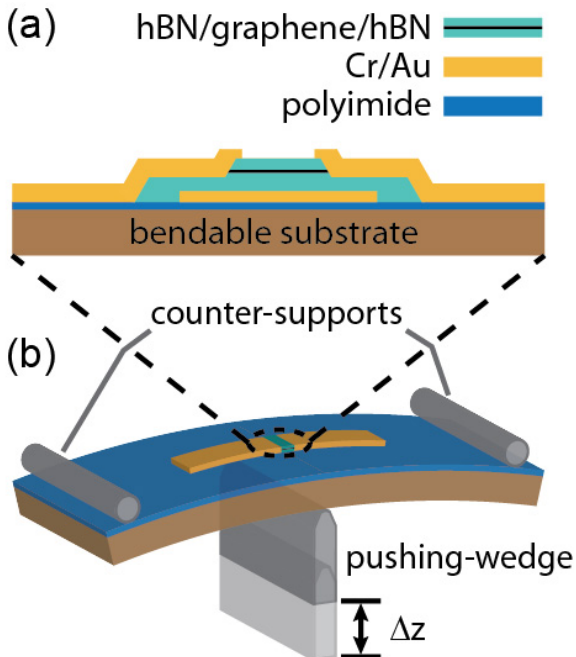


Fig. 1 Schematics of (a) the device cross section and (b) the three-point bending setup. The bending of the substrate is determined by the displacement of the pushing-wedge, Δz .

As shown schematically in figure 1a, we fabricate hBN-encapsulated graphene devices with edge contacts and an electrical bottom gate on a polyimide-coated phosphor bronze substrate. Bending the substrate in a three-point bending setup, as illustrated in figure 1b, generates a strain field in graphene. The deformation of the substrate is determined by the displacement Δz of the pushing-wedge relative to the mounting position. The metallic contacts and the gate allow us to perform transport experiments while tuning the strain in situ. The metallic contacts are essential for generating strain in a vdW heterostructure. On the basis of the assumption that the graphene sheet is pulled uniaxially by the contacts during the bending of the substrate, different strain fields can be achieved by varying the device geometries. We designed devices with two different geometries: rectangular or trapezoidal ones. For the former, the strain field is expected to be homogeneous, while for the latter a strain gradient along the direction perpendicular to the straining axis is expected.

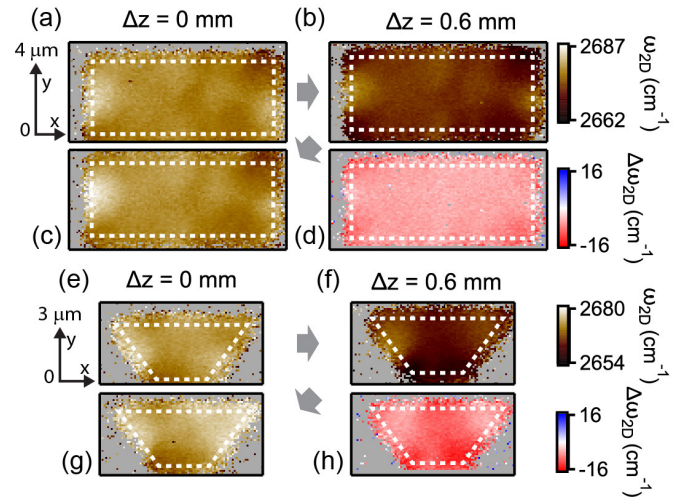


Fig. 2 (a-c) Spatially resolved Raman maps of ω_{2D} for the rectangular device at different Δz . The white dashed lines outline the device boundaries. The gray arrows show the sequence of the measurements. (d) Spatially resolved Raman maps of ω_{2D} , obtained by subtracting map (a) from map (b). (e-g) Spatially resolved Raman maps of ω_{2D} for the trapezoidal device at different Δz . (h) Spatially resolved Raman maps of ω_{2D} , obtained by subtracting map (e) from map (f).

To characterize the strain fields for different displacements Δz , we use spatially resolved Raman spectroscopy to map the strain field based on the redshift of the graphene Raman 2D peak. We first focus on the investigation of the rectangular device. In figure 2a-c, the 2D peak center frequency ω_{2D} is plotted as a function of position for increasing Δz from 0 to 0.6 mm (straining) and then decreasing back to 0 mm (relaxing), as indicated by the gray arrows. With increasing Δz , ω_{2D} shifts to lower values at all positions on the map, consistent with increasing strain everywhere in the graphene sheet. When Δz is decreased back to 0, ω_{2D} reverts back to the initial values, suggesting a good reproducibility of the strain tuning in the graphene device. The homogeneity of the externally induced strain field can be seen directly in figure 2d, which shows a

map of the change in the Raman shift, ω_{2D} , i.e. the difference between the maps figure 2a,b. For the rectangular geometry, the externally induced strain is fairly homogeneous in the bulk with a vanishing strain gradient, which is in agreement with the expected strain field. The same analysis is done for the trapezoidal device and shown in figure 2e-h. The existence of a strain gradient is visible in figure 2f. At the shorter (bottom) edge of the device, ω_{2D} shows a stronger shift than that at the longer (top) edge, which matches the predicted strain pattern for a trapezoidal geometry.

These results have been published in a Nano Letter publication this year [2].

In a recent statistical study of many graphene devices on hBN substrates [3], it has been pointed out that random strain fluctuations (RSFs) are the dominant microscopic source of scattering that limit the carrier mobility. The perfect combination of in situ strain tuning with transport experiments in our method allows us to investigate the influence of RSFs on transport properties in graphene. The increase in mobility that we find while straining, shows that RSFs in individual encapsulated graphene devices can be in situ reduced by increasing the average strain, as illustrated in figure 3.

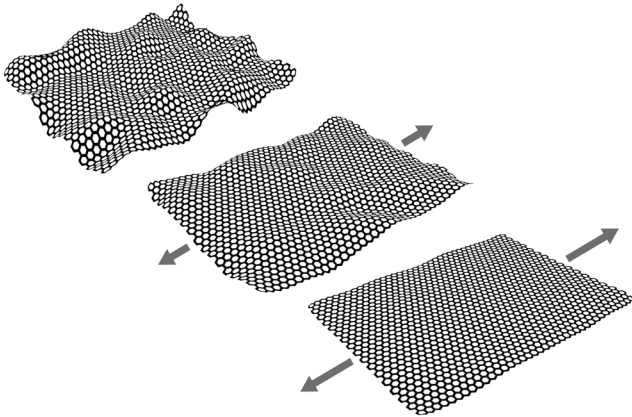


Fig. 3 Illustration of in situ reduction of the strain fluctuations. The arrows indicate the direction and the strength of the externally induced strain by substrate bending mediated by contacts.

We measured at low temperature ($T = 4.2\text{K}$) the two-terminal differential conductance G of a device as a function of the gate voltage V_g for different Δz , as shown in figure 4. The conductance increases faster when gated away from the charge neutrality point for larger Δz , suggesting an increase in the carrier mobility with increasing Δz . This effect is reversible when Δz is decreased. The in situ reduction of RSFs is further substantiated by Raman spectroscopy measurements, which can directly probe the RSFs. These findings have been submitted [4].

In studies in magnetic field in the quantum Hall regime, we have additionally find evidence for a strain-tunable pseudo-magnetic field on which we will report later on.

To conclude, we have developed a method to generate controllable strain in encapsulated graphene. This achievement is conceptually and experimentally a big step forward for the community as it clears the way for studying strain effects in transport experiments, not only for graphene but also for other 2D materials. In first low temperature transport experiments, we found that RSFs are the dominant scattering mechanism limiting the carrier mobility in most hBN-supported graphene devices.

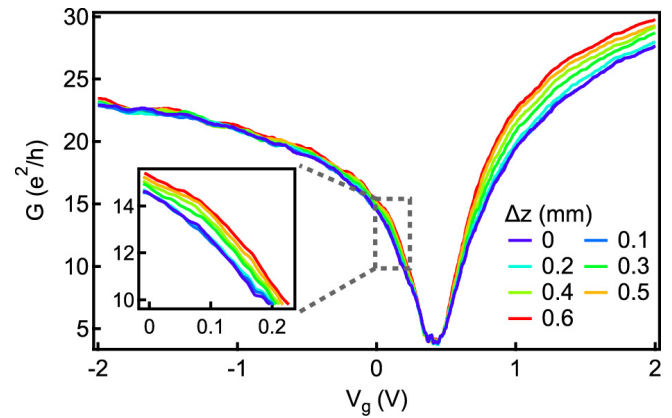


Fig. 4 Two-terminal differential conductance G plotted as a function of gate voltage V_g for different Δz . The slope of the curves becomes steeper for larger Δz , for both the electron and hole side. The inset shows a zoom-in to the hole side.

We thank F. Guinea and P. Rickhaus for fruitful discussions, and K. Watanabe and T. Taniguchi for providing high-quality hBN.

References

- [1] F. Guinea, A. K. Geim, M. I. Katsnelson, K. S. Novoselov, *Generating quantizing pseudo-magnetic fields by bending graphene ribbons*, Phys. Rev. B **81**, 035408 (2010)
- [2] L. Wang, S. Zihlmann, A. Baumgartner, J. Overbeck, K. Watanabe, T. Taniguchi, P. Makk, C. Schönenberger, *In situ strain tuning in hBN-encapsulated graphene electronic devices*, Nano Lett. **19**, 4097 (2019)
- [3] N. J. G. Couto, D. Costanzo, S. Engels, D.-K. Ki, K. Watanabe, T. Taniguchi, C. Stampfer, F. Guinea, A. F. Morpurgo, *Random strain fluctuations as dominant disorder source for high-quality on-substrate graphene devices*, Phys. Rev. X **4**, 041019 (2014)
- [4] L. Wang, P. Mark, S. Zihlmann, A. Baumgartner, D. I. Indolese, K. Watanabe, T. Taniguchi, C. Schönenberger, *Mobility enhancement in graphene by in situ reduction of random strain fluctuations*, arXiv:1909.13484 (2019)

Programmable electrostatic phased apertures

Project P1505: A programmable e-beam shaper for diffractive imaging of biological structures at Å resolution

Project Leader: S. Tsujino and J. P. Abrahams

Collaborator: P. Thakkar (SNI PhD Student)

Introduction

Phase manipulation of electron beam offers great advantages for high resolution imaging. Various experimental investigations using electrons have been repeatedly conducted in the past revealing interesting physical aspects of electron-matter interaction [1, 2]. There has been increased interest in electron beam manipulation recently to potentially offer advanced methods of imaging with electron microscopes, for instance Zernike phase plates and electron vortex beams are such examples [3, 4].

Outline of fabrication process: improvements on critical steps

We are developing a device with individually controllable nano-lenses using state-of-the-art electron beam (e-beam) lithography technique. A 3D schematic of the intended device is shown in figure 1a. It offers advantages of writing large-scale nanostructures with higher flexibility in material selection when combined with various subtractive and additive processes [5, 6]. Free standing silicon nitride membranes have been a major choice to fabricate such nano-lenses due to its mechanical stability. Nanofabrication on thin silicon nitride membranes (<300 nm) is challenging for multiple lithography steps and suffer breakage due to thermal and mechanical stresses.

Currently, we are working on a 3-aperture-array device to develop the basic fabrication method. In figure 1b, we show SEM image of an intermediate step for such a device: b fabricated on a thin (~200 nm) silicon nitride membrane with an intend to use chromium (Cr) as an active electrode material. In this approach, we want to selectively etch away the Cr layer to create individually controllable phase elements. The bright gray contrast in the image is the patterned resist which is used as a mask to etch away the underneath dark gray Cr layer to separate the electrodes. As mentioned earlier, silicon nitride membranes suffer from stresses especially in the reactive ion plasma. We've observed during the process development that the Cr layer potentially induces stresses in the membrane which reduces the stability of the membrane. We've observed that with subtractive lithography method, the throughput of the final devices reduced by quite a lot. The solution to this problem is using an additive approach by selectively depositing the material at the region of interest.

We use gold (Au) as an electrode material in this case. The phase elements are patterned in positive e-beam resist PMMA followed by evaporation of Au (~100 nm). The gold rings around the apertures and the electrodes are the pattern in the resist exposed with different dose levels to optimize the correct dose values. After lift-off of the resist, we see Au electrodes aligned to the apertures on silicon nitride membrane. As shown in figure 2b, the apertures (black) are surrounded by Au electrodes (bright gray). We also perform e-beam exposure dose tests to find optimum exposure dose levels for lift-off process. In the preliminary dose tests, we observe that the lift-off process starts to fail above certain dose levels. The edges of the overexposed resist considerably lose the geometry suitable for lift-off and hence leaves the apertures covered with gold discs as can be seen in figure 2b.

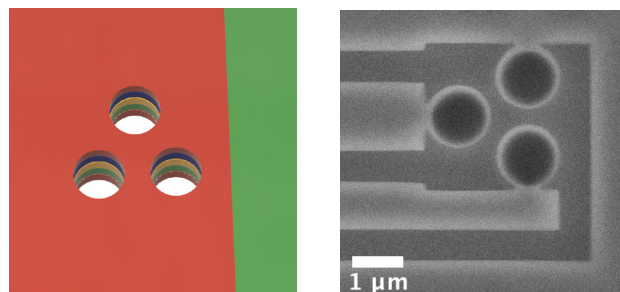


Fig. 1 (a) schematic of 3 individually controllable electrostatic phase elements (b) subtractive lithography approach: Pattern in the resist to etch away the underneath central electrode chromium layer (dark gray) around the etched apertures

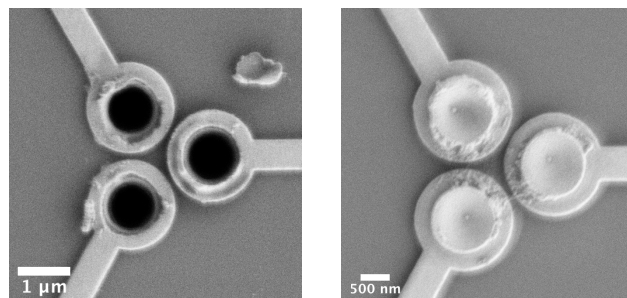


Fig. 2 (a) Lift-off of overexposed regions where the apertures are covered with gold discs (b) additive lithography approach: patterned gold electrodes (bright gray) in silicon nitride membrane around the etched apertures (black)

Expected device performance

The expected most basic performance of our device will be tested by measuring the far-field diffraction pattern of fully coherent electron beam passing through the three apertures, that should create a hexagonal lattice as depicted in the simulation assuming a 200 keV electron beam with the actual aperture size and separation in figure 3. When the phase shift through the three apertures are the same, a brightest diffraction spot should be observed at the center of the diffraction lattice (a). When the phase shift of one of the apertures is π , the whole lattice is shifted by a one-half wavelength and the center becomes dark (b). Finally, when the three phases are stepped by $2\pi/3$, a vortex beam, having an angular momentum of $+\hbar$ or $-\hbar/(2\pi)$, where \hbar is the Planck's constant (c). The vortex beam is symmetric and the electron beams negatively interfere at the center of the lattice.

Summary and Outlook

In conclusion, we have successfully developed a device with three individually programmable phased elements with more stable and reliable fabrication process. We plan to test the working of the fabricated devices in a high-energy transmission electron microscope to compare the performance with theory as well as to characterize various critical parameters such as the confinement of the electric field around the electrode, cross-talks between apertures, and the influence of the surface charging due to environment as well as the electron beam irradiation.

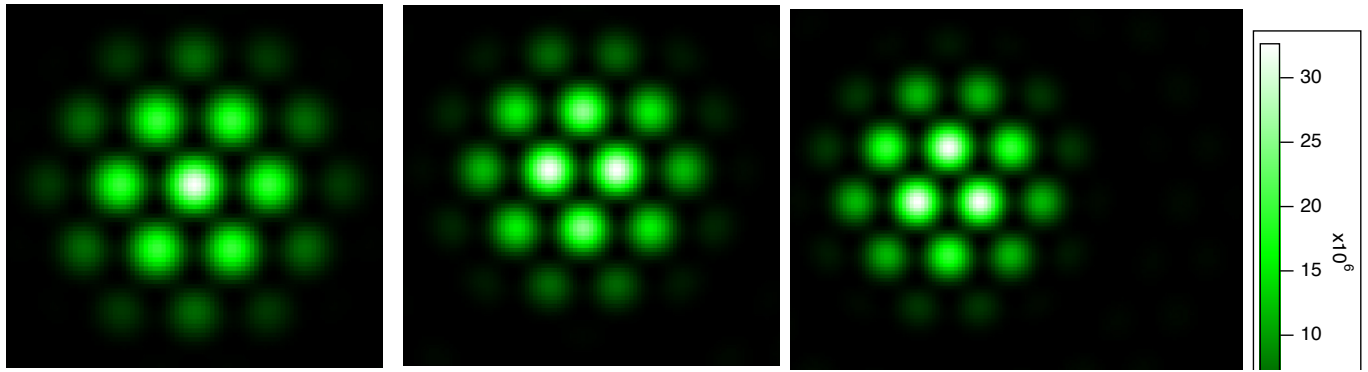


Fig. 3 Far-field diffraction of phased apertures considering the geometry of the fabricated device for 200 keV electron beam (a) phase shift for all three apertures are equal generating hexagonal first order diffraction spots (b) phase shift of one of the aperture is π shifting the diffraction pattern by half of the wavelength (c) phase shifts of all three apertures are separated by $2\pi/3$ generating a vortex singularity in the center of 3 aperture system

References

- [1] G. Möllenstedt, H. Düker, *Beobachtungen und messungen an biprisma-interferenzen mit Elektronenwellen*, *Zeitschrift für Phys.*, **145(3)**, pp. 377–397, (1956)
- [2] O. Donati, G. P. Missiroli, G. Pozzi, *An experiment on electron interference*, *Am. J. Phys.*, **41(5)**, pp. 639–644, (1973)
- [3] R. Danev, K. Nagayama, *Transmission electron microscopy with Zernike phase plate*, *Ultramicroscopy*, **88(4)**, pp. 243–252 (2001)
- [4] B. J. McMorran, A. Agrawal, I. M. Anderson, A. A. Herzog, H. J. Lezec, J. J. McClelland, J. Unguris, *Electron vortex beams with high quanta of orbital angular momentum*, *Science*, **331(6014)**, pp. 192–195 (2011)
- [5] M. Ekberg, M. Larsson, S. Hård, B. Nilsson, *Multilevel phase holograms manufactured by electron-beam lithography*, *Opt. Lett.*, **15(10)**, pp. 568–569 (1990)
- [6] V. A. Guzenko, A. Mustonen, P. Helfenstein, E. Kirk, S. Tsujino, *High-density large-scale field emitter arrays for X-ray free electron laser cathodes*, *Microelectron. Eng.*, **111**, pp. 114–117 (2013)

High aspect ratio gold nanoparticles for enhanced water splitting

Project P1601: Optical plasmonic nanostructures for enhanced photochemistry

Project Leader: E. C. Constable and S. Fricke

Collaborators: L. Driencourt (SNI PhD Student), B. Gallinet, A. Luu-Dinh, and C. E. Housecroft

Introduction

Electricity can be produced from dihydrogen gas using a fuel cell, which only emits water. However, industrial dihydrogen is currently mainly produced by steam reforming of methane which is a non-sustainable technique. Water splitting using sunlight is a promising method for clean dihydrogen production. One of the possible approaches uses two semiconductor electrodes immersed in an aqueous electrolyte and used in a tandem configuration. Such an “artificial leaf” can perform unassisted water splitting when illuminated, transforming water into dihydrogen and dioxygen. This work demonstrates a method for fabricating high aspect ratio plasmonic gold nanoparticles on a transparent conductive oxide (TCO) substrate. A water splitting photoanode is then fabricated by depositing a metal oxide layer on this nanostructured scaffold, demonstrating an increased photocurrent for such photoelectrode compared to a pure metal oxide electrode.

Growth of high aspect ratio gold nanoparticles

The fabrication process of the nanostructured gold substrate is shown in figure 1a.

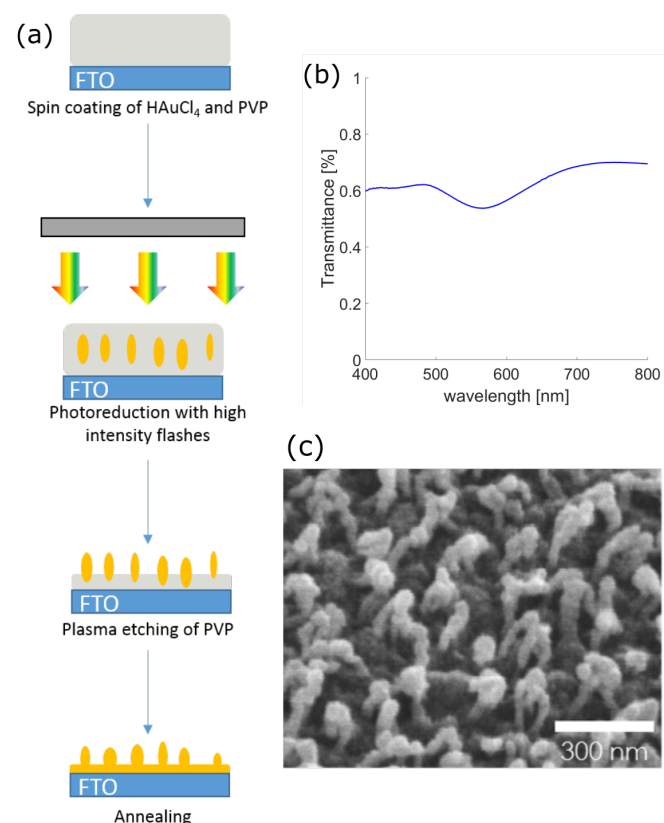


Fig. 1 Fabrication of high aspect ratio gold nanoparticles. (a) Overview of the fabrication process (b) Measured transmittance spectrum of the gold nanoparticles, fabricated on an FTO substrate, and (c) SEM image of the gold nanoparticles.

A solution containing tetrachloroauric acid HAuCl₄ and polyvinylpyrrolidone (PVP) as polymer is spin coated on a fluoride tin oxide (FTO) substrate. High intensity light flashes produced by a xenon lamp are then used to reduce the gold(III) salt to gold nanoparticles, which is visually observed by the purple color taken by the sample. The polymer is finally removed with a directional O₂ plasma etching followed by a high temperature annealing. A scanning electron microscope (SEM) image of the nanoparticles is shown in figure 1c, showing their high aspect ratio, with a diameter of about 50 nm and a height of about 200 nm. The measured transmittance spectrum of figure 1b shows a surface plasmon resonance centered at 570 nm.

Fabrication of water splitting photoelectrodes

Such a nanostructured gold substrate was then used as a scaffold for the deposition of a metal oxide semiconductor layer, with the goal of manufacturing a photoanode for water splitting. Indeed, both the high aspect ratio of the nanoparticles and their plasmonic properties give possibilities for increasing the quantity of light absorbed in the metal oxide layer. Hematite (α -Fe₂O₃) was initially investigated as a semiconductor. This material shows the highest theoretical performances among metal oxides, and using a nanostructured host is a way of overcoming its small hole diffusion length (2-4 nm) [1].

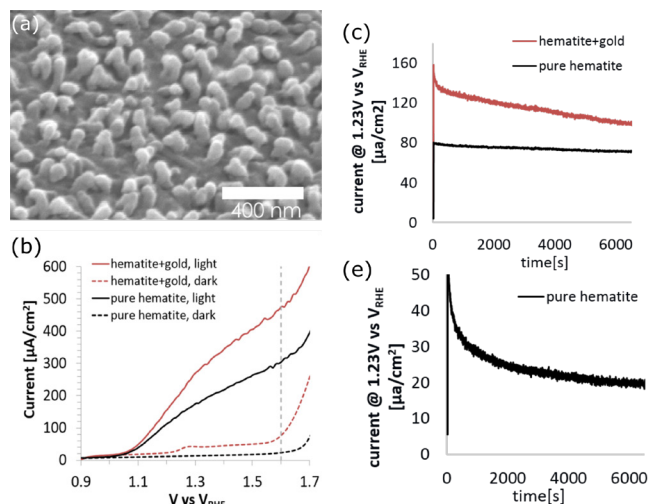


Fig. 2 Performances of a hybrid water splitting photoanode hematite/gold (a) SEM image of the fabricated electrode (b) Linear sweep voltammetry measured in 1M NaOH (pH=14). The illumination intensity was calibrated to 1 sun (c) Photocurrent stability at 1.23 V vs VRHE when 1M NaOH is used as an electrolyte. (d) Photocurrent stability of a pure hematite sample at 1.23 V vs VRHE when a pH=7 buffer is used as an electrolyte.

A conformal hematite coating (Fig. 2a) is achieved with electrodeposition from a solution containing Fe³⁺ ions followed by thermal annealing in air [2]. The performances of such electrodes are characterized by measuring the photocurrent under applied bias in an electrolyte at pH 14. The hybrid hematite/gold electrode shows an increased performance compared to pure hematite deposited on FTO (Fig. 2b). Moreover, the dark current of the hematite/gold sample shows an oxida-

tion peak of the gold nanoparticles at around 1.25 V vs VRHE. This causes a drop of the photocurrent over time (Fig. 2c). The use of less alkaline conditions is necessary for this oxidation to not interfere with the typical operating conditions of the photoelectrode. However, when the electrolyte is changed to a pH 7 buffer, the photocurrent produced by a pure hematite electrode decreases over time (Fig. 2d) because of the low stability of this material in neutral media. This requires external doping for improvement [3].

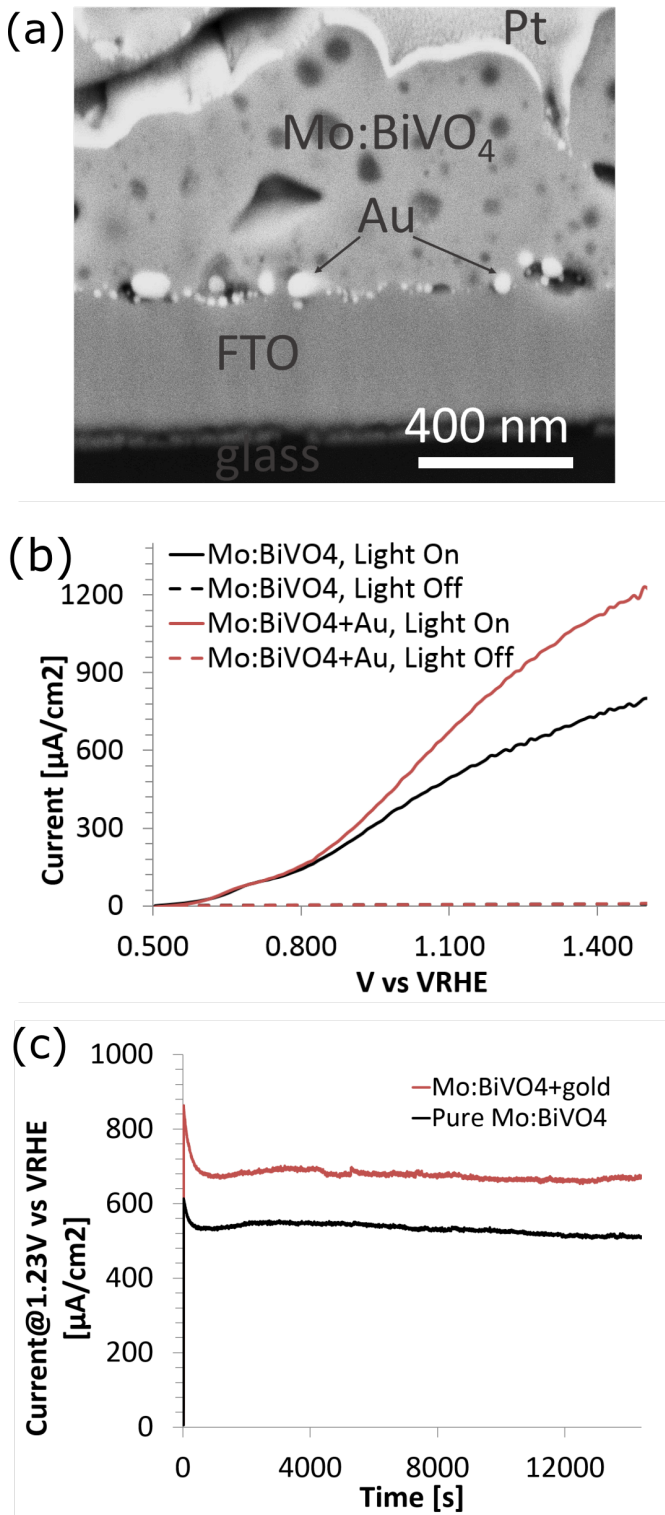


Fig. 3 Performances of a hybrid water splitting photoanode BiVO₄/gold. (a) SEM picture of a cross section obtained with focused ion beam (FIB) milling. (b) Linear sweep voltammetry measured in a pH 7 buffer. The illumination intensity was calibrated to 1 sun. (c) Photocurrent stability at 1.23 V vs VRHE.

For this reason, the metal oxide material was changed to molybdenum-doped bismuth vanadate (Mo:BiVO₄), which has a good stability at neutral pH. Moreover, photoelectrodes made of BiVO₄ have demonstrated the highest performances among fabricated metal oxide photoanodes [4]. A Mo:BiVO₄ layer is deposited on the nanostructured gold substrate by drop-casting a solution containing Bi, V and Mo ions, followed by thermal annealing in air.

An SEM image of the cross section of the final sample is shown in figure 3a. The Mo:BiVO₄ layer is thicker than the gold nanoparticles, and the surface topography is therefore similar to a pure Mo:BiVO₄ sample. In a pH 7 buffer electrolyte, the hybrid sample Mo:BiVO₄/gold shows a photocurrent increased by about 30% with respect to a pure Mo:BiVO₄ sample at 1.23 V vs VRHE. Moreover, the photocurrent of the hybrid photoelectrode shows a good stability over 4 h, similar to that of a pure Mo:BiVO₄ electrode, indicating that no oxidation of the gold nanoparticles occurs under these conditions.

Conclusion & Outlook

A method has been developed for fabricating a plasmonic substrate made with high aspect ratio gold nanoparticles. This substrate was used as a scaffold for fabricating water splitting photoanodes by depositing a metal oxide layer on top of it. A hybrid hematite/gold electrode was fabricated with electrodeposition on the gold scaffold and showed an increased photocurrent compared to pure hematite but a low stability at pH 14 and pH 7. The photocurrent increase obtained with the gold scaffold was preserved when hematite was replaced by Mo:BiVO₄, and the stability at neutral pH was improved. Further developments in the project include deposition of a surface catalyst and post injection of electron donors to improve respectively the charge transport and the charge transfer of the electrode, as well as theoretical and experimental analysis of the enhancement produced by the gold nanoparticles.

References

- [1] K. Sivula, F. Le Formal, M. Grätzel, *WO₃-Fe₂O₃ Photoanodes for Water Splitting: A Host Scaffold, Guest Absorber Approach*, Chem. Mater. **21**, 2862 (2009)
- [2] P. S. Shinde, A. Annamalai, J. Y. Kim, S. H. Choi, J. S. Jang, *Fine-Tuning Pulse Reverse Electrodeposition for Enhanced Photoelectrochemical Water Oxidation Performance of α -Fe₂O₃ Photoanodes*. J. Phys. Chem. C **119**, 5281 (2015)
- [3] J. Y. Kim, J-W. Jang, D. H. Youn, G. Magesh, J. S. Lee, *A Stable and Efficient Hematite Photoanode in a Neutral Electrolyte for Solar Water Splitting: Towards Stability Engineering*, Adv. Energy Mat., 1400476 (2014)
- [4] Y. Qiu et al., *Efficient solar-driven water splitting by nanocone BiVO₄-perovskite tandem cells*, Sci. Adv. **2**, e1501764 (2016)

Magnetic interactions in adsorbed supra molecular architectures containing trigonal prismatic units

Project P1602: Self-assembly and magnetic order of 2D spin lattices on surfaces

Project Leader: T. A. Jung and J. Dreiser

Collaborators: M. Heydari (SNI PhD Student), V. Jacobsen, N. Daffé, M. Baljovic, J. Nowakowski, O. Popova, and G. Morgan

Introduction

Many metal-organic coordination compounds with increasingly complex chemical and electronic structure have been designed and prepared in the last decade. Molecular spintronics [1], but also spin-based quantum technologies provide potential technologic applications driving the scientific activities in this field. This is the particular case for the more complex systems involving multiple spin-bearing atoms exchange coupled in a well defined, possibly tunable way. Well-defined spin-architected materials are most interesting systems to investigate the details of the magnetic exchange interaction down to the level of individual bonds. They can be investigated by comparing magnetometry data with the results of chemically sensitive X-ray spectroscopies, in particular magnetic circular dichroism and local probe spectro-microscopy. Ideally for the purpose of molecular spintronics, spin-bearing coordination compounds can be prepared in the form of surface supported Metal Organic Networks (MON's)[2]. From the plethora of magnetic coordination systems that have been synthesized and characterized in the bulk, only a minor fraction – mainly single molecule, single spin-bearing atom containing magnets – have been stable enough to assemble on surfaces without being strongly modified, or even decomposed by the effects of the surface. It is also important to note that only a few non-planar systems, e.g., the Er(trensal) molecule [3] have been successfully investigated at surfaces.

Here we introduce a new class of non-planar coordination systems which are able to survive the sublimation process in ultrahigh vacuum and the interaction with metal surfaces. These systems belong to a group of neutral or ionic transition metal complexes exhibiting a six-fold coordination with the rare trigonal prismatic geometry. Figure 1 shows one example for such an iron based complex.

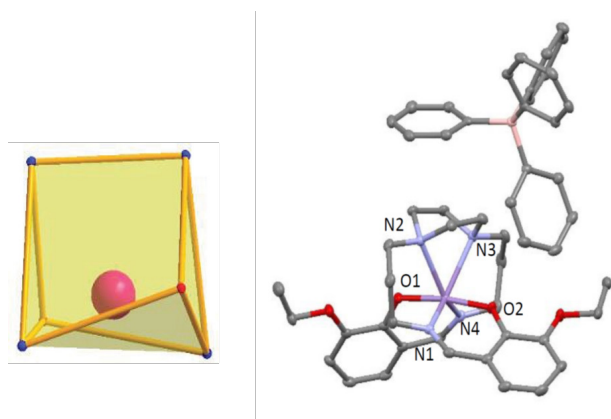


Fig. 1 First coordination shell of the $[FeL_6]$ trigonal prismatic cage (left side) and a ball-and-stick representation of the $[FeL_6]BPh_4$ salt with a tetraphenyl borate anion. Color code: red: oxygen; blue: nitrogen; grey: carbon; violet: iron; light red: boron. Hydrogen atoms have been omitted for clarity.

These trigonal prismatic complexes can be neutral denoted $[ML]^0$ (in the notation $[M(etal)L(igand)]$), if containing divalent M^{2+} ions, or they can be charged if containing a trivalent M^{3+} ion, yielding complexes denoted $[ML]^+$. In the latter case, the cation will be charge-balanced with a suitable counter ion.

In this work, we investigate these three-dimensional metal-organic complexes in the bulk, in polycrystalline powder form and as monolayers interacting with atomically flat, clean gold single crystal surfaces. We compare the magnetic moments in both species as well as the structure and symmetry of the self assembled molecular arrays.

Results

We used element specific X-ray absorption spectroscopy (XAS) in the highly surface sensitive total electron yield (TEY) detection scheme to investigate the oxidation state and the symmetry of the first coordination shell of the iron in the powder form of $[FeL_6]^+$ (Fig. 2a) and in the surface adsorbed monolayer after sublimation (Fig. 3a,b). For the powder sample, the X-ray spectra (defined as sum of the two XAS with helicity +1 and -1) exhibit main peaks at $L_{2,3}$ edges and also a smaller pre-peak at the L_3 edge while for the monolayer samples it shows only one main peak for each $L_{2,3}$ edges with slightly different shoulders in normal and grazing X-ray incident angles. There are different possibilities which could explain the presence of the pre-peaks in powder spectra while these are absent in the monolayer samples. One is that there are some species in the powder sample which contain Fe^{2+} ions and lead to the appearance of the pre-peak in powder spectra. In the case of the monolayer sample these species may be filtered out during the sublimation process. Alternatively, a modified ligand field due to the interactions with the surface may give rise to the changes of the absorption edges. To reach a precise conclusion, further analysis and possibly performing other experiments (such as EPR) are needed.

X-ray magnetic circular dichroism (XMCD) is a well-known method that can probe the absolute values of the element specific magnetic moments, e.g., contained in a surface supported monolayer. It provides information on the spin and orbital contributions. The XMCD spectrum can be obtained by subtracting two XAS spectra recorded with circularly polarized X-ray light with opposite helicities. We are using this method to probe the magnetic moment of the Fe ion in the novel compounds introduced above.

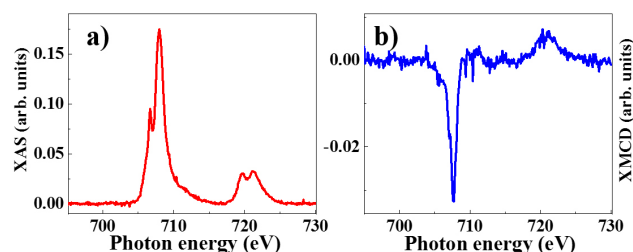


Fig. 2 XAS/XMCD spectra recorded at the Fe $L_{2,3}$ edges on powder sample of $[FeL_6]BPh_4$ at $\mu_0 H = 6.8$ T and $T = 3$ K.

The strong XMCD signal reveals a significant Fe magnetic moment for both the powder sample (Fig. 2b) and for the monolayer on Au(111) (Fig. 3c,d). XMCD recorded on the monolayer sample at grazing incidence ($\theta = 60^\circ$) plotted in (Fig. 3c, d) show a considerable change in the peak shape compared to those taken at normal incidence. For normal incidence clearly a pre-peak at lower energy compared to the main peak at the

L_3 edge appears, while in the grazing case the spectra show a broadened peak with a shoulder at lower energy. The difference between normal and grazing spectra can be due to linear dichroism which in turn could have a magnetic origin as well as a structural origin. The observation of the linear dichroism at the Fe L edge (independent of its origin) implies that there is a preferred orientation of the molecules on the gold surface.

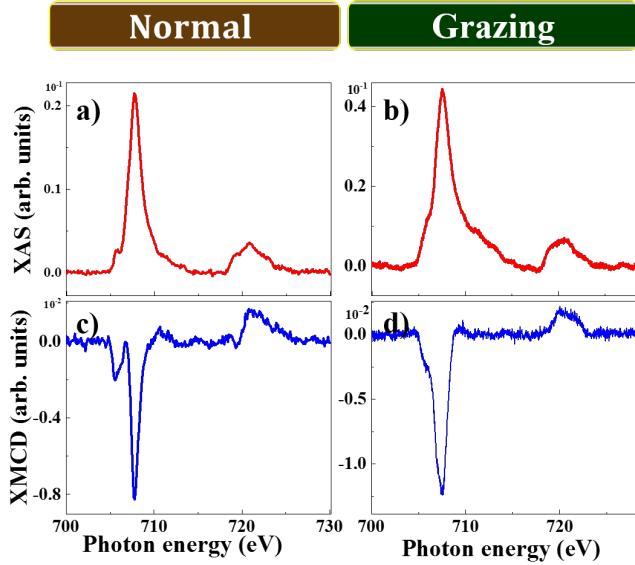


Fig. 3 XAS/XMCD spectra recorded at the Fe $L_{2,3}$ edges on monolayer sample of $[\text{FeL6}]\text{BPh4}$ at $\mu_0 H = 6.8$ T and $T = 3$ K in Normal (a,c) and Grazing (b,d) incident X-ray.

By measuring the magnetic hysteresis curve at low temperature ($T = 3$ K) we find that this particular metal complex exhibits a significant magnetic anisotropy of easy plane type with the hard axis oriented perpendicular to the Au surface.

To extract the absolute values of the spin and orbital magnetic moments, we have performed sum rule analyses with considering the number of the holes as $n_h = 5$ according to the electronic configuration $3d^5$ corresponding to the Fe^{3+} oxidation state. The results are summarized in Table.1.

Table 1. Results of the sum rule analysis of the XMCD spectra for $[\text{FeL6}]\text{BPh4}$ powder and monolayer/Au(111) samples. The values in the parentheses correspond to the experimental errors.

	$\langle L_z \rangle$ [\hbar]	$\langle S_z \rangle$ [\hbar]	M [μ_B]	
Powder	-0.3 (0.1)	-0.8 (0.1)	1.7 (0.3)	
Monolayer	$\theta = 0^\circ$	-0.5 (0.2)	-1.7 (0.1)	3.9 (0.3)
	$\theta = 60^\circ$	-0.8 (0.2)	-1.7 (0.1)	4.2 (0.3)

In all cases, the sum rule results show a strong contribution of the orbital angular momentum, but the contribution of the spin is much stronger. The interesting point in this system is that we have a remarkable orbital contribution which means the orbital moment is not fully quenched in contrast with most of the similar complexes in the same situation. In transition from the powder sample to the monolayer, modifications in the magnetism occur.

In conclusion, one example of a novel spin-bearing molecular architecture based on an ionic compound, specifically $[\text{FeL6}]\text{BPh4}$, has been successfully prepared on a diamagnetic Au(111) substrate in the monolayer regime and its orientation dependent magnetic moments have been compared with those measured on polycrystalline powder samples. These results represent the first steps towards the further in-depth assessment of this chemically and structurally tunable class of materials with their unprecedented chemically configurable magnetic and electronic properties at lower than three dimensions.

References

- [1] L. Guo, X. Gu, X. Zhu, X. Sun, *Recent Advances in Molecular Spintronics: Multifunctional Spintronic Devices*, *Advanced Materials* **31**, 1805355 (2019)
- [2] J. Girovsky, et al. *Long-range ferrimagnetic order in a two-dimensional supramolecular Kondo lattice*, *Nat. Commun.* **8**, 15388 (2017)
- [3] J. Dreiser, et al. *Exchange Interaction of Strongly Anisotropic Tripodal Erbium Single-Ion Magnets with Metallic Surfaces*, *ACS Nano* **8**, 4662–4671 (2014)

Watching molecular transport in a biological nanopore

Project P1603: A mechano-optical microscope for studying force transduction in living cells

Project Leader: R. H.Y. Lim and E. Meyer

Collaborator: T. Kozai (SNI PhD Student)

Introduction

The nucleus is a highly specialized organelle that contains the majority of the cell's genetic material and serves to maintain the integrity of the cell by regulating gene expression and DNA replication. Essential proteins, RNAs and metabolites translocate across the nuclear envelope (NE) which separates the nucleus from the cytoplasm. This translocation process [i.e., nucleocytoplasmic transport (NCT)] proceeds through aqueous channels known as nuclear pore complexes (NPCs). NPCs mediate the selective transport of biomolecules between the cytoplasm and nucleus in eukaryotic cells. However, its molecular mechanism remains disputed. This is because the NPC barrier is comprised of numerous intrinsically disordered phenylalanine-glycine nucleoporins (FG Nups) that are extremely difficult to visualize, not least at transport-relevant timescales (~ 10 ms). Recently, we used high-speed atomic force microscopy (HS-AFM) to resolve the dynamic behavior of FG Nups inside NPCs at ~ 200 ms timescales [1]. Meanwhile, structural changes of FG Nups under transporting conditions are still unclear.

In this project, we use HS-AFM to investigate dynamic changes in the FG Nups under transporting conditions. This includes: (i) FG Nups layers and (ii) FG Nups within intact isolated yeast NPCs.

Visualizing the dynamic behavior of isolated FG Nups

In order to visualize the dynamic behavior of isolated FG Nups under transporting conditions, isolated yeast Nsp1 FG-fragment that has only a disordered region is used. First, the molecular features of the Nsp1 fragments attached to a mica surface in a buffer solution were observed by HS-AFM (Fig. 1a). Here, HS-AFM resolves the globular domain and the disordered tail region of the Nsp1 FG-fragment. The globular domain appears to be well adsorbed onto the mica surface, and its position does not change significantly over time. In comparison, the disordered FG-tail region rapidly fluctuates. These fluctuations are consistent with the diffusive motion of various intrinsically disordered proteins as observed by HS-AFM [2].

Next, the Nsp1 fragments were tethered to a lipid bilayer and visualized by HS-AFM. Supported lipid bilayers (SLBs) were prepared on mica with varying fractions of metal ion chelator (DGS NTA(Ni)) containing lipids (DOPC). Nsp1 fragments were then tethered to the lipid membrane by including 6xHis-tags at their N-termini. Thus far, single molecule resolution remains challenging. Indeed, the Nsp1 fragment is mainly seen as a globule (Fig. 1b) and may be due to their highly rapid and dynamic behavior on the SLB. However, we observe that two Nsp1 globules can interact with each other. Future efforts will seek to investigate such behavior.

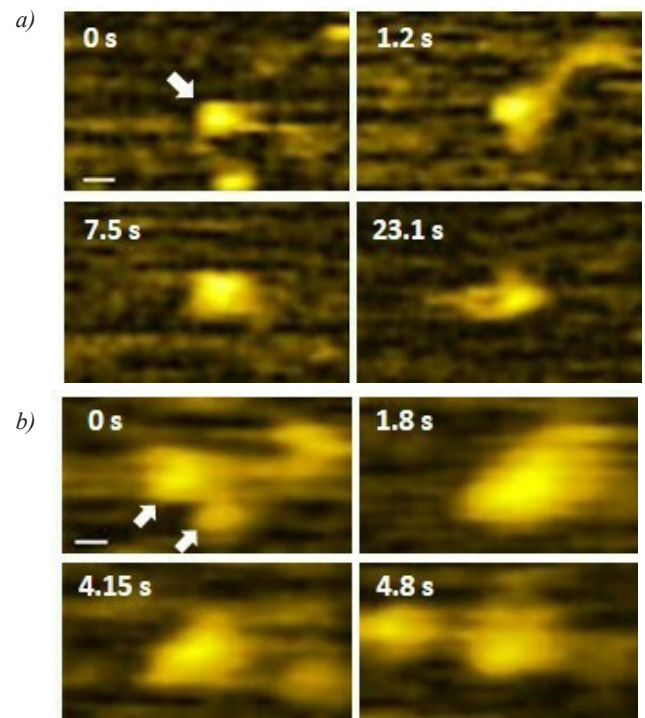


Fig. 1 (a) Successive HS-AFM images showing a fluctuation of Nsp1 FG-fragment on a mica surface. In images of 1.2 s and 23.1 s, filamentous features represent disordered regions of Nsp1 FG-fragment. Frame rate, 100 ms/frame. Scale bar: 10 nm. (b) Successive HS-AFM images showing Nsp1 FG-fragment interacting with each other on a lipid membrane. White arrows indicate Nsp1 FG-fragment. Frame rate, 50 ms/frame. Scale bar: 10 nm.

Visualizing the dynamic behavior of FG Nups inside isolated yeast NPCs

The entire structure of the isolated yeast NPC has been determined at sub-nanometre precision [3]. However, the dynamic behavior of FG Nups inside the isolated yeast NPC has yet to be resolved. In collaboration with Prof. Michael Rout (Rockefeller University), we have now visualized FG Nup dynamics inside isolated yeast NPCs for the first time. Representative HS-AFM images reveal isolated NPCs with and without cargoes “caught” in transit (known as central plugs) [4] (Fig. 2). From cross-sectional height analyses, the diameters of the NPCs with and without central plug are 60.5 ± 3.7 nm and 66.6 ± 7.5 nm, respectively. Besides, the central channel depths of the NPCs with and without central plug are 4.5 ± 2.9 nm and 17.8 ± 2.5 nm, respectively.

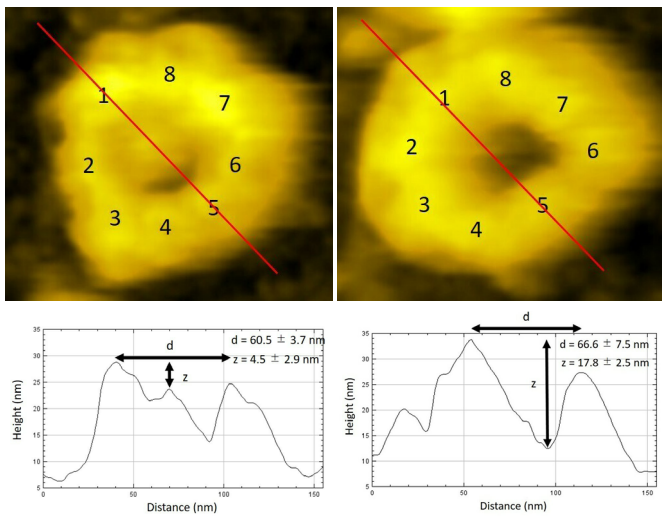


Fig. 2 (a) An isolated yeast NPC with central plug showing 8 spokes (numbered) and a height profile corresponds to cross section indicated by a red line on the AFM image. Scale bar: 20 nm. (b) An isolated yeast NPC without central plug showing 8 spokes (numbered) and a height profile corresponds to cross section indicated by a red line on the AFM image. Scale bar: 20 nm. NPC diameters (d) and central channel depths (z) from upper rims were measured.

We next focused on resolving FG Nup behavior within the central channels of isolated NPCs. In a vacant central channel, the FG Nups are seen to dynamically and repeatedly extend into and retract from the pore interior (Fig. 3a). This behavior is similar to the diffusive motion of FG Nups resolved within NPCs obtained from *Xenopus laevis* oocyte nuclei [1]. Interestingly, fluctuating FG Nups can also be resolved in the non-obscured gap between the central plug and the NPC walls (Fig. 3b). Based on our observations, it appears that FG Nups interact with the central plug dynamically and intermittently.

Central plugs might be composed of cargos and nuclear transport receptors such as karyopherins (Kaps, also known as importins and exportins). However, little is known about the central plug is formed or if it serves any function. Kap β 1, an import receptor, recognizes specific cargoes either directly or via an adaptor Kapa. Kapa mediates cargo binding to Kap β 1 via its interactions with FG Nups. Binding of Kap β 1 to the FG Nups is an energetically favored process. On the other hand, unbinding requires a GTPase known as Ran. Therefore, our next steps will be to investigate the role of Kaps in facilitating central plug formation.

Summary

We have used HS-AFM to investigate dynamic changes in the FG Nups under transporting conditions. Isolated FG Nups exhibited rapid fluctuations around a more stable globular domain. Furthermore, we have successfully visualized FG Nup dynamics within isolated yeast NPCs. This will serve to elucidate how the FG Nups behave under transporting conditions as well as clarifying the role and potential function of the central plug.

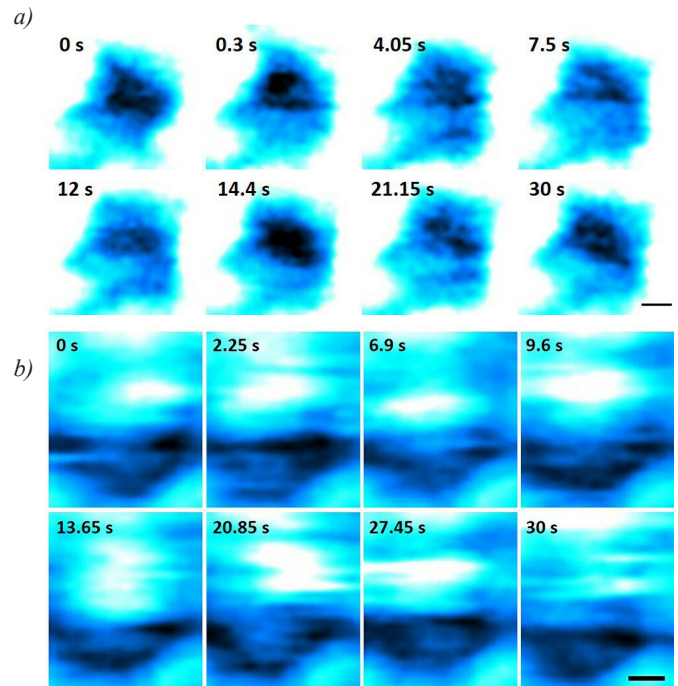


Fig. 3 (a) Dynamic behavior of FG Nups within a NPC without central plug forming a NPC barrier. Frame rate, 150 ms/frame. Scale bar: 10 nm. (b) Dynamic behavior of FG Nups and a central plug indicated by the white arrow. Frame rate, 150 ms/frame. Scale bar: 10nm.

References

- [1] Y. Sakiyama, A. Mazur, L. E. Kapinos, R. Y. H. Lim, *Spatiotemporal dynamics of the nuclear pore complex transport barrier resolved by high-speed atomic force microscopy*, *Nature Nano.* **11**, 719-724 (2016)
- [2] A. Miyagi, Y. Tsunaka, T. Uchihashi, K. Mayanagi, K. Morikawa, T. Ando, *Visualization of intrinsically disordered regions of proteins by high-speed atomic force microscopy*, *Chem. Phys. Chem.* **9**, 1859-1866 (2008)
- [3] S. J. Kim, et al., *Integrative structure and functional anatomy of a nuclear pore complex*, *Nature* **555**, 475-482 (2018)
- [4] D. Stoffler, K. N. Goldie, B. Feja, U. Aebi, *Calcium-mediated structural changes of native nuclear pore complexes monitored by time-lapse atomic force microscopy*, *J. Mol. Biol.* **287**, 741-752 (1999)

Polymer-lipid hybrid membrane: a platform to enhance the activity of Cytochrome c

Project P1604: Selective reconstitution of biomolecules in polymer-lipid membranes

Project Leader: W. Meier and U. Pielek

Collaborator: S. Di Leone (SNI PhD Student)

Introduction

Solid supported membranes have been increasingly popular in the field of engineering, biological and physical sciences since they can mimic cell membranes with near molecular precision. Besides, they can be utilized for many biotechnological applications including bio-sensing and diagnostics [1]. To date, they have been created from deposition of membrane building blocks such as phospholipids or amphiphilic block copolymers onto solid support. Mixing block copolymer with phospholipids create hybrid membranes, leading to the formation of distinct domains due to the differences in their physical characteristics. Hybrid membranes benefit from both properties of block copolymers and lipids, yielding a preferential integration of many different biomolecules into the distinct domains of the membranes [2]. We combined polydimethylsiloxane-b-poly-methyloxazoline-carboxylic acid (PDMS-b-PMOXA-COOH) and dipalmitoyl-glycero-phosphocholine (DPPC) for preparing a heterogeneous hybrid membrane on solid support [3]. We wanted to drive the cytochrome c combination towards a specific domain of the membrane, preserving the protein folding and the membrane integrity (Fig. 1).

Material and Methods

Previously, the lipid, polymer and hybrid monolayers at air-water interface were characterized in terms of stability and domain separation. Double layer membranes were deposited onto solid support with Langmuir-Blodgett and characterized to investigate their structure. Then, the membranes were combined with the protein cytochrome c (cyt c) and the interaction was monitored with quartz crystal microbalance with dissipation module (QCM-D). The combination was performed through two different approaches: either covalent bond or spontaneous insertion. Atomic Force Microscopy (AFM) was also performed on the different membranes, in order to observe whether the membrane underwent a structure modification after the protein combination. Finally, the activity of the protein combined was evaluated with fluorimetry. The comparison between the different membranes for each step was

necessary to better understand the advantages of the hybrid platform compared to ordinary lipid and polymer membranes.

Results and discussion

The combination of cyt c with the polymer, lipid and hybrid membranes was monitored by recording the changes in frequency and dissipation shifts in QCM-D (Fig. 2). In general, irrespective of the combination method, 500 mg/mL cyt c solution was injected for 30 min, followed by a PB rinsing step for 10 min. In the case of the cyt c insertion in the different membranes, there was a decrease in frequency and slight increase in the dissipation shifts, indicating changes in the adsorbed mass and viscoelastic properties of the bilayer, respectively (Fig. 2A and 2B). A similar amount of cyt c was successfully inserted into copolymer and hybrid membrane, higher when compared to the amount inserted into the lipid membranes, as observed from the change in frequency. The frequency increase of cyt c on the lipid membrane before the rinsing step, namely desorption of mass, suggested a membrane removal from the solid support. Instead, the hybrid- and the polymer membranes were able to create the suitable environment for the protein combination. The dissipation shifts showed the highest value for the conjugation (Fig. 2D) compared to the insertion in all different membranes, confirming the successful anchoring of the protein outside the membrane and so facilitating its accessibility for a substrate.

AFM measurements proved that cyt c found a suitable environment into the flexible polymer membrane and polymer domain in the hybrid membrane (Fig. 3A) while the lipid membrane underwent transformational changes, due to the capability of cyt c to remove the membrane attached to the silica (Fig. 3B). The hybrid membrane interacted peculiarly with the cyt c: no membrane removal was detected in this case, rather a membrane reorganization, where the lipid domains reorganized themselves to the top of the polymer matrix and constituted rafts that could accommodate the protein (Fig. 3C). This process is similar to the one involving membranes in nature. Regarding this peculiar behavior, the polymer membrane integrity was preserved due to its improved mechanical resistance and the lipid domains could accommodate the cyt c without being degraded. This way, we achieved a selective combination of the chosen protein with one specific membrane domain.

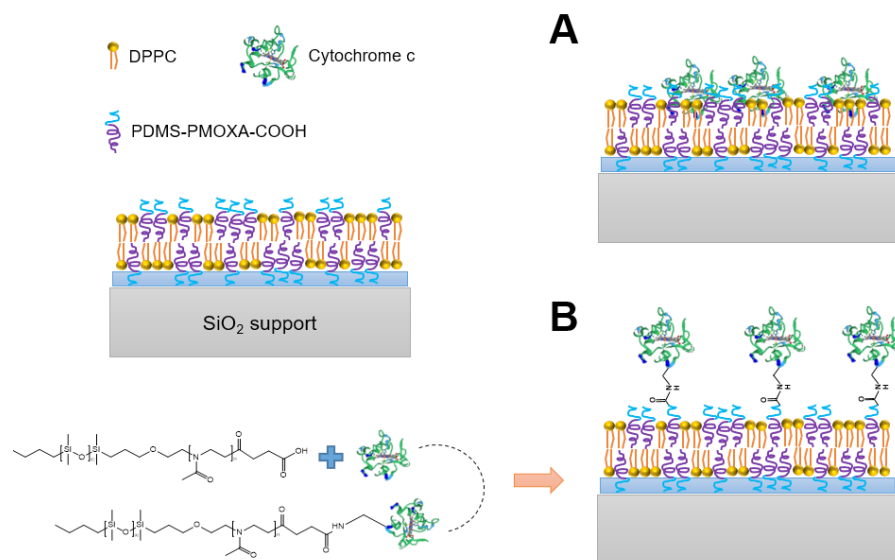


Fig. 1 Schematic representation of hybrid supported bilayer membrane and their combination with model protein cytochrome c through spontaneous insertion (A) and covalent conjugation by EDC/sNHS coupling (B).

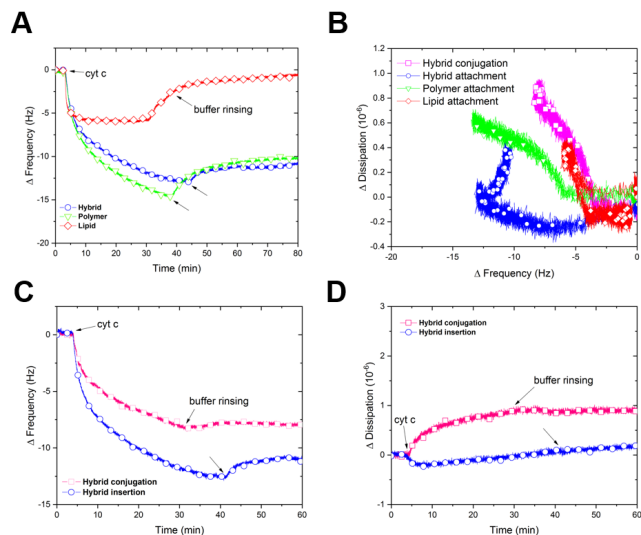


Fig. 2 QCM-D of protein-membrane combination: frequency (A) and dissipation (B) comparison of protein insertion into different types of membrane; frequency (C) and dissipation (D) comparison of protein combination with hybrid membrane with both strategies.

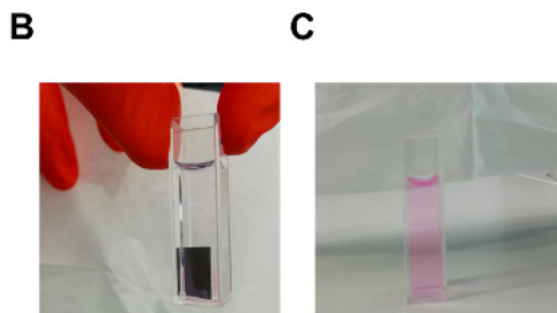
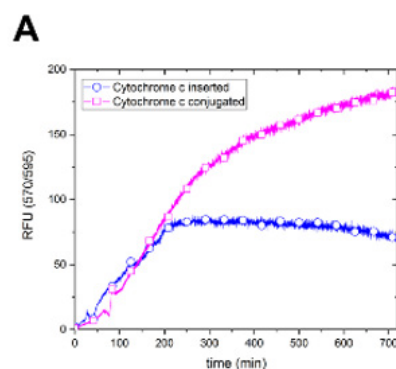


Fig. 4 Qualitative fluorimetry comparison of protein activity after combination with hybrid membrane via different strategies (A); change in colour of the PB solution over time in the presence of cyt c conjugated onto hybrid membrane after 30 minutes (B) and 12 hours (C).

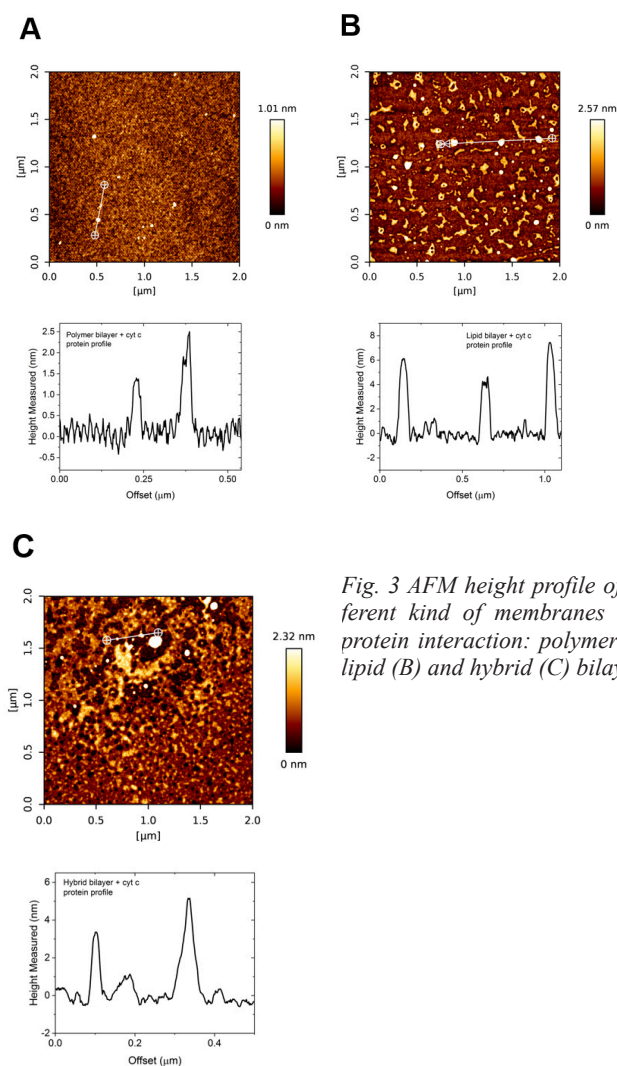


Fig. 3 AFM height profile of different kind of membranes after protein interaction: polymer (A), lipid (B) and hybrid (C) bilayers.

Conclusion

We developed hybrid solid-supported membranes suitable for combination with the model protein cytochrome c. For the first time, we found that the hybrid was able to form a bi-layer membrane on silica, stable over time and free of major defects. Both strategies of protein combination (insertion and conjugation) were successful for hybrid membranes and the protein combined was quantitatively evaluated. Moreover, we were able to selectively drive the combination of the model protein toward a specific domain that is the lipid domain in case of the insertion or the polymer domain in case of conjugation. The model bio-interface reported is of great interest for further development in the complexity and versatility of the system. In fact, the phase separation allows the combination of different proteins with different domains and the polymer functionalisation with a wide range of different ending group making the specific binding of a variety of biomolecules possible. This study represents versatile strategies for the design of new active platforms to support industrial and medical interest.

References

- [1] I. Craciun, S. D. Alexandru, G. Gunkel-Grabole, A. Belluati, G. P. Palivan, *Surfaces decorated with polymeric nanocompartments for pH reporting*, *Helv. Chim. Acta*, **101**(3), e1700290 (2018)
- [2] J. Thoma, S. Belegriou, P. Rossbach, M. Grzelakowski, K. Kita-Tokarczyk, W. Meier, *Membrane protein distribution in composite polymer–lipid thin films*, *Chem. Commun.*, **48**(70), p. 8811-8813 (2012)
- [3] J. Kowal, D. Wu, V. Mikhalevich, C. G. Palivan, W. Meier, *Hybrid polymer–lipid films as platforms for directed membrane protein insertion*, *Langmuir*, **31**(17) p. 4868-4877 (2015)

Smart peptide nanoparticles for efficient and safe gene therapy

Project P1606: Smart peptide nanoparticles for efficient and safe gene therapy

Project Leader: C. G. Palivan and J. Benenson

Collaborator: S. Tarvirdipour (SNI PhD Student)

Introduction

Gene therapy is of particular significance in the treatment of rare inherited diseases, neurological disorders, cardiac diseases, and cancer [1]. Accordingly, viral and non-viral delivery systems are used to introduce exogenous nucleic acids into host cells. The numerous disadvantages associated with viral strategies such as high immunogenicity, limitation in size of transgenic DNA, low availability, and high manufacturing cost, boosted the development of non-viral delivery systems. Peptides as non-viral delivery systems are particularly attractive as they are often able to sidestep the limitations mentioned above along with being biocompatible and biodegradable [2]. Yet, the self-assembly of supramolecular nanostructures from pure peptides for the entrapment and delivery of large DNA molecules has not been systematically investigated. This study aims at taking advantage of peptide vector properties by designing peptides that self-assemble and have physicochemical properties favoring the incorporation of different DNA types (single-stranded versus double-stranded) with variable length.

The design of our amphiphilic peptide (HR)3gT involves significant modifications of a previously published peptide H3gT [3]. (HR)3gT self-assemble into multi-compartment micellar nanoparticles (MCM-NPs) in the presence of single- and double-stranded DNA of up to 100 nucleotides in length (Fig. 1).

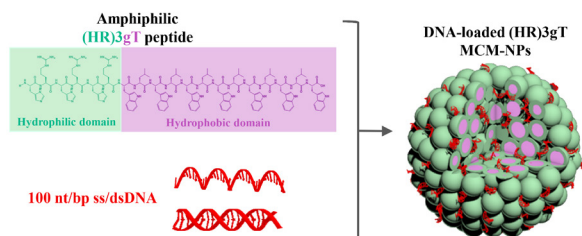


Fig. 1 Schematic representation of the amphiphilic peptide (HR)3gT that is able to self-assemble into multicompartiment micellar nanoparticles (MCM-NPs) while condensing DNA through electrostatic interactions.

Here we report the systematic analysis of (HR)3gT self-assembly in the absence and presence of 22 and 100 nucleotide long single- and double-stranded DNA (ssDNA/dsDNA).

Material and methods

(HR)3gT and H3gT comprising 19 and 10 amino acids, respectively, were synthesised on a rink amide resin, purified, and analysed by time-of-flight mass spectrometer (MALDI-TOF-MS) in positive mode.

The self-assembly of (HR)3gT and H3gT was achieved via the solvent exchange method, dialysing the organic solvent (35% ethanol) against milli-Q[®] ultrapure H₂O. MCM-NPs resulting from the self-assembly of (HR)3gT in the presence of 22- and 100-nucleotide ssDNA and corresponding dsDNA were then fully characterized as follows.

The size of DNA-free and DNA-loaded (HR)3gT MCM-NPs was measured by dynamic light scattering (DLS) together with fluorescence correlation spectroscopy (FCS) and nanoparticle tracking analysis (NTA). In addition, the surface charge of MCM-NPs was quantified by measuring their zeta potential. Furthermore, the concentration of MCM-NPs in solution and the DNA loading efficiency were determined by NTA. The supramolecular architecture and structural stability of the MCM-NPs was assessed by transmission electron microscopy (TEM) and DLS. To analyze the thermosresponse of MCM-NPs, their morphology was examined by TEM before and after incubation at 37 °C for 5 h and 24 h.

Results

We determined the hydrodynamic diameter of DNA-free and DNA-loaded (HR)3gT MCM-NPs by employing DLS, NTA and FCS, and compared the corresponding data (Table 1). In addition, the surface charge and polydispersity index (PDI) were obtained by Zeta Sizer and DLS measurements, respectively (Table 1).

Table 1 Characterization of DNA-free and DNA-loaded (HR)3gT MCM-NPs, suspended in water, pH 7.

(HR)3gT MCM-NPs	PDI	D _h (nm) DLS	D _h (nm) NTA	D _h (nm) FCS	Zeta potential (mV)
(HR)3gT NPs	0.19±0.024	112±21	102±6	N/A	+8.2±2.1
22nt ssDNA loaded (HR)3gT NPs	0.23±0.026	160±18	151±12	144±58	+2.8±3.35
22bp dsDNA loaded (HR)3gT NPs	0.22±0.023	115±19	129±10	124±62	+3.67±3.11
100nt ssDNA loaded (HR)3gT NPs	0.28±0.021	176±11	164±4	186±78	+3.46±3.87
100bp dsDNA loaded (HR)3gT NPs	0.27±0.02	165±12	150±11	174±99	+4.18±3.36

DNA-free and DNA-loaded (HR)3gT MCM-NPs have a PDI of ≤0.3, which indicates a relatively monodisperse system. The mean diameter obtained by FCS and NTA was similar to that determined by DLS for each type of (HR)3gT MCM-NPs, and all values were below 200 nm (Table 1). The surface charge of the MCM-NPs only slightly decreased by entrapment of negatively charged DNA as compared with the charge of the DNA-free (HR)3gT MCM-NPs. These results indicate the presence of the corresponding DNA payload between individual micelles of the multi-compartment rather than its accumulation on the NP surface.

NTA measurements revealed (Table 2) that independent of the type of DNA, more than 60% of the MCM-NPs were loaded. The percentage of loaded particles for dsDNA (22bp and 100bp) was clearly higher than for ssDNA (22nt and 100nt).

To obtain insight on (HR)3gT MCM-NPs stability, we analyzed their size when stored at 4°C for different periods of time by DLS (Fig 2A). Size measurements recorded every 30 days indicated that the average diameter of DNA-free and DNA-loaded (HR)3gT MCM-NPs did not change over five months. Consistently, TEM analyses (Fig 2B) showed that nanoparticles retained their multi-compartment micellar structure after 5 months when maintained at 4°C.

Table 2 Nanoparticle tracking analysis of DNA-free and DNA-loaded (HR)3gT MCM-NPs.

MCM peptide NPs	Total concentration (particles/ml)	Concentration of labelled particles (particles/ml)	Loaded particles (%)
(HR)3gT NPs	$4.29 \times 10^8 \pm 9.17 \times 10^7$	N/A	N/A
22nt ssDNA loaded (HR)3gT NPs	$5.57 \times 10^8 \pm 7.03 \times 10^7$	$3.82 \times 10^8 \pm 2.29 \times 10^7$	68.5
22bp dsDNA loaded (HR)3gT NPs	$3.02 \times 10^8 \pm 3.06 \times 10^7$	$2.87 \times 10^8 \pm 3.10 \times 10^7$	95
100nt ssDNA loaded (HR)3gT NPs	$3.29 \times 10^8 \pm 7.65 \times 10^7$	$2.25 \times 10^8 \pm 1.10 \times 10^7$	68.3
100bp dsDNA loaded (HR)3gT NPs	$3.34 \times 10^8 \pm 8.64 \times 10^7$	$2.74 \times 10^8 \pm 1.52 \times 10^7$	82

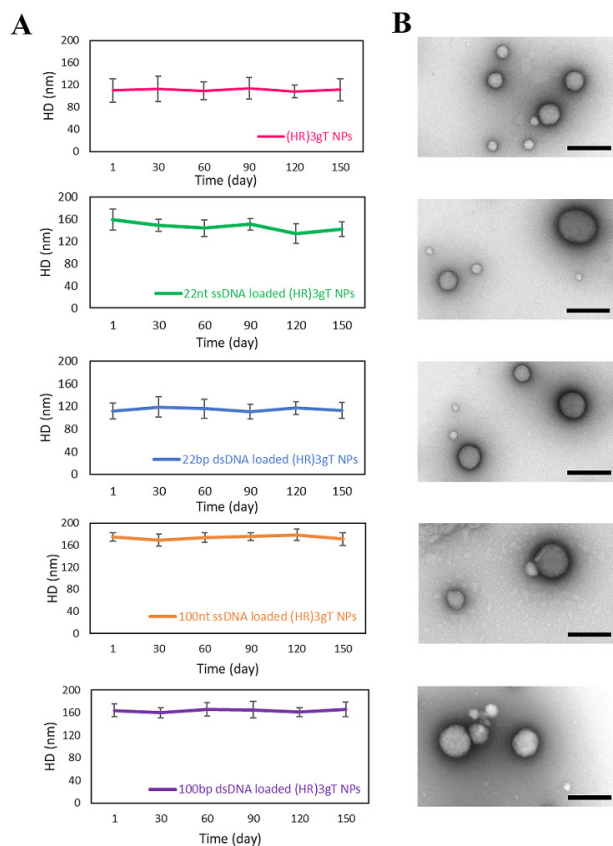


Fig. 2 Stability of (HR)3gT MCM-NPs. From top to bottom: (A) DLS over 150 days, and (B) TEM after 150 days for (HR)3gT MCM-NPs, 22nt ssDNA-loaded (HR)3gT MCM-NPs, 22bp dsDNA-loaded (HR)3gT MCM-NPs, 100nt ssDNA-loaded (HR)3gT MCM-NPs, and 100bp dsDNA-loaded (HR)3gT MCM-NPs. Scale bars=200 nm.

However, after 5 h at 37°C, DNA-free and DNA-loaded (HR)3gT MCM-NPs had disassembled into smaller MCMs and/or individual micelles (Fig. 3). TEM images after 24 h at 37°C revealed that disassembly continues over time.

All peptide MCM-NPs exhibited a similar trend in the change of their structure and size, independent of the length and type (single or double stranded) of the entrapped DNA.

Conclusion and outlook

Critical amino acid extensions and modifications in the hydrophilic and hydrophobic domain of the newly synthesized amphiphilic (HR)3gT enabled successful entrapment of single- and double-stranded DNA sequences of 100 nucleotides. DNA were entrapped inside NPs during the self-assembly process and formation of the multi-compartment micellar nanoparticles. The analysis of the molecular properties of (HR)3gT MCM-NPs in the presence of different DNA cargoes indicates that the entrapment is primarily governed by electrostatic interactions between DNA and peptide. Our future efforts are directed towards modifications of the peptide design to ultimately obtain a safe and efficient peptide-based delivery nano-system for entire protein-encoding genes.

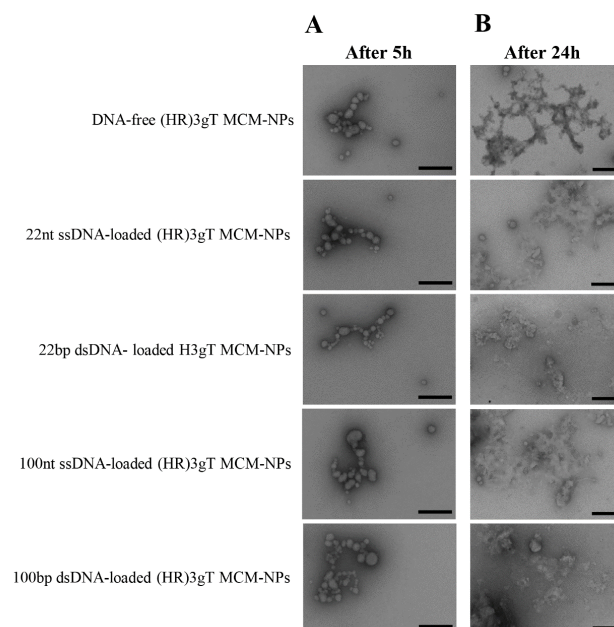


Fig. 3 TEM micrographs of (HR)3gT MCM-NPs with different DNA loads after (A) 5 h incubation, and (B) 24 h incubation at 37°C. Scale bars=200 nm.

References

- [1] S. L. Ginn, I. E. Alexander, M. L. Edelstein, M. R. Abedi, and J. Wixon, *Gene therapy clinical trials worldwide to 2012—an update*. *J. Gen. Med.*, **15**(2), 65-77 (2013)
- [2] H. Yin, R. L. Kanasty, A. A. Eltoukhy, A. J. Vegas, J. R. Dorkin, and D. G. Anderson, *Non-viral vectors for gene-based therapy*, *Nat. Rev. Gen.*, **15**(8), 541-555, (2014)
- [3] S. J. Sigg, V. Postupalenko, J. T. Duskey, C. G. Palivan, W. Meier, *Stimuli-Responsive Codelivery of Oligonucleotides and Drugs by Self-Assembled Peptide Nanoparticles*, *Biomacromolecules*, **17**(3), 935-945 (2016)

Understanding phonon propagation in nano-devices

Project P1607: Understanding and engineering of phonon propagation in nanodevices by employing energy resolved phonon emission and adsorption spectroscopy

Project Leader: I. Zardo and C. Schönenberger

Collaborators: L. Gubser (SNI PhD Student), M. Nilsson, A. Baumgartner, F. Thomas, C. Jünger, G. Fülöp, L. Sorba (Pisa), and V. Zannier (Pisa)

Introduction

During the last few decades, research has improved our knowledge and control over electrons and photons, enabling impressing advances for electronic and optoelectronic applications. The same degree of control is still lacking for phonons. The ability to manipulate phonons and phonon transport on a quantum level would lead to full control over heat flow in nanodevices. This could be used in the form of phonon transistors [1] and to realize logic gates [2].

The goal of the project is twofold. First, efficient phonon emitters and detectors have to be developed. Second, the developed devices can then be used to investigate and engineer phonon band structures. To realize the former, inelastic tunneling through the states of a double quantum dot shall be used as phonon emitter and detector.

DQD phonon emitter/detector

The group of Jason Petta has demonstrated a maser driven by single-electron tunneling through a double quantum dot (DQD) in a semiconducting nanowire (NW) [3]. Such a device is based on inelastic tunneling through the energy states of the two QDs, when the system is driven by an applied bias voltage.

A schematic of the proposed DQD structure is presented in figure 1. Under an applied bias, an electron undergoes three subsequent tunnel transitions: i) from source to eigenstate ϵ_1 of QD1; ii) from ϵ_1 to ϵ_2 in QD2; iii) from ϵ_2 to drain.

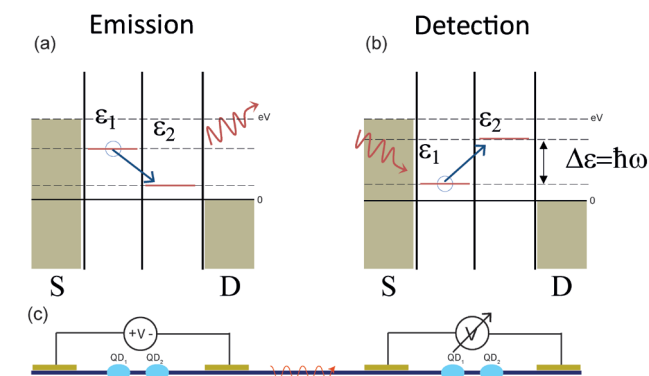


Fig. 1 Illustration of (a) a phonon emitter and (b) detector using a double quantum dot (DQD). Driven by an applied bias, inelastic tunneling is used to either emit or detect phonons. (c) Schematic of an invisaged device. Inside the semiconducting nanowire two double quantum dots (light blue) are defined by local bottom gates (red). Phonons are then generated by an applied bias through source (S)-drain (D) contacts in the left DQD system and detected by measuring the voltage in the right DQD.

Inelastic tunneling takes place if the energy levels are detuned ($\epsilon_1 \neq \epsilon_2$). The electron will then tunnel through the DQD emitting/absorbing a particle (a photon or a phonon) able to account for the energy difference. When $\epsilon_1 > \epsilon_2$, tunneling can only take place if such a particle is emitted. Hence, the device acts as a photon or phonon emitter. Analogously, when $\epsilon_2 > \epsilon_1$, tunneling can only take place if a particle is simultaneously absorbed. The device now acts as a detector.

In the work of Petta et al. [3], the DQD system was coupled to a microwave cavity, as their interest was focused on photon emission and absorption. In absence of such a cavity emission/absorption of phonons is expected to be dominant. This makes the DQD system an excellent choice to emit and detect monochromatic phonons.

Two barrier NW measurements

While QDs are often defined by narrow gate lines, this approach does not allow for a strong confinement with QD eigenstates that are separated by > 1 meV. Instead we use QDs that are defined by an InAs/InP nanowire heterostructure (Fig. 2). This approach allows for very small QDs with a large level spacing [4], see figure 2.

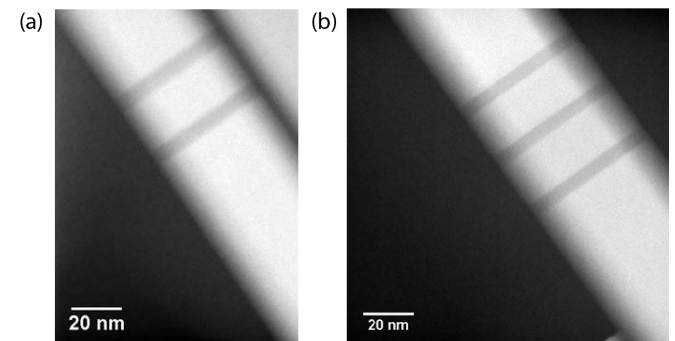


Fig. 2 Transmission electron microscope image of the InAs wires with symmetric InP barriers. Due to the difference in bandgap of the materials (InAs: 0.354 eV; InP: 1.344 eV) tunnel barriers are formed. Two barriers define a single quantum dot (a), whereas three barriers form a double quantum dot (b).

Electrical characterization of the QD formed in the two barrier NW using a two terminal contact design has been performed in collaboration with F. Thomas and C. Jünger. By analyzing the Coulomb resonance line shape from the few to the many electron regime, electrically tunable tunnel couplings from $< 1 \mu\text{eV}$ to $> 600 \mu\text{eV}$ were found, showing a transition from the temperature to the lifetime broadened regime.

From the transition between these regimes the barrier height could be extracted as ~ 350 meV. Investigating the tunnel barriers and their asymmetry, yields an asymmetry close to 1, showing the remarkable symmetry of the tunnel barriers in a regime, where semiconducting lead states are not strongly modulating the density of states. These results were recently accepted for publication [5].

Three barrier NW measurements

Initial electrical transport measurements performed on the three barrier NWs only showed indication of a strongly coupled double dot. To decrease the inter dot coupling between the designed QDs, the thickness of the middle InP segment was increased during growth.

Additionally the device fabrication was optimized, adding further side gates and decreasing their distance to the NW. The decreased distance increases the gate lever arm on the chem-

ical potential. The additional gates increase the tuneability of the potential landscape, as well as provide some screening of the electric field from the other gates, increasing the selectivity of the QD tuning side gates.

The combination of these optimization processes, allowed us to reach the weakly coupled regime of the DQD defined in the three barrier NW (Fig. 3).

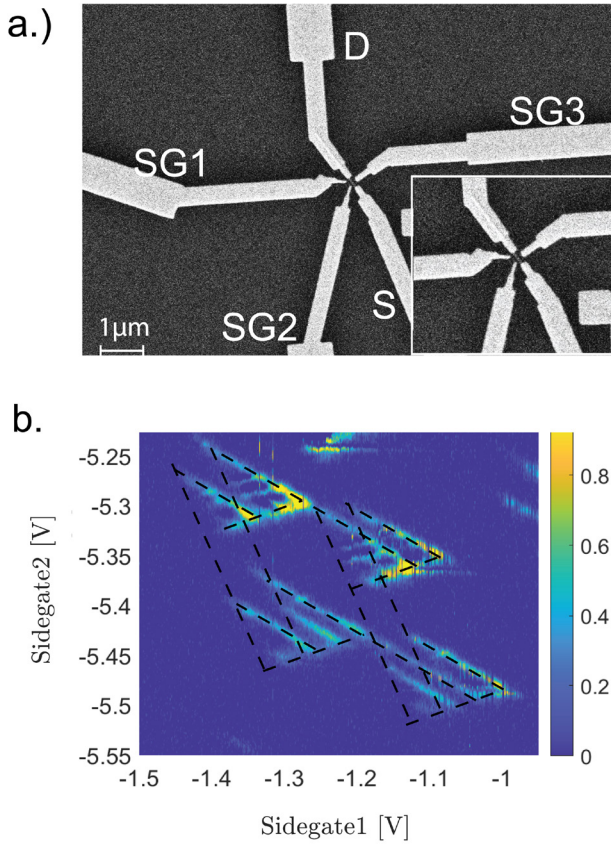


Fig. 3 (a) Scanning electron microscope image of a device consisting of an InAs nanowire with three in situ grown InP tunnel barriers of length 5.2, 6.8, 5.4 nm, separated by 19 nm of InAs forming the QDs. The NW is contacted by two Ti/Au (S/D) contacts (distanced 150 nm from the QDs) using sulphur passivation [6]. Three side gates (SG) are present at a nominal distance of 70 nm to the NW. The doped Si/SiO₂ substrate acts as a global back gate. (b) Differential conductance measurement as a function of SG1 and SG2 at 4 mV DC bias at 4 K. The remaining gates were at a constant voltage of VBG = -3 V, VSG3 = 0 V

From the charge stability measurements performed at 4 K and at a constant DC bias of 4mV, the charging energy of both QDs, EC1 = 7.9 meV, EC2 = 8 meV, as well as the inter dot charging energy, ECM = 2 meV, can be extracted. As there are clearly visible excited state lines within the bias triangles, the single particle energy spacing can also be determined to be ~1.2 meV.

Outlook

Being able to reliably tune the DQD in the three barrier NWs allows for first experiments probing phonon interaction to be performed. The DQD will be used as a phonon detector, while the phonon emission will still be provided by other means, e.g. heating and/or optical excitation.

References

- [1] B. Li, L. Wang, G. Casati, *Negative differential thermal resistance and thermal transistor*, Appl. Phys. Lett. **88**, 143501 (2006)
- [2] L. Wang, B. Li, *Thermal Logic Gates: Computation with Phonons*, Phys. Rev. Lett. **99**, 177208 (2007)
- [3] Y.-Y. Liu, J. Stehlik, C. Eichler, M. J. Gullans, J. M. Taylor, J. R. Petta, *Semiconductor double quantum dot micromaser*, Science **347(6219)**, 285-287 (2015)
- [4] S. Roddaro, A. Pescaglini, d. Ercolani, L. Sorba, F. Beltram, *Manipulation of Electron Orbitals in Hard-Wall InAs/InP Nanowire Quantum Dots*, Nano Lett., **11(4)**, 1695-169 (2011)
- [5] F. Thomas, A. Baumgartner, L. Gubser, C. Juenger, G. Fülöp, M. Nilsson, F. Rossi, V. Zannier, L. Sorba, C. Schönenberger, *Highly symmetric and tunable tunnel couplings in InAs/InP nanowire heterostructure quantum dots*, Nanotechnology 31, 135003 (2020)
- [6] D. B. Suyatin, C. Thelander, M. T. Björk, I. Maximov, L. Samuelson, *Sulfur passivation for ohmic contact formation to InAs nanowires*, Nanotechnology **18**, 105307 (2007)

Towards few layer semiconducting MoS₂ with superconducting contacts

Project P1701: Van der Waals 2D semiconductor nanostructures with superconducting contacts

Project Leader: A. Baumgartner and C. Schönenberger

Collaborators: M. Ramezani (SNI PhD student), I. C. Sampaio, K. Watanabe, and T. Taniguchi

Introduction

Many transition metal dichalcogenides (TMDCs) grow as stacks of atomically thin layers with a large variety of interesting optical and electronic properties. Examples are a valley degree of freedom potentially useful as quantum bits [1], strong electron-electron and spin orbit interaction (SOI), or the formation of topologically non-trivial phases. One of the most promising materials is the semiconductor MoS₂, with a high mobility and large mean free path, necessary for gate-defined nanostructures. In this project, we aim to establish such semiconductors as a versatile electronics platform in combination with superconducting contacts to investigate fundamental physical phenomena, like Majorana fermions or exotic Josephson effects in materials with strong SOI.

The main obstacle for achieving these goals are reliable, strongly coupled electrical contacts to the semiconductor. Conventional fabrication methods do not provide low resistance contacts to TMDCs [2], mainly due to contaminations of the material interfaces in the fabrication process. The main technical goal in this project therefore is to explore different fabrication methods, including bottom [3], Van der Waals [4], and vertical interconnect access (VIA) contacts [5], and to find fabrication processes compatible with superconducting materials.

In the previous reporting period we have demonstrated MoS₂ with superconducting MoRe bottom contacts, with a state-of-the-art low contact resistance-area products (RAPs) of ~25 kΩ. μm², assuming a scaling with the contact area. However, we could not find any conclusive signatures of a superconducting proximity effect, nor Shubnikov-de Haas oscillation (SdH) in a magnetic field, commonly taken as an indicator for high quality materials. In this reporting period, we therefore focused on the other two fabrication methods.

Superconducting Van der Waals contacts

NbSe₂ is a layered TMDC which shows Ising type superconductivity down to monolayers [6] used as contact material to other TMDCs [4]. We developed a novel method to fabricate short channel devices with NbSe₂ contacts, as illustrated in the inset of figure 1. We first use a single layer of graphene to pick up a suitable NbSe₂ flake. This heterostructure is then deposited on three gold bottom contacts developed in the previous phase. Between two of the contacts (2 and 3), we open a 200 nm wide trench in the NbSe₂ stack over which an MoS₂ flake is deposited. A topgate with a ~20 nm layer hexagonal boron nitride (hBN) allows for additional electrical tunability. Figure 1a shows the conductance $G=I_{13}/V_{23}$, determined by the current driven from contact 1 to 3 and the voltage built up between 2 and 3. These measurements were performed in a dilution refrigerator at a base temperature of 50 mK.

Using standard transport models to analyse the measured data, for example shown in figure 1, result in state of the art electron mobilities of ~5000 cm²/Vs, typical RAPs of ~10 kΩ.μm², and clear SdH oscillations. These findings demonstrate that our MoS₂ crystals are of adequate quality and that this fabrication technique is compatible with high quality electronic devices. However, while the NbSe₂ transport between contacts 1 and 2 exhibits a clear superconducting transition at a mag-

netic field of $B \sim 1$ T, we could not find any clear signatures of superconductivity in the MoS₂ junction, possibly related to the graphene contact layer.

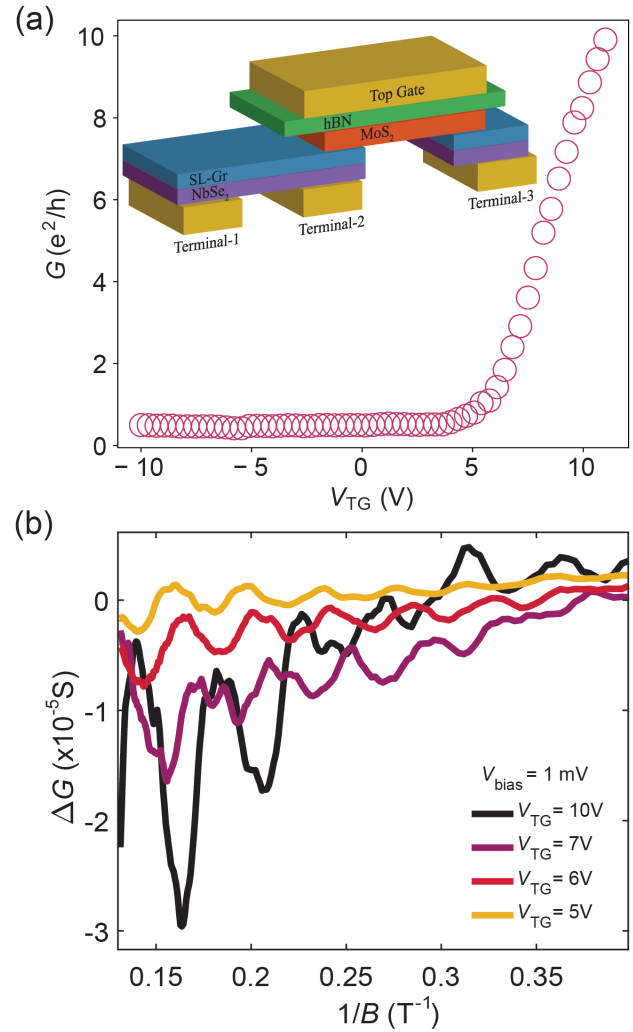


Fig. 1 a) Conductance G as a function of the topgate voltage V_{TG} . Inset: schematic of the device. b) Variation in G vs. the inverse of the magnetic field, showing periodic SdH oscillations.

VIA contacts of normal metals to MoS₂

In the VIA method one deposits prefabricated electrical contacts directly onto the active material, without fabrication steps that expose the interfaces to air or chemicals used in the fabrication. In practice, we open contact areas in selected hBN flakes, which are then filled with the contact material. Here, with gold as a test material, which forms the vertical interconnect through the hBN. This contact layer is then removed from the substrate and used to sequentially pick up the MoS₂, the bottom hBN, and a bottom graphite layer used as a backgate, all done in an inert gas atmosphere. The resulting structure is shown schematically in the inset of figure 2a. The interconnect areas are then electrically connected to bonding pads using a separate standard lithography step.

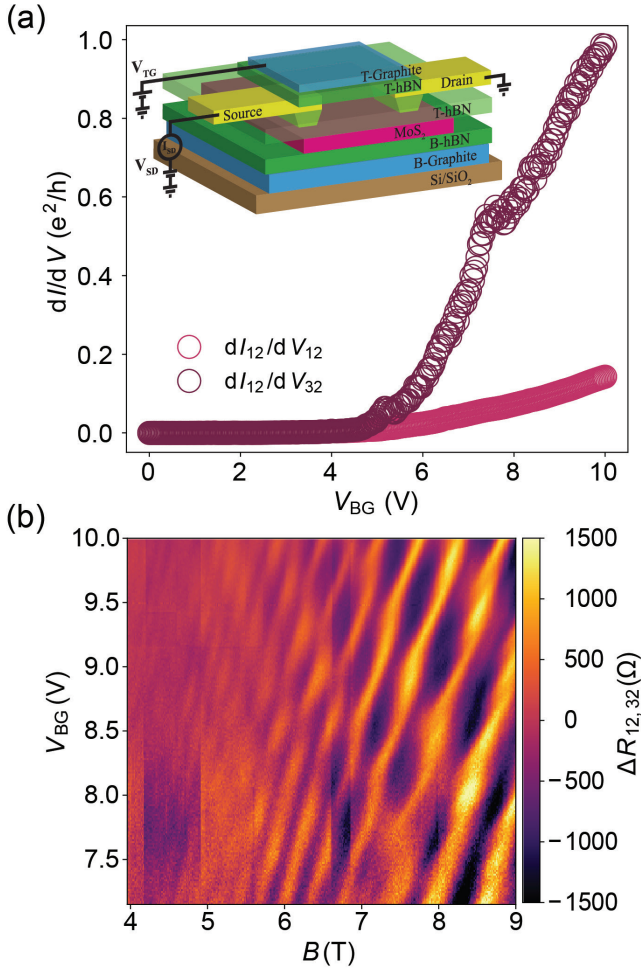


Fig. 2 a) Two and three terminal differential conductance as a function of the backgate voltage V_{BG} . Inset: schematic of a VIA contacted device. b) Differential resistance dV_{12}/dI_{32} with a smooth background subtracted vs. V_{BG} and a perpendicular magnetic field B .

Two types of multi-terminal differential conductances are plotted in figure 2a as a function of the backgate voltage, showing the expected n-type semiconductor characteristics. The lowest contact RAP is $\sim 16 \text{ k}\Omega\cdot\mu\text{m}^2$, suggesting high quality Au contacts. The magnetotransport measurements shown in figure 2b exhibit very clear SdH oscillations, suggesting a high MoS_2 quality, with a mobility of $\sim 3000 \text{ cm}^2/V_s$ and a mean free path of $\sim 180 \text{ nm}$, compatible with future gate-defined nanostructures. Most interestingly, we find two sets of SdH resonances (Landau fans) with different subband energies, which exhibit strong anti-crossings. These findings are not expected and possibly related to a large SOI energy [3] or strong electron-electron interactions [7].

Summary and Outlook

We find very promising preliminary results for devices fabricated using the VIA method, which we will now try to combine with superconducting contact materials. The Van der Waals heterostructure contacts might be further investigated as well, but since it is of rather little versatility, they will not be the focus of our work.

References

- [1] Q. Wang, K. Kalantar-Zadeh, A. Kis, J. N. Coleman, M. S. Strano, *Electronics and optoelectronics of two-dimensional transition metal dichalcogenides*, Nat. Nanotech. **7**, 699–712 (2012)
- [2] D. Lembke, B. Simone, A. Kis, *Single-layer MoS_2 electronics*, Acc. Chem. Res. **48**, 100-110 (2015)
- [3] R. Pisoni et al., *Interactions and magnetotransport through spin-valley coupled Landau levels in monolayer MoS_2* , Phys. Rev. Lett. **121**, 247701 (2018)
- [4] J. Guan, H. Chuang, Z. Zhou, D. Tomanek, *Optimizing charge injection across transition metal dichalcogenide heterojunctions: Theory and experiment*, ACS nano **11**, 3904-3910 (2017)
- [5] J. E. Telford et al., *Via method for lithography free contact and preservation of 2d materials*, Nano letters **18**, 1416-1420 (2018)
- [6] X. Xi, Z. Wang, W. Zhao, J.-H. Park, K. T. Law, H. Berger, L. Forro, J. Shan, K. F. Mak, *Ising pairing in superconducting NbSe_2 atomic layers*, Nat. Phys. **12**, 139-143 (2016)
- [7] J. G. Roch, G. Froehlicher, N. Leisgang, P. Makk, K. Watanabe, T. Taniguchi, R. J. Warburton, *Spin-polarized electrons in monolayer MoS_2* , Nat. Nanotechnol. **14**, 432–436 (2019)

Grayscale lithography for 3D microfluidics towards the diagnosis of Parkinson's disease

Project P1702: Single organelle size sorting by a nanofluidic device

Project Leader: Y. Ekinici and H. Stahlberg

Collaborator: T. Mortelmans (SNI PhD Student)

Research context

Despite the substantial progress made towards the unraveling the multi-faceted disease pathology of Parkinson's disease, as of today, the exact cause of the disease still has to be confirmed [1]. Moreover, in a clinical setting, it is not always possible to diagnose the disease at an early stage of development. This causes a delay between disease onset and treatment. Also, it should be pointed out that there is no curative therapy available [2]. Therefore, it is of great importance to further ameliorate our understanding of the disease progression and pinpoint its origin.

The role of mitochondrial dysfunction in the onset of Parkinson's disease has been well-established [3–5]. In addition, it is suggested that there is a shift in their size and density distribution attributed to mitochondrial alterations [6]. As such, a device that can enable a fast and simple method to quantify these changes would provide researchers with valuable insights to understand the underlying bio-mechanisms and eventually could be used for diagnosis purposes. Nevertheless, fabrication of such a device is challenging and requires the 3D fabrication techniques on nanoscale.

In this annual report, the first steps towards the fabrication of a 3D microfluidic device are outlined. Firstly, grayscale e-beam lithography (g-EBL) was explored as a technique to pattern 3D shapes by exposing PMMA 950K, which is a high molecular weight polymer resist. Secondly, nano-imprint lithography (NIL) was used to replicate the 3D profile in a low-cost free-standing PMMA film. The obtained protocol paves the way for increasing the throughput of the device fabrication and possible elucidation of neurodegenerative disease profiles.

Results and discussion

A key difference between standard binary lithography and grayscale lithography is the behavior of the resist material. In binary lithography, a high-contrast is wanted, whereas in grayscale lithography, a linear relationship between exposure dose and development rate is of importance [7]. This dose-response behavior for a given resist material is called the contrast curve and allows us to correlate our designed 3D shape with actual electron doses.

Firstly, as g-EBL has mostly been used in the sub-micron regime [8] and mitochondrial sizes are in the micrometer regime [9], we had to extend its use towards the patterning of structures which are several micrometers in height. To achieve this, two test patterns with 14 z-steps were used: a pie-shape and a dome. After extensive optimization, we were able to reproducibly achieve a total z-span of 4 μm (Fig. 1) with excellent vertical resolution. The achieved results will enable g-EBL to be used for applications in various scientific research fields with a need for 3D micro-structuring.

It should be noted that g-EBL is an accurate and versatile technique, but as it is a direct-write technique, it inherently has a low-throughput, making it unsuitable for cost-effective microfluidic device fabrication. To address this issue, the precision of g-EBL was combined with scalability of NIL. Firstly, a microfluidic channel containing a 3D wedge was patterned in PMMA 950K and its topography was characterized with a pro-

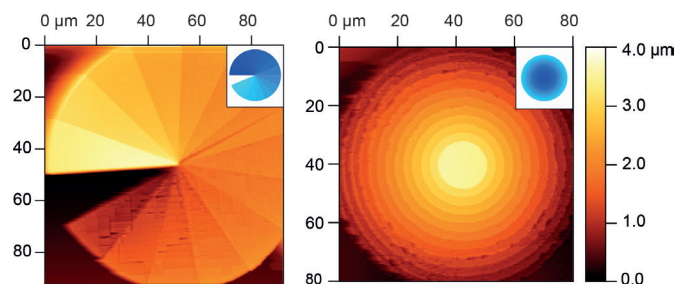


Fig. 1 AFM images of a 4 μm high pie-shape (left) and dome (right) in PMMA 950K fabricated with g-EBL. The inset of the figures shows a graphical representation of the designed shape.

filometer (Dektak, Veeco; Fig. 2). The required height variation of 2.5 μm was accurately obtained over a channel length of 1 mm. The wedge has small amounts of inherent roughness, which are possibly attributed due to minute fluctuations in exposure dose. Nevertheless, we have achieved almost nanometer control over the height profile on a millimeter scale.

Subsequently, to enable NIL, a negative copy (stamp) of the 3D structure was made by using OrmoStamp (MicroResist) in combination with conventional replication procedures [10, 11]. Next, the stamp was used to thermally imprint the wedge structure into a free-standing film of PMMA and the resulting profile was compared to the original e-beam pattern (Fig. 2). It can be seen that there are slight variations in the profile, but the 3D profile is largely maintained, evidencing the success of the combination of g-EBL and NIL.

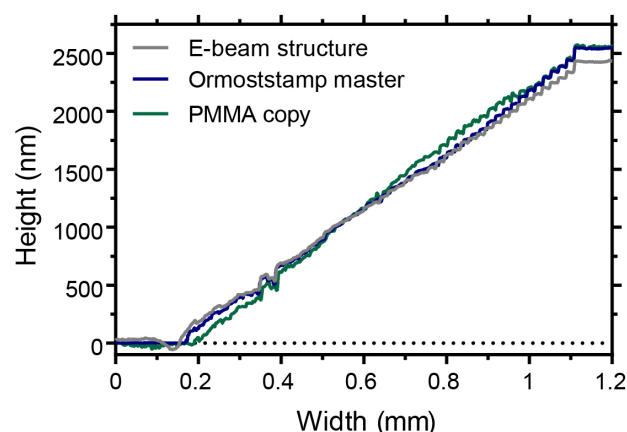


Fig. 2 Staircase profile in the e-beam resist (PMMA 950K) in the Ormostamp master and in a free-standing PMMA film.

To finalize the fabrication of the 3D PMMA microfluidic device, the patterned channel was bonded to a pristine PMMA sheet by combining UV (173 nm)/ozone-mediated surface activation with thermal bonding (Fig. 3). However, because of the 3D profile in the channel, the distance between the two PMMA layers is continuously decreasing and renders the channel prone to collapse. To prevent this, a supporting semi-hexagonal pillar array was incorporated in the channel and collapse-free bond-

ing was achieved as can be seen in figure 3. Furthermore, because of the 3D channel topography a thin film interference effect can be seen, which is evidenced by alternating lines of different colors.

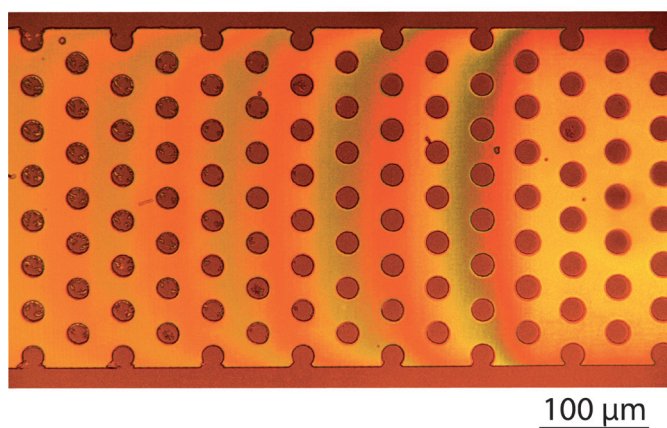


Fig. 3 Light microscopy image of a bonded 3D PMMA microfluidic device with supporting pillars with a diameter of 20 μm and a 40 μm pitch.

To summarize, the presented fabrication method, which combines g-EBL and NIL, allows for 3D structures to be rapidly synthesized and increases the cost-effectiveness of the fabrication procedure. For future work, the trapping abilities of the 3D microfluidic device will be evaluated using polystyrene beads, after which we will progress towards the monitoring of single organelle changes in neural cells affected by Parkinson's disease to unravel unknown pathophysiological mechanisms of the disease.

References

- [1] S. Przedborski, *The two-century journey of Parkinson disease research*, Nat. Rev. Neurosci. **18**, 251–259 (2017)
- [2] W. Poewe, K. Seppi, C. M. Tanner, G. M. Halliday, P. Brundin, J. Volkman, A. E. Schrag, A. E. Lang, *Parkinson disease*, Nat. Rev. Dis. Prim. **3**, 1–21 (2017)
- [3] J.-S. Park, R. L. Davis, C. M. Sue, *Mitochondrial Dysfunction in Parkinson's Disease: New Mechanistic Insights and Therapeutic Perspectives*, Curr. Neurol. Neurosci. Rep. **18**, 21 (2018)
- [4] S. H. Shahmoradian et al. *Lewy pathology in Parkinson's disease consists of a crowded organellar membranous medley*. Nat. Neurosci. **22(7)**, 1099–1109 (2017)
- [5] E. M. Simcox, A. Reeve, D. Turnbull, *Monitoring mitochondrial dynamics and complex I dysfunction in neurons: implications for Parkinson's disease*, Biochem. Soc. Trans. **41**, 1618–1624 (2013)
- [6] A. Bose, M. F. Beal, *Mitochondrial dysfunction in Parkinson's disease*, J. Neurochem. **139**, 216–231 (2016)
- [7] R. Kirchner, V. A. Guzenko, M. Rohn, E. Sonntag, M. Mühlberger, I. Bergmair, H. Schiff, *Bio-inspired 3D funnel structures made by grayscale electron-beam patterning and selective topography equilibration* Microelectronic Engineering Bio-inspired 3D funnel structures made by grayscale electron-beam patterning and selective topography equilibra, Microelectron. Eng. **141**, 107–111 (2015)
- [8] A. Schleunitz, C. Spreu, M. Vogler, H. Atasoy, H. Schiff, *Combining nanoimprint lithography and a molecular weight selective thermal reflow for the generation of mixed 3D structures*, J. Vac. Sci. Technol. B, **29**, 06FC01 (2011)
- [9] B. DuBoff, M. Feany, J. Götz, *Why size matters - balancing mitochondrial dynamics in Alzheimer's disease*, Trends Neurosci. **36**, 325–335 (2013)
- [10] M. A. Gerspach, N. Mojarad, D. Sharma, T. Pfohl, Y. Ekinici, *Soft electrostatic trapping in nanofluidics*, Microsystems Nanoeng. **3**, (2017)
- [11] F. Liu, Y. Yao, J. A. van Kan, *Nuclear Instruments and Methods in Physics Research B OrmoStamp mold fabrication via PBW for NIL*, Nucl. Inst. Methods Phys. Res. B **348**, 229–232 (2015)

Directed evolution of affinity proteins for biomedical applications

Project P1704: Evolving protease enzymes with new sequence specificity using peptide-hydrogel cell encapsulation

Project Leader: M. Nash and S. Reddy

Collaborator: J. López Morales (SNI PhD Student)

During biological evolution, iterated mutation and natural selection provide solutions for challenges that organisms face in the natural world. However, the traits that result from natural selection only occasionally overlap with features of biomolecules that are sought by humans for engineering applications and/or therapeutic purposes. In order to guide molecular evolution and access useful artificial properties more frequently, directed evolution in the laboratory has been used to mimic natural evolution. Here, a diverse library of genes is translated into a corresponding library of proteins and screened/selected for functional variants in a manner that maintains the correspondence between genotype (genes) and a desired phenotype (proteins and their functions). These functional mutant genes are replicated and serve as starting points for subsequent rounds of diversification and screening. Over many generations, these beneficial mutations accumulate, resulting in a successively improved phenotype for specific biological events. Here, we aim to enhance protein receptor-ligand interactions using directed evolution to improve mechanical properties of molecules for biomedical applications.

Firstly, a specific Cohesin domain (Coh) was chosen as a molecular template. It has been reported to form a complex with its corresponding ligand with outstanding stability and it is also highly resistant to unfolding under mechanical tension. The biophysical properties of the Coh domain, such as high thermal stability, and resistance to chemical and proteolytic denaturation [1, 2], along with its small size, and ease of production in large quantities can, therefore, be considered ideal for developing a biomedically relevant binding scaffold.

Secondly, a bioinformatic-guided design aided the construction of Coh mutant libraries to accelerate and improve the possibilities of finding optimal hits during a directed evolution campaign by focusing the diversity on specific regions of the protein to maintain the desired properties. Three libraries were then created following the guided output using oligo-based *in vitro* gene assembly coupled to overlap extension polymerase chain reactions (PCRs): a naive library, where the loops of interest were randomly mutated; a focused library, where only certain positions in the loops were randomized in a highly precise way and an error-prone library, where identified foreign loops that have a strong interaction with a therapeutic target were grafted into the scaffold and finally the whole gene sequence was randomly mutagenized. These libraries offer different but complementary scenarios for the most efficient directed evolution of a Coh scaffold with new properties (Fig. 1).

Besides, yeast cells were employed as the carrier organism of mutant Coh libraries due to the high efficiency of homologous recombination exploited for *in vivo* library cloning, their widespread use for directed evolution, and their easy manipulation during force analysis and measurements, used in combination with yeast surface display as part of the screening method.

The yeast surface display system consists of genetically encoded mutant library plasmids thermo-chemically introduced into yeast cells that expose the C-terminal part of the anchoring protein AGA₂ and the mutant construct fusion to the me-

dium. The displayed construct contains different peptide sequences that can be labeled with fluorescent antibodies for imaging and flow cytometric analysis. Furthermore, the high throughput screening (HTS) method then takes advantage of single-cell analysis of labeled libraries and their interaction with a labeled ligand of interest [3].

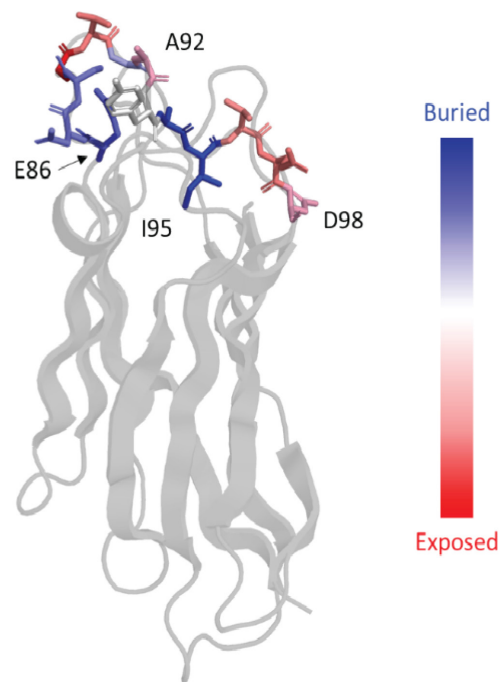


Fig. 1 Cohesin libraries design. Bioinformatic analysis of intrinsically disordered regions in the framework of Coh guided the generation of mutations in specific amino acid positions in exposed loops for binding activity. Three different libraries were created and consist of fully randomized loops, site-directed mutagenesis on restricted positions and finally full gene randomization after grafting foreign loops. Exposed positions in the selected loops are more prone to mutations while maintaining the mechanical properties of the Coh scaffold.

In the present work, a biological ligand with strong therapeutic potential that can be mechanically improved is fibrin, the major protein constituting thrombi during blood clotting. Fibrin is a human biopolymer that originates from the proteolytic digestion by thrombin of soluble fibrinogen, after which, processed fibrin monomers polymerize laterally to form insoluble protofibrils. Later, these fibrils are covalently crosslinked and form a 3D matrix that will entrap blood cells and clotting factors in response to a bleeding event. However, the insoluble nature of polymerized fibrin renders its usage highly challenging as a ligand for biomedical developments. Therefore, a soluble model of fibrin was prepared and labeled for its application in FACS against Coh libraries. Shortly, a human clot was prepared at physiological conditions and degraded with plasmin until the formation of degradation complexes was observed. The DD(E) fragment is a complex that contains the crosslinked sites of fibrin monomers and structurally resembles fibrin. Consequently, the DD(E) fragment was produced, purified and conjugated to a fluorescent marker to function as a soluble model of fibrin.

Furthermore, labeled mutant libraries displayed on yeast cells were incubated with labeled DD(E) ligand (Fig. 2), screened for binding interactions, and isolated using differential FACS in several rounds at decreasing concentrations of ligand. After several rounds of sorting, the enriched population of mutants with high specificity for fibrin will undergo three rounds of mutagenesis to mature their affinity.

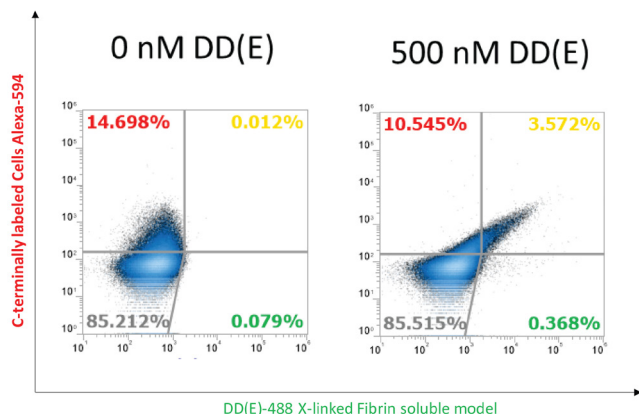


Fig. 2 FACS screening of fibrin binders. Coh mutant libraries were displayed and labeled on yeast cells (red), incubated with AF488-DD(E) (green) at varying concentrations and sorted by FACS using a SONY MH900 cell sorter when doubly labeled cells were observed. Positive interactions between controls and libraries with the labeled ligand shift the displaying population diagonally to the right, allowing the proper gating and sorting of positive binders.

Finally, selected variants will be analyzed by atomic force microscopy-based-single molecule force spectroscopy (AFM-SMFS), where ligands of interest will be functionalized on a surface and the mutant Coh will be functionalized onto a cantilever [4]. Then the protein complex with the highest mechanical strength can be further analyzed with different pulling geometries and finally coupled to different biomedical applications.

We hypothesize that this strategy will yield a novel domain with a high affinity for a relevant ligand and with overall enhanced stability properties, making it the first binder domain with ameliorated mechanical features. Moreover, we envision that the outcome of this project will offer a molecule with biomedical impact in diseases that currently lack treatments or diagnosis tools, and an efficient platform for directed evolution of proteins within the rising field of mechanobiology.

References

- [1] W. Ott, M. A. Jobst, C. Schoeler, H. E. Gaub, M. A. Nash, *Single-molecule force spectroscopy on polyproteins and receptor-ligand complexes: The current toolbox*, *J. Struct. Biol.* **197(1)**: 3-12 (2017)
- [2] M. Otten, W. Ott, M. A. Jobst, L. F. Milles, T. Verdorfer, D. A. Pippig, M. A. Nash, H. E. Gaub, *From genes to protein mechanics on a chip*, *Nat. Meth.* **11(11)**: 1127-1130 (2014)
- [3] T. Verdorfer, R. C. Bernardi, A. Meinhold, W. Ott, Z. Luthey-Schulten, M. A. Nash, H. E. Gaub, *Combining in Vitro and in Silico Single-Molecule Force Spectroscopy to Characterize and Tune Cellulosomal Scaffoldin Mechanics*, *J. Am. Chem. Soc.* **139(39)**: 17841-17852 (2017)
- [4] E. T. Boder, K. D. Wittrup, *Yeast surface display for screening combinatorial polypeptide libraries*, *Nat. Biotechnol.* **15**, 553-557 (1997)

Towards label-free HTS in enzyme engineering

Project P1705: Genetic selection of nanocatalysts
Project Leader: S. Panke, P. S. Dittrich, and T. R. Ward
Collaborator: E. Rousounelou (SNI PhD Student)

Introduction

Homogeneous catalysis plays a crucial role in the production of chemicals but designing and optimizing catalysts with high activity and selectivity rank among the most challenging tasks in synthetic chemistry [1]. In this respect, the catalytic proficiency of enzymes acting on native substrates has inspired a range of approaches to engineer enzymes for chemical synthesis, whilst expanding their reaction scope [2]. Although proteins can be engineered via rational design [3], this is tricky when there is only limited biochemical and/or structural data available, as it is often the case. Directed evolution is a powerful tool for generating enzymes with desired properties [2]. Its success relies heavily on the efficiency of screening methods for the identification of desired variants. Current methods allow the analysis of many variants while relying on optical (fluorescent) readouts [4]. However, an optical readout is usually not easily related to the outcome of a practically useful chemical reaction. Alternatively, label-free analysis methods, such as mass spectrometry (MS), can directly analyze products of useful chemical reactions but are currently slow and destructive. As a consequence, they require elaborate workflows to separately store genetic information that can be retrieved in case of success.

To overcome this fundamental problem dichotomy, we are developing a novel high-throughput screening (HTS) method that [i] addresses the speed issue by coupling droplet-based microfluidics with MALDI MS and [ii] compensates the destructiveness of MS analysis by co-analyzing unique peptide barcodes that maintain the genotype-phenotype linkage. In figure 1, an overview of the method is illustrated. Firstly, a library of unique DNA and peptide barcode combinations is generated, which is identified via next generation sequencing. The enzyme variant library is then cloned into the barcoded vectors so that every variant is associated with a unique combination of a DNA and a peptide barcode. The barcoded enzyme library is transformed into *E. coli* competent cells, followed by single cell droplet encapsulation (Fig. 1.1), droplet spotting onto a picolitre array and cell lysis (Fig. 1.2). After in vitro transcription/translation, each sample is incubated with candidate substrate(s) and cofactor(s) (Fig. 1.2) and the reaction is analyzed by MALDI-TOF MS. The mass spectrum of each sample delivers information about the product amount or distribution, but also its unique identity via the peptide barcode (Fig. 1.3). The latter is uniquely linked to the variant, but also to a DNA barcode and thus, after designing DNA primers specific to the DNA barcode, the desired variant can be retrieved by PCR, from a large pool of variants, and the genotype can be determined by sequencing. (Fig. 1.4).

Designing the peptide barcode library

The peptide barcodes uniquely identify each variant. Therefore, they are encoded on the same replicon that encodes the enzyme variant, ensuring their presence in a suitable com-

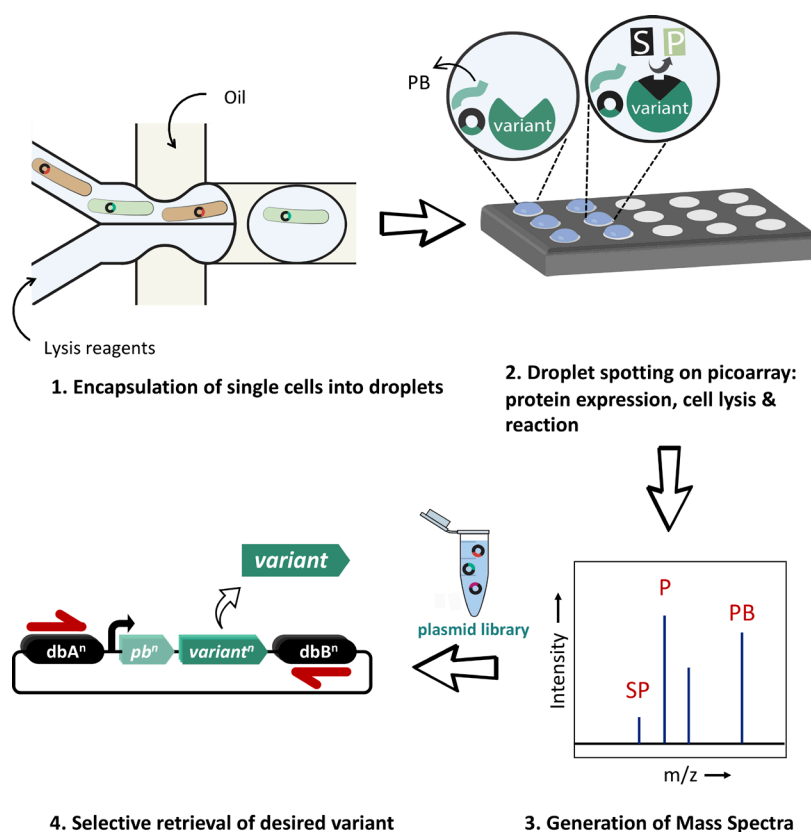


Fig. 1 Simplified overview of the proposed HTS method. For further details, refer to text. db: DNA barcode; pb: peptide barcode; S: substrate; P: product; SP: side-product; arrow: promoter

partment. Moreover, their sequence should allow the production of a robust and unique mass signal that can be unambiguously linked to a unique DNA barcode and subsequently to a unique enzyme variant.

Towards that direction, a python script was generated that allows the design of a large number of peptide barcodes. The input parameters included the length profile and sequence composition of the peptides. More specifically, the generated peptide barcodes are between 10-16 amino acid long and are devoid of methionines and cysteines which cause oxidation and cross-linking. They also carry at least one proline residue to facilitate peptide sequencing via collision-induced fragmentation (CID). Moreover, they contain one basic amino-acid at the C-terminus to improve ionization. Although basicity increases ionization efficiency, hydrophilicity has the reverse effect and therefore, the peptide sequence is devoid of basic residues at central positions.

Subsequently, the generated peptides were analysed in silico for their detectability, an analysis that was based exclusively on their amino acid sequences. The final set of peptides will be tested experimentally for their ability to be expressed efficiently and to produce robust and unique mass signals.

Co-expression of peptide barcode & enzyme

The proposed method rests on the quasi-concomitant detection of a peptide barcode and the reaction product in the MS-signal. Consequently, we need to ensure that both peptide barcodes and enzyme variants are expressed sufficiently. Although recombinant protein synthesis in *E. coli* is a standard method in genetic engineering, the synthesis of short peptides is not; short peptides are an important nutrient source in *E. coli* and are easily targeted by endogenous peptidases. This problem is currently tackled by attaching the B1 domain of Streptococcal protein G (GB1) at the N-terminus of the peptide barcode. This small fusion partner is known to increase peptide solubility and expression level, while it protects the fused peptide from degradation [5].

Moreover, to ensure efficient peptide and protein synthesis, we have investigated how the relative position of the peptide gene to the gene of the enzyme variant influences the expression of both genes. Five modular constructs were designed implementing different possibilities to co-produced peptide and protein and were tested against different expression conditions. Subsequently, we concluded that the gene of the peptide will be positioned downstream of the enzyme variant gene, and that both genes will be under the control of two different promoters. That is to eliminate any influence of the peptide barcode expression into the enzyme variant expression levels.

In order to test the expression levels of each peptide barcode individually, a sixth modular construct was designed in which the gene of the peptide barcode is linked via a translational coupling cassette (TCC) to the gene of the green fluorescent protein (gfp). The TCC is encoding a mRNA sequence that forms a secondary structure in the absence of translation and contains the translational start sequence of *gfp*. Only when the upstream peptide barcode gene is fully translated, the secondary structure is resolved, allowing the translation of *gfp* and therefore, fluorescence to be observed. Moreover, the fluorescent signal is proportional to the expression level of the upstream peptide barcode that is analysed each time. This system is now being tested and it will allow the characterisation of the expression levels of every peptide barcode present in the library. Only the peptides that are expressed efficiently will be tested for their ability to produce unique and robust mass signals.

Designing the DNA barcode library

While the peptide barcode uniquely identifies the variant that was analyzed, the sample that was assayed is destroyed in the process and with it the improved enzyme variant and its encoding gene (located on a plasmid). To retrieve the primary structure of the enzyme, we need to map the peptide barcode information back to the specific plasmid from which it originated and which is still available from a duplicate of the plasmid library. In this direction, each peptide barcode is co-localized on the same plasmid with two unique DNA sequences that flank the gene template of the enzyme variant (Fig. 1.4).

In an initial proof-of-principle experiment, we confirmed our ability to retrieve a specific gene from a pool of similar genes. More specifically, a pool of DNA barcodes that flank *gfp* was generated. The DNA barcodes were random 30bp nucleotide sequences with similar GC content ensuring a high theoretical diversity and that for each DNA barcode two primers with similar melting temperature can be designed. Subsequently, the gene for yellow fluorescent protein (*yfp*) flanked with specific DNA barcodes was mixed in different ratios with the DNA bar-coded *gfp* pool and was each time successfully and selectively retrieved. The two genes differ only in five point mutations, so we can safely assume that our power to selectively retrieve the *yfp* gene is not influenced by the gene sequence. In contrast, the gene products can be easily told apart due to their different fluorescence properties.

The success of a selective retrieval relies heavily on the ability to design primers that would bind only to the DNA barcode that is uniquely associated with a desired variant. In order to have more control on the DNA barcode design and to its corresponding PCR primers, a python script was written which generates DNA barcodes of a defined length, GC content and homopolymer length, as well as Levenshtein distance (the minimum number of insertions, deletions or substitutions that can transform one DNA barcode to another). The generated DNA barcodes will now be tested for the ability to selectively retrieve a desired variant.

References

- [1] T. R. Ward, *Artificial Metalloenzymes Based on the Biotin-Avidin Technology : Enantioselective Catalysis and Beyond*, *Artificial Metalloenzymes Based on the Biotin-Avidin Technology : Enantioselective Catalysis and Beyond*, Acc. Chem. Res. **44**, 47–57 (2011)
- [2] U. T. Bornscheuer, G. W. Huisman, R. J. Kazlauskas, S. Lutz, J. C. Moore, K. Robins, *Engineering the third wave of biocatalysis*, *Nature* **485**, 185-194 (2012)
- [3] P. S. Huang, S. E. Boyken, D. Baker, *The coming of age of de novo protein design*, *Nature* **537**, 320 - 327 (2016)
- [4] M. Wójcik, A. Telzerow, W. J. Quax, Y. L. Boersma, *High-throughput screening in protein engineering: Recent advances and future perspectives*, *Int. J. Mol. Sci.* **16**, 24918–24945 (2015).
- [5] Y. Cheng, D. J. Patel, *An efficient system for small protein expression and refolding*, *Biochem. Biophys. Res. Commun.* **317**(2), 401-405 (2004)

Fiber-based cavity optomechanics

Project P1706: Ultrasensitive force microscopy and cavity optomechanics using nanowire cantilevers

Project Leader: M. Poggio and F. Braakman

Collaborator: D. Jäger (SNI PhD Student)

Introduction

Nanoscale mechanical resonators such as thin membranes or nanowire crystals have the potential to uniquely enrich the capabilities of force microscopy. Currently, force microscopy techniques rely heavily on micron-sized cantilevers as force transducing elements, such as silicon beams or quartz tuning forks. In recent years, a new direction has emerged that replaces these conventional cantilevers with bottom-up grown nanoscale structures, such as carbon nanotubes or nanowires. Their small size and nearly defect-free crystal structures leads to potentially record force sensitivities, low mechanical losses and high operation frequencies. Several experiments have recently demonstrated the potential and versatility of this approach. In our own lab, we have demonstrated a new type of force microscopy using nanowires, in which we have shown sensitivity not only to the magnitude of forces, but also their direction [1].

Furthermore, nanomechanical resonators enable fundamental studies into the hybridization of different physical quantities, such as light and mechanical motion. Such hybrid systems form a promising platform to implement measurements operating at the limits imposed by quantum uncertainty and quantum non-demolition measurements. They may also allow investigation of quantum decoherence mechanisms, entanglement, and ultimately the transition from quantum to classical physics. We focus on two types of particularly interesting hybrid structures: nanowire heterostructures and 2D membranes with defects. Both systems can combine excellent mechanical properties with bright optically active qubits in the form of embedded quantum dots or crystal defects. These qubits themselves already form interesting objects of study, as they are potentially very sensitive meters of localized electric and strain fields [2]. Moreover, when coupled to a mechanical degree of freedom, qubits can through their nonlinear character generate very large enhancement of the radiation pressure interaction between light and matter, as well as boost optical cooling of the mechanical resonator [3].

Our aim is to enable operation of such hybrid systems in regimes dominated by quantum effects, by improving optical excitation and detection of the mechanical resonator and embedded quantum emitters. To reach this goal, we will:

- 1: Integrate such hybrid systems into high-finesse optical cavities. Read-out of both the mechanical motion and of the photons emitted by embedded quantum emitters can be much improved by placing the system inside an optical cavity. Moreover, such a cavity allows to strongly couple the motion as well as quantum emitters to the cavity light field. In particular, this provides a straightforward path to the realization of a tri-partite hybrid system [3]. Such a tri-partite system allows to significantly enhance optical cooling and will allow the observation and utilization of quantum states of motion.

- 2: Implement resonant excitation of quantum emitters in a force microscopy setup. This will significantly reduce the optical linewidth of the dots and should allow for mechanical displacement sensitivity reaching the Heisenberg uncertainty limit.

Optical Setup

In the first year, we have constructed an optical setup that serves as the basic platform for our experiments. The main elements of the setup are a highly tunable laser, two double-pass acousto-optic modulator units, and two low-noise photodiodes. The setup allows to insert two beams of light into an optical cavity with tunable frequency difference between the beams. The cavity can be measured through reflection or transmission. This will enable basic optomechanical experiments, such as optical cooling of a mechanical oscillator, as well as basic cavity QED experiments, allowing the measurement of a tri-partite hybrid system.



Fig. 1 A photograph of our fiber Fabry-Perot cavity. Two fiber-based ablated concave mirrors face each other in an alignment rig, creating an optical cavity between the front facets.

This year, we have used this optical setup to characterize first fiber-based Fabry-Perot cavities (Fig. 1), showing optical finesse of over 10000. In addition, we have added an electro-optic modulator and a fast photodetector to our setup, enabling us to perform Pound-Drever-Hall stabilization of the cavity length.

Membranes

As a first step towards creating a tri-partite hybrid system, we have started working with membranes made from flakes of two-dimensional materials. In particular, we focus on membranes of hexagonal boron nitride (hBN), which has been shown to contain crystal defects that can serve as quantum emitters. These emitters are ultra-bright, highly stable and can be observed at room temperature [4]. Furthermore, hBN membranes are mechanical oscillators with favorable frequencies (MHz regime), low mass, and high quality factors. Finally, hBN can be etched directly by electron beams, allowing for straightforward patterning of flakes. This would for instance allow the fabrication of photonic crystals, trampoline resonators, or venting holes on the membranes.

For the defects to form, additional fabrication steps are necessary. The simplest approach is to anneal the hBN flakes at high temperature, resulting in defects located at edges of the flakes. Using this method, we were able to observe several of these emitters in spectroscopy measurements (Fig. 2).

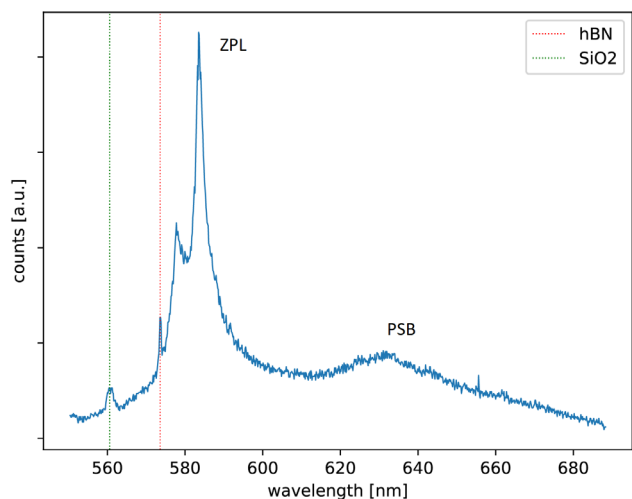


Fig. 2 Spectrum of an emitter found in an exfoliated and subsequently annealed hBN flake. The strong zero-phonon line emission is clearly visible next to a weak phonon sideband.

To use these flakes as mechanical resonators that can be placed inside our cavity, we have developed a wet transfer technique that allows us to place them on top of silicon nitride hole grids ('Holey membranes' manufactured by Norcada), resulting in hBN drum resonators (Fig. 3).

While we were already able to observe a potential emitter at the edge of one of these drums, a method to implant emitters in a deterministic way is necessary. In particular, the emitters have to be placed in a location where the dynamic strain of the oscillator is high, and where it can be positioned well within the cavity field without introducing clipping losses caused by the silicon nitride frame. To this end, we have begun to pattern holes into our drum resonators with the help of a focused ion beam. It has been reported that emitters form with high fidelity at these patterned locations [5]. We are also investigating the possibility of other techniques to implant emitters away from boundaries, such as electron irradiation of the hBN flakes.

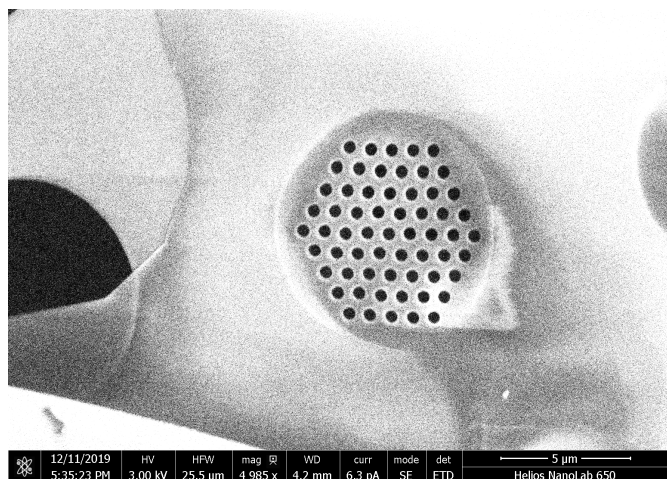


Fig. 3 SEM image of a patterned hBN flake spanning across a hole in a silicon nitride membrane, creating a drum resonator.

All these fabrication steps introduce surface contamination to the sample, resulting in an increase in fluorescence background. This background can overshadow the quantum nature of the emitted light. We were successful in removing most of this background by employing a cleaning procedure based on UV-Ozone cleaning and annealing in air at high temperatures.

Outlook

Building on these results, our next steps will be to:

- insert an hBN flake membrane into a fiber-cased optical cavity and measure the optomechanical coupling strength.
- perform correlation measurements to confirm single-photon emission from hBN defects.
- measure strain-mediated coupling between hBN flake motion and an embedded emitter.

References

- [1] N. Rossi, F. R. Braakman, D. Cadeddu, D. Vasyukov, G. Tütüncüoğlu, A. Fontcuberta i Morral, M. Poggio, *Vectorial scanning force microscopy using a nanowire sensor*, *Nat. Nanotechnol.* **12**, 150 (2017)
- [2] M. Montinaro, G. Wüst, M. Munsch, Y. Fontana, E. Russo-Averchi, M. Heiss, A. Fontcuberta i Morral, R. J. Warburton, M. Poggio, *Quantum dot opto-mechanics in a fully self-assembled nanowire*, *Nano Lett.* **14**, 4454 (2014)
- [3] J. Restrepo, C. Ciuti, I. Favero, *Single-Polariton Optomechanics*, *Phys. Rev. Lett.* **112**, 013601 (2014)
- [4] T. T. Tran, K. Bray, M. J. Ford, M. Toth, I. Aharonovich, *Quantum emission from hexagonal boron nitride*, *Nat. Nanotechnol.* **11**, 37–41 (2016)
- [5] J. Ziegler, R. Klaiss, A. Blaikie, D. Miller, V. R. Horowitz, B. J. Alemán, *Deterministic Quantum Emitter Formation in Hexagonal Boron Nitride via Controlled Edge Creation*, *Nano Lett.* **19** (3), 2121-2127 (2019)

First-order magnetic phase-transition of mobile electrons in monolayer MoS₂

Project P1707: Nano-photonics with van der Waals heterostructures

Project Leader: R. J. Warburton and I. Zardo

Collaborator: L. Sponfeldner (SNI PhD Student), J. Roch, and N. Leisgang

In a Van der Waals heterostructure, a device is constructed from individual monolayers, for instance graphene, hexagonal-BN, MoS₂, and so on. These heterostructures provide a promising platform to study interaction-driven physics. It was shown that the electronic ground-state in monolayer MoS₂ is spin-polarized at low electron densities [1], corresponding to the formation of a ferromagnetic state. The ferromagnetic ordering is driven by strong interactions between the electrons. At high electron densities, single-electron physics (simple band filling) will dominate, such that the strong magnetic ordering disappears and the system becomes paramagnetic. A phase transition can be expected between the ferromagnetic state at low density and the paramagnetic state at high density. The magnetization can change gradually on crossing the phase boundary. This behavior is classified as a “second-order” phase transition. Conventional ferromagnets, e. g. iron, exhibit a second-order phase transition. Conversely, an abrupt change in magnetization is classified as a “first-order” phase transition. A first-order phase transition is potentially useful in spintronics: a small change of an experimental parameter causes the system to cross the phase boundary, resulting in a massive change in the magnetization.

We present experimental evidence that electrons in a MoS₂ monolayer undergo a first-order phase transition between a ferromagnetic phase at low electron densities and a paramagnetic phase at higher densities [2].

Here, we study the semiconducting transition-metal dichalcogenide (TMD) monolayer MoS₂. The band edges of MoS₂ are located at the K and K' points, see figure 1a. A circularly polarized $\sigma+$ ($\sigma-$) photon couples the conduction band and valence band with spin- \downarrow (\uparrow) at the K (K') point, a consequence of strict optical selection rules. The structure of our sample is shown in figure 1b. An electrically contacted monolayer of MoS₂ is encapsulated in h-BN. The charge carrier density n in the monolayer is capacitively controlled by applying a voltage to a metallic contact.

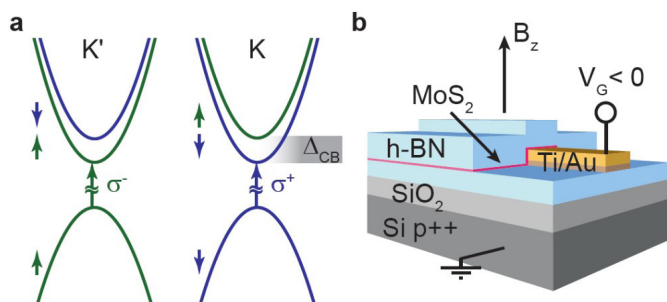


Fig. 1 a) Band structure of monolayer MoS₂. Following strict valley-selective optical selection rules, circularly polarized $\sigma+$ ($\sigma-$) photons address the optical transition at the K (K') point of the Brillouin zone. b) Schematic of the studied van der Waals heterostructure consisting of monolayer MoS₂ encapsulated in h-BN.

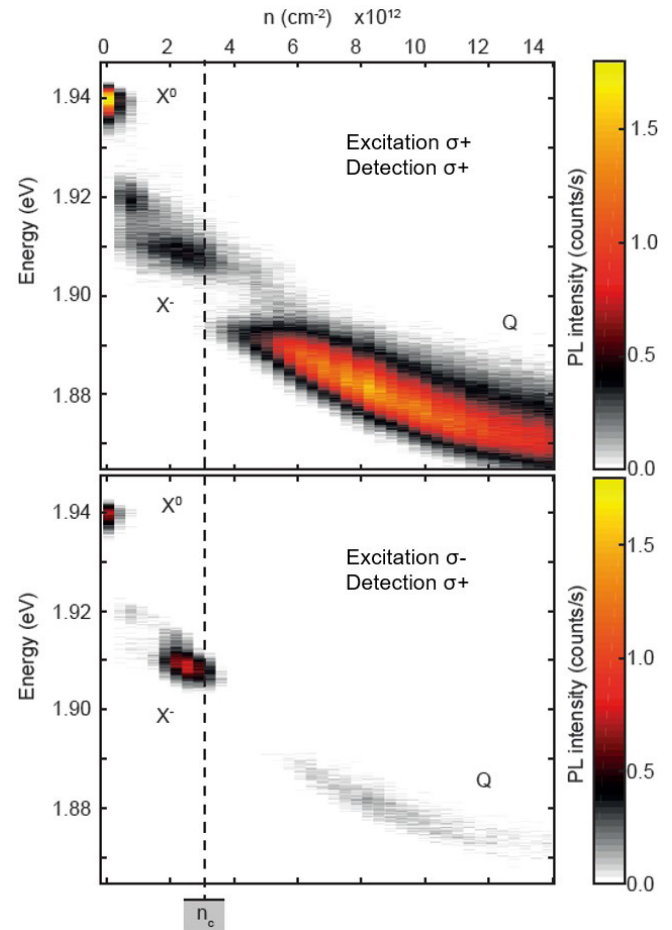


Fig. 2 Photoluminescence of gated monolayer MoS₂. The excitation with photon energy 1.959 eV is $\sigma+$ (top) or $\sigma-$ (bottom), while the detected PL signal is $\sigma+$. The colour map shows the PL intensity at a perpendicular magnetic field B_z of 9 T and at a temperature of 1.6 K. At the critical density n_c there is a jump in the PL energy and the polarization behavior changes abruptly.

The electronic ground-state is probed optically with photoluminescence (PL) spectroscopy. Figure 2 shows the detected polarization-resolved PL as a function of electron concentration n . The measurement is performed at a perpendicular magnetic field $B_z = 9$ T and at a temperature of 1.6 K. The magnetic field B_z creates a stable spin-polarized ground-state at low electron densities [1]. At very low n , the peak labeled X^0 dominates the PL. This resonance corresponds to the creation of a tightly bound electron-hole pair, the so called exciton. As n increases, X^0 loses its oscillator strength and is replaced by a red-shifted trion resonance (X^-). The X^- consists of two electrons with opposite spin and a hole. At higher densities, the X^- peak weakens and vanishes; it becomes unbound. The PL is then dominated by a broad, red-shifted peak labeled Q. Strikingly, there is no smooth transition between the X^- and Q resonances. This is different to the behavior of two-dimensional electron gases in other 2D semiconductor systems (GaAs, CdTe). At $n = n_c$ there is an abrupt jump in the PL spectrum. This is the first evidence for a first-order phase transition.

The second evidence becomes apparent when studying the polarization of the PL. As a consequence of spin-valley locking in monolayer MoS_2 , the PL signal of excitons is polarization-preserving: $\sigma+$ ($\sigma-$) polarized excitation results in a $\sigma+$ ($\sigma-$) polarized PL signal, see figure 2. The Q resonance is also strongly polarization-preserving. On the other hand, X is polarization-non-preserving. Excitation with $\sigma-$ polarized light leads to a strong $\sigma+$ polarized PL (Fig. 2). The change in symmetry of the overall polarization behavior is also abrupt on crossing the critical density.

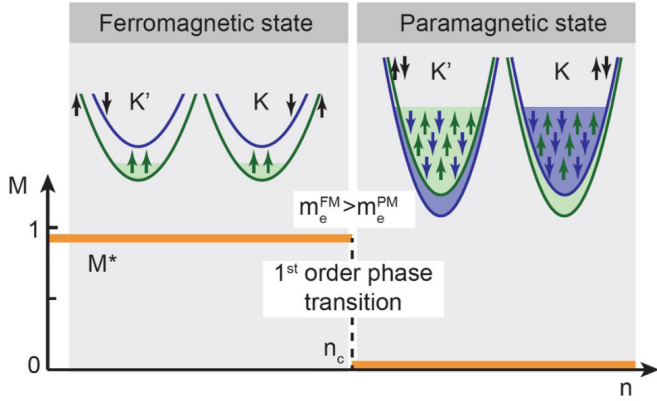


Fig. 3 Band occupation in the ferromagnetic state (left) and the paramagnetic state (right). At $n = n_c$ the magnetization changes abruptly. In the ferromagnetic phase, intravalley and intervalley exchange favors the occupation of two bands with the same spin. In the paramagnetic phase, all four bands are occupied.

The evolution of the ground state of the mobile electrons in monolayer MoS_2 as a function of the density is sketched in figure 3. In agreement with our results, spin ordering at low electron densities and a first-order phase transition between a ferromagnetic and a paramagnetic phase has been predicted by recent theory [3].

In conclusion, we show that the magnetization in monolayer MoS_2 can be controlled by a small change in electron density n , a consequence of the first-order phase transition between ferromagnetic and paramagnetic phases. The small change in n is achieved simply by a small change to a gate voltage which is fast and easily realizable in experiments. In a next step, the spin polarization may be stabilized at lower magnetic fields by coupling to an insulating 2D ferromagnet in a van der Waals heterostructure. Additionally, it would be interesting to quantify and image the magnetization directly, especially upon crossing the phase boundary. This could be carried out with individual magnetic nanowires that recently have been established as scanning magnetic force sensors [4].

References

- [1] J. Roch, G. Froehlicher, N. Leisgang, P. Makk, K. Watanabe, T. Taniguchi, R. J. Warburton, *Spin-polarized electrons in monolayer MoS_2* , Nat. Nanotechnol. **14**, 432-436 (2019)
- [2] J. Roch, D. Miserev, G. Froehlicher, N. Leisgang, L. Sponfeldner, K. Watanabe, T. Taniguchi, J. Klinovja, D. Loss, R. J. Warburton, *First-order magnetic phase-transition of mobile electrons in monolayer MoS_2* , arXiv, 1911.10238 (2019)
- [3] D. Miserev, J. Klinovaja, D. Loss, *Exchange intervalley scattering and magnetic phase diagram of transition metal dichalcogenide monolayers*, Phys. Rev. B **100**, 014428 (2019)
- [4] H. Mattiat, N. Rossi, B. Gross, J. Pablo-Navarro, C. Magén, R. Badea, J. Berezovsky, J. M. De Teresa, M. Poggio, *Nanowire magnetic force sensors fabricated by focused electron beam induced deposition*, arXiv, 1911.00912 (2019)

Freeform optical structure

Project P1708: Non-visual effects of LED lighting on humans

Project Leader: E. Meyer and R. Ferrini

Collaborator: T. Aderneuer (Associate SNI PhD Student)

Freeform optics

The interest for freeform optics has increased rapidly in the last few years. Freeform optical components are commonly defined as optical surfaces with no translational nor rotational symmetry. This symmetry removal brings advantages for imaging and non-imaging applications as light can be redirected according to patterns that are impossible to achieve with standard optical components. On the one hand, aberrations can be corrected, which cannot usually be with symmetric optical structures. Moreover, freeform optics enables one to shape light effectively into specific target illumination patterns for electronic and optical components (e.g. for sensors, waveguides, fibers, etc.) [1]. On the other hand, nowadays there is a high demand for miniaturized optical components and specifically for freeform microlens arrays (FMLAs) that reduce the amount of material, thus lowering cost and weight, while their compactness facilitates system integration.

With the increasing interest in freeform structures and new fabrication technologies there is a high need to develop and improve methods for the quality control for these processes. Cost competitive processes of large area production first originate a master for the designed freeform structure e.g. by ultra-precision diamond milling which is then be replicated e.g. by injection molding. Both, the origination and replication, need characterization methods to ensure high quality freeform optics.

Design of free form micro optical structures

The step from macro to micro freeform optical components leads to specific design challenges, which currently limit their application to e.g. collimated sources and relative simple optical effects such as square/rectangular uniform illuminance distributions. We approached the design of microscopic freeform structures for illumination targets relevant for lighting applications. Different design methods have been proposed: ray mapping, SMS method, Monge-Ampere PDEs, etc. Finally, we chose the raymapping method [2]. This latter method allows us to consider an angular variation of the light source and a gradual change in the spatial target illumination.

The sketch of an exemplary freeform beam shaping lens is shown in figure 1. Aim is to have a defined target illumination as well as a light source placed at a specific working distance. It is then calculated how the optical structure in front of the light source has to be shaped. To design a free form micro optical structure the algorithm is adapted in order to specify a maximum thickness that can be accepted. Figure 2 shows an example of a computed freeform lens in macro and micro scale and the respective resulting illumination when testing the lens with a raytracing software. The example case of a hexagon is chosen as it can be used as base to design a closely packed pattern FMLA.

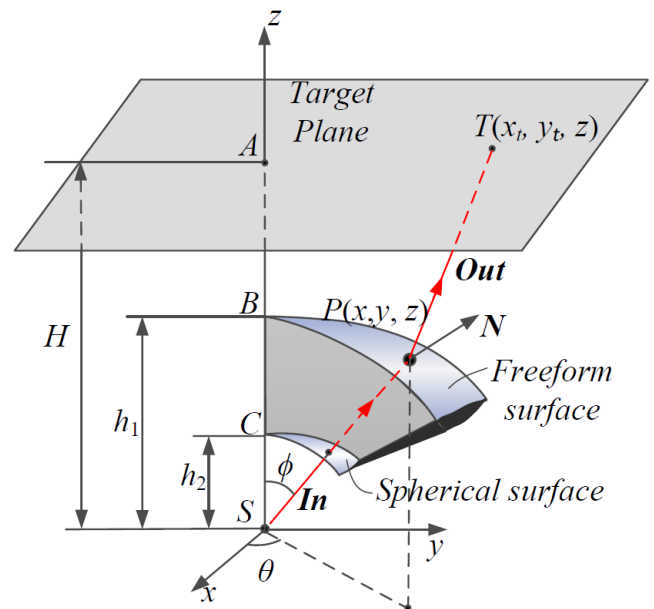


Fig. 1 Geometrical layout of freeform lens design [3]. A light source is placed at the origin S . A target illumination at a distance H is defined. Then point by point the shape of a surface in between is calculated which guides the light rays to the defined area.

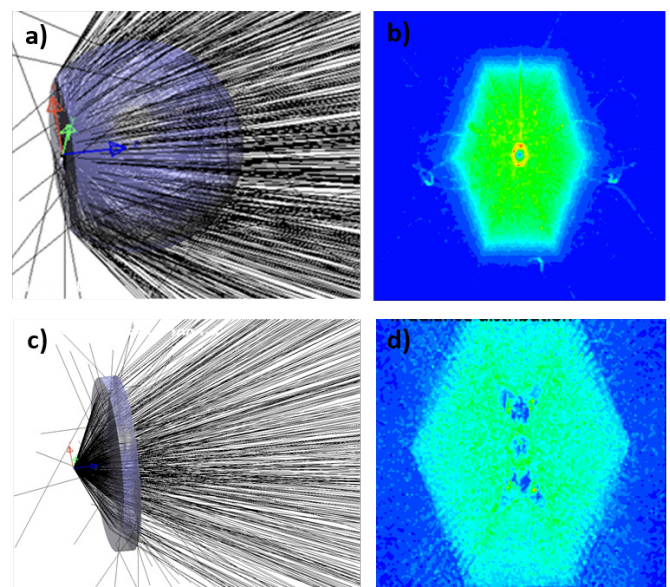


Fig. 2 a) Raytracing of designed macro film freeform optical structure for a hexagonal target illumination. b) Resulting Illumination of the lens when tested with raytracing software. c) Raytracing of the designed microscale thin film freeform structure with the same target specifications. d) Resulting Illumination of the microscale freeform structure.

In the design of freeform lenses for LED light sources, several parameters must be taken into account: extended light sources (in contrast to point sources), different intensity distributions (e.g. Lambertian, cosine, etc.), fabrication restrictions (e.g. no negative contact angles, thickness reduction), etc.

Characterization of free form micro optical structures

Freeform structures in micro structures are not only challenging in their design but also require specific characterization methods. Macro scale optics can be analyzed by measuring significantly less data points as for micro scale optics. For the latter, the point density increases tremendously as the surface has smaller features that have to be modelled correctly. Macro freeform structures can typically be described by mathematical functions. For micro freeform structure, the surface description is often not existing but defined by data points. In order to tackle these newly arising demand for characterization, we develop a method to link topological deviation to optical performance.

The manufacturing of FMLAs with UV imprint technologies requires precise and effective characterization techniques that enable the analysis of deviations that may occur in the origination and replication processes [3]. The characterization of FMLAs is indeed not trivial, as well-known methods used for standard microlenses are not applicable. Freeform optics can have larger slopes or sharp edges that are far more difficult to measure, while the non-symmetry of freeform structures demands for different figures of merit, in order to define their morphology and quantify any potential deviation. We work therefore on the selection and improvement of the most suited characterization methods. The first step is to construct a 3D CAD model that can be used for optical simulations and can reproduce all surface characteristics with high fidelity and accurately predictable (simulated) optical performance. In a second step, a method is developed to link the optical performance to the morphology, which can be eventually used to significantly improve the fabrication process.

The surface of free form microoptical structures has to be measured with high precision. This can be done by contact measurements with a stylus profilometer or non-contact methods, such as white light interferometry and confocal microscopy. The latter is a good choice for a relatively fast measurement of a large surface with high resolution and with view limitation of the slope angles. Figure 3 shows a top view of a FMLA.



Fig. 3 Top view of a FMLA consisting of hexagonal arranged lenses of the same base area but of different height and slopes. The image is taken with a confocal microscope.

To derive a significant and suitable 3D CAD model from the measurements, an extremely high resolution is required, thus leading to a tremendous amount of data. An additional challenge resides in the necessity to have a model that can be handled by an optical software, while being very precise. Note that small deviations can cause large changes in the optical output.

Access to such 3D CAD models enables a fast quality assessment not only of the manufactured microstructures, but also of the subsequent replicas without the need of highly demanding experimental set-ups.

References

- [1] T. Gissibl, S. Thiele, A. Herkommer and H. Giessen, *Two-Photon Direct Laser Writing of Ultracompact Multi-Lens Objectives*, Nat. Photon. **10**, 554–560 (2016)
- [2] D. Ma, *Exploration of ray mapping methodology in freeform optics design for non-imaging applications*, The University of Arizona (2015)
- [3] L.Kong, Y. Ma, M. Ren, M. Xu, C. Cheung, *Generation and characterization of ultra-precision compound freeform surfaces*, Sci.Prog. (2019)

Bioinspired nanoscale drug delivery systems for efficient targeting and safe in vivo application

Project P1801: Bioinspired nanoscale drug delivery systems for efficient targeting and safe in vivo application

Project Leader: J. Huwlyer and C. Palivan

Collaborator: C. Alter (SNI PhD Student)

Introduction

In the human body, 150 billion out of 37 trillion cells die every day. Prompt clearance of dead cells is crucial to maintain tissue homeostasis and is supported by both professional immune phagocytes (macrophages, monocytes) and non-professional tissue phagocytes (epithelial cells, fibroblasts)[1]. The mechanisms of apoptotic cell clearance have until now been scarcely exploited in nano-drug development, and mainly focused on delivery to professional phagocytes. The aim of this project is to design a “nano” apoptotic carrier, based on top-down designed nano apoptotic bodies, targeting both professional immune and non-professional tissue phagocytes. This is of great importance as it opens paths for drug delivery to both immune and epithelial cells.

Upon stress, the cell enters an irreversible apoptotic program, which induces morphological changes such as cell shrinkage and membrane blebbing. Nucleotides such as ATP and UTP are released and serve as “find-me” signals to attract phagocytes and facilitate the engulfment [2]. Caspases also irreversibly cleave and deactivate the membrane protein flippase, which flips phosphatidylserine (PS) in viable cells from the outer to the inner leaflet of the membrane (Fig. 1A). Thus, along with membrane proteins, PS is exposed on the outer membrane of the apoptotic cell (Fig. 1B)[1].

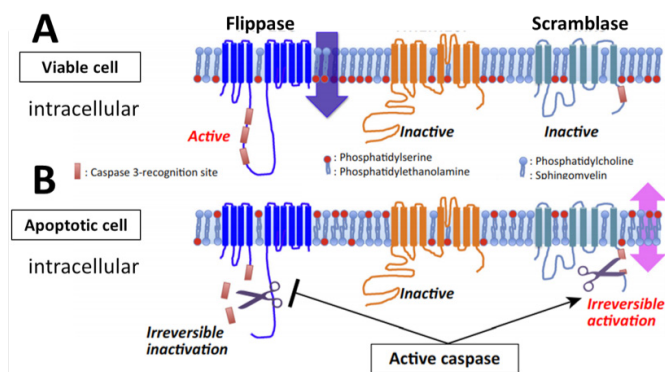


Fig. 1 In viable cells, flippase actively flips phosphatidylserine (red) to the inner leaflet of the cell. In apoptotic cells, caspase irreversibly inactivates flippase and activates scramblase which starts to mix PS to the outer leaflet [3].

PS acts as an “eat-me” signal through phosphatidylserine receptors (PSR) and leads to clearance of apoptotic cell/fragments (efferocytosis). The T-cell immunoglobulin and mucin domains 1 and 3 (TIM 1/3) and the TAM (Tyro3, Axl, and Mer) receptors, which belong to the tyrosine kinases, are the most important PSR [2]. We investigated the importance of the “eat-me” signal PS for cell derived nano-sized apoptotic bodies (ApoBDs) and a PS containing liposome formulation by incubation on A549 (epithelial, lung adenocarcinoma), HepG2 (tissue, hepatocellular carcinoma) and differentiated THP-1 (monocytic leukemia) cells.

Material and methods

Apoptotic bodies (ApoBDs) were produced by inducing apoptosis in donor cell lines with the chemical vesiculation agents: paraformaldehyde (PFA) and dithiothreitol (DTT). The blebbing process started few minutes after incubation (37°C and 5% CO₂) and ApoBDs (blebs) were harvested from the cells after 6 hours (Fig. 2A).

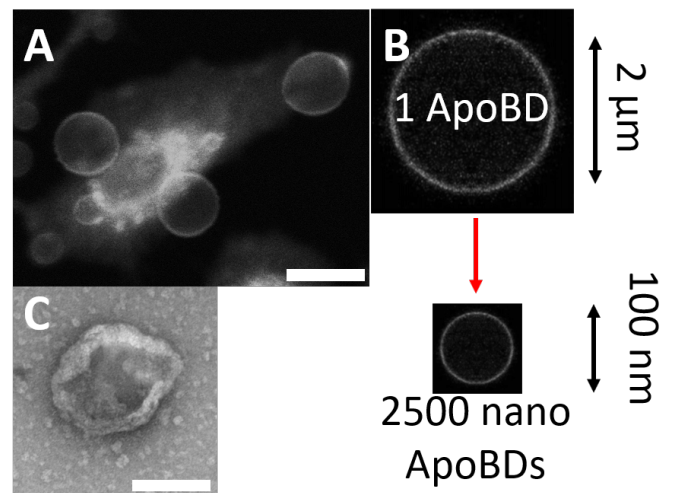


Fig. 2 A: Live cell image of ApoBDs (blebs) formation of A549 cells, scale bar = 3 µm. B: By extrusion of a 2 µm large ApoBD around 2500 100-120 nm small nano-sized ApoBDs were produced. C: TEM image of an extruded nano-sized ApoBDs, scale bar = 100 nm.

In a next step, the ApoBDs were stained with a lipophilic dye (DiI) and extruded through a filter with 100 nm pore size. Around 2500 nano-sized (100-120 nm) ApoBDs are produced out of one 2 µm large ApoBDs (Fig. 2B). The nano-sized ApoBDs had a size in TEM and DLS of around 130 nm (Fig. 2C). DOPC and DOPC:PS (9:1 molar ratio) liposomes were produced by thin film hydration method followed by staining and extrusion through a 100 nm filter.

Results and discussion

Nano-sized ApoBDs derived from A549 and HepG2 cells, DOPC and DOPC:PS liposomes were incubated on A549, HepG2 and THP-1 cells for 15 minutes, 1, 4 and 24 hours. The uptake of these fluorescent labeled nanoparticles in the mentioned cell lines was measured by fluorescence activated cell sorting (FACS). The epithelial cell line A549 showed a 3-5-fold higher uptake of nano-sized ApoBDs compared to HepG2 and THP-1 cells after 15 minutes, 1 and 4 hours incubation. HepG2 and THP-1 engulfed similar after 15 minutes and 1 hour. The highest uptake over all was seen in THP-1 macrophages after 24 hours incubation. A549 and HepG2 favored DOPC:PS (positive control) over DOPC (negative control) liposomes, but the opposite was measured for THP-1 macrophages. Since THP-1 macrophages are professional phagocytes, they need more signals than PS for internalization. Additional signals can be several CD factors, such as CD31 and 47, TSP-1 and apoptotic cell associated molecular patterns (ACAMPs). [X] These results showed that PS, which is present in ApoBDs and DOPC:PS liposomes, is an important “eat-me” signal for the uptake of lipid nanopar-

ticles in different cell lines, but that the PS alone is not sufficient for recognition by professional phagocytes such as THP-1 cells. We also found that the epithelial cell line A549 is very fast and efficient in clearing particles and shows high efferocytotic activity compared to the tissue cell line HepG2. THP-1 macrophages are much more selective and need time for the internalization of PS particles but rapidly clear ApoBDs.

the TIM3 receptor is not present or simply not used for the uptake of DOPC:PS liposomes in A549 cells. In summary, by using antibodies to PSR we lowered the uptake of liposomes because recognition of the “eat-me” signal PS was prevented.

Conclusion

We were able to produce nano-sized cell derived apoptotic mimics from various cancerous and non-cancerous cell lines. With our in vitro experiments, we found that PS in ApoBDs and liposomes is very important for uptake in cells. Blocking of the “eat-me” signals or of the PS receptors strongly reduced the uptake of particles in cells. Furthermore, high efferocytotic activity was seen of epithelial cells, low efferocytosis of tissue cells and high uptake after 24 hours in macrophages. These results offer new perspectives for the design of therapeutic gene delivery systems.

References

- [1] M. R. Elliot, K. S. Ravichandran, *The dynamics of apoptotic cell clearance*, *Dev Cell.* **38**, 147 (2016)
- [2] K. S. Ravichandran, *Find-me and eat-me signals in apoptotic cell clearance: process and conundrums*, *JEM* **207(9)**, 1807 (2010)
- [3] K. Segawa, S. Nagata, *An apoptotic “eat me” signal: Phosphatidylserine exposure*, *Trends in Cell Biology* **25(11)**, 639 (2015)

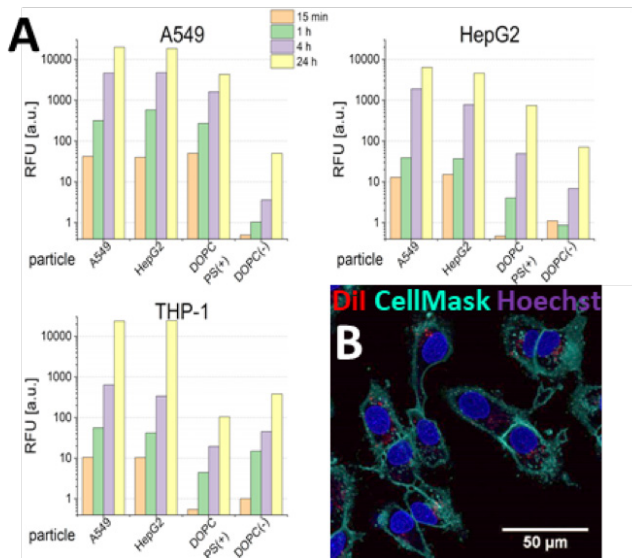


Fig. 3 A: Uptake of A549 and HepG2 derived nano-sized ApoBDs, DOPC:PS and DOPC liposomes in A549, HepG2 and THP-1 cells after 15 minutes, 1, 4 and 24 hours incubation. B: Uptake of fluorescent labeled nanoparticles (red: DiI) in cells was also confirmed with CLSM.

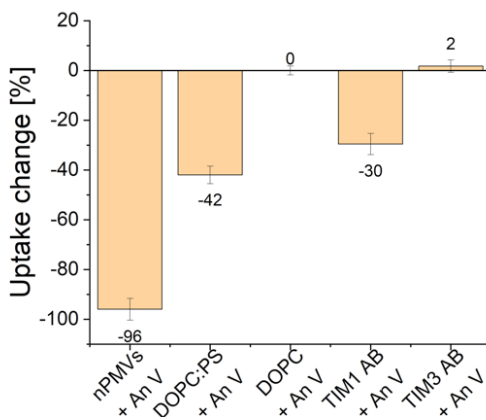


Fig. 4 A: Uptake changed when particles were treated with annexin V or cells with TIM antibodies. B: Live cell imaging after 1 hour incubation showed no uptake when nPMVs were treated with annexin V.

In a next step, we used the protein annexin V, which specifically binds to PS, to block the “eat-me” signal on side of the particles. The uptake of nano-sized ApoBDs and DOPC:PS liposomes in A549 cell was reduced by 96% respectively 42%. As expected, the uptake of pure DOPC liposomes did not change after addition of annexin V. With this experiment, we showed that annexin V binds to PS on particles and reduces the uptake by blocking the “eat-me” signal.

TIM 1 and 3 antibodies were added to A549 cells prior to incubation with particles in order to block the TIM receptors on the cells and investigate the influence on the uptake of particles. The uptake of DOPC:PS liposomes was reduced by 30 % when cells were treated with TIM1 antibody. In contrast, treatment with TIM3 antibody did not change the internalization of liposomes. In this case, we still need to investigate if either

Energy dissipation on suspended graphene

Project P1803: Nanoscale mechanical energy dissipation in quantum systems and 2D-materials

Project Leader: E. Meyer and M. Poggio

Collaborator: A. Ollier (SNI PhD Student)

Introduction

Surface deformations of graphene show quantum dot-like (QD) behavior, with the possibility of controlling their charge state by electrostatic gating [1]. Here, the sample is a circular free-standing graphene (FSG) sheet, where the surface deformations have a 1D-ribbon-like (1DRG) shape. The measured dissipation exhibits single electron charging features, namely dissipation peaks, due to tip gating of the 1DRG structures. Tip oscillations over a 1DRG – quantum dot leads to charging and discharging events between the QD and the metallic substrate located nearby the FSG. These effects are detectable using various scanning probe microscopy (SPM) techniques [1], and in the atomic force microscopy (AFM) it is characterized by jumps in the cantilever frequency shift parabola followed by the peak in the dissipation curve [2]. In the real space, the dissipation peaks are detected as Coulomb rings (CR) [3]. Here, we employ the pendulum AFM (p-AFM), which uses very soft cantilevers to measure the dissipation. In this configuration, the cantilever is positioned perpendicularly to the sample surface to avoid the tip snapping into the contact. That way, p-AFM is few orders of magnitude more sensitive to the acting forces than conventional AFM. The measurements were performed under ultra-high vacuum conditions and at low temperatures (5 K).

Single electron charging dissipation peaks

Figure 1 shows the typical frequency shift and dissipation spectra recorded over FSG. The blue curve corresponds to the frequency shift. Its parabolic shape is due to the capacitive coupling of the oscillating tip and the underlying surface. In addition to the parabolic background, several irregularities are visible at various bias voltages (red arrows) [2]. These jumps are attributed to the rapid change of the electrostatic force due to single electron tunneling between the 1DRG-QD and the metallic substrate that serves as electron reservoir. The phenomena is known as Coulomb blockade (CB) and the jumps in the frequency shift spectra are accompanied by peaks in the energy dissipation signal (Fig. 1 – black curve).

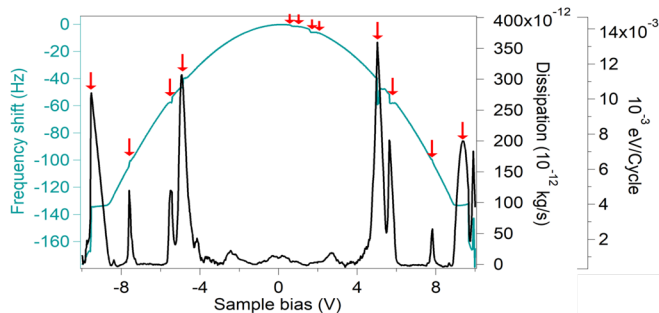


Fig. 1 Frequency shift and energy dissipation of the p-AFM cantilever oscillating over 1DRG-QD as a function of the sample bias voltage. The arrows point to the jumps in the cantilever frequency shift caused by single electron charging. The charging events appear as peaks in the dissipation spectra.

1D Coulomb ring

Figure 2 shows the real space, constant height image of one dissipation peak taken at fixed sample bias voltage equal to $U=-7,84$ V. The obtained image corresponds to a CR. Several

bright ring structures are contour lines of constant charging voltage, which are attributed to the dissipation peaks in the spectra visible in figure 1. The CRs radially surround the 1DRG-QD center, so that the ring furthest from the center corresponds to the first electron entering the QD [2]. Another important feature is that the rings don't show a circular shape, as it could be expected for single point QD, but their elongation reflects the one-dimensional character of graphene wrinkle (Fig. 2, inset). Thus, the CB ring shape is a validation of the quantum dot like behavior of 1DRG.

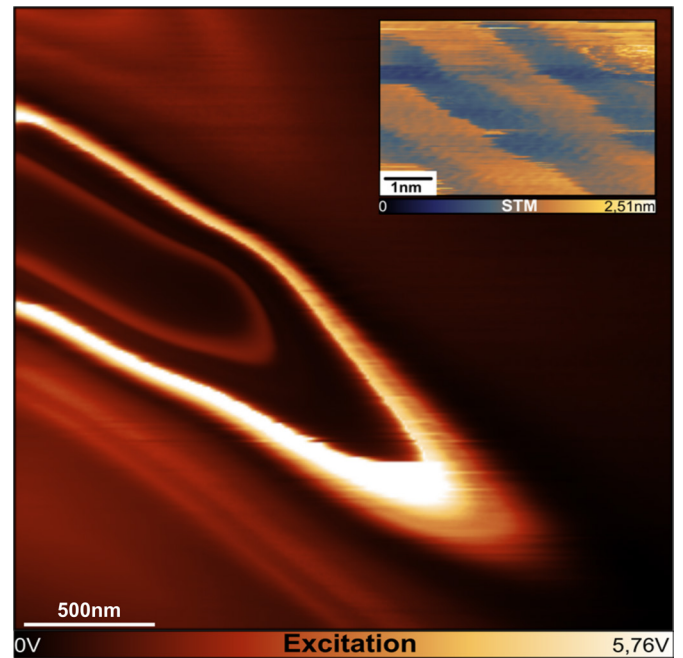


Fig. 2 Dissipation image of CR taken at constant height and at sample bias equal to $U=-7,84$ V. The inset is the STM image of the wrinkle on the free-standing graphene sheet. The direction of the wrinkle is the same as the direction of the ring elongation.

Magnetic field dependence

When a magnetic field rises, the peaks start to slightly loose intensity until they completely disappear at magnetic field around $B=\pm 1,2$ T. Figure 3 shows energy dissipation versus magnetic field and sample bias voltage. The bright contrast corresponds to the large dissipation. The maps reveal an offset (0,3 T) of the maximum intensity, presumably due to the presence of pseudo-magnetic field induced by non-uniform strain present in the suspended graphene [4]. The vanishing of the dissipation peaks at larger B field suggests a crossover from quantum dot confinement (QDC) and the magnetic field confinement (MFC). This is possible when the characteristic size of the QDC equal to $l_v=(\lambda^2\hbar_{vF}/E)^{1/3}$ [5] is comparable to the size of the MFC: $l_b=(\hbar/eB)^{1/2}$, where $\lambda=2$ nm is the size of the QD, \hbar is the reduced Planck constant, $v_F=10^6$ m/s the Fermi velocity of graphene, $E\approx 500$ meV is the estimate QD confining potential, e is the electron charge and $B=1.3$ T is the magnetic field when dissipation peaks vanish. The calculation yields $l_v=17$ nm and $l_b=20$ nm, hence $l_v\approx l_b$, which indeed confirms confinement by magnetic field.

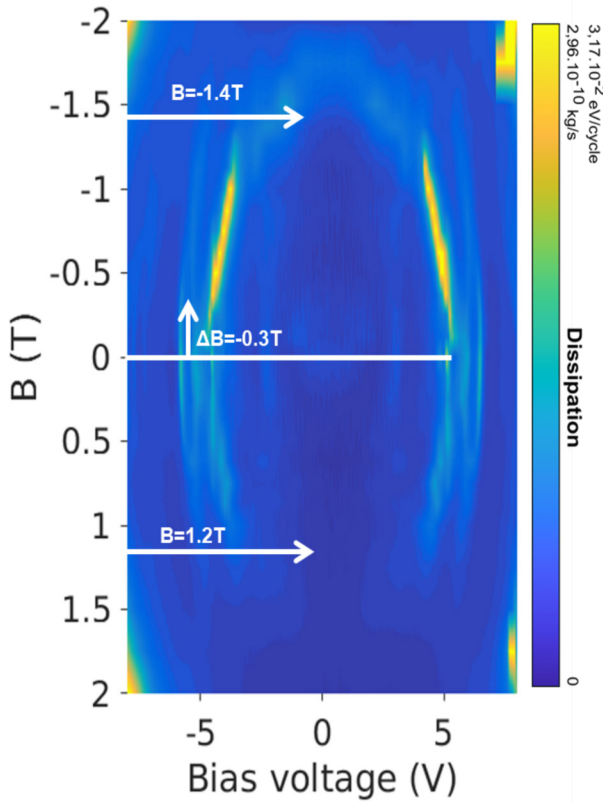


Fig. 3 Dissipation maps showing the magnetic field B dependence of the dissipation peaks and the transition between quantum dot confinement to the magnetic field confinement at about $B=1.3$ T.

This transition is also visible in the real space. Figure 4 shows the CR recorded at different magnetic field. The sample bias is the same as in figure 2 ($U=-7,84$ V). For $B=0$ T all the CR features are clearly visible, then for $B=1$ T the features become less pronounced (Fig. 4b) until they disappear completely for $B=2$ T (Fig. 4c).

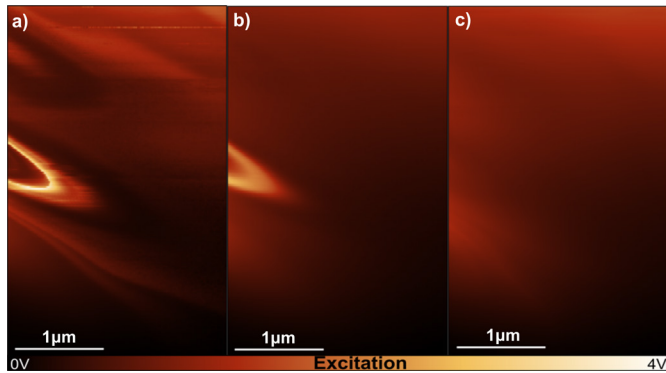


Fig. 4 Dissipation images recorded at a bias sample voltage $U=-7,84$ V and for different magnetic field. a) $B=0$ T, b) $B=1$ T and c) $B=2$ T. The Coulomb rings disappear at large magnetic field similarly to the dissipation peaks in figure 3.

Conclusion

In conclusion, the measurement shows that wrinkles of the free-standing graphene sheet act as QDs. The charge state of such QDs can be controlled by the oscillating cantilever tip. The 1D ribbon-like shape is reflected in elongated shape of Coulomb rings. Moreover, the disappearance of dissipation peaks and the Coulomb rings in magnetic field is due to a transition from quantum dot confinement to the magnetic field confinement.

References

- [1] J.-B. Qiao, H. Jiang, H. Liu, H. Yang, N. Yang, K.-Y. Qiao, L. He, *Bound states in nanoscale graphene quantum dots in a continuous graphene sheet*, PRB **95**, 081409 (2017)
- [2] R. Stomp, Y. Miyahara, S. Schaer, Q. Sun, H. Guo, P. Grutter, S. Studeniki, P. Poole, A. Sachrajda, *Detection of single-electron charging in an individual InAs Quantum dot by noncontact atomic force microscopy*, PRL **94**, 056802 (2005)
- [3] L. Cockins, Y. Miyahara, S. D. Bennett, A. A. Clerk, S. Studenikin, P. Poole, A. Sachrajda, P. Grutter, *Energy levels of few-electron quantum dots imaged and characterized by atomic force microscopy*, PNAS **107(21)**, 9496-9501 (2010)
- [4] N. Levy, S. A. Burke, K. L. Meaker, M. Panlasigui, A. Zettl, F. Guinea, A. H. Castro Neto, M. F. Crommie, *Strain-Induced Pseudo-Magnetic Fields Greater Than 300 Tesla in Graphene Nanobubbles*, Science **329**, 544 (2010)
- [5] C. Gutiérrez, D. Walkup, F. Ghahari, C. Lewandowski, J. F. Rodriguez-Nieva, K. Watanabe, T. Taniguchi, L. S. Levitov, N. B. Zhitenev, J. A. Stroscio, *Interaction-driven quantum Hall wedding cake-like structures in graphene quantum dots*, Science **361**, 789-794 (2018)

Circuit quantum electrodynamics with semi-conducting nanowires

Project P1807: Andreev Spin Qubit (ASQ) in Ge/Si Nanowires

Project Leader: C. Schönberger, F. Braakman, I. Zardo, and D. Zumbühl

Collaborators: J. H. Ungerer (SNI PhD Student), J. Ridderbos, R. Haller, L.Y. Cheung, P. Krogstrup, J. Nygård, and C. Schönberger

Spin-based circuit quantum-electrodynamics

In circuit quantum-electrodynamics (QED), single photons confined in a superconducting resonator coherently couple to a quantum system. These photons can be used for implementing long-range qubit-qubit interactions [1, 2] and hence contribute to scaling-up quantum processors. A particularly promising contender for realizing quantum computers are spins in semiconductor quantum dots due to their long coherence times and well known fabrication techniques [3, 4].

Recently, ultra-fast Rabi oscillations of a quantum dot hole-spin in a Ge/Si core/shell nanowire have been realized and the read-out of a superconducting Andreev spin qubit was observed using an InAs nanowire Josephson junction. These experiments demonstrate the feasibility of full qubit control based on electric-dipole spin resonance. Simultaneously, they present the possibility of coupling a superconducting resonator to a nanowire spin in a circuit QED experiment. Our goal is its implementation.

Fabrication of high quality, high-impedance, magnetic field resilient resonator

We plan to couple a superconducting resonator to the spin-orbit induced electric dipole moment of a spin confined in a semiconducting nanowire. In order to reach strong coupling to a spin, the resonator needs to have a large quality factor and maintain it even at finite magnetic fields. In favor of increasing the electric-dipole coupling strength, the resonators should additionally possess a large impedance. These three properties are combined in a thin-film NbTiN coplanar waveguide resonator with a small center conductor cross-section [5].

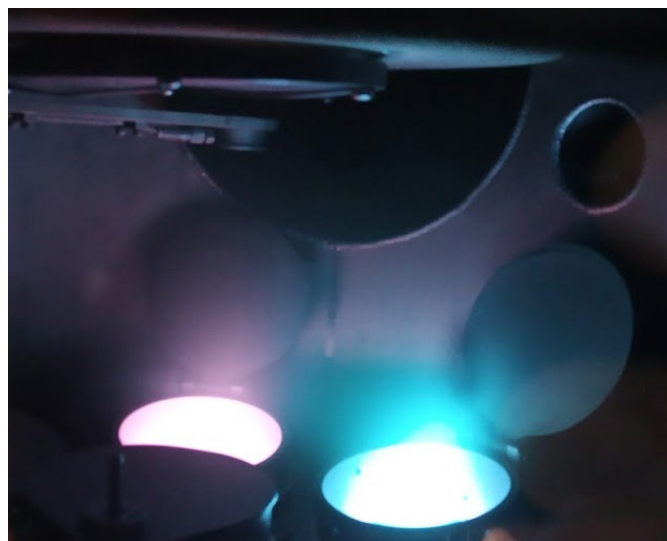


Fig. 1 Image of two plasmas with different concentrations of argon and nitrogen.

Fabrication of those resonators is challenging due to the large aspect ratios and the large amount of degrees of freedom during film deposition by plasma sputtering. A crucial parameter is the nitrogen content in the plasma. Figure 1 shows two spatially separated plasmas in the deposition chamber. Their

colors differ because of a non-equilibrium distribution of the nitrogen content in the gas composition within the chamber. By monitoring the dc voltage across the plasma as a function of nitrogen flow, the optimum deposition window can be found. Another improvement of the film quality was obtained by installing a substrate shutter in the sputter system. The shutter allows to improve the vacuum by pre-sputtering.

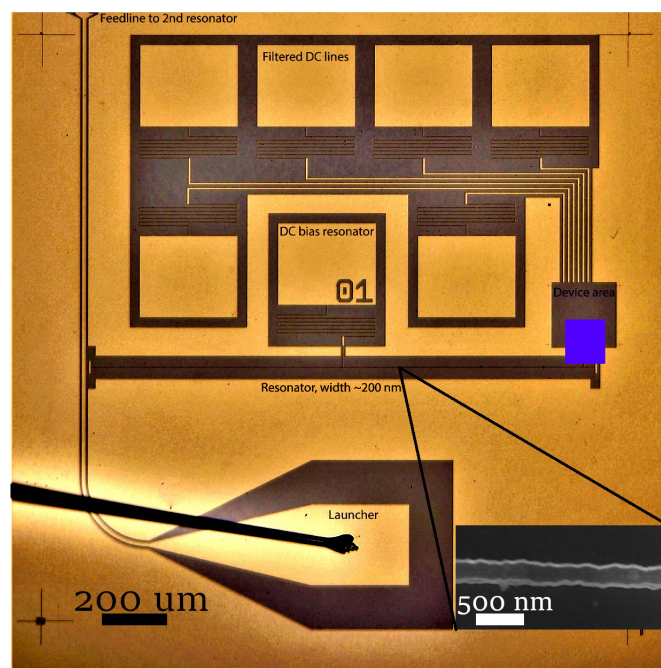


Fig. 2 Optical micrograph of a high-impedance resonator with filtered dc lines. NbTiN appears in the figure in yellow and Si in gray. The nano-scaled device, shown later in figure 4, is fabricated in the blue marked area. Inset: Scanning electron microscope image of the center conductor.

After deposition of a NbTiN film on the whole substrate, the resonators are lithographically defined by electron-beam lithography and etched using a reactive-ion plasma. Figure 2 shows a microscope image of a typical device. The device consists of a coplanar waveguide resonator whose center conductor has a width of 200 nm and is located in the middle of figure 2 (aligned horizontally, but barely visible in the optical image). The inset in figure 2 shows a scanning electron microscope image of the center conductor of a similar device. For resonator readout, the resonator is capacitively coupled to a feedline. The resonator impedance of 1.3 k Ω is much higher than 50 Ω , the transmission line impedance conventionally used. The fundamental mode of this resonator is a half-wavelength mode with electric-field antinodes at the ends of the center-conductor. The left side is coupled to the feedline, while at the right side, an area is defined in which the NbTiN is removed. This area is labeled 'Device area' (blue area in Fig. 2) and will be used to fabricate nanowire devices. The required dc lines ending in the device include meandered NbTiN sections forming part of an effective low-pass filter.

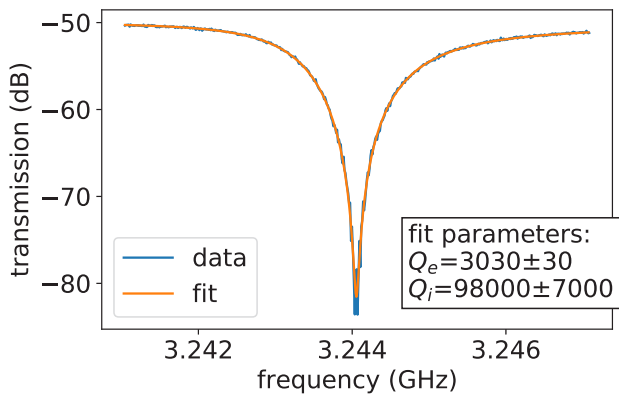


Fig. 3 Resonance dip in the transmission amplitude through the feedline. From the fit, internal and external quality factors, Q_i and Q_e , of the resonator are deduced.

Using the feedline, a resonance dip in transmission amplitude as a function of frequency can be measured. An example is shown in figure 3. The optimization of our film deposition protocol recently resulted in internal quality factors as high as 105.

An architecture for nanowire-based circuit QED

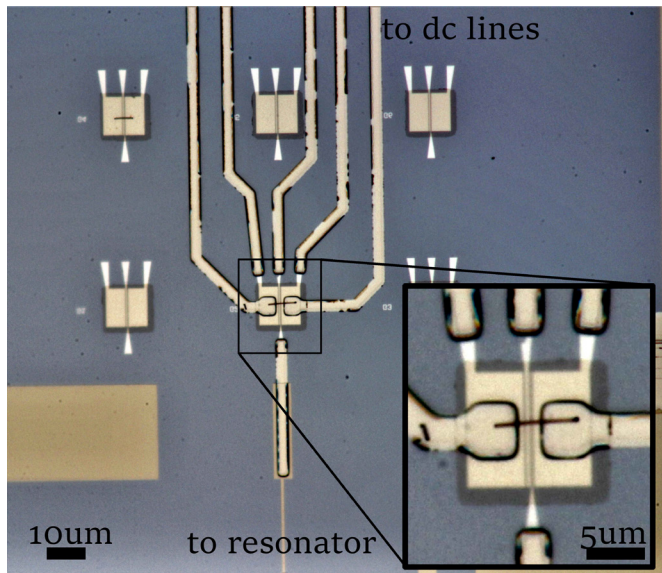


Fig. 4 Zoom of the device area. An InAs nanowire (NW) with Al shell forms a Josephson junction. The NW is best seen in the bottom-right inset as a black horizontal line of length $\sim 8 \mu\text{m}$, located on top of metallic bottom gates that couple capacitively to the NW. The middle bottom gate is additionally galvanically contacted to the resonator through the line leaving downwards.

After having realized high quality, high-impedance resonators, the next step consists of fabricating nanowire devices. In those devices, the nanowire is capacitively coupled to a gate being galvanically connected to the resonator at its electric field antinode. Figure 4 shows the first experimental realization of a Josephson junction, etched into an InAs nanowire with epitaxially grown Al facets and coupled capacitively to the resonator. The nanowire lies on top of a bottom gate stack covered with a thin dielectric HfO_2 film. Our goal is to realize resonator-spin coupling based on the spin-orbit interaction that is naturally present in those semiconducting nanowires. This will extend previous implementations of spin-based circuit QED architectures [6 - 8] towards capacitive coupling of spin states in semiconducting nanowires.

References

- [1] J. Majer, J. M. Chow, J. M. Gambetta, J. Koch, B. R. Johnson, J. A. Schreier, L. Frunzio, D. I. Schuster, A. A. Houck, A. Wallraff, A. Blais, *Coupling superconducting qubits via a cavity bus*, Nature **449**, 443 (2007)
- [2] D. J. van Woerkom, P. Scarlino, J. H. Ungerer, C. Müller, J. V. Koski, A. J. Landig, C. Reichl, W. Wegscheider, T. Ihn, K. Ensslin, A. Wallraff, *Microwave photon-mediated interactions between semiconductor qubits*, Phys. Rev. X **8**, 41018 (2018)
- [3] R. Hanson, L. P. Kouwenhoven, J. R. Petta, S. Tarucha, L. M. Vandersypen, *Spins in few-electron quantum dots*, Rev. Mod. Phys. **79**, 1217 (2007)
- [4] F. A. Zwanenburg, A. S. Dzurak, A. Morello, M. Y. Simmons, L. C. Hollenberg, G. Klimeck, S. Rogge, S. N. COPpersmith, M. A. Eriksson, *Silicon quantum electronics*, Rev. Mod. Phys. **85**, 961 (2013)
- [5] N. Samkharadze, A. Bruno, P. Scarlino, G. Zheng, D. P. DiVincenzo, L. DiCarlo, L. M. K. Vandersypen, *High-kinetic-inductance superconducting nanowire resonators for circuit QED in a magnetic field*, Phys. Rev. Appl. **5**, 44004 (2016)
- [6] N. Samkharadze, G. Zheng, N. Kalhor, D. Brousse, A. Sammak, U. C. Mendes, A. Blais, G. Scappucci, L. M. K. Vandersypen, *Strong spin-photon coupling in silicon*, Science, **359**, 1123 (2018)
- [7] X. Mi, M. Benito, S. Putz, D. M. Zajac, J. M. Taylor, G. Burkard, J. R. Petta, *A coherent spin-photon interface in silicon*, Nature, **555**, 599 (2018)
- [8] A. J. Landig, J. V. Koski, P. Scarlino, U. C. Mendes, A. Blais, C. Reichl, W. Wegscheider, A. Wallraff, K. Ensslin, T. Ihn, *Coherent spin-photon coupling using a resonant exchange qubit*, Nature, **560**, 179 (2018)

Coupling an ultracold ion to a metallic nanowire

Project P1808: Quantum dynamics of an ultracold ion coupled to a nanomechanical oscillator

Project P1407: Coupling a single ion to a nanomechanical oscillator

Project Leader: S. Willitsch and M. Poggio

Collaborators: M. Weegen (SNI PhD Student) and P. Fountas (SNI PhD Student)

Introduction

The development of solid state-atomic interfaces aims at providing hybrid quantum systems which combine the advantages of the individual platforms. Trapped ultracold ions in radio frequency ion traps offer excellent coherence properties and can be controlled and manipulated very precisely on the quantum level [1]. Nanowires are nanomechanical oscillators that are highly integrable, easily manipulable and can be interfaced with a variety of quantum devices [2, 3]. In combination with trapped ions, they can act as sensitive probes for manipulating the quantum motion of the atomic particles, as well as offering additional possibilities for fine-tuning the trapping potentials.

Here, we report progress towards the implementation of an ion-nanomechanical interface consisting of an ultracold $^{40}\text{Ca}^+$ ion and a metallic Ag_2Ga nanowire in an ion trap. The two subsystems are coupled via electric fields.

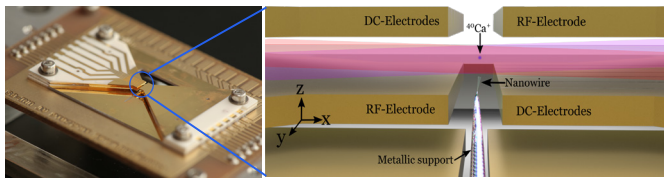


Fig. 1 Left: Miniaturized segmented-layer ion trap consisting of a stack of gold-coated alumina wafers mounted on a printed circuit board. Right: Schematic representation of the setup around the trapping region, showing a trapped $^{40}\text{Ca}^+$ ion, the electrodes generating the trapping fields and the nanowire on its mechanical support.

Experimental Implementation

The core of the experimental setup is formed by a home-built segmented-layer wafer ion trap shown in figure 1. The trap consists of gold-coated alumina wafers as electrodes to which radiofrequency (RF) and static (DC) voltages are applied to trap ions. The DC electrodes are partitioned into segments that can be individually addressed in order to shape the trapping potential for the ion as needed.

Calcium atoms are emitted from a calcium getter source underneath the trap assembly and ionized in the trapping region. The ionization of the atoms is implemented via a two-step ionization process using diode laser beams at 423 nm and 375 nm for generating calcium ions to be confined by the electric fields of the trap.

The Ag_2Ga nanowire with an approximate length of 50 μm and diameter of 200 nm is mounted on top of a metallic holder attached to a stack of nanopositioners (see Fig. 1 and Fig. 2). Thus, the position of the nanowire relative to the ion can be adjusted on the fly in all three spatial directions with tens of nanometer precision. By applying a voltage to the nanowire, electrical coupling to the ion is established. An integrated piezzo actuator enables the excitation of the nanowire with adjustable frequencies and amplitudes.

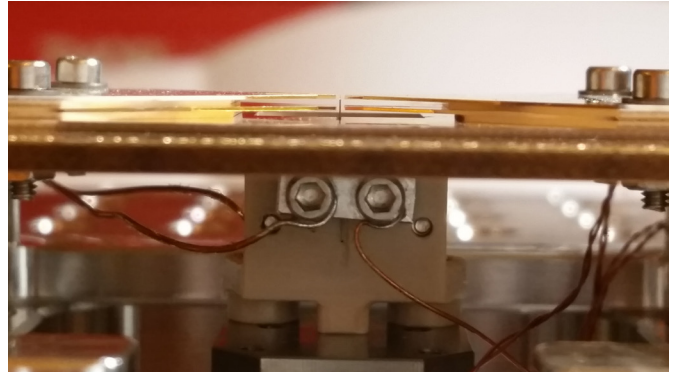


Fig. 2 Side view of the ion trap including the nanowire in its center.

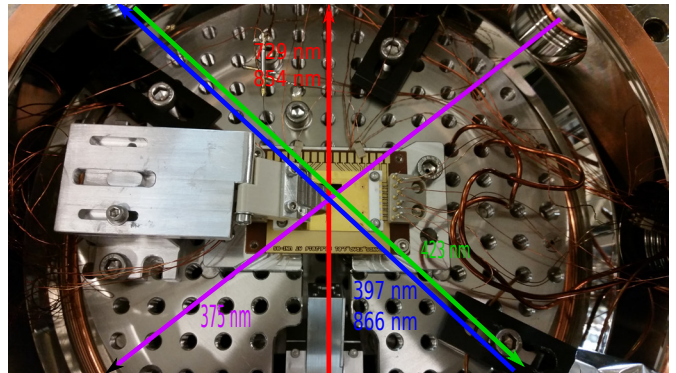


Fig. 3 Top view of the experimental setup showing schematically the laser beams for Ca ionization as well as Doppler laser cooling and ground-state cooling of the Ca^+ ion.

For the Doppler laser cooling of the Ca^+ ion, laser beams at 397 nm and 866 nm are aligned into the trapping region in order to achieve a closed optical cycle connecting the $(4s) ^2S_{1/2}$, $(4p) ^2P_{1/2}$ and $(3d) ^2D_{3/2}$ states of the atom (see Fig. 3). Cooling of the ion to its motional ground state in the trap is achieved by resolved-sideband cooling on the $(4s) ^2S_{1/2} \rightarrow (3d) ^2D_{3/2}$ transition using a narrow-bandwidth laser beam at 729 nm and repumping population into the cooling cycle using a laser beam at 854 nm.

The 866 nm laser beam also serves as a probe to characterize the vibrations of the nanowire by absorption imaging. Figure 4 shows a vibration spectrum recorded by inducing oscillations in the nanowire by the piezo and scanning the applied oscillation frequency. A number of resonances can be observed, which are attributed to different oscillatory modes of both the nanowire and its support. A detailed assignment of this spectrum is currently in progress. These resonances provide degrees of freedom for manipulating the trapped ion at different excitation frequencies.

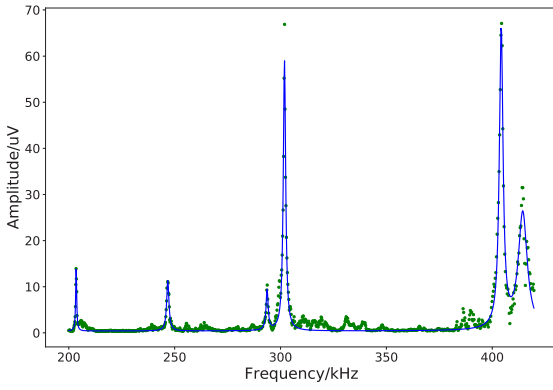


Fig. 4 Vibration spectrum of the Ag_2Ga nanowire under a variable mechanical drive recorded by absorption imaging using a laser beam at 866 nm. The peaks correspond to oscillatory modes of the nanowire and its mechanical support. Green dots: data points, blue line: fits to the data.

Theoretical Modelling

Simulations of the 1D quantum dynamics of the ion under the action of an oscillating nanowire were performed [4]. In this modelling, the nanowire was assumed to behave like an oscillating point charge, leading to an Hamiltonian of the form $H = \omega(a^\dagger a + 1/2) - s(a^\dagger + a)^2 + g(a^\dagger + a) \cos(\omega_{\text{nw}} t)$, where the first term describes the quantum harmonic oscillator of the trapped ion, while the last two terms arise from a series expansion of the ion-nanowire interaction.

Our theoretical modelling indicates the possibility for creating highly excited coherent states of the ion motion using a resonant drive of the nanowire, when the ion was initially prepared in its motional ground state (Fig. 5). Such coherent states with large amplitudes are very difficult to produce by purely optical means and thus illustrate the additional control capabilities offered by the mechanical drive of the nanowire.

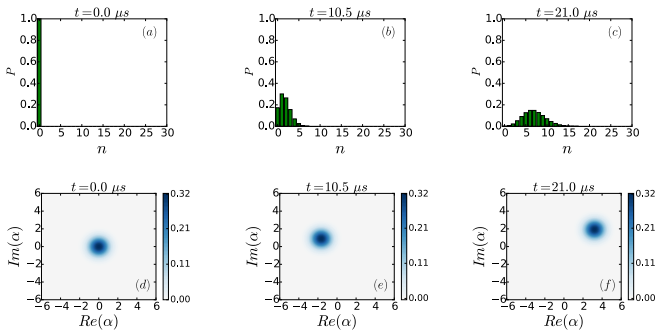


Fig. 5 Creation of highly excited coherent states of the ion motion using a resonant drive by the nanowire [4].

By adding anharmonicities to the trapping potential, which can be engineered by applying tailored voltages to the trap electrodes, while driving the ion motion via the coupling to the nanowire, also non-classical quantum states of the ion motion can be generated (Fig. 6). Different anharmonicities lead to the creation of different motional states of the ion, e.g., Schrödinger cat-type states as shown in figure 7, which appear at specific points in time during its motional dynamics.

It is worth noting that the nanowire itself offers an additional degree of freedom for engineering such as anharmonicities as it acts, as an additional flexible electrode in the system.

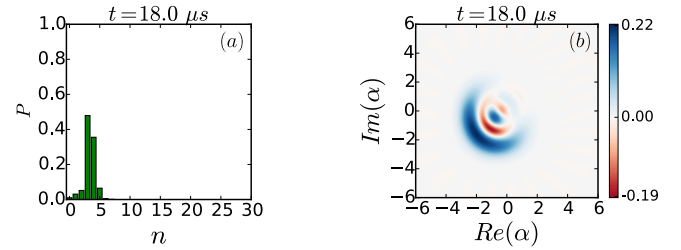


Fig. 6 Creation of non-classical states of the ion motion under the influence of a fourth-order anharmonicity term of the trapping potential, $D(a^\dagger + a)^4$, of strength $D = 8$ kHz which can be generated by tailored voltages applied to the electrodes of the trap [4].

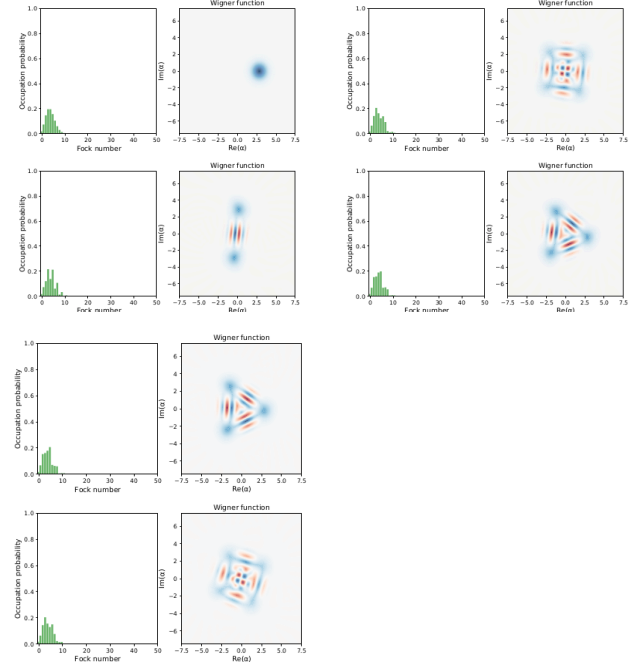


Fig. 7 Evolution of a coherent state under the influence of a third-order anharmonicity, $C(a^\dagger + a)^3$ with $C = 10$ kHz, without an additional drive. The initial coherent state was prepared by a mechanical drive of the ion with the nanowire. Under the influence of the anharmonicity, Schrödinger cat-like states are generated at specific points in time of the ion motion.

References

- [1] S. Willitsch, *Coulomb-crystallised molecular ions in traps: methods, applications, prospects*, *Int. Rev. Phys. Chem.* **31**(2), 175 (2012)
- [2] M. Montinaro, G. Wüst, M. Munsch, E. Fontana, E. Russo-Averchi, M. Heiss, A. Fortcumberta I Morral, R. J. Warburton, M. Poggio, *Quantum dot opto-mechanics in a fully self-assembled nanowire*, *Nano Letters* **14**(8), 4454 (2014)
- [3] J. M. Pirkkalainen, S. Cho, F. Massel, J. Tuorila, T. Heikkilä, P. Hakonen, M. A. Sillanpää, *Hybrid circuit cavity quantum electrodynamics with a micromechanical resonator*, *Nat. Commun.* **6**, 6981 (2015)
- [4] P. N. Fountas, M. Poggio, S. Willitsch, *Classical and quantum dynamics of a trapped ion coupled to a charged nanowire*, *New J. Phys.* **21**(1), 013030 (2019)

Microfluidics to determine the atomic structure of proteins

Project A12.10: MiPIS (University of Basel C-CINA, FHNW Muttenz, leadXpro AG Villigen)

Project Leader: T. Braun

Collaborators: M. Hürzeler, M. Chami, M. Hennig, M. Botte, C. Schmidli, L. Rima, and T. Stohler

Introduction

The recent improvements in cryogenic EM (cryo-EM) caused a revolution in structural biology, and are now regarded as a standard method for the structural analysis of protein-complexes to atomic resolution. However, (i) protein isolation and (ii) sample preparation methods lag behind, and cryo-EM is performed at far from full efficiency. Here, we present a microfluidic method for the rapid isolation of a target protein from minimal amounts of cell lysate and for its direct preparation for high-resolution cryo-EM [1].

In the single-particle cryo-EM approach, an unsupported, thin layer of isolated protein complexes in amorphous (vitrified) ice is imaged at close to physiological conditions. Only several thousand to a few million imaged particles are needed to calculate a high-resolution, three-dimensional (3D) structure. Nevertheless, protein production, purification, and sample preparation for cryo-EM are nowadays considered the bottleneck for structure determination. We have identified two dominating reasons for this: Firstly, significant amounts of protein must be produced. Conventional sample preparation for cryo-EM requires several microliters of a purified protein solution at a concentration of approx. 1 mg/ml per grid, from which extensive filter-paper blotting later removes the vast majority of protein particles. Secondly, both, protein purification and cryo-EM sample preparation are lengthy and harsh procedures. Mostly, high-yield expression systems are employed, and one or two chromatographic steps are needed to purify the protein particles. In addition, the classical cryo-EM sample preparation process that follows is a rough procedure, primarily because of the blotting step, and many proteins denature.

Microfluidic cryo-EM grid preparation

We recently developed a microfluidic cryo-EM grid preparation system termed cryoWriter, allowing the preparation of cryo-EM specimens from nanoliters of sample-solution [2-4]. Since the cryoWriter does not use paper blotting, it ensures that grid preparation is gentle and virtually lossless. Here we report the atomic model of the tobacco mosaic virus (TMV). From 25 nL sample two EM samples were prepared using the cryoWriter. One sample was enough to solve the TMV structure with a resolution of 1.9 Å (Fig. 1A). This resolution is enough to resolve the holes in aromatic side chains (Fig. 1B, C).

Microfluidic protein isolation of the untagged, human proteasome 20S

We now report the combination of sample grid preparation using the cryoWriter with microfluidic protein purification, to determine the 3.5 Å cryo-EM structure of the untagged human 20S proteasome complex [1], which is the “catalytic core” of the ubiquitin-proteasome system involved in 80 % of protein degradation and an important drug target.

Figure 2 shows the principles of the microfluidic protein isolation and cryo-EM grid preparation. We use ‘fragment antigen binders’ (Fab) to recognize and extract untagged target proteins from the raw cell lysate. We covalently modified the Fab fragments with a photo-cleavable cross-linker ending with a biotin moiety, which strongly binds to the streptavidin functionalization of the magnetic bead (Fig. 2B).

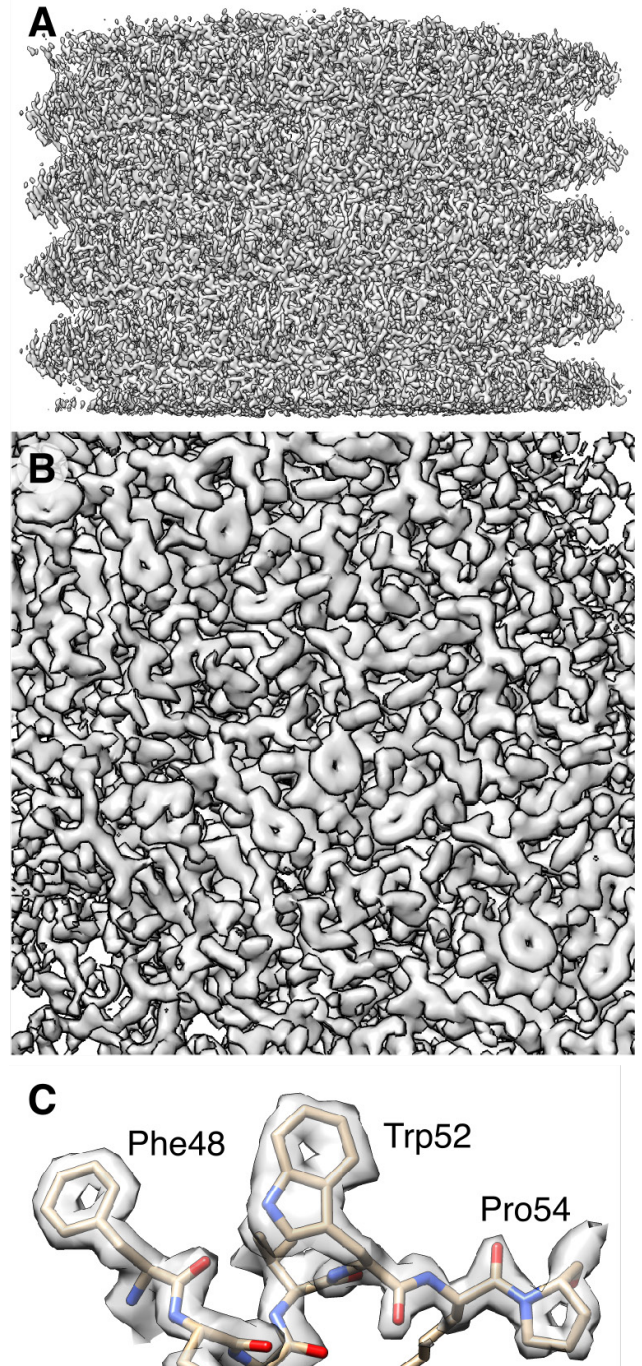


Fig. 1 TMV resolved to 1.9 Å resolution. Two EM grids were prepared from 25 nL of TMV sample. One grid was enough to solve the atomic structure. A) Side view of the TMV. B) The zoom-in demonstrates the high-resolution features of the map. At this resolution it is possible to see the holes of the aromatic rings (C).

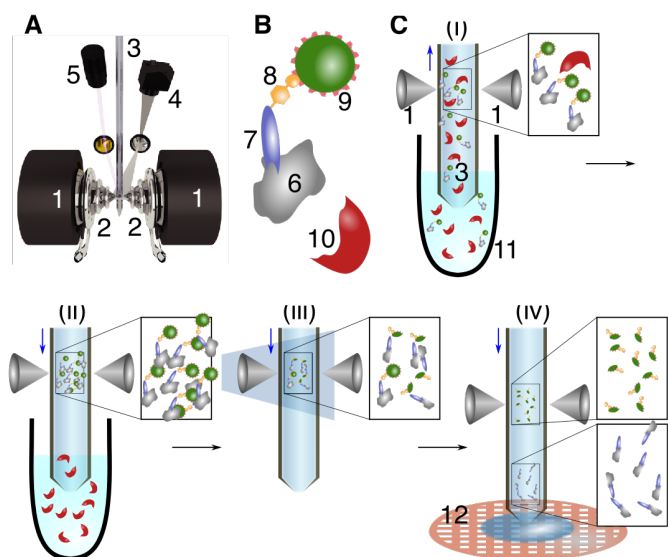


Fig. 2 Schematic workflow for microfluidic protein isolation and cryo-EM grid preparation. **A)** The electromagnetic trap consists of two electromagnets (1) that produce a strong magnetic field gradient via their water-cooled iron tips (2). Sample processing in the capillary (3) is monitored by a camera (4), and a UV LED (5) allows photo-cleavage of the linker, both via mirrors. **B)** Composite material for 'protein fishing.' The target protein (6) is recognized by a Fab (7) that is covalently modified by a photo-cleavable cross-linker (8). The linker molecule ends with a biotin moiety, which strongly binds to the streptavidin-coated bead (9). Proteins, which are not targeted (contaminants) are shown in red (10). **C)** Isolation work-flow. (i) Magnetic beads are incubated with biotinylated Fabs and cell lysate to capture the target structures in a miniaturized vessel (11). Less than 900 nL of sample is aspirated into the microcapillary for the protein isolation. (ii) The magnetic beads are immobilized in the magnetic trap (1). Non-bound lysate components (red, 10) are flushed out. (iii) Illumination with UV light breaks the cross-linker. (iv) The target protein is separated from the superparamagnetic beads, and the isolated target proteins are directly deposited on a cryo-EM grid (12) for vitrification. The blue vertical arrows indicate the pump direction.

Figure 2C shows the principles of the microfluidic protein isolation: First, the cell lysate is incubated with Fab fragments. Then paramagnetic, streptavidin coated particles are added to bind the biotinylated Fab fragments. From this solution, a volume of approx. 900 nL is aspirated in the microcapillary. The paramagnetic particles are immobilized by a magnetic field gradient generated with two electromagnets (see Fig. 2A). Therefore, only the Fab target-proteins are trapped while other proteins can be washed away. The photo-cleavable cross-linker, connecting the Fab to the magnetic bead, is cracked by UV light, resulting in a 20 nL eluate. The isolated protein is directly used to prime two cryo-EM grids, while the magnetic particles are retained in the microcapillary. For cryo-EM grid preparation, the integrated cryoWriter set-up was used, allowing a virtually lossless grid preparation without paper blotting [2-4].

The 3.5 Å structure of the human proteasome 20S core is shown in figure 3.

Isolation of his-tagged proteins

Many proteins are purified using his-tags engineered into the protein. These proteins can be purified using Ni-NTA columns. For our microfluidic approach, we developed photo-cleavable NTA tags, as shown in figure 4. These newly developed cross-linkers were successfully used to isolate proteins in preliminary tests (data not shown).

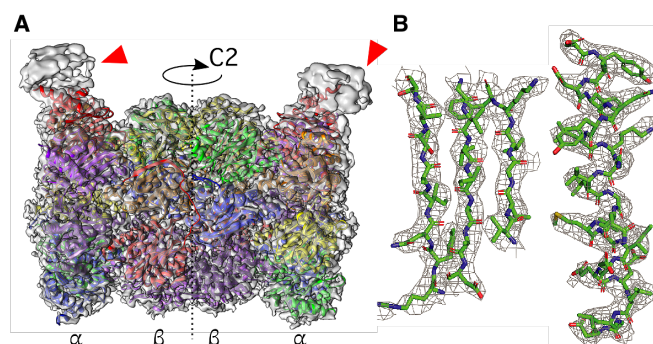


Fig. 3 High-resolution structure and atomic models of the human 20S proteasome. **A)** 3D reconstruction of the human 20S proteasome at a global resolution of 3.5 Å. The red arrowheads indicate the Fabs used to extract the protein. The side view shows the two α and two β rings, models of all 14 subunits are fit into the mass-densities. Parts of the two bound Fabs are visible at a lower resolution, due to the high flexibility of the attached Fabs (red arrowheads). The C2 symmetry-axis is indicated. **B)** An enlarged view of three strands of a β -sheet and a helix are shown as an example.

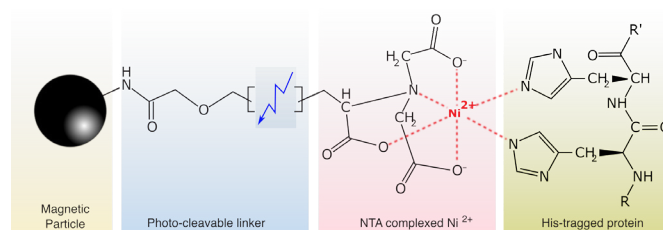


Fig. 4 Photo-cleavable NTA cross-linker for the isolation of His-tagged proteins. The His-tagged protein is coupled to the superparamagnetic bead via a Nitrilotriacetic acid (NTA) linker. The NH₂ coated beads are commercially available and can be functionalized via the N-hydroxysuccinimide esters (NHS esters) forming a stable peptide bond with primary amines. At the other end of the linker, the protein binds via His-tags to the NTA-chelated Ni²⁺. The photo-cleavable linker allows the decoupling of the NTA group from the beads by illumination with UV-light (365 nm) for elution. Note, that this specific elution releases significantly less unspecifically bound proteins than competitive elution.

References

- [1] C. Schmidli, S. Albiez, L. Rima, R. Righetto, I. Mohammed, P. Oliva, L. Kovacic, H. Stahlberg, T. Braun, *Microfluidic protein isolation and sample preparation for high-resolution cryo-EM*, Proc. Natl. Acad. Sci. U.S.A., **116**(30), 15007 (2019)
- [2] S. A. Arnold, S. Albiez, N. Opara, M. Chami, C. Schmidli, A. Bieri, C. Padeste, H. Stahlberg, T. Braun, *Total sample conditioning and preparation of nanoliter volumes for electron microscopy*, ACS Nano, **10**(5), 4981–4988 (2016)
- [3] S.A. Arnold, S. Albiez, A. Bieri, A. Syntchaki, R. Adaixo, R.A. McLeod, K.N. Goldie, H. Stahlberg, T. Braun, *Blotting-free and lossless cryo-electron microscopy grid preparation from nanoliter-sized protein samples and single-cell extracts*, JSB **197**, 3 (2017)
- [4] C. Schmidli, L. Rima, S. A. Arnold, T. Stohler, A. Syntchaki, A. Bieri, S. Albiez, K. N. Goldie, M. Chami, H. Stahlberg, T. Braun, *Miniaturized Sample Preparation for Transmission Electron Microscopy*, JoVE; e57310 (2018)

3D printable nanoporous Cellophil® membranes for tissue regeneration applications

Project A12.17: 3D Cellophil® membrane (FHNW Muttenz, University of Basel HFZ, CIS Pharma AG Bubendorf)

Project Leader: U. Pieleas and F. Koch

Collaborators: S. Stübinger and C. Geraths

Introduction

The project aims for the development of multilayered membrane composed of the new biocompatible polymer family “Cellophil®” and gradients of hydroxyapatite to be utilized in a molding process (layer by layer polymerization). The functional membranes are formed during a UV light induced polymerization of a monomer solution and an integrated crosslinking agent. The so formed polymer network provides a barrier function on the soft tissue side and a porous structure on the hard tissue side of the membrane, allowing cells (osteoblasts) to grow and the bone tissue to regenerate. Furthermore, the membrane should later be functionalized by e.g. growth factors to assist the regeneration process. The immobilization of the selected factors is planned to be accomplished by non-covalent interactions due to so called coiled-coil peptides, where one coil is attached to the membrane and the other coil to the factor. These peptides interact with each other by building up a super-coiled conformation. The super-coiled conformation shows strong ionic and hydrophobic affinities (Kd up to 10-10). The peptides should be produced by genetic engineering and expressed in E. Coli. Because the binding is based on non-covalent interaction, the immobilization of the growth factors will take place under very mild conditions and is universally applicable. Furthermore, the number of bound molecules can be controlled very precisely.

Mechanical characterization of the multilayer membrane

Since the originally intended strategy to use pre-polymers (see 2nd Project report 2018) did not deliver the expected result and was time and labor consuming the process was adapted to a layer by layer polymerization of a Cellophil® monomer solution (first proof of concept later in 2018). This concept was further characterized and optimized in the third year of the project. Several membranes with different crosslinking conditions (monomer concentration, UV intensity, incubation time and crosslinking degree) were produced and characterized for their visco-elastic properties using a nano indenter (OPTICS-11). Depending on the crosslinking degree the mechanical stiffness of the resulting hydrogels could be varied between 7.1 kPa and 90.4 kPa. These values are compatible with different cell types so that the hydrogel can be adjusted to the target tissue e.g. muscle cells which prefer approx. 10 kPa or cartilage cells 50 kPa. The integration of hydroxyapatite nano-particles further results into an increase of mechanical stiffness up to 500 kPa which is useful for bone tissue or osteointegration. With this characterization the proof of concept of the multilayer membrane with different stiffness at the interface of soft/hard tissue was achieved.



Fig.1 Exemplary Multilayer hydrogel. Hydrogel with integrated hydroxyapatite nanoparticles. From left to right the mechanical stiffness increases step-wise.

The membrane was further characterized in a long-term experiment by incubation in a buffer with a weak basic pH. This incubation results into the intended slow dissolution of the hydrogel over several weeks due to degradation of the crosslinkers (verified visually as well as SEC measurement of supernatants). Depending on the crosslinking degree the velocity of this process could be varied. Experiments with enzymes e.g. esterases are planned to simulate the condition in a biologic environment e.g. the oral cavity.

Behavior of multilayer membrane in cell culture

Since the adjusted process uses a monomer solution for formation of the membrane, the effect of residual monomers and crosslinkers was analyzed in cell culture, as they might have a negative influence on cell growth. In these experiments, a high biocompatibility of the Cellophil® monomers was seen with no cytotoxic effects detectable up to 5 mM in a 14-day metabolic assay. Therefore, negative effects due to residual monomers are not expected. Nevertheless, the crosslinking agent shows some toxic effects so that a Cellophil® alternative was envisioned to optimize the hydrogel but could not be synthesized in due time.

The multilayer membrane was subsequently characterized in long-term experiments and their influence on proliferation of osteoblasts as well as fibroblasts was studied. These experiments revealed that the cells could proliferate but show sometimes “non-natural” shapes. This may be a result of a too smooth upper surface of the hydrogel which was seen in SEM images. Since the “inside” of the membrane was highly porous and ideal for cell integration, this could be led back to the setup of the UV light exposure from above. This may have led to a too high radiation dose on the upper monomer solution which potentially results in very short polymers with a high crosslinking density. Cells seem to have issue to attach and differentiate on these smooth surface areas.

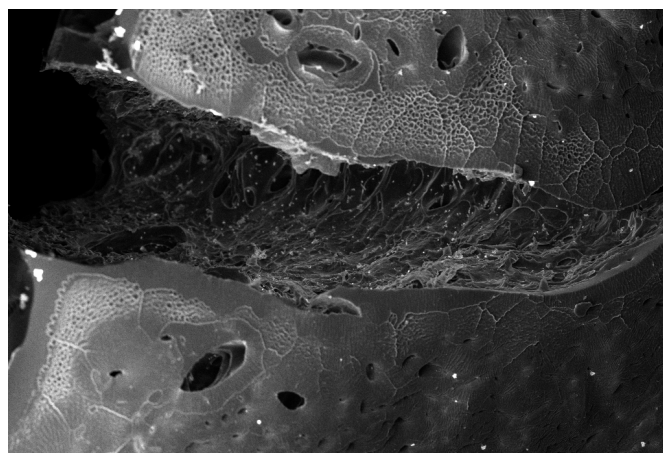


Fig.2 Hydrogel with high crosslinker. The hydrogel shows a smooth surface and is highly porous inside.

Different strategies to overcome this effect were discussed but could only be tested in pre-experiments, where drying and rehydration of the hydrogel to increase micro roughness show promising results. Further optimization has to be performed before in vivo experiments can be started.

In additional experiments, the effect of surface charge was also analyzed by integration of conventional acrylic monomers with different charges. Due to this, a net positive charge could be identified to be advantageous for cell proliferation. In this regard, a new Cellophil® monomer was synthesized, containing such a positive charge, but could not be tested due to time reasons.

SEM Visualization of Membrane

Several types of hydrogel membranes were analyzed in detailed scanning electron microscopy (SEM). Thereby, a high influence of the crosslinker and nano-particle on the porosity of the membrane was revealed, which was in line with the mechanical characterization.

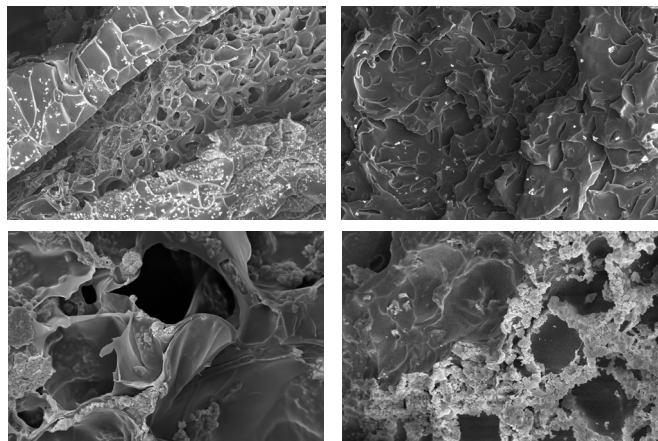


Fig 3. SEM pictures of different types of membranes. A: low crosslinker concentration, 1000X. B: high crosslinker concentration, 1000X. C: low crosslinker concentration, with hydroxyapatite nanoparticles, 2000X. D: high crosslinker concentration, with hydroxyapatite nanoparticles, 2000X

Outlook

In the last year of this SNI funded project, the in 2018 established proof of concept strategy for a multilayer membrane was extensively characterized in regard to the mechanical properties and behavior in cell culture. These experiments delivered key parameters needed for the adjustment of the membrane to the target tissue. Some new identified aspects like the surface charge or micro roughness of the membrane have still to be optimized in order to initiate in vivo experiments. Further, the planned integration of proteins e.g. growth factors by the coiled-coil peptide linker system (POC established end 2018) has to be finalized, as this part of the project could not be finished due to an alternative focus, time and change in personnel.

CIS Pharma, the FHNW and UNI Basel are keen to pursue this interesting project further and bring the novel membrane closer to the dental market.

References

- [1] A. L. Boyle, D. N. Woolfson, *De novo designed peptides for biological applications*, Chem. Soc. Rev., **40**, 4295–4306 (2011)
- [2] D. N. Woolfson, *The design of coiled-coil structures and assemblies*, Adv. Protein Chem., **70**, 79–112 (2005)

Efficient capturing of mRNA for single-cell-transcriptomics

Project A13.04: ecamist (FHNW Muttenz, D-BSSE ETH Basel, Memo Therapeutics AG Basel)

Project Leader: G. Lipps

Collaborators: R. Dreier, S. Schmitt, and M. Held

Single cell transcriptomics

Single cell transcriptomics (SST) or single cell RNA-seq (scRNA-seq) is becoming a broadly used genome-wide technology to detect cellular identities and dynamics, e.g., cell subpopulations, cell state marker genes and pathways, cell state transitions, and cell trajectories and allows the comparison of the transcriptomes of individual cells [1]. Therefore, a major use of scRNA-seq has been the assessment of transcriptional similarities and differences within a population of cells. By looking at events on single-cell level, phenomena may be observed, which would be usually averaged out if the experiment was conducted in bulk. For that reason, scRNA-seq is used in many fields of study e.g. in the development of new precision cancer therapies, in the discovery of new drug targets and in the fast growing field of medicinal antibodies development [2, 3]. Currently, there are several methods available for scRNA-seq. A systematic comparison of the performances of diverse single cell RNA sequencing protocols has shown that Drop-seq is the most cost-efficient method for transcriptome quantification of large numbers of cells [4]. The method in brief: A microfluidic device joins two aqueous flows before their compartmentalization into separate droplets. One flow contains cells, the other flow contains beads suspended in lysis buffer. Immediately after droplet formation, the cell is lysed and releases its mRNA (approximately 100'000 mRNA molecules per cell), which then hybridizes to the beads (Fig. 1). The hybridization happens via an interaction of the poly adenine-tail of the mRNA and the oligo thymine-tail of the bead.

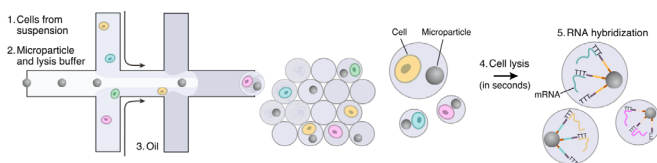


Fig. 1 Graphical representation of Drop-seq method. Adapted from Macosko et al. [5].

After hybridization, the droplets are broken and the microbeads are collected and washed. The captured mRNAs are then reverse transcribed in bulk and further analyzed [5]. One of the major drawbacks of this method can occur at the stage of breaking down the droplet emulsion: Because the interaction between mRNA and bead is weak, it is possible that mRNA dehybridizes from one bead and rehybridizes on another bead (so called cross talk) leading to undesired results. The intention of ECAMIST was to reduce cross talk and effectively bind mRNA to microbeads.

Oligo modification of microbeads

As described before, modified microbeads are needed for an efficient capturing of mRNA from single cells.

In preliminary work, it was shown that the synthetic route via click chemistry is the preferred way to modify beads with a catcher oligonucleotide. In short: an azide-modified microbead reacts with a DBCO-modified oligonucleotide. The reaction takes place under mild, aqueous conditions at low temperatures with a high yield [6], making this approach the preferred way for modifications with biomolecules (Fig. 2).

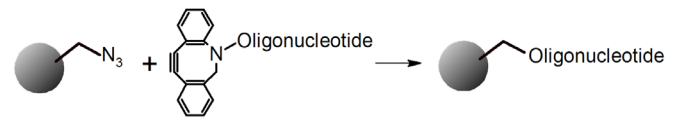


Fig. 2 Surface modification of microbeads with oligonucleotides, using click chemistry.

Surface modification of microbeads

A possible solution to the problem of cross talk might be addressed by using less, but bigger microbeads. Ideally, there would be one bead per droplet and cell. Beads being bigger than 1 μm in diameter and containing an azide-modified surface are not commercially available. Therefore, the surface of polystyrene beads (\varnothing 2.5 μm) with an amine modified surface, needs to be converted into an azide group. For that reason, a diazo transfer reagent was synthesized and used for the modification of the amine beads (Fig. 3) [7, 8].

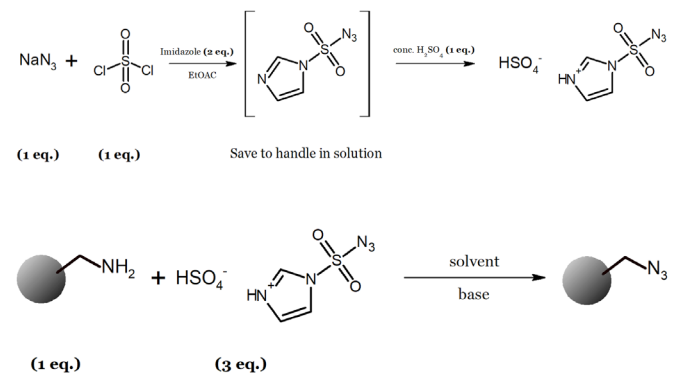


Fig. 3 Reaction scheme for the synthesis of diazo transfer reagent and subsequent modification of amine beads to azide beads.

Stabilization of mRNA hybrid

Another possible approach for stabilization is the use of an enzyme during the lysis step, which stabilizes the hybrid between catcher oligonucleotide and mRNA. As the hybridization usually takes place in a high salt environment, it is crucial that the enzyme is highly salt tolerant (Fig. 4).

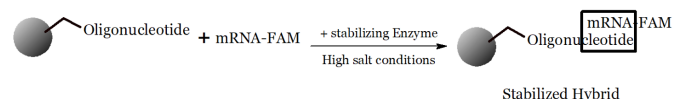


Fig. 4 Hybridization of mRNA to microbeads followed by stabilization of hybrid by a halophilic enzyme.

To prove the stabilizing effect of the enzyme, oligonucleotide modified beads were incubated with a solution of fluorescently labeled RNA in presence or absence of enzyme and analyzed by FACS (Fig. 5, red signals). Followed by the first analysis, the beads were heated to 70°C, washed with hot buffer and once more analyzed by FACS (Fig. 5, green signals). If the enzyme indeed has a stabilizing effect, the fluorescence signal should not decrease after heating up the beads in hot buffer, as the

enzyme increases the melting temperature of the oligo-RNA hybrid.

Results

Magnetic microbeads were modified with oligonucleotides using click chemistry. The number of oligonucleotides per bead was calculated to be ~36 000. In addition, a diazo-transfer reagent was successfully synthesized in high yields (76%) and used for the modification of amine microbeads into azide-modified beads. The results were confirmed by FT-IR and fluorescent microscopy (data not shown).

An enzyme, which increases the stability of the RNA-DNA hybrid, was expressed in *E. coli* and tested. It kept its activity under high salt concentrations as well as under other trying conditions.

The stabilizing effect was shown by FACS experiments: The addition of the enzyme during the incubation of microbeads and fluorescent RNA solution revealed an increased signal, which was still elevated after heating up.

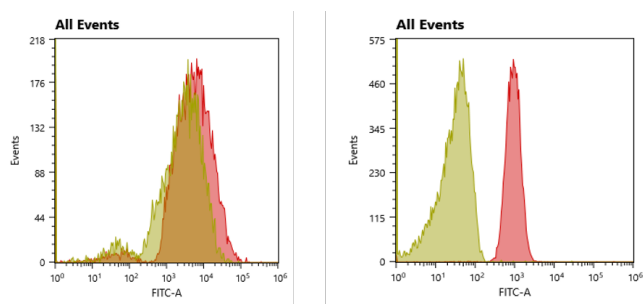


Fig. 5 Left: Stabilizing effect experiment with addition of an enzyme, right: without enzyme. The red signals show the beads before heating up, the green signal after the heating up step.

Finally, application studies in droplets showed that a new developed lysis buffer did not lyse the cells optimally. Therefore, the stabilizing effect of the enzyme was masked. Further optimization of the lysis puffer is required to achieve a more robust capturing of low abundance transcripts.

References

- [1] Q. H. Nguyen, S. W. Lukowski, H. S. Chiu, A. Senabouth, T. J. C. Bruxner, A. N. Christ, N. J. Palpant, J. E. Powell, *Single-cell RNA-seq of human induced pluripotent stem cells reveals cellular heterogeneity and cell state transitions between subpopulations*, *Genome Res.* **28**, 1053–1066 (2018)
- [2] Y. F. S. Seah, H. Hu, C. A. Merten, *Microfluidic single-cell technology in immunology and antibody screening*, *Mol. Aspects Med.* **59**, 47–61 (2018)
- [3] J. Spaethling, J. H. Eberwine, *Single-cell transcriptomics for drug target discovery*, *Curr. Opin. Pharmacol.* **13**, 786–790 (2013)
- [4] C. Ziegenhain, B. Vieth, S. Parekh, B. Reinius, A. Guillaumet-Adkins, M. Smets, H. Leonhardt, H. Heyn, I. Hellmann, W. Enard, *Comparative Analysis of Single-Cell RNA Sequencing Methods*, *Mol. Cell* **65**, 631–643.e4 (2017)
- [5] Macosko, E. Z. et al., *Highly parallel genome-wide expression profiling of individual cells using nanoliter droplets*, *Cell* **161**, 1202–1214 (2015)
- [6] G. Walden, X. Liao, G. Riley, S. Donell, M. J. Raxworthy, A. Saeed, *Synthesis and Fabrication of Surface-Active Microparticles Using a Membrane Emulsion Technique and Conjugation of Model Protein via Strain-Promoted Azide-Alkyne Click Chemistry in Physiological Conditions*, *Bioconjug. Chem.* **30**, 531–535 (2019)
- [7] G. T. Potter, G. C. Jayson, G. J. Miller, J. M. Gardiner, *An Updated Synthesis of the Diazo-Transfer Reagent Imidazole-1-sulfonyl Azide Hydrogen Sulfate*, *J. Org. Chem.* **81**, 3443–3446 (2016)
- [8] V. Castro, J. B. Blanco-Canosa, H. Rodriguez, F. Albericio, *Imidazole-1-sulfonyl azide-based diazo-transfer reaction for the preparation of azido solid supports for solid-phase synthesis*, *ACS Comb. Sci.* **15**, 331–334 (2013)

Disruptive power storage technology applying electrolyte nano dispersions

Project A13.08: MEGAnanoPower (FHNW Muttentz, CSEM Muttentz, Aigys AG Rheinfelden)

Project Leader: U. Pieleles

Collaborators: S. Fricke, J. Schleuniger, M. Zinggeler, M. Waser, and A. Schimanski

Background

The Aigys power storage technology is based on so-called redox-flow principle. The patented Aigys Power-Cell® technology uses solid dispersions instead of dissolved chemical compounds as charge carriers. This project aims to develop stable nano-dispersions as high capacity energy storage media and to apply surface enlarged nano/micro structured electrodes as efficient current collectors.

Introduction

In a first phase of the project electrolyte dispersion made of well-known lithium-based compounds were used to test the working principle a solid dispersion redox-flow battery and to understand the basic behavior of particle based electrolyte dispersions. In the second stage of the project, the focus was on developing a water-based battery, which consist of environmental friendly non-toxic and non-hazardous active components. A screening of potential materials, which have been already used for active components for batteries, led to iron oxides, which fulfil a large number of criteria, e.g. several oxidation stages, poor solubility in alkaline media, enormous availability and complete harmlessness.

Iron oxide dispersion battery based on nano-particulate iron oxides

In a dispersion flow battery the dispersion consists ideally of stabilized nanoparticles with a small particle size, high concentration and low viscosity and thus enables a free flow of the dispersion, high contact surface area of particle to electrode and high energy density. γ - Fe_2O_3 and Fe_3O_4 in sizes from 2-20 nm were synthesized by basic precipitation of Fe^{2+} and Fe^{3+} in water.

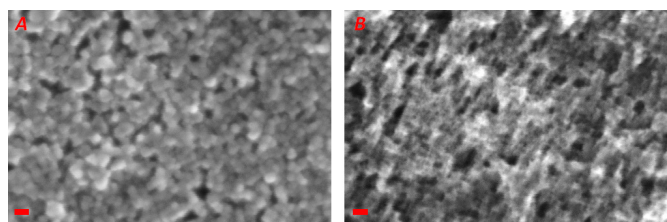


Fig. 1 SEM images showing nanoparticles of Fe_3O_4 15nm (A) and γ - Fe_2O_3 5nm (B); scale bar: 20 nm

Different stabilizers have been used in order to obtain ferrofluids (table 1). While all stabilizers provide good stability up to pH 12 ammonium citrate seemed the most versatile in combination with other ions and concentrations of up 38% by weight while maintaining a fluid consistency could be obtained.

Table 1 stabilizers used for γ - Fe_2O_3 and Fe_3O_4

Stabilizer	Silane	Nitrodopamine	Ammonium citrate
Structure			$(\text{NH}_4)_3\text{C}_6\text{H}_5\text{O}_7$

Apart from γ - Fe_2O_3 and Fe_3O_4 also α - Fe_2O_3 was synthesized, however due to a hydrothermal process required nanoparticle size was limited to a minimum diameter of 50 nm and stabilization was weak.

Electrochemical characterization

In a first step, screen-printed carbon electrodes have been coated with a slurry of different iron oxides to do a simplified electrochemical screening (Fig. 2). This is a basic test, if the materials show ability for reduction and oxidation (Fig. 3).

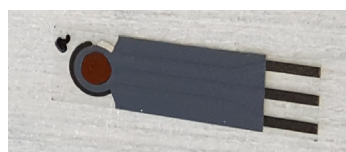


Fig. 2 Screen-printed carbon electrode with casted Fe_2O_3 for characterization.

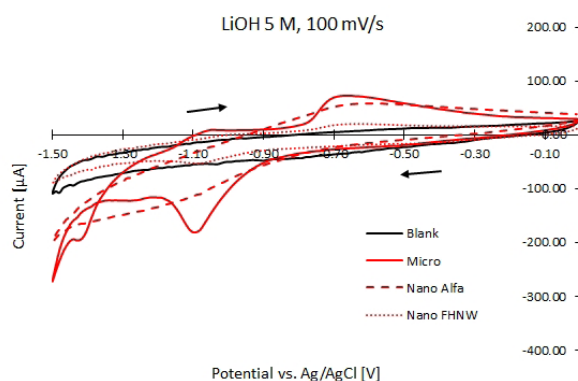


Fig. 3 Measured CV curves for different solid casted Fe_2O_3 samples.

The samples were characterized using a custom-made electrochemical setup. The half-cell setup (Fig. 4) contained an Ag/AgCl reference electrode and a platinized Ti-mesh as a counter electrode. As the working electrode, the solid casted samples or different current collector materials, such as carbon or metals were connected.

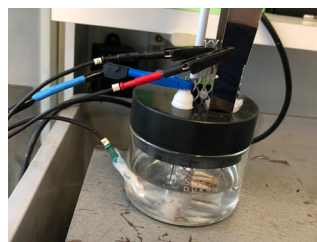


Fig. 4 Half-cell setup with Ag/AgCl reference electrode, platinized counter electrode and working electrode

While solid casted samples were then immersed in an electrolyte solution (typically 5 M LiOH), the current collectors were immersed in different iron oxide suspensions, which were mechanically stirred.

Beside synthesized iron oxide nanoparticles, commercially available α - Fe_2O_3 nano- and microparticles (Alpha Aesar) were used as reference materials. Besides the different iron oxide materials, a variety of different parameters have been studied: influence of alkaline medium, temperature, particle size and concentration, sodium sulfide addition and working electrode materials.

In addition to cyclic voltammetry (CV) measurements, chronoamperometric (CA) measurement have been performed to measure the possible charging/discharging currents of the

studied systems. The basic CA procedure was a combination of three measurements. In a first step, a short oxidation at 0 V vs. Ag/AgCl was performed for a short time (typically 1 min) to measure background current. In a second step, reduction of the material is performed at -1.1 V for at least 1 h. Because hydrogen evolution is already observed at this potential, specific reduction currents cannot be measured accurately. Therefore, a second oxidation is performed for 1 h at 0 V as the third step in order to quantify the specific back-oxidation current of the material (= back-oxidation current – background, Fig. 5) with the area under the curve (i.e. integral) depicting the charging capacity of the material.

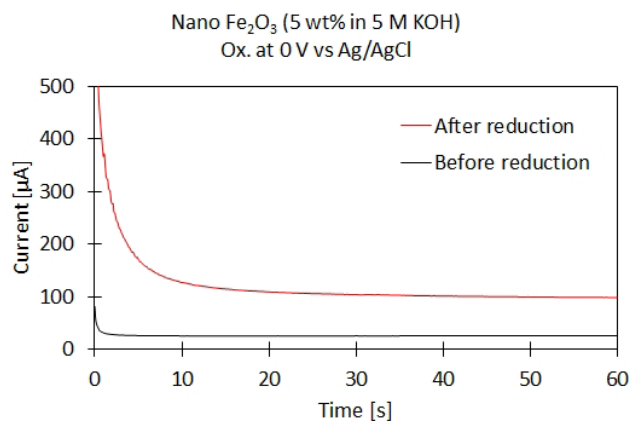


Fig. 5 Example of measured CA oxidation curves for a nano- Fe_2O_3 suspension before and after reduction at -1.1 V vs. Ag/AgCl.

In a first step, the influence of different alkaline media (lithium hydroxide, potassium hydroxide mixtures of both) with commercially available nano- Fe_2O_3 particles was evaluated. No profound difference was observed between the two bases. The overall charging/discharging capacities were only in the order of 0.1°C, which represents electrons from roughly 30 ppm of the available Fe-atoms, which was even lower at 50°C. Then particle sizes and concentrations were compared. Surprisingly, micro particles showed slightly better back-oxidation than nanoparticles. Due to the low concentration during the test, it might be attributed to a physical phenomenon of a higher collision rate. Higher concentrations increased viscosity too much. All these tests were performed using screen-printed carbon electrodes of 3 cm² as current collector. To evaluate current collector materials, tests were made with carbon felt, carbon plate and pure nickel electrodes. Photonic pulse activated carbon felt to increase wetting by creation of surface OH-groups was also used. While OH-groups have been reported to boost the performance of vanadium oxide batteries [1], no beneficial effect was observed for the dispersions but it led to a narrowed potential window (Fig. 6). This strongly increased background current in the performed measurements.

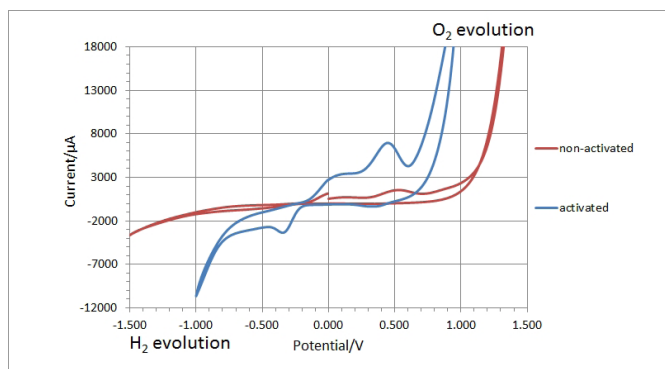


Fig. 6 Measured CV curves of carbon felt electrode (before and after thermal activation) in blank electrolyte.

Increase of the iron oxide concentration (up to 30 wt%), change of the current collector material, or addition of 0.02 M Na_2S , which was reported to stabilize iron species in the reduced

state and hence improve their availability for back-oxidation [2], did not help; the redox behavior remained extremely sluggish.

The experiments above were performed using commercially available iron oxides. Further tests, using freshly synthesized $\alpha\text{-Fe}_2\text{O}_3$ nano-particles, showed promising back oxidation currents, which are more than 4-times higher than for commercial available Fe_2O_3 nanoparticles.

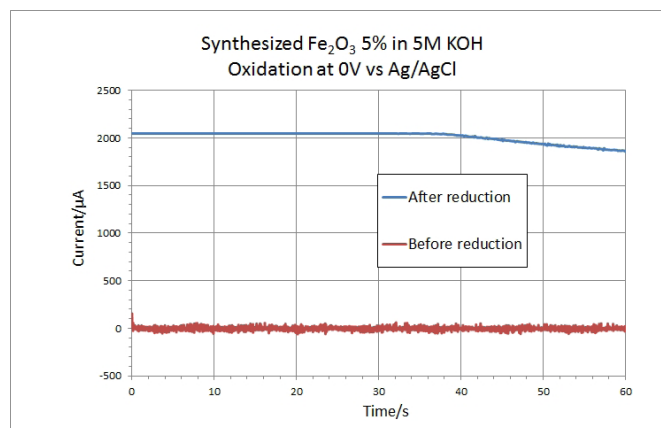


Fig. 7 Oxidation CA curves of synthesized Fe_2O_3 nano-particle

To understand the huge charge flow during back-oxidation, further tests are ongoing with the supernatant of the solution to exclude effects caused by solved species (e.g. reaction by products or educts). Detailed analysis of these materials and its results are still ongoing and will be part of the cost-neutral prolongation.

References

- [1] B. Sun, M. Skyllas-Kazacos, *Modification of graphite electrode materials for vanadium redox flow battery application - I. Thermal treatment*, *Electrochim. Acta*, **37**, 1253, (1992)
- [2] K. Micka, Z. Zabransky, *Study of iron oxide electrodes in an alkaline electrolyte*, *J. Power Sources*, **19(4)**, 315 (1987)

Biomimetic growth of calcium phosphate ceramics on Ti implants

Project A13.09: NanoCoat (PSI, FHNW Muttenz, Medicoat AG Mägenwil, Atesos Medical AG Aarau, Hager & Meisinger GmbH Neuss, Deutschland)

Project Leader: A. Testino

Collaborators: M. de Wild, E. Mueller, A. Carino, F. Dalcanale, P. Gruner, and W. Moser

Summary of the project progress

The main targets of the second year of the project NanoCoat were the process scale up and the evaluation of the stability and robustness of the coating protocol. This procedure was accomplished in two stages, first on Ti discs ($\varnothing=10$ mm and a thickness 1 mm, as those used in the protocol optimization) and then on dental implants of different size. All substrates were pre-treated (sand blasted and acid etched) before coating. In addition, discs ($\varnothing=14$ mm) were machined and pre-treated for in-vitro tests. In total about 200 ($\varnothing=10$ mm) discs, 60 ($\varnothing=14$ mm) discs, and more than 200 dental screws were processed during the second year of the project. The process optimization and the rationalization of each step allowed to increase the efficiency of the production process. At laboratory scale, about one part every two minutes can be processed. Figure 1 shows one of the processing step.



Fig. 1 A single lot of about 50 dental $\varnothing 4$ mm implants positioned on an alumina holder and ready for the thermal treatment. A single holder can allocate up to about 100 implants.

Under the guide of the industrial partners, the process window was investigated and the limits for the process parameters were defined. Worst-case scenarios as well as the reproducibility of the process were successfully tested. The reproducibility was tested by processing three independent lots with ten implants each. All of these implants were analyzed by SEM/EDX and one implant per lot was FIB milled in order to evaluate the coating cross section. Figure 2 summarized the results of the EDX analyses on implants coated for the reproducibility study. Chemical compositions (Ca, P and Na) are reported for each lot (Ti and O not showed). The average surface composition corresponds to 2.9, 1.3, 2.6, 26.6, and 66,6 at% for Ca, P, Na, Ti, and O respectively. The average thickness of the coating layer corresponds to 0.8 – 1.5 μm (e.g. see later). These results confirm the formation of a porous grafting layer with a micrometric ceramic layer composed of sodium titanate (where part of the sodium is replaced by Ca) and decorated by calcium phosphate.

The mechanical properties of the implants after coating were evaluated, since the coating protocol include surface modifications and thermal treatments. Fatigue tests were conducted according to the ISO 14801 standard at FHNW and at Meisinger GmbH (Fig. 3) in order to ensure the mechanical integrity.

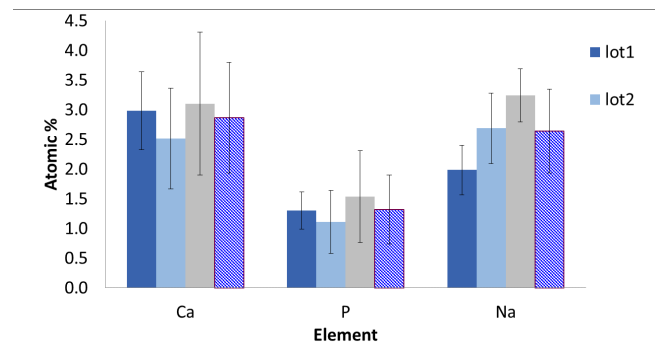


Fig. 2 EDX analysis results for Ca, P, and Na surface composition performed on three lots of treated implants. The error bar correspond to $\pm\text{SD}$ ($n=30$).



Fig. 3 Equipment used for dynamic loading test for endosseous dental implants according to the ISO14801. A certain load is applied with a defined angle and frequency over time and until mechanical failure.

The bioactivity of the implants was tested as well, on both discs and dental implants. All tests were comparatively conducted on discs at different level of production: machined, pre-treated (SLA), with grafting layer (GL), and NanoCoat treated. Cytotoxicity assays using MG63 cells were performed for 40 h and showed no differences between samples with NanoCoat or reference surfaces. MG63 cells cultured on NanoCoat surfaces proliferated and spread well, i.e. exhibiting a healthy morphology (Fig. 4). Alkaline phosphatase (ALP) activity as an indicator of osteoblastic (bone-like) differentiation was evaluated after 2 weeks and calibrated to protein content. The results of the ALP tests (Fig. 5) clearly identify differences among the four substrates tested. The NanoCoat surface induced osteoblastic differentiation with ALP activities being double in comparison to the gold-standard reference SLA surface.

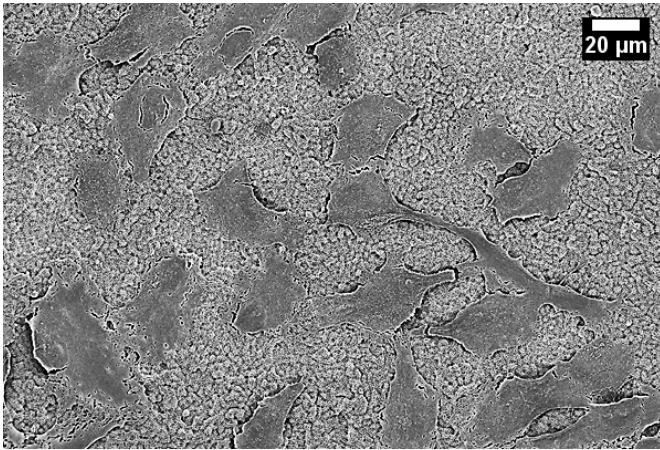


Fig. 4 MG63 cell spreading and proliferation on a NanoCoat substrate.

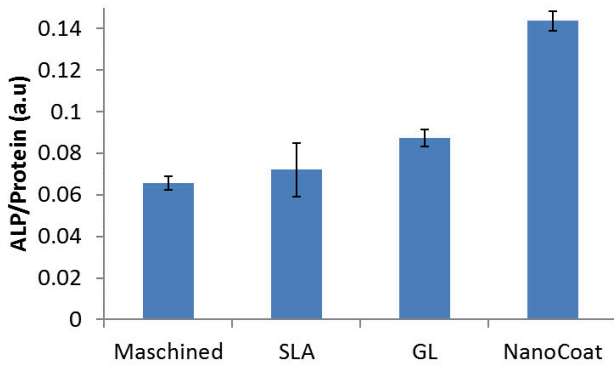


Fig. 5 Comparative ALP assay carried out on four different substrates. The machined sample corresponds to pure Ti Gr4 substrate; SLA denotes a sand blasted and acid etched titanium surface; GL identify substrates where the grafting layer were grown; NanoCoat corresponds to the NanoCoated surface according to the defined protocol. The error bar correspond to $\pm SD$ ($n = 5$).

In order to evaluate the adhesion strength of the coating layer on the metal substrate, dental implants were professionally placed into synthetic saw bone material (30 pcf) as well as in cortical bone of calf tibia (Fig. 6) up to a load of 60 Ncm, which corresponds to value much larger than what is normally applied in dental surgery. The samples were then removed by cutting the bone and the implant surface was analyzed. Both EDX analysis and FIB cross section confirmed that the NanoCoat layer was unaffected by the insertion into bone. No defects due to delamination were detected on implants placed into saw bone (Fig. 7).



Fig. 6 Dental implants inserted into the calf tibia to test damaging of the coating.

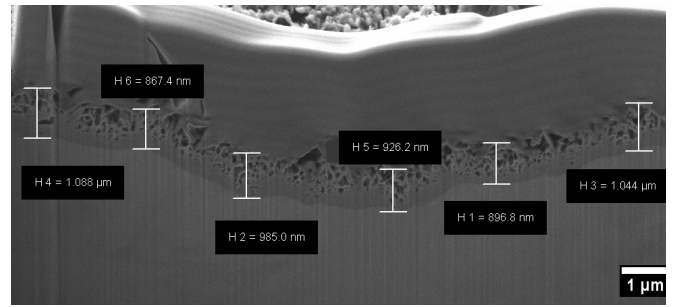


Fig. 7 FIB cross section of a dental implant after mechanical insertion test into sawbone. The NanoCoat layer is present and no delamination defects were identified.

The experimental results collected so far, combined with the process stability evidences show the potential of NanoCoat as a surface treatment for dental implants.

Some of the results were presented during a conference talk [1,2] and it is the goal to present latest results in conferences in 2020. The technology transfer is ongoing and Medicoat AG will lead the continuation of the research activities and product development, in collaboration with the project partners. In our opinion, it is remarkable that a new surface treatment was developed that far within a two-year timeframe project. Such a results, has been achieved thanks to the focused effort of all partners. We express our deepest gratitude to the essential support of the Swiss Nanoscience Institute that made this project possible.

References

- [1] A. Carino, A. Testino, E. Mueller, M. de Wild, F. Dalcana-
le, P. Gruner, W. Moser, B. Hoechst, *Novel biomimetic
approach for titanium surface treatment by calcium
phosphate: Towards the production of implants with
improved bioactivity*, European Cells and Materials, Col-
lection 4; SSB+RM Conference Abstracts (page 8) (2019)
- [2] A. Carino, A. Testino, E. Mueller, M. de Wild, F. Dalca-
nale, P. Gruner, W. Moser, B. Hoechst, *Implant surface
modification by a controlled biomimetic approach*, Euro-
pean Cells and Materials, Online Periodical, Collection 1;
Meet the Expert Conference Abstracts, (page 2) (2019)

Nano-switchable GPCR-arrestin biochip for drug discovery

Project A13.12: NanoGhip (InterAx Biotech AG, University of Basel Dept. of Chemistry and Biozentrum, PSI)

Project Leader: J. Gobrecht (a.i.), M. K. Ostermaier until Oct. 31, 2019

Collaborators: S. Yorulmaz Avsar, J. Mühle, E. Lesca, L. E. Kapinos-Schneider, C.-A. Schönenberger, M. K. Ostermaier, R. Y. H. Lim, G. F. X. Schertler, and C. G. Palivan

Introduction

G protein-coupled receptors (GPCRs) are the largest family of membrane proteins. As cellular master regulators, they control a multitude of vital signal transduction processes with high pharmacological relevance. They are in fact the single most important class of drug targets. However, for more than 70% of all pharmacologically relevant GPCRs, the therapeutic potential remains so far untapped as they are challenging targets due to their inherent instability outside of their native environment. Thus, many of the current drug screening and characterization assays are not applicable. Besides the eponymous G proteins, arrestins are the most prominent intracellular binding partners for GPCRs. Arrestins play an essential role in signal-termination: By binding to the core region of the receptor, they sterically hinder the agonist-activated GPCR to further propagate G protein-dependent signaling and they trigger receptor internalization. Lead compounds that may be further developed into drugs, are usually characterized with respect to their direct interaction with the receptor and their ability to alter signaling processes, mainly G protein signaling and desensitization by arrestins.

Materials and methods

The GPCR JSR1 was constitutively expressed in HEK293 cells. Cells were lysed and the lysate was reconstituted with 9-cis retinal. After solubilization in the detergent DDM, the protein was purified by affinity chromatography using an anti-1D4 antibody followed by size exclusion chromatography (Superdex 200). His-tagged constructs of arrestin 3 (Arr3) WT and mutants I386A (Arr3-X) and R393E (Arr3-Y) were expressed in E-coli and purified with Metal Affinity Chromatography followed by Heparin chromatography. Sample concentration and purity were assessed using SDS-PAGE, and in addition for JSR1 UV-Vis spectroscopy. Quartz crystal microbalance with dissipation monitoring (QCM-D), surface plasmon resonance (SPR) and biolayer interferometry (BLI) were employed to characterize the interaction of GPCRs with Arr3 proteins that were immobilized on functional biosensors. Ni-NTA functional lipids (1,2-dioleoyl-sn-glycero-3-[(N-(5-amino-1-carboxypentyl) iminodi acetic acid) succinyl] (nickel salt), DGS-NTA (Ni^{2+}) containing supported lipid bilayer (SLB) and supported lipid monolayer (SLM) were created on QCM-D and SPR biosensors (Fig. 2), respectively, and Arr3 proteins were immobilized through their his tag. In BLI, commercially available, NTA (Ni) functional BLI tips were used.

Results

JSR1 was chosen as a target as it is a temperature stable bi-stable photoreceptor. Activation upon photon absorption triggering cis-to trans isomerization can be followed using UV-vis spectroscopy (Fig. 1) to assess the activity of the receptor.

Interaction of GPCR with Arr3 proteins on BLI, SPR and QCM-D sensor surfaces

Interactions of purified JSR1 in DDM micelles with Arr3 and its mutants Arr3-X and Arr3-Y were monitored by different biosensor technologies including BLI, SPR and QCM-D. In order to immobilize Arr3 proteins, a SLM was deposited on the hydrophobic HPA sensor chip for the SPR assay whereas a SLB was deposited on a silicon oxide sensor for QCM-D. Immobilization of Arr3 proteins was achieved through interactions of

the his-tag of Arr3 and the nickel charged tris-nitrilotriacetic (NTA (Ni^{2+})) exposed BLI tips, SLM, and SLB.

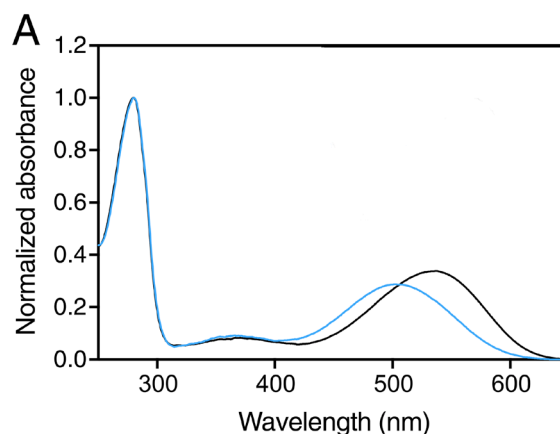


Fig. 1 In vitro activation of JSiR1. Normalized UV-vis spectra of JSiR1 (9-cis retinal, λ_{max} 505 nm). Ground state (inactive) is depicted in blue and the active state (λ_{max} 535 nm) in black.

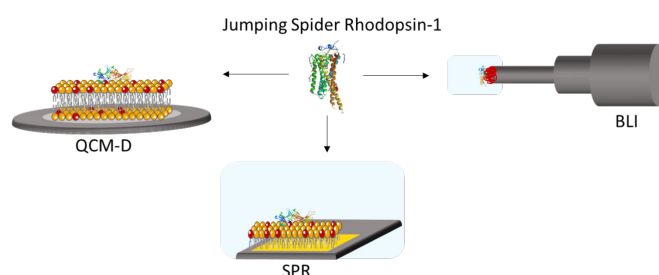


Fig. 2 Schematic representation of platforms used to measure the interaction between JSR1 and Arr3 proteins

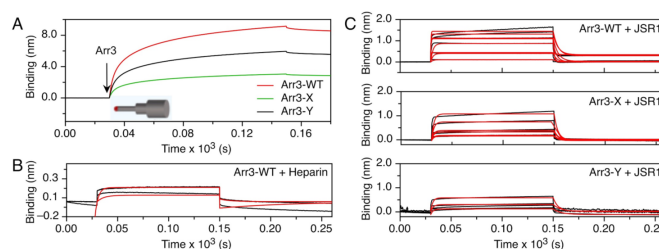


Fig. 3 Immobilization of Arr3 proteins to on the Ni^{2+} -NTA functionalized BLI tips (A), addition of (B) heparin or (C) JSR1 in DDM micelles to Arr3 proteins immobilized on the tip.

The interaction of the GPCR, e.g. the light-activated JSR1 in DDM micelles, with the surface-immobilized Arr3 and its mutants was validated using all three biosensor platforms (Fig. 2). Arr3 proteins (Arr3-WT, Arr3-X, Arr3-Y) were added to NTA (Ni^{2+}) functionalized BLI biosensors. Upon immobilization of Arr3 proteins on the BLI biosensor, the interference pattern of the reflected light changes causing a wavelength shift that was recorded as a function of time (Fig. 3A). Arr3 activity was

tested by adding 100 nM heparin yielding a dissociation constant, $K_D = 400 \pm 103$ nM (Fig. 3B). Binding of JSR1 stabilized in DDM micelles to immobilized Arr3 proteins was tested at 5 different concentrations (0.125, 0.250, 0.500, 1, and 4.3 μ M) (Fig. 3C). The highest K_D was observed for Arr3-X (389 \pm 59 nM) and the lowest K_D for Arr3-Y (112 \pm 12 nM). Association and dissociation kinetic constants show that JSR1 binds relatively fast to Arr3-WT or its mutants.

The SLM formation process on an HPA sensor was monitored by SPR (Fig. 4A). Real-time changes in the refractive index at the sensor surface were recorded as resonance units (RU), being proportional to the amount of the material deposited on the sensor. After SLM formation, the typical SPR response was obtained within the range of 1500-2500 RU as is expected for a good lipid monolayer formation on the sensor chip surface. When Arr3 proteins were immobilized to SLM, the results indicated that Arr3-WT led to a final response of 306 ± 52 RU whereas the final responses from Arr3-X and Arr3-Y were similar (about 1000 RU) and higher than the Arr3-WT response (Fig. 4B). For more quantitative equilibrium and kinetic binding analyses, a number of JSR1 concentrations (16.5, 31.25, 62.5, 125, 250, 500, 1000 nM) were injected into all flow channels followed by 0.2 M NaOH to remove JSR1 between concentrations (Fig. 4C). After the reference subtraction, the sensorgrams were fitted using a 1:1 binding model to obtain the kinetic constants (Fig. 4C) or the response vs concentration was plotted and fitted to the Langmuir isotherm (Fig. 4B). The kinetic and equilibrium dissociation constants derived from SPR measurements indicate that binding of JSR1 to Arr3-X and Arr3-Y was similar, but different to the binding to Arr3-WT.

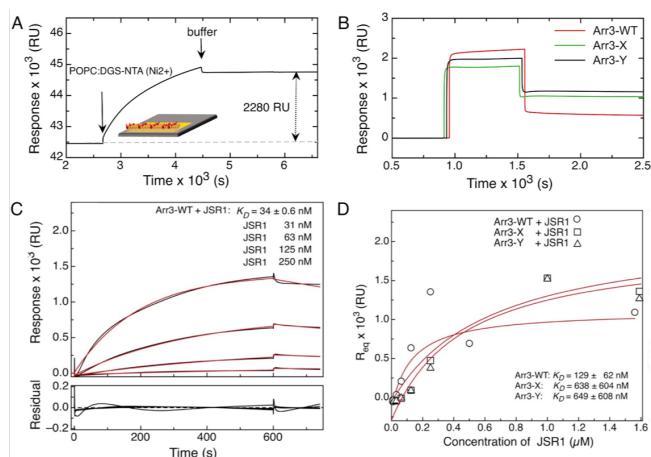


Fig. 4 (A) Changes in the SPR response upon formation of SLM on the HPA sensor chip. (B) Immobilization of Arr3 proteins to SLMs, and (C) addition of JSR1 in DDM micelles to SLMs corrected for the response in the reference channel together with the kinetic fits (red solid lines) (D). JSR1 binding response was also plotted depending on the JSR1 concentration, and K_D s were obtained by fitting to Langmuir isotherm.

A supported lipid bilayer (SLB) was deposited on a silicon oxide sensor for QCM-D (Fig. 5A). The decrease in frequency reflects an increase in adsorbed mass. For SL formation, the final frequency corresponded to ΔF values of -24.04 ± 2.17 Hz which agrees well with literature values obtained for SLB formation. Upon injection of Arr3 proteins, a decrease in frequency was observed (Fig. 5B). Injection of Arr3-WT led to a frequency shift of -29.87 ± 6.10 Hz, indicative of an immobilization of the Arr3-WT protein to the SLB. Similarly, ΔF was obtained when Arr3-X and Arr3-Y were added to a corresponding platform. When heparin was injected to SLBs with immobilized Arr3 proteins, a decrease in ΔF was observed (Fig. 5C). Although heparin specifically bound to all three Arr3 proteins, the surface density of heparin on the SLB platforms containing Arr3-X and Arr3-Y was higher than on SLB functionalized with Arr3-WT. The interaction of light-activated JSR1 in DDM micelles with different Arr3 proteins immobilized on SLBs is shown in figure 5D. The binding of JSR1 to Arr3 was analyzed

by fitting to the data to a 1:1 binding model. The results from JSR1-Arr3 complex formation indicated that JSR1 has the strongest affinity for Arr3-Y.

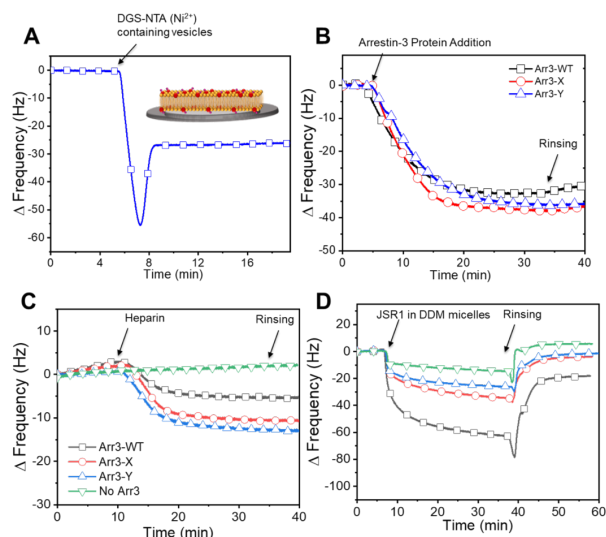


Fig. 5 Changes in frequency was recorded upon formation of SLB on silicon dioxide (A), immobilization of Arr3 proteins to SLBs (B), addition of heparin on SLBs with and without Arr3 proteins (C), and addition of JSR1 in DDM micelles to SLBs with and without Arr3 (D).

Summary

We have developed biosensor-based assays that directly and specifically report GPCR binding to arrestin. Different Arr3 proteins (wild type, mutant Arr3 I386A and R393E) could be stably immobilized on sensors in a defined orientation. The Arr3 proteins were immobilized via his-tags to NTA (Ni^{2+}) containing sensor coatings. Using BLI, SPR, and QCM-D, we were able to follow the interactions between Arr3 proteins and a representative GPCR, JSR1, in a label-free manner in real-time. The interactions were quantified as binding affinity, association and dissociation rates. With a K_D of 112 nM from BLI, 96.7 nM from SPR and 914 nM from QCM-D measurements, the Arr3-R393E mutant showed the strongest binding to JSR1. Taken together, this work introduces direct, label-free biosensor-based screening approaches that can be easily adapted for testing interactions of GPCRs with any effector protein.

References

- [1] S. Yorulmaz Avsar, M. Kyropoulou, S. Di Leone, C.-A. Schoenenberger, W. P. Meier, C. G. Palivan, *Biomolecules turn self-assembling amphiphilic block co-polymer platforms into biomimetic interfaces*, *Frontiers in Chemistry*, (2019)
- [2] M. Garni, R. Wehr, S. Yorulmaz Avsar, C. John, C. G. Palivan, W. Meier, *Polymer membranes as templates for bio-applications ranging from artificial cells to active surfaces*, *European Polymer Journal*, 2018.
- [3] R. S. Haider et al., *Arrestin-1 engineering facilitates complex stabilization with native rhodopsin*, *Scientific Reports* **9(439)**, (2019)
- [4] N. Varma, E. Mutt, J. Mühle, V. Panneels, A. Terakita, X. Deupi, P. Nogly, G.F.X. Schertler, E. Lesca, *Crystal structure of jumping spider rhodopsin-1 as a light sensitive GPCR*, *PNAS* **116(29)**, 14547–14556 (2019)

Nanophotonics for quantum sensing technology

Project A13.15: NQsense (University of Basel Dept. of Physics, PSI, Qnami Basel)

Project Leader: P. Maletinsky

Collaborators: F. Favaro de Oliveira, M. Munsch, G. Seniutinas, and C. David

Introduction

Magnetic field imaging at the nanoscale is of paramount importance for researchers and industries with applications ranging from basic science to biology. Developing novel magnetic and electronic nano-devices as well as investigating proteins or other biomolecules requires sensitivity and resolution that current classical sensing technologies fail to address.

Quantum sensing based on spin defects in diamond offers a disruptive approach to these challenges. The nitrogen-vacancy (NV) center in diamond presents excellent properties for such nanoscale magnetic field sensing. This optically addressable spin has already been successfully used in several breakthrough applications [1].

Scanning probe microscopy (SPM) employing NV-centers in diamond for magnetic imaging has been originally developed and implemented by Prof. P. Maletinsky [2]. The successful research and vast application areas of this technology have triggered the creation of QNAMI, a spin-off company that is bringing diamond based quantum sensing technologies to the market by offering, e.g. a full, turn-key solution for magnetic nano-imaging using spin defects in diamond.

During the Nano-Argovia project NQsense, activities were focused towards improving performance of diamond sensors by optimizing geometry of the scanning probes and by establishing a scalable route of device fabrication via collaboration between the partners from the public and private sectors in the region of Northwestern Switzerland. The main project outcomes are 1) the improved sensor performance as a result of numerical simulations and concomitant design optimization, as well as 2) to establish a route to scaling up the production by using the industry-standard nano-fabrication facilities at the PSI.

Theoretical investigation of the photon collection efficiency for improved sensitivity

The single-spin quantum sensors pursued within the NQsense project consist of an all-diamond cantilever with a sub-micrometer sharp tip containing a single NV center spin at its apex. The signal from the embedded NV center sensor is read out optically using spin-dependent fluorescence, where the sensitivity to magnetic fields is inversely proportional to the square-root of the number of collected photons [1]. However, due to high refractive index of diamond, only a very small fraction (a few percent) of photons emitted by the embedded NV center manage to reach the collection optics. Thus, by increasing the number of collected photons, one significantly increase the sensitivity of the sensor.

The sharp tip containing the NV center not only acts as a high resolution scanning probe, but also serves as a wave-guide for the emitted photons. Hence, optimizing the tip geometry to guide more photons towards the detection optics leads automatically to devices with improved sensitivity. The design was first numerically optimized employing Finite Difference Time Domain (FDTD) simulations.

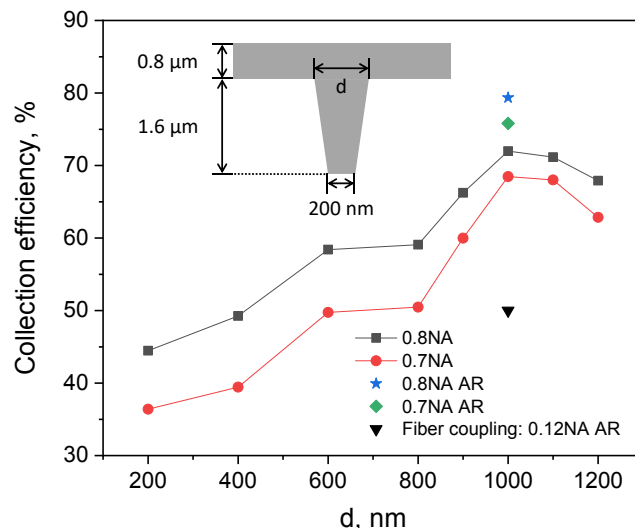


Fig. 1 FDTD simulation results of wave-guiding properties of nanoscale quantum sensors. The figure presents the photon collection efficiency vs different top diameters (d) of the wave-guide for collection optics with different NA values.

Tapering of the cylindrical pillar (making it a cone-like structure, see inset of Fig. 1) was investigated to shape the far field emission profile to better match the numerical aperture (NA) of the detection optics. Simulation results are summarized in figure 1 where dependence of the photon collection efficiency on the top diameter of the wave-guiding structure is presented. The graph presents results for two NA values 0.7 and 0.8, which are typical for sensor implementation.

As shown in figure 1, the collection efficiency increases by tapering the structure and reaches a maximum of $\sim 70\%$ (into NA=0.7) at a top pillar diameter of 1000 nm. To further increase the efficiency, losses occurring due to internal reflection in the diamond are mitigated by introducing a ~ 110 nm thin SiO_2 anti-reflection (AR) coating on top of the cantilever to the simulations. This further increased the predicted collection efficiency to around 76% for NA = 0.7 – a two times enhancement compared to the cylindrical pillar, that was the established geometry before starting the project. Moreover, a compact readout configuration using pigtail fiber instead of free space optics was numerically investigated. The simulation results indicate that collection efficiencies of $\sim 50\%$ could be achieved in an optical fiber having NA of 0.12 (Fig. 1).

Nano-fabrication of quantum sensors with enhanced properties

The numerically optimized geometries were experimentally implemented in the next generation of prototype sensors. A careful and extensive optimization of diamond dry-etching processes allowed to achieve a half-taper wall angle of 6° in prototype devices, which agrees well with the targeted value from simulations (5° to 10°).

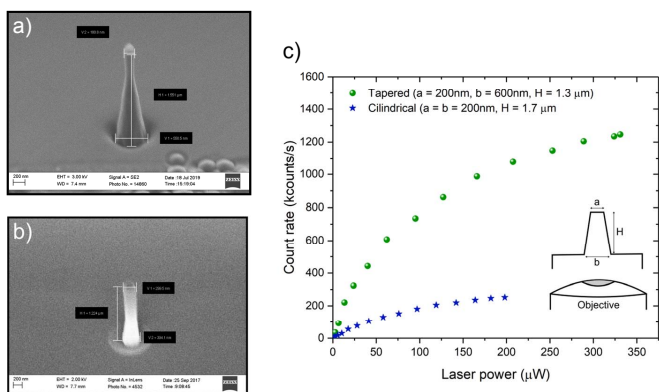


Fig. 2 a) and b): SEM images of the wave-guide shapes from the new, tapered diameter sensor and the previous, cylindrical, sensor geometries, respectively. c) Total photon count rate of wave-guides containing single NV centers. Blue and green correspond to the cylindrical and tapered wave-guide geometries.

Figure 2a and b present scanning electron microscopy (SEM) images of the new generation (tapered) and the previous generation (cylindrical) wave-guides, respectively. The devices were then benchmarked against each other using fluorescence confocal microscopy. As seen in figure 2c, the total number of photons emitted by individual NV centers embedded into wave-guides with the two described geometries is increased by a factor of six using the tapered walls, with a corresponding improvement in the device sensitivity to magnetic fields.

Scaling up the production

The last phase of the project was dedicated to establishing a scalable route of device production. Fabrication flows developed during the prototyping phase at the University of Basel, were successfully transferred to the industry-standard clean-room at the PSI. The achieved production throughput and yield satisfies demand projected by Qnami for the upcoming years. As a figure of merit, the production yield increased from < 25% to more than 75% by transferring the fabrication process from the University of Basel to the PSI. This is mainly attributed to a higher clean room class and the use of industry-standard machinery that reduce significantly the failure rate due to i.e. human inaccuracy.

An optical micrograph of a fragment of a large area chip fabricated at the PSI containing hundreds of quantum sensors is shown in figure 3a. The developed processes at the PSI allow for large area patterning with excellent uniformity. As seen in figure 3b and c, the optimized dry etching steps yield smooth cantilever surfaces while still preserving optimal tapering angle of the wave-guiding structure. The new generation of devices are now the main magnetic sensor line in QNAMI's product portfolio.

Summary

The results of the NQsense project have led to significant improvements in sensor performance for magnetic field imaging at the nano-scale and set up a path for scalable production. This represents not only advances in the technology capabilities, but also positions Qnami as a leader in the commercialization of highly sensitive quantum sensors made of diamond. The new generation of sensors commercialized by Qnami is already in use in several countries world-wide, which represents significant traction for the young start-up and provides the needed feedback to further establish and advance the technology. With this, project NQsense also contributed to the creation of two new positions that are now part of the growing team of the company Qnami.

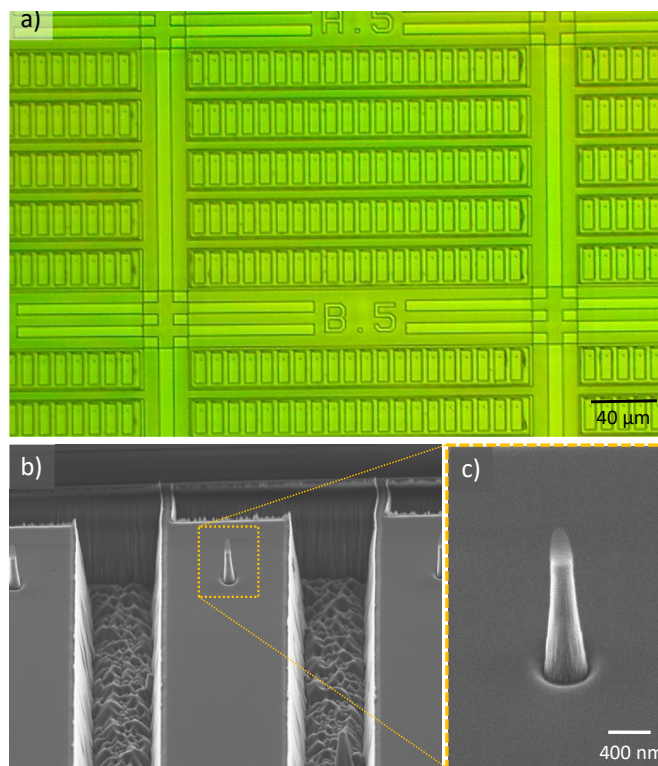


Fig. 3 a) optical micrograph capturing a few cantilever sectors produced at the PSI. b) and c) 45-degree-tilt view SEM images of etched nano-photonic structures and close-up view of the tapered pillar with the top diameter of 200 nm, respectively.

References

- [1] L. Rondin, J.-P. Tetienne, T. Hingant, J.-F. Roch, P. Maletinsky, V. Jacques, *Magnetometry with nitrogen-vacancy defects in diamond*, Rep. Prog. Phys. **77** 056503 (2014)
- [2] P. Maletinsky, S. Hong, M. S. Grinolds, B. Hausmann, M. D. Lukin, R. L. Walsworth, M. Loncar, A. Yacoby, *A robust scanning diamond sensor for nanoscale imaging with single nitrogen-vacancy centres*, Nat. Nanotechnol. **7**, 320–324 (2012)

A detector for pesticides in drinking water

Project A14.04: DeePest (FHNW Muttenz, FHNW Windisch, Mems AG Birnenstorf)

Project Leader: J. Pascal

Collaborators: D.-V. Nguyen, M. Olesinska, P. Shahgaldian, N. Karlen, E. Weingartner, and D. Matter

Introduction

The foremost goal of the DeePest project (a Detector for Pesticides in Drinking Water) is to develop a novel pesticide monitoring system based on the remarkable molecular recognition capabilities of engineered nanostructured polymers associated to a bimodal electronic detector. The system shall first concentrate the pesticide by flowing water through the polymer and then detect it with a bimodal detector.

Nanostructured polymers: glyphosate-binding gels

DeePest detector relies on the high adsorption properties of a polymeric based pesticide concentrator cartridge. We are developing a polymeric system capable of molecular recognition [1], with targets ranging from small molecules and ions to large molecular assemblies.

Currently, several types of hydrogels have been synthesised in order to optimise their structural and mechanical properties such as porosity, swelling, durability, strength as well as the pesticide-unique recognition, adsorption and triggered release capabilities (Fig. 1). Hydrogels with diverse monomer composition and different density of cross-links were formulated through a free radical polymerisation with azobisisobutyronitrile (AIBN) as a radical initiator. We used three types of monomers i.e. maleic anhydride (MA), N-Isopropylacrylamide (NIPAM), acrylamide (AAM) and a cross-linker N,N'-methylene-bis-acrylamide (MBA) to first form unfunctionalised generation of hydrogels H1-H8 (where H4 is a physically cross-linked gel). On account of different polymeric backbone, these hydrogels display distinct morphology, water content and swelling behaviour. Hydrogels H1 and H2 that were synthesised with higher density of a cross-linker are brittle and have microporous structure (Table 1 and Fig. 2 right). Hydrogel H2 has also high water absorptivity. The swelling degree Q , measured as the weight ration of absorbed water to dried hydrogel, for H2 at room temperature is 14 g/g. Hydrogels with lower cross-linker density have more homogeneous structure (Table 1 and Fig. 2 left), and the swelling degree for H3 at room temperature is only 3.5 g/g. Further test on morphology and mechanical properties of hydrogels will be conducted.

Described above, polymeric systems after appropriate modification will be used to adsorb glyphosate from drinking water. First steps in synthesis of functionalised hydrogels MA1, MA2 and MA3 have been done (Fig. 1). Maleic anhydride monomers bearing recognition units for glyphosate molecules such as amine or urea moiety are currently in preparation. Based on controlled pH change, the adsorption or desorption of pesticide will be achieved.

Table 1 Hydrogels composition. Molar ratio of monomers and a cross-linker used in free radical synthesis (water/ethanol (1:1), AIBN)

	Reaction feed (Molar ratio)							
	H1	H2	H3	H4	H5	H6	H7	H8
MA	10	10	10	2.5	12.5	2.5	-	10
NIPAM	10	10	10	17.5	7.5	-	-	10
AAM	-	-	-	-	-	17.5	20	-
MBA	2	7	1	-	1	1	1	0.2

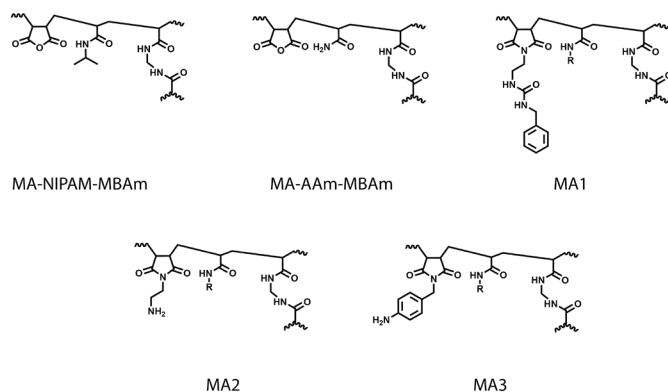


Fig. 1 Schematic representation of hydrogels structure, where $R = -NH_2$ or $-NMe_2$

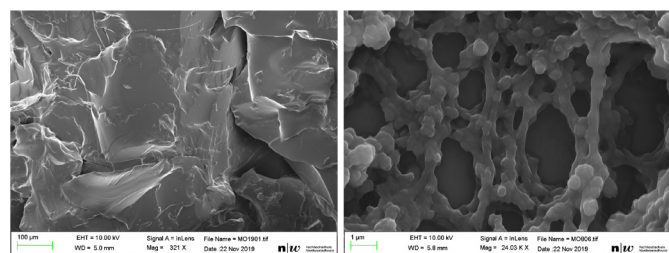


Fig. 2 SEM image of 60°C oven dried hydrogel H3 (left) and H2 (right)

Miniaturized NMR-detector

The first detection modality is based on an NMR signal acquisition. We developed an NMR probe (Fig. 3A) capable of working within a low magnetic field generated by palm size permanent magnets (typically 0.5 to 1.5 T). The circuitry (NMR transceiver TxRx) necessary to generate the proton excitation and to perform the resonance signal acquisition is under development. The NMR signal can be acquired with a validated in-house mixer ASIC (Receiver electronics Rx). The excitation signal (Excitation Tx) has been so far applied with a commercial benchtop NMR device.

Beside the development of an NMR probe including miniaturized coil, matching capacitor and transceiver electronics that has been described above, we have characterized different palm size permanent magnets, mainly Halbach structures and ring shape magnets as well as electromagnets. Those magnets shall reach sufficient homogeneity for NMR spectroscopy and for the detection with a 0.5 T magnet of atrazine and glyphosate within a solvent such as acetonitrile. We obtained a field strength of maximal 0.9 T and homogeneity of 1% over 1 mm³. This lack of homogeneity leads us to the integration of shim coils in order to reach a field homogeneity sufficient for the pesticide detection with an NMR experiment. Depending on the NMR method (relaxometry based on spin-echo sequences or spectroscopy), we shall reach a homogeneity of 10 ppm to max 1000 ppm.

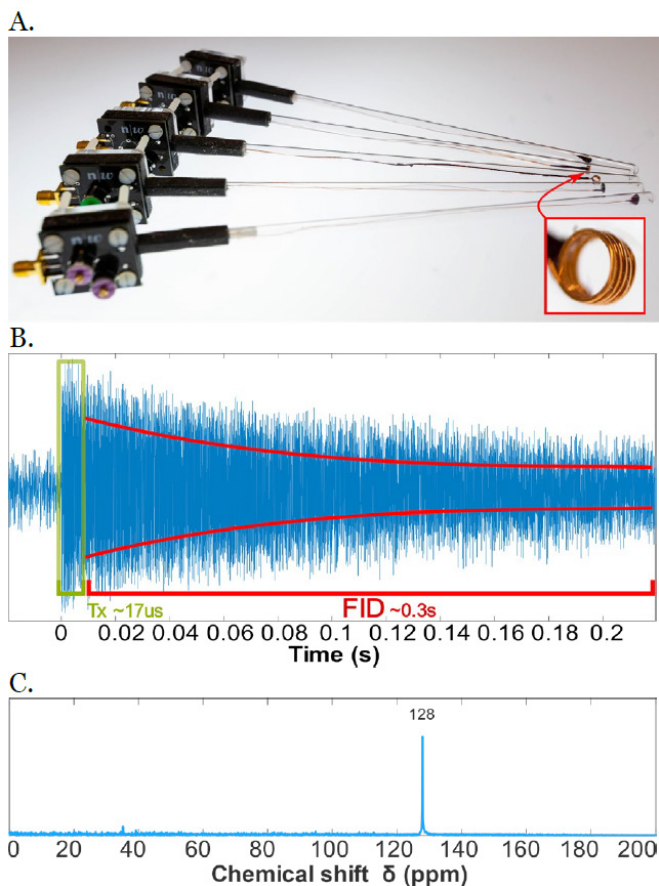


Fig. 3 DeePest NMR detector A) Miniaturized coils are inserted within a 5 mm NMR-tube with matching capacitors at the tube output. B) Free Induction Decay FID signal obtained in a 1.5 T permanent magnet. C) ^1H NMR spectrum of water obtained with DeePest probe.

Fluorescence Detection of PAHs and Pesticides

The third module of the continuous monitoring system is a development to detect PAHs and pesticides by fluorescence. A literature research showed the similarity of the fluorescence properties of various PAHs and pesticides: Excitation light needs a wavelength in the range of around 220 to 280 nm while fluorescence emission light wavelength is around 330 to 420 nm [2]. A first measurement setup with a cuvette and a mercury lamp was established for the proof-of-concept (Fig. 4).

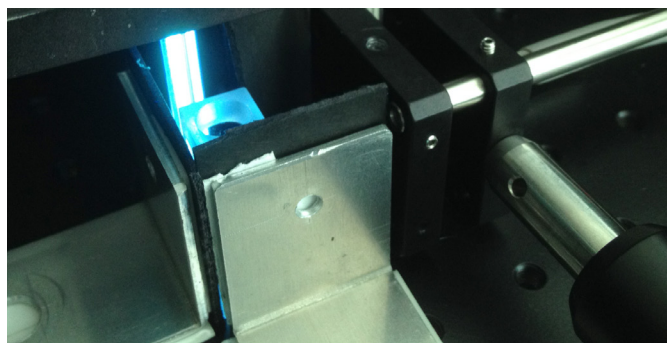


Fig. 4 Setup for proof-of-concept of fluorescence detection of PAHs and pesticides

The above mentioned investigations allowed a detailed overview concerning the requirements for an improved setup (numbered regions see Fig. 5):

- 1: No absorption of eluent/PAHs/pesticides desired
- 2: No absorption or fluorescence of eluent allowed
- 3, 4: High Stokes Shift (3) leads to few overlap (4)

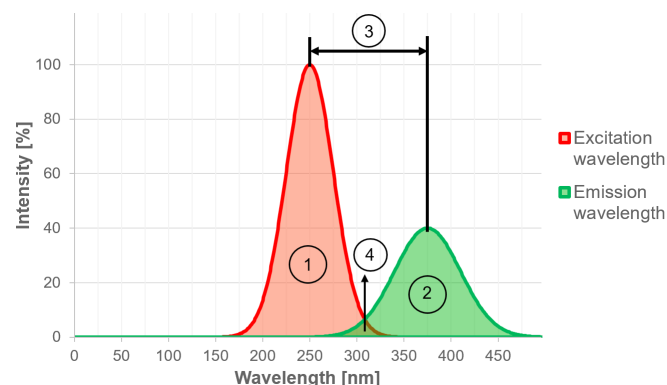


Fig. 5 Requirements for an improved fluorescence setup

The improved setup will use a continuous flow cell for in-situ measurements as well as optical filters to prevent cross-sensitivity to direct excitation light. Furthermore, the design is planned to be optimised for maximum light emitting efficiency by using a spiralled or coiled glass tubing with the liquid inside. The excitation light will be guided through the tube walls by total reflexion while the fluorescence light will be detected from above by a photomultiplier.

Conclusion

The combination of a concentrator cartridge based on nano-structured polymers with a bimodal electronic detector opens the way to the design of a low cost and portable device, capable of detecting pesticides in drinking water.

References

- [1] M. Moradi, L. G. Tulli, J. Nowakowski, M. Baljovic, T. A. Jung, P. Shahgaldian, *Two-Dimensional Calix [4] arene-based Metal–Organic Coordination Networks of Tunable Crystallinity*, *Angew. Chem. Int. Ed.*, **56(46)**, 14395- 99 (2017)
- [2] N. Ferretto, M. Tedetti, C. Guigue, S. Mounier, R. Redon, M. Goutx, *Identification and quantification of known polycyclic aromatic hydrocarbons and pesticides in complex mixtures using fluorescence excitation–emission matrices and parallel factor analysis*, *Chemosphere*, **107**, 347 (2014)

Origami heart model based on nano-patterned paper scaffold for tissue engineering

Project A14.07: KOKORO (FHNW Muttenz, University of Basel DBM, Omya International AG Oftringen)

Project Leader: M. R. Gullo

Collaborators: J. Köser, A. Banfi, A. Marsano, and J. Schoelkopf

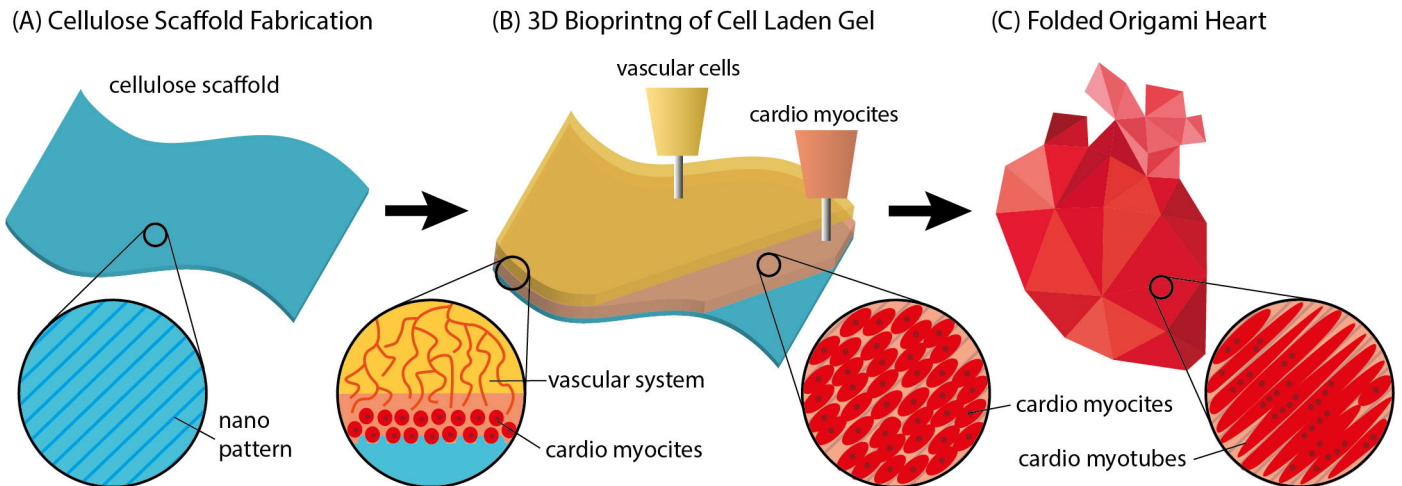


Fig. 1 Schematic representation of project goals: (A) A cellulose scaffold with the desired stiffness and nano-patterns. (B) Hydrogels containing myocardial cells and vascularizing cells will be 3D bioprinted onto the scaffold. (C) The scaffold sheets containing the differentiated/aligned myotubes will be folded into a heart shape by origami techniques.

Myocardial infarction is the leading cause of death (34% in 2015) and the third-leading cause of hospitalization (13% in 2015) in Switzerland. Current research efforts focus on in-vitro heart models for understanding the mechanistic function of healthy and diseased hearts, and test the efficacy of potential therapeutics. In particular, 3D contractile cardiac chambers are required to assess the effect on ventricle pressure, contractile forces, electro-physiological aspects and volume dynamics. Current efforts in 3D bioprinting such chambers, resulted in fragile structures, rather suited for single prototypes [1 - 3]. However, for a representative assay, a much larger number of models is necessary. The current project aims to address this challenge by developing nano-structured cellulose scaffolds for vascularized myocardial tissue growth. By origami methods, the planar tissue will then be folded into an anatomic 3D heart ventricle shape. Figure 1 shows a schematic representation of the project goals.

Nano-Patterned Cellulose Scaffold Fabrication

Different micro cellulose slurries were prepared in order to obtain scaffolds with the desired elasticity and fiber orientation, promoting myocardial cell differentiation and alignment. To simplify the process, the optimal dimensions for cell alignment were first assessed and validated on patterned gelatin. For this purpose, line patterns with various line width, heights and spacings were transferred into gelatin beds on top of the cellulose scaffolds by molding techniques. Fibroblast model cells were seeded and their alignment was evaluated. As a result, cellulose fibers in the range of 25 μm were chosen to fabricate the scaffolds. The biocompatibility of the cellulose sheets was validated through cytotoxicity assays. This implicates that paper samples with oriented cellulose fibers as such, could induce cell alignment. Different origami patterns for folding a heart ventricle were evaluated. A slightly modified Miura pattern was selected due to its unilateral deformability (Fig. 2A). In order to enable the folding of a miniaturized origami pattern, we developed an imprinting method to manufacture pre-folded cellulose scaffolds (Fig. 2B).

3D Bioprinting and Hydrogel Development

Different blends of cell-laden hydrogels have been assessed for patterning cells onto the cellulose scaffolds. The cell-laden hydrogel showed high biocompatibility, printability and stability during cell culture. The printed structures kept stable for over 6 days in cell culture and the cardiomyocytes successfully developed into pacing cells. Printed cells showed excellent long-term viability, comparable to the control cell cultures in dishes and cells embedded in casted hydrogels.

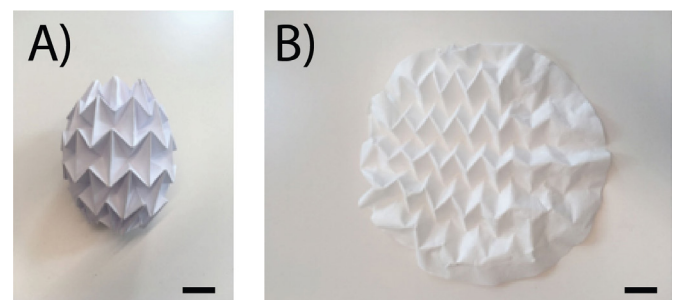


Fig. 2 A) Prototype origami heart ventricle model; B) Preformed cellulose scaffold. (all scale bars are 1cm).

Vascular Cells 3D Culture and Differentiation

We investigated the combination of endothelial cells (HUVEC) with bona fide pericyte-like cells (adipose-derived stromal cells, ASC), in order to establish the cell type composition required to generate vascular structures. Only this cell combination gave rise to organized multi-cellular structures with a clear vessel morphology, indicating that the presence of mural cells is required for vascular structure establishment. The embedding of cells in a fibrin hydrogel ensured a true 3D distribution of the cells with the consequent formation of three-dimensional vascular networks. Hydrogel composition (fibrinogen and crosslinking enzyme concentrations) significantly regulates the process of endothelial cell assembly. Cell densities between 1 and $10 \times 10^6/\text{ml}$ were tested. After two

weeks of culture, the number of vessels clearly increased with cell density. To determine whether the generated vascular structures displayed features of physiological blood vessels, gels were stained for laminin and podocalyxin, which mark specifically the basal and luminal compartments of functionally differentiated vascular cell structures in-vivo, respectively. The network composed of vascular structures showed a clear apicobasal polarization of the endothelium, with laminin on the basal side, podocalyxin on the luminal side and physiological lumens (Fig. 3). The same experiments were performed on cellulose scaffolds which were covered with a layer of gelatin similar to the hydrogel system described before. Preliminary experiments showed that the presence of cellulose and gelatin did not significantly affect the efficiency of vascular network formation, showing the feasibility of the overall construct.

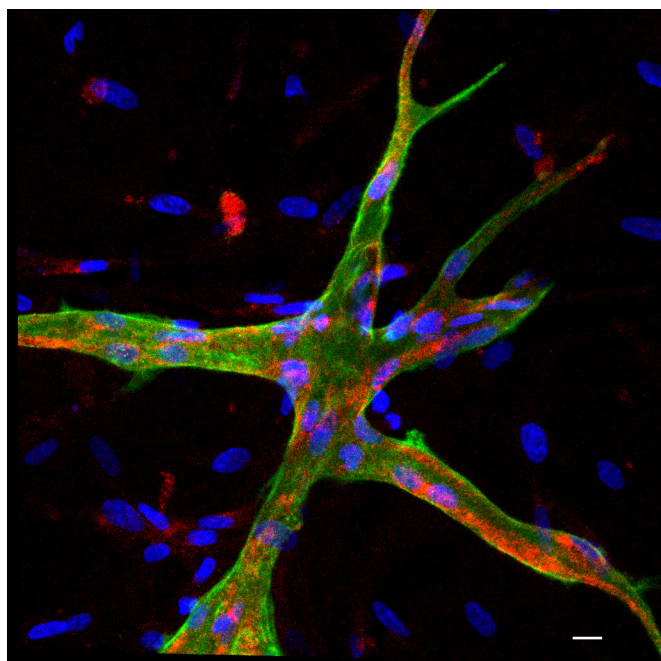


Fig. 3 Immunostaining of vascular structures showing physiological apicobasal polarization of endothelium (marked by podocalyxin (red) and laminin (green), respectively) and a hollow lumen (scale bar is 30 μm).

Myocardial Cells Differentiation and Contraction

Cardiomyocytes have been cultured on different gelatin concentrations to assess the effect of substrate stiffness on the cell maturation. Cells cultured on substrates with a stiffness of 11 kPa promoted the best cardiomyocyte functionality in terms of lower excitation threshold (ET) and increased area of deformation. Cardiomyocytes have been cultured on tissue culture plastic and gelatin with or without electrical stimulation. The tissues cultured on gelatin with electrical stimulation showed a superior functionality in terms of lower ET. The cardiomyocyte alignment on fibronectin-coated elastomer line patterns with different dimensions was evaluated after 5 days in culture. As predicted by the preliminary alignment experiments, 25 μm spaced line patterns showed the most promising results. Therefore, cardiomyocytes were cultured on gelatin coated paper-scaffolds with and without 25 μm line patterns for 6 days, again with and without electrical stimulation. The assay showed that only the patterned paper substrates promoted sufficient cell maturation to enable the tissue sheet contraction upon electrical pacing. In addition, cell alignment and contractility have been investigated in 3D fibrin gel based constructs. The excitation threshold results showed, that there is a trend of improving the cardiac functionality by applying electrical stimulation. Preliminary analysis of the deformation map (Fig. 4) demonstrate that the presence of line patterns on one side of the 3D construct supported a uniform contraction throughout the entire tissue.

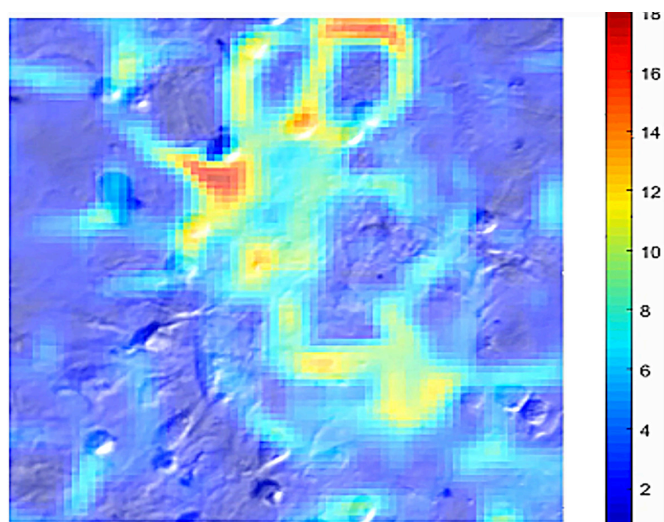


Fig. 4 Deformation map of the cardiac layer in finite strain equivalent %. 250 x 250 μm image.

References

- [1] K. H. Benam, et al. *Engineered in vitro disease models*, *Annu Rev. Pathol.* **10**, 195 (2015)
- [2] E. Tzatzalos, O. J. Abilez, P. Shukla, J. C. Wu, *Engineered heart tissues and induced pluripotent stem cells*, *Adv. Drug Deliv. Rev.* **96**, 234 (2016)
- [3] L. A. MacQueen, et al. *A tissue-engineered scale model of the heart ventricle*, *Nat. Biomed. Eng.* **2**, 930 (2018)
- [4] K. Ng, et al. *Paper-based cell culture platform and its emerging biomedical applications*, *Materials today* **20**, 32 (2016)
- [5] S-H. Kim, et al. *Hydrogel based paper scaffold system for origami based tissue engineering*, *PNAS* **112**, 15426 (2015)
- [6] H-J. Park, S. J. Yu, K. Yang, Y. Jin, A. N. Cho, J. Kim, B. Lee, H. S. Yang, S. G. Im, S. W. Cho, *Paper-based bioactive scaffolds for stem cell-mediated bone tissue engineering*, *Biomaterials* **35**, 9811 (2014)
- [7] B. Mosadegh, B. E. Dabiri, M. R. Lockett, R. Derda, P. Campbell, K. K. Parker, G. M. Whitesides, *Three-dimensional paper-based model for cardiac ischemia*, *Adv. Health. Mater.* **7**, 1036 (2014)

Laser ablation of polymers for advanced origination of micro-optical elements

Project A14.08: LASTRUPOL (FHNW Windisch, PSI, Gemalto AG Aarau)

Project Leader: P. M. Kristiansen and J. Werder

Collaborators: C. Sailer, L. Davoine, A. Egli, M. Guilherme, P. Vollenweider, R. Holtz, H. Schiff, K. Vogelsang, M. Marhöfer, M. Grob, N. Petelinsek, and M. Binkowska

Introduction

The creation of complex 3D topographies by different origination pathways is receiving increasing attention from both the academic community as well as a wide range of industry sectors for applications in microfluidics, micro-optics and photonics, security, advanced design elements and functional surfaces in general. For laser micromachining of polymers, there is a clear trend towards ultrashort pulse durations (10's of ps to 100's of fs), which reduce the thermal impact and lead to higher shape accuracy. UV lasers generally show better ablation characteristics with smaller heat-affected zones and virtually no recast layers as observed for IR-Lasers [1].

The aim of this project is to develop an advanced manufacturing technology enabling origination of tailored three-dimensional surface topographies with sub-micron feature resolution and very low surface roughness, suitable for use as optical elements and/or security features. For this purpose, we combined high precision laser-based subtractive manufacturing of polymeric substrates with strategies for contactless polishing of structured polymer surfaces to yield optical quality roughness levels. This required extension of the contactless polishing procedure [2], previously applied to microlens arrays in the Nanoargovia project SurfFlow, to smoothening of topographies with higher initial surface roughness.

Laser micro machining on polymers

The interactions of a laser beam with the polymer are very complex, since different phenomena such as self-focusing, absorption mechanism and melting effects occur simultaneously and interact with each other. Due to this inherent complexity, it was necessary to investigate and optimize the laser ablation of structures in depth, initially starting with single pulses, followed by 1D (lines), 2D (surfaces) and finally 3D topographies.

The thermoplastic material used is amorphous and thus transparent in its unprocessed state. Due to the high level of transmission at the wavelength used (355 nm), only a small fraction is absorbed by the material within the top layer, thus hampering the coupling into the medium at the low laser energy. Therefore, samples were coated with graphite and the effect of single laser pulses on the material was compared. If the degree of absorption is increased by coating of the surface, an ablation process can be triggered even if the pulse energy remains the same. However, the coating was detached after single pulse, which is not suitable for writing 2D or 3D structures.

Laser micromachining of 3D topographies into high performance polymers (PEEK, PI)

Due to the encountered limitations for PMMA, i.e. melting effects and high surface roughness after laser ablation, the focus of the project was switched to the laser processing of poly(ether ether ketone) (PEEK) and polyimide (PI) in order to use them for embossing of PMMA. Both of these materials feature strong absorption at the wavelength of 355 nm and are thermally more resistant than engineering thermoplastics. Effects as seen for PMMA (Fig. 2) are no longer visible on PI at similar laser energies. The achieved roughness is currently at $R_a = 0.25 \mu\text{m}$, which corresponds to a very good surface roughness, but is still not sufficient for micro-optical structures.

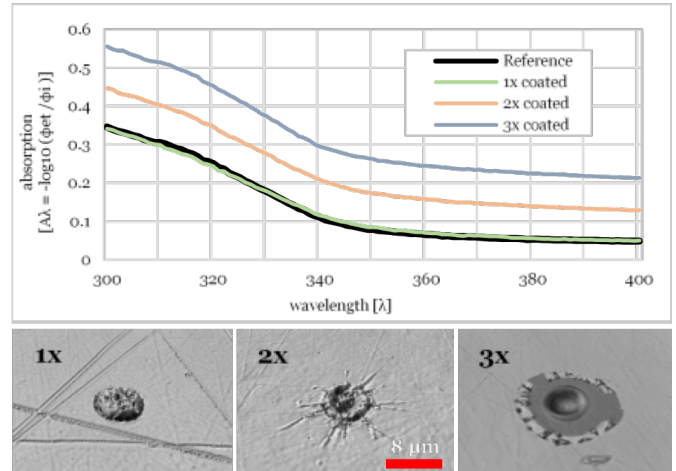


Fig. 1 If the absorption coefficient is increased by coating of the surface, an ablation process can be triggered at constant pulse energy.

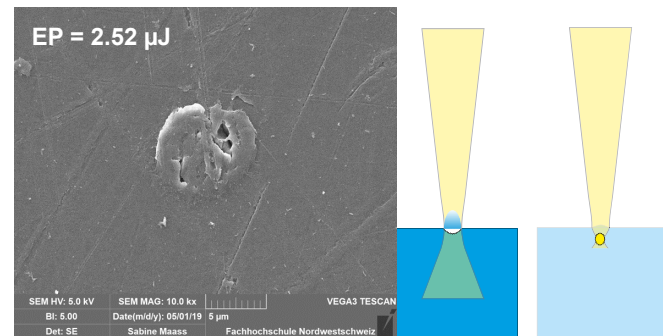


Fig. 2 SEM analysis of a single pulse on a single coated substrate. It is clearly visible that the material in the laser irradiated area has not been removed. The observed deformation of the surface most likely results from the Kerr effect (visualized on the right side). The latter causes the absorption of the laser radiation to take place below the surface (within the material) and a swelling of the observed area can be detected [3].

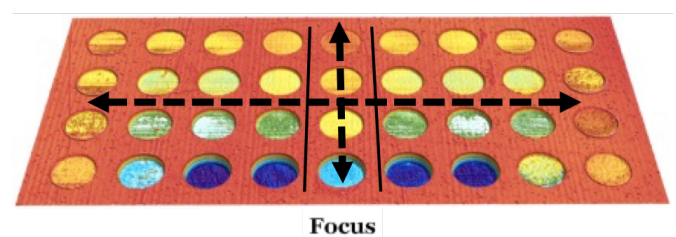


Fig. 3 Investigation of the laser ablation on PI and PEEK foils. Here: On-off-focus analysis for $\Theta_0 = 0.684 \text{ J/cm}^2$ on polyimide. If the substrate surface is not perfectly in the focus of the laser (on-off-focus), the material is degraded.

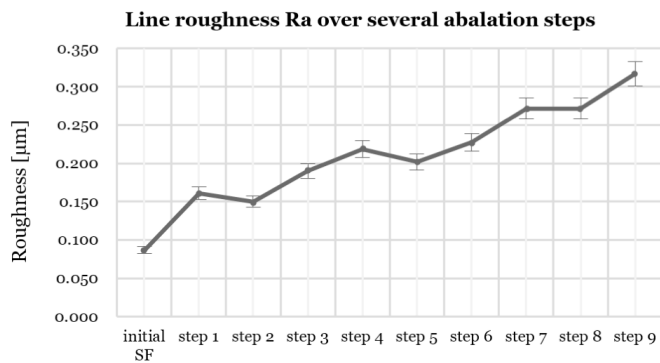


Fig. 4 Changes in surface roughness of PI over nine successive ablation steps. The roughness is transferred to the lower layer and therefore steadily increases.

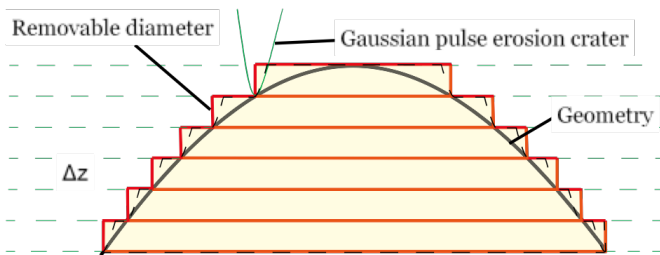


Fig. 5 Slicing of structures: Contour resolution can be controlled via the layer height Δz . Errors in layer thickness lead to visible contour errors at the vertex. The resolution is improved by simply increasing the number of layers: More layers \rightarrow thinner layers \rightarrow less energy needed.

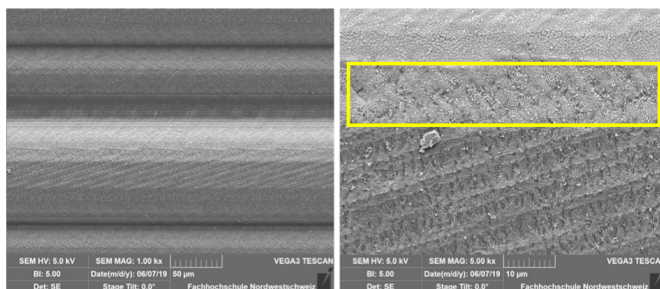


Fig. 6 SEM analysis of laser ablated structures on PI: Wave-like patterns are present in the boards area. These patterns are caused by the polarization of the laser beam. Intensity and fluence of the Gaussian beam are highest in the center [3]. In general, the structures do not appear to be 100 % continuous due to the layered structure.

Surface smoothing

The TASTE process was originally established for thin layers of PMMA resists [4]. For smoothing out surface roughness, surface confined exposure can be done with a range of processes. Among all processes performed, UV-C (172 nm) is clearly the best pre-treatment. The glass transition temperature T_g is thereby lowered within a top layer extending approximately 200 nm into the material. Due to the shift from engineering plastics to high performance polymers (PI and PEEK), the process chain was adapted, i.e. PMMA was embossed with the laser structured PI or PEEK foil and subsequently subjected to a smoothing process. PMMA samples were irradiated with UV-C for up to 5 minutes and then smoothed at 10°C below T_g for 15 minutes. The micro roughness can thereby be removed very efficiently, while the macro roughness originating from the different layers is still present.

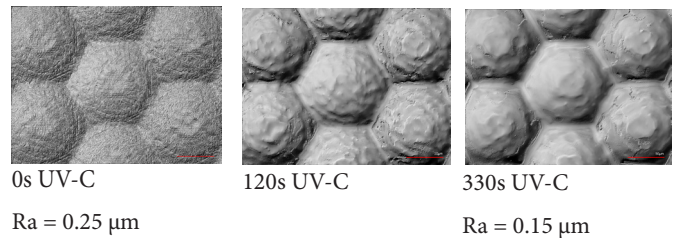


Fig. 7 Surface smoothing of embossed PMMA. Due to the low penetration depth of the UV-C rays, only the micro roughness is reduced, the macro roughness remains.

Conclusions and outlook

The originally targeted process chain currently cannot be applied. The roughness on PMMA is too large to be completely removed by the UV-assisted reflow process. However, laser ablation on PI and PEEK shows good dimensional accuracy and lower surface roughness, but still too high for optical structures. More fundamental research on the laser ablation of transparent thermoplastic is required. The reflow process on PMMA is still interesting. Further investigations on the penetration depth of the UV radiation are in process and should be completed by the end of the project. Furthermore, the formation of an amorphous boundary layer during laser ablation will be further investigated, taking into account the degradation pathways of polymers during the laser ablation process [5].

References

- [1] Q. Du, T. Chen, J. Liu and X. Zeng, *Surface microstructures and chemistry of polyimide by single pulse ablation of picosecond laser*, Appl. Surf. Sci. **434**, 588-595 (2018)
- [2] R. Kirchner, H. Schift, *Thermal reflow of polymers for innovative and smart 3D structures*, Mater. Sci. Semicon. Process., **92**, 58-72 (2008)
- [3] J. Meijer, K. Du, A. Gillner, D. Hoffmann, V.S. Kovalenko, T. Masuzawa, A. Ostendorf, R. Poprawe, W. Schulz, *Laser machining by short and ultrashort pulses, state of the art and new opportunities in the age of the photons*, CIRP Annals **51**, 531-550 (2002)
- [4] A. Schleunitz, V.A. Guzenko, M. Messerschmidt, H. Atasoy, R. Kirchner, H. Schift, *Novel 3D micro- and nanofabrication method using thermally activated selective topography equilibration (TASTE) of polymers*, Nano Convergence **1**(7) (2014)
- [5] A. Pascual, M. Toma, P. Tsoira, M.C. Grob, *On the stability of PEEK for short processing cycles at high temperatures and oxygen-containing atmosphere*, Polymer Deg. Stab. **165**, 161-169 (2019)

Novel cancer-targeted nanoparticles

Project A14.13: NCTNano (University of Basel, Dept. of Chemistry, D-BSSE ETH Basel, TargImmune Therapeutics, Basel)

Project Leader: M. Zigler

Collaborators: S.-L. Abram, A. Jarzebinska, J. Schreiber, I. Craciun, Y. Benenson, and C. G. Palivan

Challenges in cancer therapy

Significant advances have been made in the field of cancer therapy in the past few years. Numerous treatment modalities have been developed and approved for solid tumors including small molecules, antibodies and cell-based therapies. However, most of them are non-curative and resistance continuously emerges due to tumor heterogeneity as well as escape from anti-tumor immune responses. Thus, cancer remains a major contributor to morbidity and mortality worldwide. In the last decade, the huge potential of immune system activation has been recognized and several approaches were developed such as: anti-cancer antibodies, therapeutic and prophylactic vaccines, pattern recognition receptor agonists [1] or CAR-T cells [2].

Profound effects of synthetic dsRNA analogues in anti-tumor therapy have led to cancer-directed human immunotherapy studies, with some limited success as adjuvants [3]. However, as in the case with any nucleic acid-based therapy, the bottleneck is payload delivery: it has to be protected from enzymatic degradation, delivered to the target cells, internalized and released from endosomes into the cytosolic compartment depending on the final cellular target. Therefore, the focus in the field has shifted towards designing efficient delivery systems. In this respect, nanoscience-based solutions are the main focal point due to their ability to combine efficient protection of the payload with targeting and improved cellular uptake [4]. Since systemic delivery of nucleic acid analogues in a non-targeted manner can be toxic due to strong systemic immune response, targeted delivery systems are highly desired [1].

Generating a holistic therapy by Novel Cancer-Targeted Nanoparticles

A unique chemical vector system for nucleic acid delivery that can potentially overcome these challenges is developed by TargImmune Therapeutics. This vector exploits receptor overexpression as a trojan horse to target cancer cells selectively for the efficient delivery of a synthetic dsRNA analogue as active pharmaceutical ingredient (API). Successful intracellular delivery mimics viral infection and thus induces cancer cell death while simultaneously stimulating anti-tumor immunity, generating a holistic anti-tumor therapy. The primary aim of the NCTNano project is to obtain detailed insights into the structure and morphology of the nanoparticles assembled from the chemical vector and the API, called TAR001. Secondly, the project addresses the Mode of Action (MoA) and uptake mechanisms of TAR001 to validate their *in vitro* behavior. These data will be useful to deduce structure-activity relationships that will help to evaluate the efficacy of different formulations, and to define Drug Product Specifications suitable for an Investigational New Drug (IND) submission and progressing to Phase I clinical trials.

Physicochemical characterization: nanoparticle morphology

Nucleic acid delivery by nanocarriers (efficacy and safety), is strongly affected by their physicochemical properties such as size, shape and surface charge (represented by zeta potential) [5]. Importantly, these properties might change over time depending on the storage medium or temperature. Freshly prepared nanoparticles were subjected to dynamic light scatter-

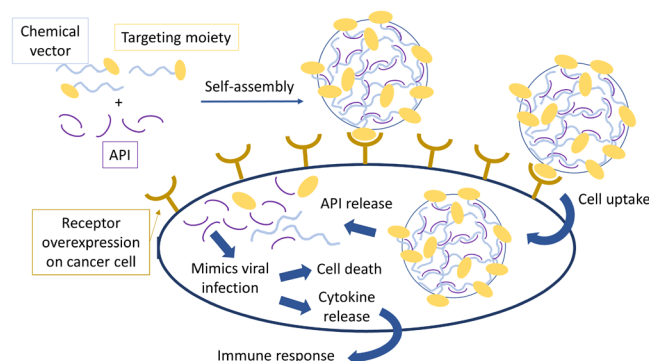


Fig. 1 Concept of anti-tumor immunotherapy using TargImmune Therapeutics' platform technology Cancer-Targeted Nanoparticles.

ing (DLS) measurements, nanoparticle tracking analysis (NTA) and transmission electron microscopy (TEM). By utilizing these three complementary techniques, we were able not only to determine the particle size distribution, but also estimate the particle concentration (NTA) and study their morphology and shape (TEM). Moreover, the stability of the samples was assessed by investigating changes of the z-average diameter obtained from DLS measurements in backscattering mode over time. With this panel of physicochemical methods, we systematically studied the influence of the API's molecular weight, the vector composition and the formulation on the nanoparticles and their reproducibility.

Figure 2 shows that the chosen techniques gave coherent results and were suitable to identify some critical quality attributes of the nanoparticles. Utilizing nanoparticles varying in composition and formulation, we found that the high aspect ratio seen in TEM correlated to drastic increase in z-average diameter over time and multiple particle populations in NTA. Low efficiency in particle formation could be identified by ill-defined shapes in TEM, low concentrations and smaller particle sizes in NTA and DLS. Cross-correlation of the physicochemical properties of different nanoparticles and formulations with their biological activity *in vitro*, enabled us to propose draft specifications of our API, gain better understanding of TAR001 structure-activity relationships and advance the further formulation development.

Components of TAR001 were fluorescently labelled by random alkylation of RNA (Cy5 label) and covalent binding of Alexa Fluor 488 to the vector. The labeling density of RNA was optimized by measuring size distribution (DLS), cytotoxicity and brightness of three differently labeled molecules. Fluorescence correlation spectroscopy (FCS) measurements confirmed sufficient brightness of the lowest dye concentration labeling. Further studies with fluorescently labeled nanoparticles will facilitate quantification of the free components, evaluation of the stability in biofluids as well as understanding the uptake mechanism and intracellular fate of the nanoparticles.

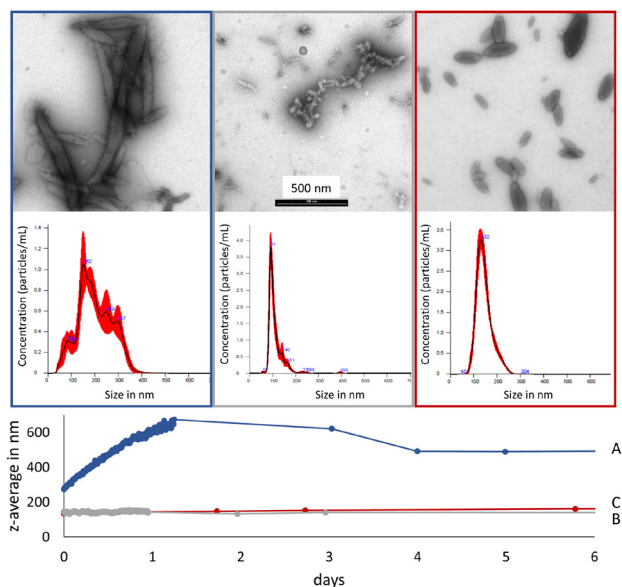


Fig. 2 Three exemplary characterization results of TAR001 depending on formulation as well as chemical composition of vector and API. Compound and formulation from Left to right; A (Blue), B (Grey), C (Red). From top to bottom: TEM, NTA, and DLS measurements.

Mode of Action: pathway activation and downstream effects

To shed light on Cancer-Targeted Nanoparticles' mode of action (MoA), we deep sequenced treated and untreated cells on Illumina's Nextseq platform. 2'600 out of 50'000 transcripts were differentially regulated, with high consistency between duplicates. Key results include: i) Cancer-Targeted Nanoparticles caused differential gene expression in a dose-dependent manner and ii) TAR001-regulated transcripts included genes with immunological relevance and distinct transcription factor families. Both are eligible to serve as genetic reporters in future experiments.

Following the successful completion of the pilot experiment, we are now re-examining the TAR001-mediated transcriptional changes, using the necessary replicates for a comprehensive statistical analysis, and including as controls cell lines that are unresponsive towards TAR001 due to low receptor expression, non-tumorigenic cells, and cells treated with non-functional API-mimics or without the payload.

In parallel, suitable gene candidates, which are differentially expressed could be exploited to develop reporters for TAR001 efficacy. We have selected a set of cytokines to be tested in ELISAs, as well as transcription factors, for which appropriate transcriptional activity assays can be developed. This could form the basis for medium-throughput screening of the formulations and facilitate biomarker choice for clinical studies.

Summary and conclusion

The obtained data, supported by SNI, significantly contributed to the development of TAR001 and advanced the program towards IND. The studies conducted, supported setting the specifications for the TAR001 components and its formulation development as well as preliminary insight on the MoA.

A panel of physicochemical methods for the characterization of TAR001 nanoparticles were established during this project along with preliminary understanding of the structure-activity relationships. Further studies will be also complemented by additional methods including atomic force microscopy, cryo-TEM and static light scattering experiments.

The pilot MoA study revealed transcriptional changes indicating the pathways activated upon TAR001 treatment. Further studies will enable selection of potential molecular reporters of TAR001 efficacy that will be utilized for medium-throughput screen of TAR001 variants.

References

- [1] A. Levitzki, *Targeting the Immune System to Fight Cancer Using Chemical Receptor Homing Vectors Carrying Polyinosine/Cytosine (PolyIC)*, *Front Oncol*, **2**, 4 (2012)
- [2] S. Kakarla, S. Gottschalk, *CAR T cells for solid tumors: armed and ready to go?*, *Cancer Journal*, **20**, 151-155 (2014)
- [3] D. Schaffert, M. Kiss, W. Rodl, A. Shir, A. Levitzki, M. Ogris, E. Wagner, *Poly(I:C)-mediated tumor growth suppression in EGF-receptor overexpressing tumors using EGF-polyethylene glycol-linear polyethylenimine as carrier*, *Pharm Res*, **28**, 731-741 (2011)
- [4] G. Gunkel-Grabole, S. Sigg, M. Lomora, S. Lörcher, C. G. Palivan, W. P. Meier, *Polymeric 3D nano-architectures for transport and delivery of therapeutically relevant bio-macromolecules*, *Biomaterials Science*, **3(1)**, 25-40 (2015)
- [5] F. Caputo, J. Clogston, L. Calzolari, M. Rosslein, A. Prina-Mello, *Measuring particle size distribution of nanoparticle enabled medicinal products, the joint view of EUNCL and NCI-NCL. A step by step approach combining orthogonal measurements with increasing complexity*, *J Control Release*, **299**, 31-43 (2019)

Nano-in-nano composites for bioresponsive drug delivery

Project A14.15: PERIONANO (FHNW Muttentz, University of Basel HFZ, Credentis AG Windisch)

Project Leader: F. Koch

Collaborators: O. Germershaus, U. Pieles, S. Stübinger, and M. Hug

Introduction

Peri-implant inflammations represent serious diseases after dental implant treatment, which affect the surrounding hard and soft tissue. Due to prevalence of up to 56%, peri-implantitis can ultimately lead to the loss of the implant without prevention and appropriate therapeutic treatment. For the treatment of peri-implant disease, various conservative approaches are available, such as application of systemic or local antibiotics. Most of the current therapeutic approaches aim at eliminating the bacterial infection. However, a treatment strategy that possesses antimicrobial as well as regenerative potential is still missing.

Within this project, an easily applicable construct based on self-assembling peptides that possess antimicrobials as well as regenerative potential will be developed. To this end, a variety of nano- and microcapsules containing different drugs will be combined with a hydrogel matrix possessing regenerative potential. This composite material is intended to support the physiological wound healing process by providing a suitable environment for cell migration, tissue regeneration and local suppression of microbial growth.

Evaluation of therapeutic compounds

Prior to the development of compound-loaded particles, a detailed evaluation of suitable compounds was performed. This evaluation on the one hand included selection of compounds based on review of the scientific literature, and on the other hand on the investigation of key properties of the selected compounds.

Eight different compounds were selected for further investigation within the study based on a literature study focusing on the indication and route of application of the envisaged drug delivery system, on the availability of drug master files as well as on physicochemical properties such as solubility in aqueous media, estimated diffusivities and molecular properties (e.g. molecular weight, charged moieties at physiological pH). These compounds belonged to different therapeutic classes, ultimately enabling a drug delivery system combining different therapeutic actions.

Subsequently, several of the selected compounds were investigated with regards to their regenerative potential *in vitro*. Two different cell culture models were applied, focusing on proliferative potential and osteogenic differentiation. The results showed incubation time dependent effects of the investigated compounds, necessitating careful optimization of time until readout. However, a key biomarker for cell proliferation was affected by most of the selected compounds, further supporting their proliferative potential.

The proliferative potential was also assessed by scratch assay, monitoring the efficiency of closure of a cell gap in a cell monolayer *in vitro*. Compounds with proliferative potential result in increased cell spreading and proliferation leading to faster closure of the cell gap compared to cell culture medium control without the compound. The assay was established using a suitable cell line and was tested using two different compounds at different concentration and at different timepoints (Fig. 1). Pronounced improvement of cell proliferation was ob-

served in the presence of both compounds after incubation for 21 h, confirming results of the previously performed assays. Investigation of the remaining compounds and quantitative analysis of the results is ongoing.

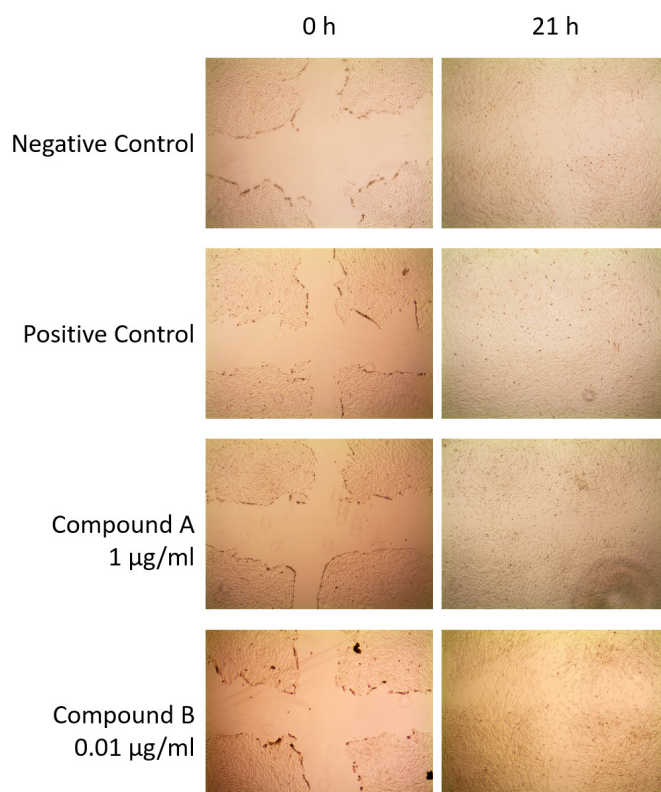


Fig. 1 Evaluation of proliferative potential using scratch assay after 21 h incubation. Cell culture medium without fetal bovine serum (FBS) was used as negative control, medium with FBS was used as positive control. Incubation of compounds was performed in the absence of FBS.

These experiments confirmed effective concentrations in the range of 0.1 to 1 µg/mL, which will be used as a starting point for the development of compound-loaded particles and will be further refined in the course of the following experiments.

Preparation of compound-loaded particles

The envisaged composite system requires development of various particulate delivery systems employing different compounds. The focus of the first stage of development was put on efficient generation of various particle types, efficient compound encapsulation within these particles and suitable release characteristics. A biodegradable and regulatory acceptable polyester matrix was used for the preparation of micro- as well as nanoparticles. Furthermore, several different natural polymer matrices were investigated.

Development of compound-loaded microparticles was initiated using one of the selected compounds by testing several different preparation techniques, including single emulsion, double emulsion, and suspension-based encapsulation. As ex-

pected, preparation technique affected microparticle diameter (Fig. 2), encapsulation efficiency and drug release. As the selected compound was quite hydrophilic, suspension-based encapsulation was found to be the most efficient encapsulation method. However, encapsulation efficiency was still not fully satisfactory; further optimization of the process is ongoing.

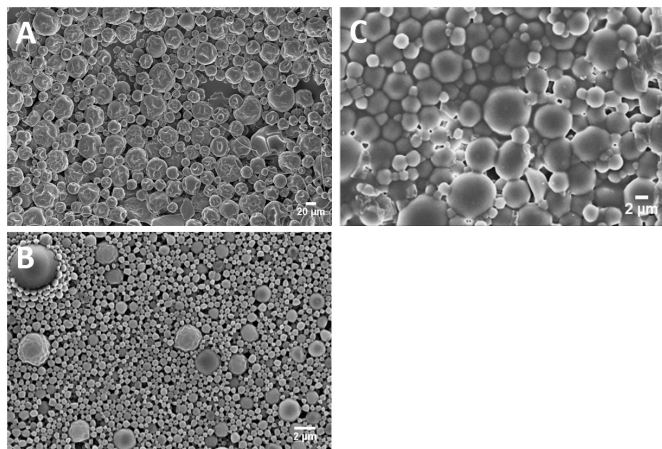


Fig. 2 Evaluation of particle size and morphology of compound-loaded particles by scanning electron microscopy. (A) particles obtained using single emulsion technique, (B) particles obtained using double emulsion process and (C) particles obtained from suspension-based process

Based on the results obtained in the first set of encapsulation experiments, subsequent encapsulation of hydrophilic compounds was mainly performed by suspension-based methods.

Four further compounds were successfully encapsulated using suspension-based processing into microparticles and compound release was investigated using compound-specific analytical methods (Fig. 3).

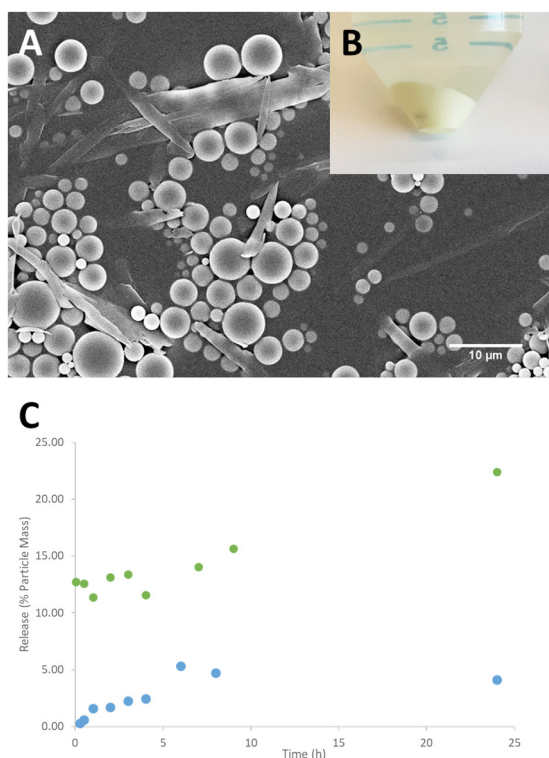


Fig. 3 Encapsulation of Compound A into polyester-based microparticles using suspension-based process. (A) Scanning electron micrograph of particles, (B) macroscopic appearance of microparticles after first centrifugation step, (C) drug release from microparticles using water (blue points) and phosphate buffered saline solution with Polysorbate 80 (green points) as release medium.

It was found that the developed encapsulation method resulted in microparticles of appropriate size and morphology and with suitable encapsulation efficiency for most compounds. Drug release characteristics varied significantly, which can be mainly attributed to different physico-chemical characteristics of the compounds.

Finally, preparation of compound-loaded nanoparticles was established. The preparation was based on single emulsion – solvent evaporation process. Through selection of suitable surfactants and process conditions, not only microparticles, but also nanoparticles could be prepared. It was found that compound-loaded nanoparticles of approximately 300 nm with zeta potential of approximately -25 mV with appropriate encapsulation efficiency could be prepared. Drug release was investigated using a compound-specific analytical method and was found to be quick and characterized by drug supersaturation in the release medium at early timepoints.

Summary and outlook

Several compounds were evaluated with regards to their suitability for the intended delivery system and indication, both through literature review as well as in vitro testing, and were selected for further investigation. Subsequently, different methods for the preparation of micro- and nanoparticles were evaluated. It was found that both, micro- and nanoparticles could be successfully prepared. Future studies will focus on optimization of compound encapsulation and -release. Subsequently, compound-loaded particles will be incorporated into a hydrogel matrix, and stability of this composite as well as compound release will be optimized.

Customized, nanostructured grating compressors for high repetition rate ultrafast laser

Project A14.19: UltraNanoGRACO (CSEM Muttenz, FHNW Windisch, Menhir Photonics AG Basel)

Project Leader: F. Lütolf

Collaborators: B. Resan, F. Emaury, G. Basset, B. Rudin, and R. Ferrini

Introduction

Grating compressors are widely used in the field of ultrafast lasers, as they allow for a technique of so called “chirped pulse amplification” (CPA). CPA is the process of stretching an ultrafast laser pulse spectrally and temporally before amplifying and finally recombining it with said compressor. This technique has proven to be absolutely crucial for reaching state of the art pulse energies as prior to CPA, the amplifier could simply not support the enormous peak energies reached in such systems.

The goal of UltraNanoGRACO is to not only build an efficient, compact and robust grating compressor, but also to find a way of customizing it for the innovative laser source developed by Menhir Photonics AG. The ambitious goal thereby is the recompression of higher order phase components present in the pulse, which cannot be compensated for by simple adjustments in the compressor. To that end, nanostructured optical components will be developed and tested during the project.

The grating compressor

The operating principle of a grating compressor as used in the current project is outlined in figure 1: The stretched pulse impinges on a first grating, which disperses the pulse into its spectral components. Two lenses focus and re-collimate this output, before the laser light is sent through the setup a second time in reverse. This specific geometry is called a “4-f compressor layout”, where f stands for the focal distance of the lens used. Assuming $L=f$ in figure 1, the distance between the two gratings would be exactly four times f . In that case, the pulse would pass through the system without any distortions. By changing L , the quadratic dispersion introduced to the incoming light pulse can seamlessly be tuned.

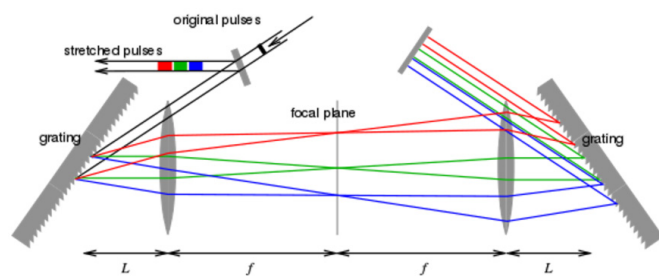


Fig. 1 4-f compressor layout

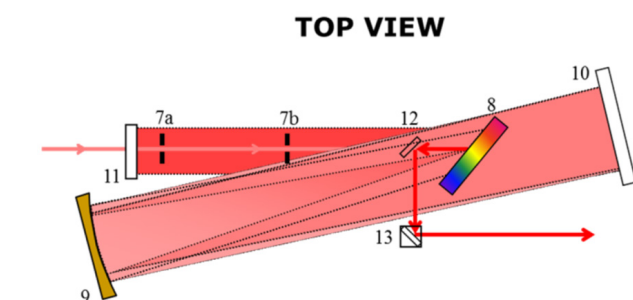


Fig. 2 Example of a folded compressor design

The final layout in development at FHNW will rely on a folded version of this compressor, which minimizes the footprint of the system and will rely on a single grating operated in transmission. The detailed design will be one of the main topics of the second phase of the project but figure 2 gives an impression of how such a folded version could look like.

The gratings

The clearly most important components in a grating compressor are the actual gratings. The optical grating separates the light pulse into its spectral components much like a spectrophotometer. It is worth noting that the light travels through each grating twice, which means that there are four diffraction events taking place. This underlines the importance of the grating quality, as any loss would scale to the power of four and a respectable grating efficiency of about 80% would lead to an overall performance of only 41%. The ambitious target for the efficiency in this project was hence set to be 97% at the main wavelength of 1550 nm, which could be reached in the simulations shown in figure 2 with a rather simple grating geometry. The best fabricated grating could achieve 88% so far and by applying an antireflective coating, this number could ideally increase by another 6 - 7% and come very close to the theoretical maximum.

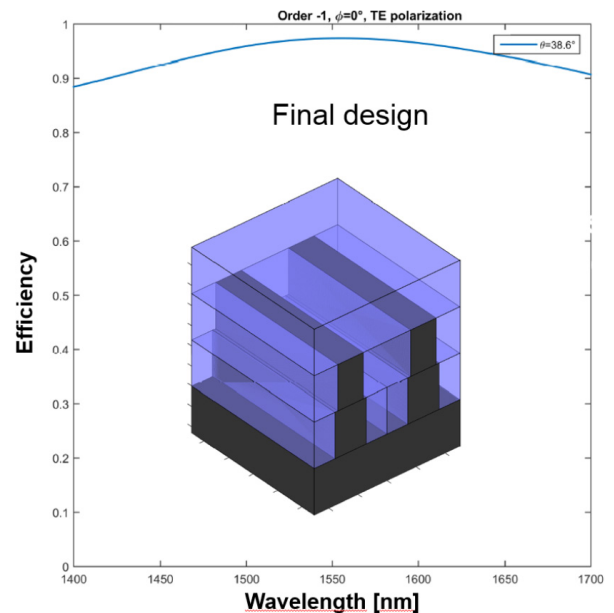


Fig. 3 Grating model used to reach 97% efficiency

Sub-wavelength nanostructures were determined to be the best solution for antireflection as they should achieve decent anti-reflective properties with < 1% residual reflectivity, while being easily scalable in fabrication. Multilayer stacks, so called Bragg reflectors, would be the main alternative and the gold standard for antireflection, but they are much more intricate to fabricate. In this project we aim for a purely replication-based production, with the diffraction grating replicated on the front side, and an antireflective structure on the back-side of a quartz substrate. Clear advantages of such a process are its reproducibility and cost-efficiency.

While the antireflective structure is straight-forward to replicate, the deep grating structure is not. A process relying on a semi-soft mold was developed and could successfully be utilized to replicate $\frac{1}{4}$ of a wafer (Fig. 3), but scaling the process to full-wafer is still a final challenge to be tackled in the second phase. In summary, the development of the grating solution was very successful, and all preliminary tests suggest that a reliable supply of efficient components can be ensured with a cost-efficient process for the 2nd phase of the project and beyond.

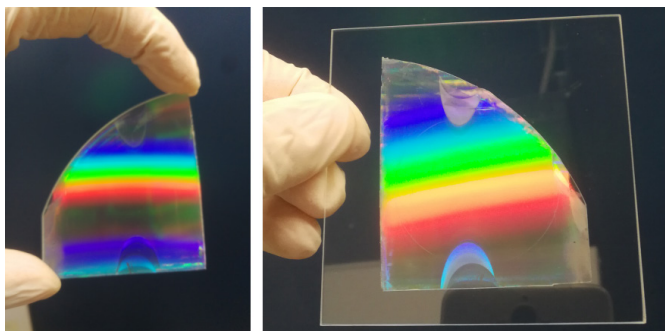


Fig. 4 The original grating (left) and its replica (right)

The laser

The first lasers developed and assembled by Menhir Photonics AG were already able to reach more than 1 W of power at 1 GHz frequency after the first year. They are a turn key solution with a very compact and robust design; all properties which should finally also apply to the compressor.

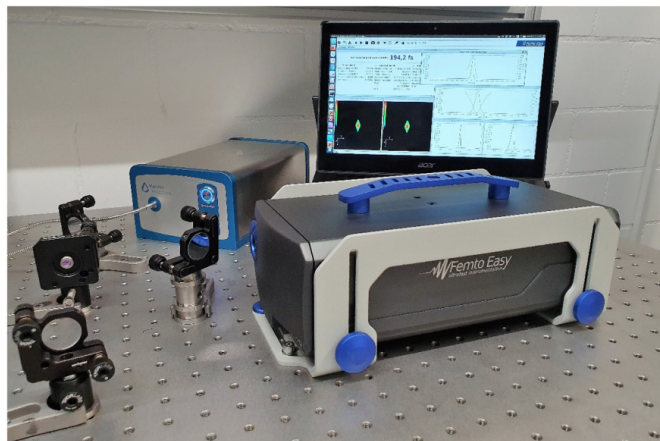


Fig. 5 The compact laser source of Menhir Photonics (without amplifier/compressor) shown together with the FROG from FemtoEasy.

Pulses have been measured with a FROG instrument from FemtoEasy (Fig. 5) after compression with an assembly based on the design from FHNW detailed in figure 1 and built with the gratings manufactured by CSEM. The results are shown in figure 5.

The pulses were stretched to 8 ps during amplification but could be properly recompressed to < 250 fs with the compressor developed in the project. Figure 5 shows the presence of higher order residual phase though, which has to be compensated if pulses should become even shorter. In the end, this very specific phase behavior asks for a customized solution and tackling this very problem will be the main subject of the second phase of the project.

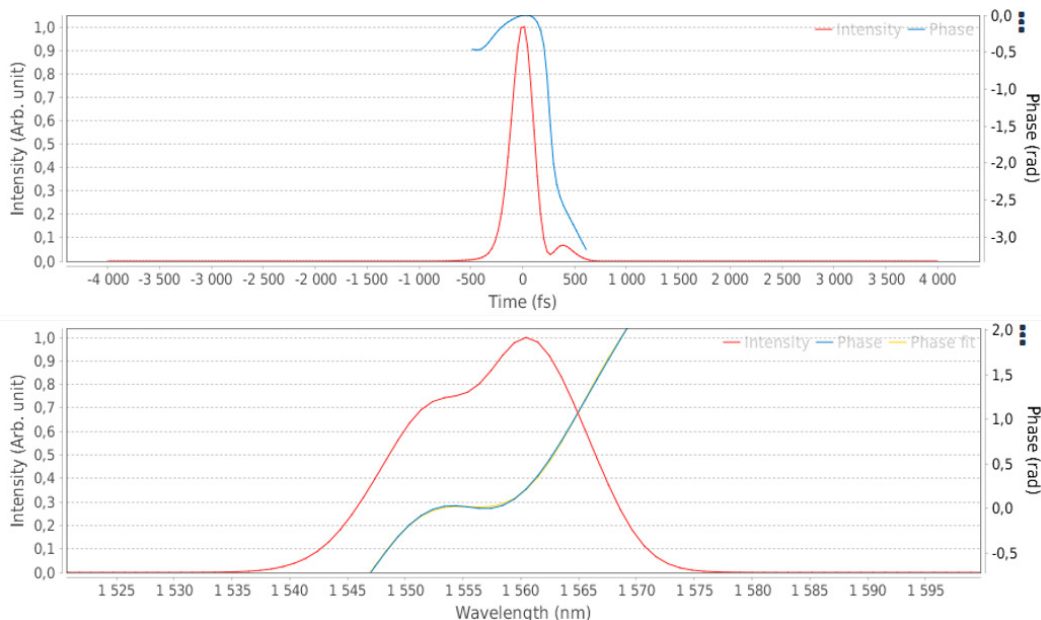


Fig. 6 Pulses of Menhir Photonics' laser after recompression

Publication list (peer-reviewed)

Acosta VM, Bouchard LS, Budker D, Folman R, Lenz T, Maletinsky P, et al. *Color Centers in Diamond as Novel Probes of Superconductivity*. J Supercond Nov Magn. **32(1)**, 85-95, <https://doi.org/10.1007/s10948-018-4877-3> (2019)

Aeschi Y, Drayss-Orth S, Valasek M, Haussinger D, Mayor M. *Aqueous Assembly of Zwitterionic Daisy Chains*. Chem-Eur J. **25(1)**, 285-95, <https://doi.org/10.1002/chem.201803944> (2019)

Aeschi Y, Jucker L, Haussinger D, Mayor M. *Slow Formation of Pseudorotaxanes in Water*. Eur J Org Chem. **2019(21)**, 3384-90, <https://doi.org/10.1002/ejoc.201801864> (2019)

Ahsan A, Mousavi SF, Nijs T, Nowakowska S, Popova O, Wackerlin A, et al. *Phase Transitions in Confinements: Controlling Solid to Fluid Transitions of Xenon Atoms in an On-Surface Network*. Small. **15(3)**, <https://doi.org/10.1002/sml.201803169> (2019)

Ahsan A, Mousavi SF, Nijs T, Nowakowska S, Popova O, Wackerlin A, et al. *Watching nanostructure growth: kinetically controlled diffusion and condensation of Xe in a surface metal organic network*. Nanoscale. **11(11)**, 4895-903, <https://doi.org/10.1039/C8NR09163C> (2019)

Appel P, Shields BJ, Kosub T, Hedrich N, Hubner R, Fassbender J, et al. *Nanomagnetism of Magnetoelectric Granular Thin-Film Antiferromagnets*. Nano Lett. **19(3)**, 1682-7, <https://doi.org/10.1021/acs.nanolett.8bo4681> (2019)

Avsar SY, Kyropoulou M, Di Leone S, Schoenenberger CA, Meier WP, Palivan CG. *Biomolecules Turn Self-Assembling Amphiphilic Block Co-polymer Platforms Into Biomimetic Interfaces*. Front Chem. **6**, <https://doi.org/10.3389/fchem.2018.00645> (2019)

Barfuss A, Kasperczyk M, Kolbl J, Maletinsky P. *Spin-stress and spin-strain coupling in diamond-based hybrid spin oscillator systems*. Phys Rev B. **99(17)**, <https://doi.org/10.1103/PhysRevB.99.174102> (2019)

Braakman FR, Poggio M. *Force sensing with nanowire cantilevers*. Nanotechnology. **30(33)**, <https://doi.org/10.1088/1361-6528/ab19cf> (2019)

Brunner MAT, Rufenacht S, Bauer A, Erpel S, Buchs N, Braga-Lagache S, et al. *Bald thigh syndrome in sighthounds-Revisiting the cause of a well-known disease*. Plos One. **14(2)**, <https://doi.org/10.1371/journal.pone.0212645> (2019)

Camenzind LC, Yu LQ, Stano P, Zimmerman JD, Gossard AC, Loss D, et al. *Spectroscopy of Quantum Dot Orbitals with In-Plane Magnetic Fields*. Phys Rev Lett. **122(20)**, <https://doi.org/10.1103/PhysRevLett.122.207701> (2019)

Ceccarelli L, Vasyukov D, Wyss M, Romagnoli G, Rossi N, Moser L, et al. *Imaging pinning and expulsion of individual superconducting vortices in amorphous MoSi thin films*. Phys Rev B. **100(10)**, <https://doi.org/10.1103/PhysRevB.100.104504> (2019)

Clabbers MTB, Gruene T, van Genderen E, Abrahams JP. *Reducing dynamical electron scattering reveals hydrogen atoms*. Acta Crystallogr A. **75**, 82-93, <https://doi.org/10.1107/S2053273318013918> (2019)

De Luca M, Fasolato C, Verheijen MA, Ren YZ, Swinkels MY, Kolling S, et al. *Phonon Engineering in Twinning Superlattice Nanowires*. Nano Lett. **19(7)**, 4702-11, <https://doi.org/10.1021/acs.nanolett.9bo1775> (2019)

Ditzinger F, Scherer U, Schonenberger M, Holm R, Kuentz M. *Modified Polymer Matrix in Pharmaceutical Hot Melt Extrusion by Molecular Interactions with a Carboxylic Coformer*. Mol Pharmaceut. **16(1)**, 141-50, <https://doi.org/10.1021/acs.molpharmaceut.8bo0920> (2019)

Dutta D, De DS, Fan D, Roy S, Alfieri G, Camarda M, et al. *Evidence for carbon clusters present near thermal gate oxides affecting the electronic band structure in SiC-MOSFET*. Appl Phys Lett. **115(10)**, <https://doi.org/10.1063/1.5112779> (2019)

El Abbassi M, Sangtarash S, Liu XS, Perrin ML, Braun O, Lambert C, et al. *Robust graphene-based molecular devices*. Nat Nanotechnol. **14(10)**, 957-+, <https://doi.org/10.1038/s41565-019-0533-8> (2019)

Fessler G, Sadeghi A, Glatzel T, Goedecker S, Meyer E. *Atomic Friction: Anisotropy and Asymmetry Effects*. Tribol Lett. **67(2)**, <https://doi.org/10.1007/s11249-019-1172-9> (2019)

Fountas PN, Poggio M, Willitsch S. *Classical and quantum dynamics of a trapped ion coupled to a charged nanowire*. New J Phys. **21**, <https://doi.org/10.1088/1367-2630/aaf8f5> (2019)

Fremy-Koch S, Sadeghi A, Pawlak R, Kawai S, Baratoff A, Goedecker S, et al. *Controlled switching of a single CuPc molecule on Cu(111) at low temperature*. Phys Rev B. **100(15)**, <https://doi.org/10.1103/physrevb.100.15427> (2019)

Freund S, Hinaut A, Marinakis N, Constable EC, Meyer E, Housecroft CE, et al. *Comparing a porphyrin- and a coumarin-based dye adsorbed on NiO(001)*. Beilstein J Nanotech. **10**, 874-81, <https://doi.org/10.3762/bjnano.10.88> (2019)

Gigli L, Kawai S, Guerra R, Manini N, Pawlak R, Feng XL, et al. *Detachment Dynamics of Graphene Nanoribbons on Gold*. ACS Nano. **13(1)**, 689-97, <https://doi.org/10.1021/acsnano.8bo7894> (2019)

Heidler J, Pantelic R, Wennmacher JTC, Zaubitzer C, Fecteau-Lefebvre A, Goldie KN, et al. *Design guidelines for an electron diffractometer for structural chemistry and structural biology*. Acta Crystallogr D. **75**, 458-66, <https://doi.org/10.1107/S2059798319003942> (2019)

Jannesar M, Sadeghi A, Meyer E, Jafari GR. *A Langevin equation that governs the irregular stick-slip nano-scale friction*. Sci Rep-Uk. **9**, <https://doi.org/10.1038/s41598-019-48345-4> (2019)

Jung M, Rickhaus P, Zihlmann S, Eichler A, Makk P, Schönenberger C. *GHz nanomechanical resonator in an ultraclean suspended graphene p-n junction*. Nanoscale. **11(10)**, 4355-61, <https://doi.org/10.1039/C8NR09963D> (2019)

Junger C, Baumgartner A, Delagrance R, Chevallier D, Lehmann S, Nilsson M, et al. *Spectroscopy of the superconducting proximity effect in nanowires using integrated quantum dots*. Commun Phys-Uk. **2**, <https://doi.org/10.1038/s42005-019-0162-4> (2019)

- Karg TM, Gouraud B, Treutlein P, Hammerer K. *Remote Hamiltonian interactions mediated by light*. Phys Rev A. **99**(6), <https://doi.org/10.1103/PhysRevA.99.063829> (2019)
- Kassianidou E, Kalita J, Lim RYH. *The role of nucleocytoplasmic transport in mechanotransduction*. Exp Cell Res. **377**(1-2), 86-93, <https://doi.org/10.1016/j.yexcr.2019.02.009> (2019)
- Kolbl J, Kasperczyk M, Burgler B, Barfuss A, Maletinsky P. *Determination of intrinsic effective fields and microwave polarizations by high-resolution spectroscopy of single nitrogen-vacancy center spins*. New J Phys. **21**(11), <https://doi.org/10.1088/1367-2630/ab54a8> (2019)
- Krieg M, Fläschner G, Alsteens D, Gaub BM, Roos WH, Wuite GJL, et al. *Atomic force microscopy-based mechanobiology*. Nature Reviews Physics. **1**(1), 41-57, <https://doi.org/10.1038/s42254-018-0001-7> (2019)
- Lennon DT, Moon H, Camenzind C, Yu LQ, Zumbuhl DM, Briggs GAD, et al. *Efficiently measuring a quantum device using machine learning*. Npj Quantum Inform. **5**, <https://doi.org/10.1038/s41534-019-0193-4> (2019)
- Makita M, Vartiainen I, Mohacsi I, Coleman C, Diaz A, Jönsson HO, et al. *Femtosecond phase-transition in hard x-ray excited bismuth*. Sci Rep-Uk. **9**(1), 602, <https://doi.org/10.1038/s41598-018-36216-3> (2019)
- Mendil J, Trassin M, Bu Q, Schaab J, Baumgartner M, Murer C, et al. *Magnetic properties and domain structure of ultra-thin yttrium iron garnet/Pt bilayers*. Physical Review Materials. **3**(3), 034403, <https://doi.org/10.1103/PhysRevMaterials.3.034403> (2019)
- Moradi M, Opara NL, Tulli LG, Wackerlin C, Dalgarno SJ, Teat SJ, et al. *Supramolecular architectures of molecularly thin yet robust free-standing layers*. Sci Adv. **5**(2), eaav4489, <https://doi.org/10.1126/sciadv.aav4489> (2019)
- Neumann S, Kerzig C, Wenger OS. *Quantitative insights into charge-separated states from one- and two-pulse laser experiments relevant for artificial photosynthesis*. Chem Sci. **10**(21), 5624-33, <https://doi.org/10.1039/C9SC01381D> (2019)
- Neumann S, Wenger OS. *Fundamentally Different Distance Dependences of Electron-Transfer Rates for Low and High Driving Forces*. Inorg Chem. **58**(1), 855-60, <https://doi.org/10.1021/acs.inorgchem.8b02973> (2019)
- Oliva P, Bircher BA, Schoenenberger CA, Braun T. *Array based real-time measurement of fluid viscosities and mass-densities to monitor biological filament formation*. Lab Chip. **19**(7), 1305-14, <https://doi.org/10.1039/c8lc01343h> (2019)
- Overbeck J, Barin GB, Daniels C, Perrin ML, Braun O, Sun Q, et al. *A Universal Length-Dependent Vibrational Mode in Graphene Nanoribbons*. ACS Nano. **13**(11), 13083-91, <https://doi.org/10.1021/acsnano.9b05817> (2019)
- Overbeck J, Borin Barin G, Daniels C, Perrin ML, Liang L, Braun O, et al. *Optimized Substrates and Measurement Approaches for Raman Spectroscopy of Graphene Nanoribbons*. physica status solidi (b). **256**(12), 1900343, <https://doi.org/10.1002/pssb.201900343> (2019)
- Panatala R, Barbato S, Kozai T, Luo JH, Kapinos LE, Lim RYH. *Nuclear Pore Membrane Proteins Self-Assemble into Nanopores*. Biochemistry-US. **58**(6), 484-8, <https://doi.org/10.1021/acs.biochem.8b01179> (2019)
- Pawlak R, Hoffman S, Klinovaja J, Loss D, Meyer E. *Majorana fermions in magnetic chains*. Prog Part Nucl Phys. **107**, 1-19, <https://doi.org/10.1016/j.pnpnp.2019.04.004> (2019)
- Pawlak R, Vilhena JG, Hinaut A, Meier T, Glatzel T, Baratoff A, et al. *Conformations and cryo-force spectroscopy of spray-deposited single-strand DNA on gold*. Nat Commun. **10**, <https://doi.org/10.1038/s41467-019-08531-4> (2019)
- Piquero-Zulaica I, Abd El-Fattah ZM, Popova O, Kawai S, Nowakowska S, Matena M, et al. *Effective determination of surface potential landscapes from metal-organic nanoporous network overlayers*. New J Phys. **21**, <https://doi.org/10.1088/1367-2630/ab150e> (2019)
- Rath P, Sharpe T, Kohl B, Hiller S. *Two-State Folding of the Outer Membrane Protein X into a Lipid Bilayer Membrane*. Angew Chem Int Edit. **58**(9), 2665-9, <https://doi.org/10.1002/anie.201812321> (2019)
- Rehmann MK, Kalyoncu YB, Kisiel M, Pascher N, Giessibl FJ, Muller F, et al. *Characterization of hydrogen plasma defined graphene edges*. Carbon. **150**, 417-24, <https://doi.org/10.1016/j.carbon.2019.05.015> (2019)
- Rohner D, Happacher J, Reiser P, Tschudin MA, Tallaire A, Achard J, et al. *(111)-oriented, single crystal diamond tips for nanoscale scanning probe imaging of out-of-plane magnetic fields*. Appl Phys Lett. **115**(19), <https://doi.org/10.1063/1.5127101> (2019)
- Rossi N, Gross B, Dirnberger F, Bougeard D, Poggio M. *Magnetic Force Sensing Using a Self-Assembled Nanowire*. Nano Lett. **19**(2), 930-6, <https://doi.org/10.1021/acs.nanolett.8b04174> (2019)
- Rouse I, Willitsch S. *The energy distribution of an ion in a radiofrequency trap interacting with a nonuniform neutral buffer gas*. Mol Phys. **117**(21), 3120-31, <https://doi.org/10.1080/00268976.2019.1581952> (2019)
- Ruelle T, Poggio M, Braakman F. *Optimized single-shot laser ablation of concave mirror templates on optical fibers*. Appl Optics. **58**(14), 3784-9, <https://doi.org/10.1364/AO.58.003784> (2019)
- Schatti J, Kriegleder M, Debiossac M, Kerschbaum M, Geyer P, Mayor M, et al. *Neutralization of insulin by photocleavage under high vacuum*. Chem Commun. **55**(83), 12507-10, <https://doi.org/10.1039/C9CC05712A> (2019)
- Schmidli C, Albiez S, Rima L, Righetto R, Mohammed I, Oliva P, et al. *Microfluidic protein isolation and sample preparation for high-resolution cryo-EM*. P Natl Acad Sci USA. **116**(30), 15007-12, <https://doi.org/10.1073/pnas.1907214116> (2019)
- Schulzendorf M, Hinaut A, Kisiel M, Johr R, Pawlak R, Restuccia P, et al. *Altering the Properties of Graphene on Cu(111) by Intercalation of Potassium Bromide*. ACS Nano. **13**(5), 5485-92, <https://doi.org/10.1021/acsnano.9b00278> (2019)
- Stano P, Hsu CH, Camenzind LC, Yu LQ, Zumbuhl D, Loss D. *Orbital effects of a strong in-plane magnetic field on a gate-defined quantum dot*. Phys Rev B. **99**(8), <https://doi.org/10.1103/PhysRevB.99.085308> (2019)
- Strocov VN, Chikina A, Caputo M, Husanu MA, Bisti F, Bracher D, et al. *Electronic phase separation at LaAlO₃/SrTiO₃ interfaces tunable by oxygen deficiency*. Physical Review Materials. **3**(10), <https://doi.org/10.1103/PhysRevMaterials.3.106001> (2019)

Syntyckaki A, Rima L, Schmidli C, Stohler T, Bieri A, Sutterlin R, et al. "Differential Visual Proteomics": Enabling the Proteome-Wide Comparison of Protein Structures of Single-Cells. *J Proteome Res.* **18(9)**, 3521-31, <https://doi.org/10.1021/acs.jproteome.9b00447> (2019)

Thiel L, Wang Z, Tschudin MA, Rohner D, Gutierrez-Lezama I, Ubrig N, et al. *Probing magnetism in 2D materials at the nanoscale with single-spin microscopy.* *Science.* **364(6444)**, 973-+, <https://doi.org/10.1126/science.aav6926> (2019)

Vijayakumar J, Bracher D, Savchenko TM, Horisberger M, Nolting F, Vaz CAF. *Electric field control of magnetism in Si₃N₄ gated Pt/Co/Pt heterostructures.* *J Appl Phys.* **125(11)**, <https://doi.org/10.1063/1.5083148> (2019)

Vladyka A, Perrin ML, Overbeck J, Ferradas RR, Garcia-Suarez V, Gantenbein M, et al. *In-situ formation of one-dimensional coordination polymers in molecular junctions.* *Nat Commun.* **10**, <https://doi.org/10.1038/s41467-018-08025-9> (2019)

Wang LJ, Zihlmann S, Baumgartner A, Overbeck J, Watanabe K, Taniguchi T, et al. *In Situ Strain Tuning in hBN-Encapsulated Graphene Electronic Devices.* *Nano Lett.* **19(6)**, 4097-102, <https://doi.org/10.1021/acs.nanolett.9b01491> (2019)

Wang LJ, Zihlmann S, Liu MH, Makk P, Watanabe K, Taniguchi T, et al. *New Generation of Moire Superlattices in Doubly Aligned hBN/Graphene/hBN Heterostructures.* *Nano Lett.* **19(4)**, 2371-6, <https://doi.org/10.1021/acs.nanolett.8b05061> (2019)

Weiland KJ, Brandl T, Atz K, Prescimone A, Haussinger D, Solomek T, et al. *Mechanical Stabilization of Helical Chirality in a Macrocyclic Oligothiophene.* *J Am Chem Soc.* **141(5)**, 2104-10, <https://doi.org/10.1021/jacs.8b11797> (2019)

Weiland KJ, Munch N, Gschwind W, Haussinger D, Mayor M. *A Chiral Macrocyclic Oligothiophene with Broken Conjugation - Rapid Racemization through Internal Rotation.* *Helv Chim Acta.* **102(1)**, <https://doi.org/10.1002/hlca.201800205> (2019)

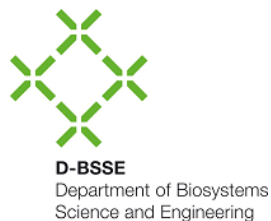
Wennmacher JTC, Zaubitzer C, Li T, Bahk YK, Wang J, van Bokhoven JA, et al. *3D-structured supports create complete data sets for electron crystallography.* *Nat Commun.* **10**, <https://doi.org/10.1038/s41467-019-11326-2> (2019)

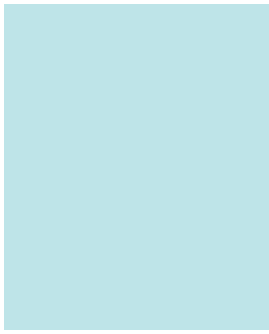
Wyss M, Gliga S, Vasyukov D, Ceccarelli L, Romagnoli G, Cui JZ, et al. *Stray-Field Imaging of a Chiral Artificial Spin Ice during Magnetization Reversal.* *Acs Nano.* **13(12)**, 13910-6, <https://doi.org/10.1021/acs.nano.9b05428> (2019)

Yildiz D, Kisiel M, Gysin U, Gurlu O, Meyer E. *Mechanical dissipation via image potential states on a topological insulator surface.* *Nat Mater.* **18(11)**, 1201-+, <https://doi.org/10.1038/s41563-019-0492-3> (2019)

Zihlmann S, Makk P, Castilla S, Gramich J, Thodkar K, Caneva S, et al. *Nonequilibrium properties of graphene probed by superconducting tunnel spectroscopy.* *Phys Rev B.* **99(7)**, <https://doi.org/10.1103/PhysRevB.99.075419> (2019)

Swiss Nanoscience Institute – A research initiative of the University of Basel and the Canton of Aargau





**Educating
Talents**
since 1460.

University of Basel
Petersplatz 1
P.O. Box 2148
4001 Basel
Switzerland
www.unibas.ch

Swiss Nanoscience Institute
University of Basel
Klingelbergstrasse 82
4056 Basel
Switzerland
www.nanoscience.ch